Agronomy Research

Established in 2003 by the Faculty of Agronomy, Estonian Agricultural University

Aims and Scope:
Agronomy Research is a peer-reviewed international Journal intended for publication of broad-spectrum original articles, reviews and short communications on actual problems of modern biosystems engineering incl. crop and animal science, genetics, economics, farm- and production engineering, environmental aspects, agro-ecology, renewable energy and bioenergy etc. in the temperate regions of the world.

***Agronomy Research* online:**
Agronomy Research is available online at: http://agronomy.emu.ee/

Acknowledgement to Referees:
The Editors of *Agronomy Research* would like to thank the many scientists who gave so generously of their time and expertise to referee papers submitted to the Journal.

Abstracted and indexed:
SCOPUS, EBSCO, CABI Full Paper and Thompson Scientific database: (Zoological Records, Biological Abstracts and Biosis Previews, AGRIS, ISPI, CAB Abstracts, AGRICOLA (NAL; USA), VINITI, INIST-PASCAL.)

Subscription information:
Institute of Technology, EULS
St. Kreutzwaldi 56, 51014 Tartu, ESTONIA
E-mail: timo.kikas@emu.ee

ISSN 1406-894X

CONTENTS

I PRODUCTION ENGINEERING 973

R. Chotěborský and M. Linda
Determination of chemical content of soil particle for abrasive wear test 975

P. Hrabě, M. Müller and Č. Mizera
Mechanical properties of polymer matrix composites filled with Jatropha Curcas L. 984

H. Kallakas, M. Martin, D. Goljandin, T. Poltimäe, A. Krumme and J. Kers
Mechanical and physical properties of thermally modified wood flour reinforced polypropylene composites 994

A. Kešner, R. Chotěborský and M. Linda
Determination of the heat flux of steel for the heat treatment model of agricultural tools 1004

T. Koppel, A. Shiskin, I. Hussainova, H. Haldre and P. Tint
Electromagnetic shielding properties of ceramic spheres coated with paramagnetic metal 1015

V. Krasnyy, V. Maksarov and J. Olt
Improving fretting resistance of heavily loaded friction machine parts using a modified polymer composition 1023

A. Krofová, P. Kic and M. Müller
Influence of dust pollution in the laboratory on the strength of adhesive bond 1034

V. Maksarov, A. Khalimonenko and J. Olt
Effect of porosity on the performance of cutting ceramics 1043

V. Mironovs, I. Boiko, T. Koppel and M. Lisicins
Cellular tubular structures from perforated metallic tape and its application 1053

V. Mironovs, O. Ozernovs, V. Lapkovskis and D. Golyandin
Production of Crumb Ruber – Iron Powder Mixture for perspective synthesis of Carbon-Iron powder sorbent 1063

Č. Mizera, D. Herák and P. Hrabě
Relaxation and creep behaviour of false banana's fibre (*Ensete ventricosum*) 1069

M. Müller and R. Chotěborský
Impact strength behaviour of structural adhesives 1078

V. Osadcuks and A. Pecka
Electrical field based detection of fruits and vegetables for robotized horticulture..... 1088

J. Sander and T. Jehlička
Use of spiral conveyor in the processing of granular waste materials..... 1099

R. Šemjakin, A. Ruus, K. Kirtsi and E. Tungel
Water vapour transmission properties of linseed oil paint 1107

P. Valášek
Study on impact strength of sisal fibers reinforced epoxy composites using experimental methods 1116

J. Volf, V. Novák and V. Ryzhenko
Effect of conductive ink on transfer characteristics of pressure into electric signal for tactile sensors 1123

A. Yonetken and A. Erol
Production and characterization of Ni-Co (WC) composites materials..... 1130

J. Zavrtálek, M. Müller and V. Šléger
Low-cyclic fatigue test of adhesive bond reinforced with glass fibre fabric..... 1138

M. Zeps, A. Gailis, J. Smilga, O. Miezite, L. Sisenis and I. Zariņa
Hybrid aspen clone wood mechanical properties..... 1147

II POWER ENGINEERING & RENEWABLE ENERGY..... 1153

M. Bloch-Michalik and M. Gaworski
Practical usage of additional heat from biogas plant 1155

A. Gedzurs
Operation reliability of induction motors at egg processing plant 'Balticovo'..... 1161

V. Malijonytė, E. Dac, F. Romagnoli and M. Gedrovics
Methodology for determining the mixing ratio of selected solid recovered fuels.... 1169

M. Mimra, M. Kavka and R. Renfus
Analysis and Evaluation of the Waste Management in the Municipality 1180

A. Mäkiranta, J.B. Martinkauppi and E. Hiltunen
Correlation between temperatures of air, heat carrier liquid and seabed sediment in renewable low energy network 1191

V. Papez and S. Papezova
Optimization of a solar power station with $LiFePO_4$ accumulators 1200

S. Papezova and V. Papez
Automated Measuring Station for Accumulator Testing 1212

Týbl, J. and P. Kic
Thermal properties and reduction of energy consumption of buildings 1222

Z. Vondrášek
Numerical Modelling of Transient Phenomena in a Synchronous Machine 1232

I PRODUCTION ENGINEERING

Agronomy Research **14**(Sp.1), 975–983, 2016

Determination of chemical content of soil particle for abrasive wear test

R. Chotěborský[1] and M. Linda[2,*]

[1]Czech University of Life Sciences in Prague, Faculty of Engineering, Department of material Science and Manufacturing Technology, Kamýcka 129, CZ 165 21 Praha – Suchdol, Czech Republic
[2]Czech University of Life Sciences in Prague, Faculty of Engineering, Department of Electrical Engineering and Automation, Kamýcka 129, CZ 165 21Praha – Suchdol, Czech Republic
[*]Correspondence: linda@tf.czu.cz

Abstract. Soil is an extremely abrasive environment that causes a change in the part dimension of agricultural tools like as chisels or ploughshares. Dry rubber wheel test according to ASTM G65 is one of standard to wear testing. For this test is used Ottawa sand (SiO2 particles) which have a spherical shape. The actual soil contains sand, but also particles of other minerals with higher or lower abrasion than sand. This article is focuses on identifying the abrasive particles in the soil by electron microscopy with EDS analysis. The results should be used for mixing the abrasive particles to the rubber wheel test, but also to identify the mineral composition of the soil profile. The aim of the research is closer to the real test of wear on the field and laboratory tests on the device with a rubber disc. Results shown that the soil contents alumina oxide particles with high hardness or silumina complex chemical composition with sharp shape. The ratio of amount these abrasive particles in the soil is influenced by geological position in earth and this ratio of particle amount influence wear rate in actual soil.

Key words: abrasives, soil particle, EDS analysis, electron microscope, rubber wheel test.

INTRODUCTION

Soil is formed due to natural weathering of rocks and it takes millions of years for soil formation. Clay minerals are the essential component of a soil in controlling its physical properties and are essential for supporting the plant growth on soils. Dominant mineral in soil – quartz is abundant in soils, mainly originating from physical weathering (fragmentation) of the parent material but also, by solution weathering, from carbonate parent materials. It may also be present as exogenous quartz through eolian deposition. (Langford et al., 2011; Chen et al., 2014; Hao et al., 2015; He et al., 2015; Martín-García et al., 2015)

Soil minerals with size upper than 0.2 mm are very abrasive and it participation on abrasive wear of agriculture tools is higher than 80 percentage (Chotěborský et al., 2008; Jankauskas et al., 2008a; Chotěborský, 2013; Kučera & Chotěborský, 2013). Compared with the unlubricated sliding wear, the value of the wear coefficient, i.e. the dimensionless quotient of the amount of volumetric wear times the hardness of the

wearing material divided by the normal load and the sliding distances, as estimated from practical experience, can be substantially greater in abrasive or erosive wear (Zimba et al., 2003; Sahin et al., 2007; Sellami et al., 2014). Wear mechanisms occurring in an actual tribosystem as a function of the operating conditions and properties of the triboelements involved, which can result in changes of the wear coefficient value by some orders of magnitude. In abrasive wear, the material is displaced or detached from the solid surface by hard particles or hard particles between or embedded in one or both of the two solid surfaces in relative motion, or by the presence of hard protuberances on the counterface sliding with the velocity v relatively along the surface (Gahr, 1998; Buchely et al., 2005; Correa et al., 2007).

General trends of the wear loss of materials depending on the properties of the abrasive particles and the wearing materials as well as the operating conditions. With increasing hardness of the abrasive particles (Fig. 1), the wear loss can increase by about one to two orders of magnitude from a low to a high level, fundamentals are described by Stachowiak's researches with respect to shape of abrasive particles (Stachowiak, 2000; Stachowiak & Stachowiak, 2001a; 2001b). Hard and soft abrasive particles, i.e. harder or softer than the reinforcing phase in matrix of composites, and also small and large sizes of the reinforcing phase are distinguished. Hard abrasive particles can easily dig out small phases and cut or crack larger ones. Soft abrasive particles are able to dig out small phases or produce large pits. The indentation depth of soft abrasive particles is substantially reduced by hard reinforcing phases if the mean free path between them is smaller than the size of the abrasive particles. Large phases deficiently bonded to the matrix can be pulled out. However, large phases strongly bonded to the matrix can blunt or fracture soft abrasive particles. This general knowledge led to inovation of new wear resistant materials, particle reinforces metallic material (Gahr, 1998; Correa et al., 2007; Jankauskas et al., 2008b; Badisch at al., 2009a; 2009b; Chotěborský et al., 2009a; 2009b; Chung et al., 2009; Kazemipour et al., 2010; Sabet et al., 2011; Chotěborský & Hrabě, 2013; Kolaříková et al., 2013; Cardoso at al., 2014). The structures of modern composites are designed considering the prevailing type and composition of mineral particles of abrasive. Mechanical propertie such as hardnes of composites are in width limits from QT steels to sintered carbides.

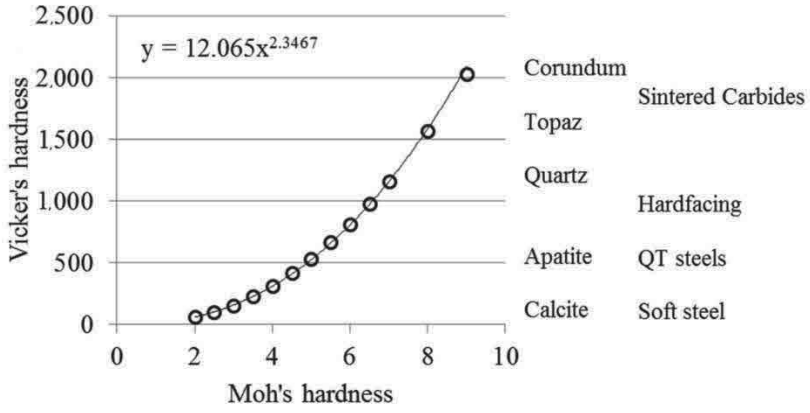

Figure 1. Relationships between Moh's and Vicker's hardness with typical minerals and engineering materials. Data taken from (Taylor et al., 1949).

The standard abrasive wear test according to ASTM G65 (ASTM G65-04, 2010) use Ottawa sand. Content of this mineral is participating in soil in major ratio. But soil also contents other minerals which are harder than sand and minerals with sharp shape. These particles with higher abrasiveness can participate on wear loss more than sand particles (Chotěborský et al., 2009a). Particles for dry rubber wheel test can be prepared as a mixture of major minerals in soil. It should lead to higher correlation between results from dry rubber wheel test and practical test on field.

The aim of this article is shown one of methods for determination minerals content in soil particle by energy dispersion spectra.

MATERIALS AND METHODS

Representative bulk samples were collected from field surface to 15 cm depth (typical depth for no tillage soil processing – soil saver chisel plow) on 3 places (fields 50°17'49.4"N 14°14'35.5"E – sample 1; 50°14'53.6"N 14°09'02.9"E – sample 2; 50°07'40.6"N 14°22'31.5"E – sample 3), sample dimension was 8 cm diameter and 15 cm hight. The soil bulk specimens were dried and fractionalized on sieves. Fractions larger than 0.1 mm were analysed using light optical microscopy and fractions were divided to translucent particles and opaque particles. Mass of particles was weighed on scales with an accuracy of 0.001 gram. Representative numbers of particles larger than 0.1 mm were cleaned, dried and casted in acrylic resin. These samples were grinded by diamond suspension and polished by colloidal suspension of alumina. The last step was analysis with scanning electron microscopy.

Light optical microscopy (LOM) was used for determination of sand particle (translucent) and others minerals. Figure analysis of LOM determinate quantitative volume of sand particle in soil. Soil particle were also analyzed by SEM-EDS (Vodyanitskii et al., 2007; Mavris et al., 2012; Pachauri, 2013; Leal et al., 2014; Venkatarama Reddy & Latha, 2014; Byeon et al., 2015; Hao et al., 2015; Ren et al., 2015; Sánchez-Marañón et al., 2015). The SEM-EDS analysis was carried out with the help of computer controlled field emission scanning electron microscope SEM (Tescan Mira 3 GXM) equipped with an energy dispersive X-ray (Oxford X-Max^N). All the samples were mounted on acrylic resin for carbon coating. A very thin film of carbon was deposited in (Quorum Q150R ES), where it prepare 6 samples at a time. The fine coating of carbon makes the samples electrically conductive. The samples were placed in the corner of SEM-EDS chamber. The working conditions were set at an accelerating voltage of 20 kV, a beam current of 40–50 μA and a Si (Li) detector 15 mm away from the samples to be analyzed. X-ray detection limit is ~0.1%. The Oxford X-Max^N EDS system, resolution at 5.9 keV – 124 eV is capable of collecting spectrum from multiple points, lines across the interface and elemental mapping.

RESULTS AND DISCUSSION

Fractionalizing analysis show that soil sample 1 contents 11 wt.% of sand particles larger than 0.1 mm, soil sample 2 contents 15 wt.% of sand particles and soil sample 3 contents 9 wt.% of sand particles. It would be possible to say that the soil sample 2 should be with higher abrasiveness than other soil samples. But abrasiveness also depends on hardness of abrasive particles, their shapes and size (Woldman et al., 2012;

Woldman et al., 2015). If we know a chemical compostion of praticles in the soil, it can be used to determination mechanical properties of particles and abrasiveness. The results from EDS analysis shown that each of soil sample contents a different volume of mineral particles.

Fig. 2 shows typical large mineral (size higher than 2 mm) particles in the soil specimens in sand fraction. The translucence particles were identified as amourfous quartz particles.

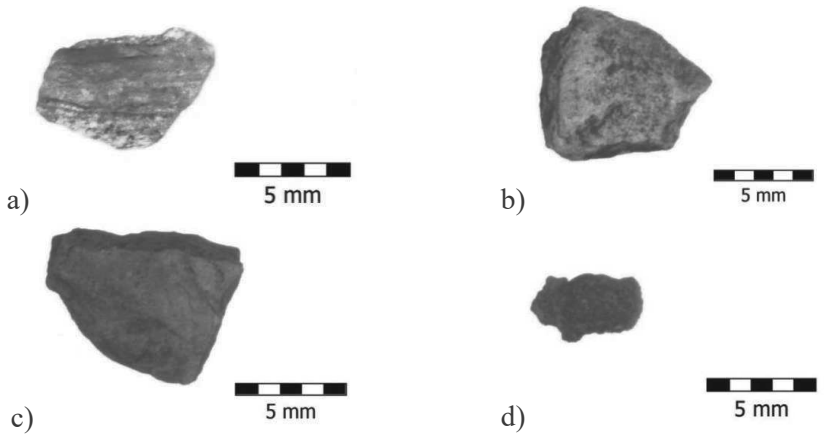

Figure 2. Picture representative large particles in soil bulk.

The opaque big particles were white, red and black. The white particle was calcium rich mineral (Fig. 3), these particles also include small size quart and silumina-alumina rich particles in the lime matrix (Fig. 4), kvantitative ratio of minerals particle was determined by EDS maps, it is shown in Fig. 4. The red particles were identified as alumina-iron rich silicates. The red particles contents small quartz particles in Si-Al-Fe-O matrix with quartz laths. Although the black particles contents silumina particles, their matrix consist from porous alumina-iron rich minerals (Table 1).

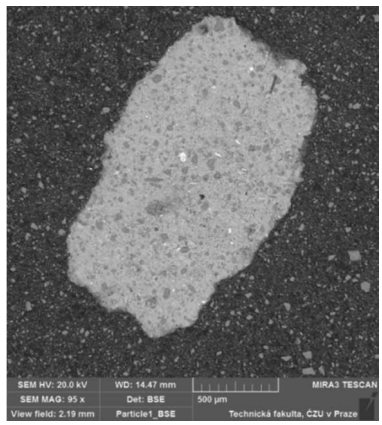

Figure 3. SEM micrograph (back-scattered electrons BSE) calcium rich soil particle.

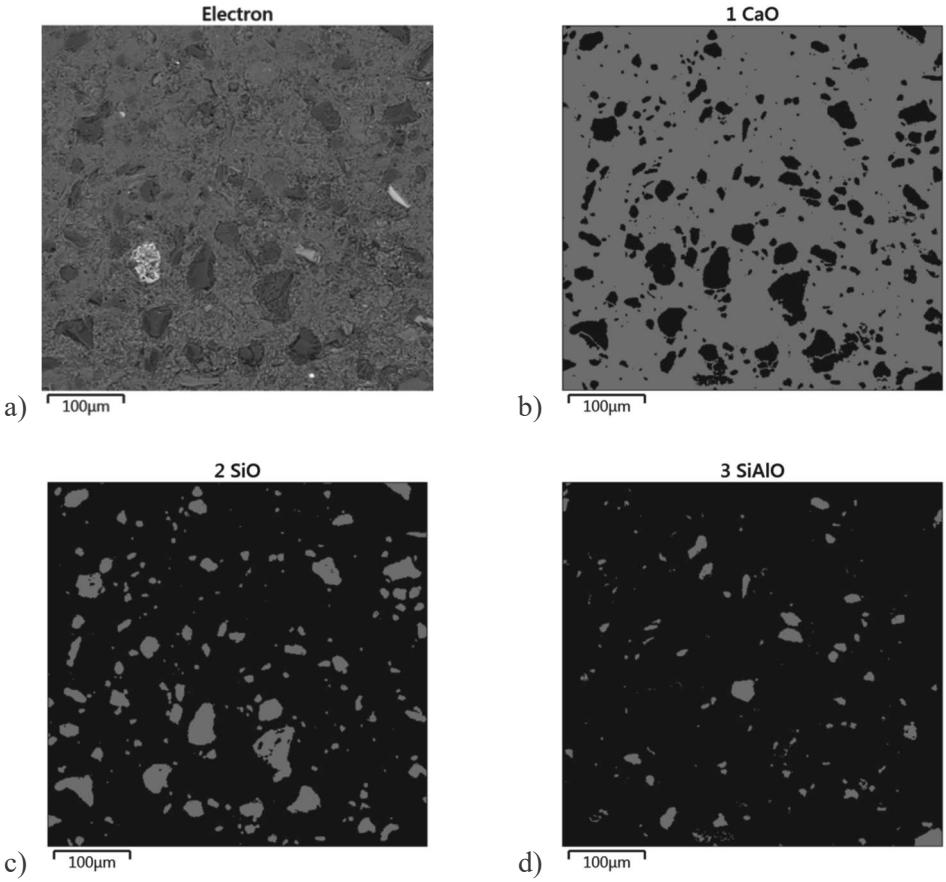

Figure 4. Picture from EDS analysis of calcium rich soil particle, see Fig. 3.

Table 1. Typical mineral contents and their chemical contents in at. % (EDS)

	(vol.%)	O	Mg	Al	Si	K	Ca	Mn	Fe	Na
	calcium rich particle (Fig. 2b)									
Ca-O	81	71.9	0.57	2	5.33	0.39	17.49	0.56	1.76	-
Si-O	11	67.37	-	0.47	30.53	-	1.62	-	-	-
Si-Al-O	8	64.35	0.33	8.92	18.57	2.91	1.99	-	0.55	2.38
	alumina-silicon rich particle (Fig. 2c)									
SiO	47	65.79	-	-	34.21	-	-	-	-	-
SiAlO	38	61.5	-	9.85	21.53	1.1	-	-	1.01	5.01
SiFeAlO	15	62.1	2.9	8.97	17.27	1.33	-	-	6.27	1.15
	alumina-iron rich silicates particle (Fig. 2d)									
SiAlO	69	64.62	-	10.79	22.08	0.81	0.44	-	1.27	-
SiO	18	66.55	-	-	33.45	-	-	-	-	-
SiFeAlO	13	54.85	0.38	10.96	24.47	1.52	1.27	-	5.66	-

EDS maps of particles were background to determination of chemical contents limint in feature analysis. Particles of soil were bonded on conductive adhesive carbon tabs. The feature analysis of particles was set on average chemical composition

determined by EDS maps. The EDS feature analysis showed that the fraction lower than 2 mm consist from Si-O, Si-Al-O, and Al-Si-O particles up to 95 vol.% and volume balance were particles with size higher than 2 mm. Results of feature analysis are presented in Fig. 5. Results shown that each of soil samples contains a different volume of quartz and aluminosilicates, and feature analysis shown a few volume of calcium rich particles about 2 vol.%.

The standard dry rubber wheel test used only quartz sand with no respect the true composition of soil. The aluminosilicate particles are more hardness than quartz and their abrasiveness is higher than abrasiveness of quartz. One of way how to respect abrasiveness of soils is using quartz sand and other minerals mixture for a test (Rabinowicz et al., 1961; Hamblin & Stachowiak, 1995; Knuuttila et al., 1999; Stachowiak & Stachowiak, 2001a). Low cost dry rubber wheel test can be let if we used a mixture of soft and hard particles with low price - quartz sand and alumina oxides. The ratio of soft and hard particles we can determinate thanks to hardness ratio with respect to mixture rule (1).

$$V_{Al_2O_3} \cdot HV_{Al_2O_3} + V_{SiO_2} \cdot HV_{SiO_2} = \\ = V_{Si-O} \cdot HV_{Si-O} + V_{Si-Al-O} \cdot HV_{Si-Al-O} + V_{Al-Si-O} \cdot HV_{Al-Si-O} \quad (1)$$

where V is relative volume (-) and HV is hardness (Vicker's test). The hardness of minerals depend on their chemical compositions and crystallographic orientations. Vicker's hardness of the quartz is in range 1,150–1,350, and aluminosilicate is in range 1,260 HV to 1,800 HV. Opposite, Vicker's hardness of calcium rich minerals is about 120 (Toureng, 1966). The volume of abrasive minerals of the tested soils is schematically presented in Fig. 5.

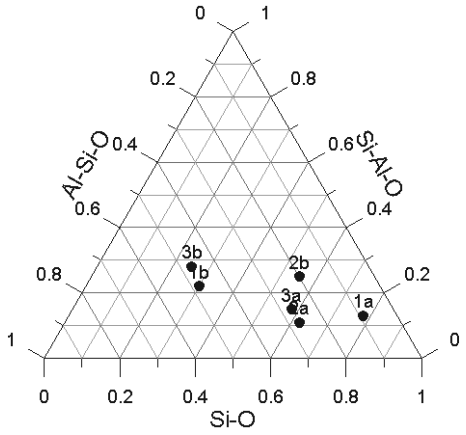

Figure 5. Ternary diagram of soil minerals tested soils 1 to 3, with respect to size of particles 0.1–2 mm (b) and large (higher than 2 mm) (a).

CONCLUSIONS

The results presented in this article can be summarized in the following conclusions:

– The energy diffraction spectrum is one of usable methods to determination of chemical composition of minerals in the soil and it can be used for feature analysis of minerals particles.

– Each of soil sample contained different ratio of minerals, it is obvious from results, and it depends on position in the land.

– The minerals composition of the soil is not the same as the Ottawa sand that is used in ASTM G65 tests. The dry rubber wheel test should be modified according to respect of the hardness ration of mixture sand and alumina oxides particles.

ACKNOWLEDGEMENT. Supported by 31140/1414/314107 Technological agency of Czech Republic, 'R & D of working tools for agricultural machines'.

REFERENCES

ASTM G65-04 Standard. 2010. Test Method for Measuring Abrasion Using the Dry Sand/Rubber Wheel Apparatus.

Badisch, E., Ilo, S. & Polak, R. 2009a. Multivariable Modeling of Impact-Abrasion Wear Rates in Metal Matrix-Carbide Composite Materials. *Tribology Letters* **36**(1), 55–62.

Badisch, E., Ilo, S. & Polak, R. 2009b. Multivariable Modeling of Impact-Abrasion Wear Rates in Metal Matrix-Carbide Composite Materials. *Tribology Letters* **36**(1), 55–62.

Buchely, M.F., Gutierrez, J.C., León, L.M. & Toro, A. 2005. The effect of microstructure on abrasive wear of hardfacing alloys. *Wear* **259**(1–6), 52–61.

Byeon, S.-H., Willis, R. & Peters, T. 2015. Chemical Characterization of Outdoor and Subway Fine (PM2.5–1.0) and Coarse (PM10–2.5) Particulate Matter in Seoul (Korea) by Computer-Controlled Scanning Electron Microscopy (CCSEM). *International Journal of Environmental Research and Public Health*, **12**, 2090–2104.

Cardoso, P.H.S., Israel, C.L. & Strohaecker, T.R. 2014. Abrasive wear in Austempered Ductile Irons: A comparison with white cast irons. *Wear* **313**(1–2), 29–33.

Correa, E.O., Alcântara, N.G., Tecco, D.G. & Kumar, R.V. 2007. The Relationship between the Microstructure and Abrasive Resistance of a Hardfacing Alloy in the Fe-Cr-C-Nb-V System. *Metallurgical and Materials Transactions A* **38**(8), 1671–1680.

Gahr, K.-H.Z. 1998. Wear by hard particles. *Tribology International* **31**(10), 587–596.

Hamblin, M.G. & Stachowiak, G.W. 1995. A multi-scale measure of particle abrasivity. *Wear* **185**(1–2), 225–233.

Hao, L., Wei, Q., Zhao, Y., Lu, J. & Zhao, X. 2015. Optimization method for quantitative calculation of clay minerals in soil. *Journal of Earth System Science* **124**(3), 675–680.

He, B., Han, P., Lu, C. & Bai, X. 2015. Effect of soil particle size on the corrosion behavior of natural gas pipeline. *Engineering Failure Analysis* **58**(P1), 19–30.

Chen, X., Zhang, J. & Li, Z. 2014. Shear behaviour of a geogrid-reinforced coarse-grained soil based on large-scale triaxial tests. *Geotextiles and Geomembranes* **42**, 312–328.

Chotěborský, R. 2013. Effect of heat treatment on the microstructure, hardness and abrasive wear resistance of high chromium hardfacing.

Chotěborský, R. & Hrabě, P. 2013. Effect of destabilization treatment on microstructure, hardness and abrasive wear of high chromium hardfacing. *Research in Agricultural Engineering* **59**(4), 128–135.

Chotěborský, R., Hrabě, P., Müller, M., Savková, J. & Jirka, M. 2008. Abrasive wear of high chromium Fe-Cr-C hardfacing alloys. *Research in Agricultural Engineering* **54**(4), 192–198.

Chotěborský, R., Hrabě, P., Müller, M., Savková, J., Jirka, M. & Navrátilová, M. 2009a. Effect of abrasive particle size on abrasive wear of hardfacing alloys. *Research in Agricultural Engineering* **55**(3), 101–113.

Chotěborský, R., Hrabě, P., Müller, M., Válek, R., Savková, J. & Jirka, M. 2009b. Effect of carbide size in hardfacing on abrasive wear. *Research in Agricultural Engineering* **55**(4), 149–158.

Chung, RJ., Tang, X., Li, D.Y., Hinckley, B. & Dolman, K. 2009. Effects of titanium addition on microstructure and wear resistance of hypereutectic high chromium cast iron Fe–25wt.%Cr–4wt.%C. *Wear* **267**(1–4), 356–361.

Jankauskas, V., Kreivaitis, R., Kulu, P., Antonov, M., Milčius, D. & Varnauskas, V. 2008a. Research of abrasive erosion wear for Fe-C-Cr-B hard layers. *Mechanika* **72**(4), 71–76.

Jankauskas, V., Kreivaitis, R., Milčius, D. & Baltušnikas, A. 2008b. Analysis of abrasive wear performance of arc welded hard layers. *Wear* **265**(11–12), 1626–1632. Retrieved from http://www.scopus.com/inward/record.url?eid=2-s2.0-54349112126&partnerID=tZOtx3y1

Kazemipour, M., Shokrollahi, H. & Sharafi, S. 2010. The Influence of the Matrix Microstructure on Abrasive Wear Resistance of Heat-Treated Fe–32Cr–4.5C wt% Hardfacing Alloy. *Tribology Letters* **39**(2), 181–192.

Knuuttila, J., Ahmaniemi, S. & Mäntylä, T. 1999. Wet abrasion and slurry erosion resistance of thermally sprayed oxide coatings. *Wear* **232**(2), 207–212.

Kolaříková, M., Chotěborský, R., Savková, J. & Bryksí Stunová, B. 2013. Local Mechanical Properties of Borides in Fe-B Steels. *Key Engineering Materials* **586**, 170–173.

Kučera, M. & Chotěborský, R. 2013. Analysis of the process of abrasive wear under experimental conditions. *Scientia Agriculturae Bohemica* **44**(2), 102–106.

Langford, H., Hodson, A. & Banwart, S. 2011. Using FTIR spectroscopy to characterise the soil mineralogy and geochemistry of cryoconite from Aldegondabreen glacier, Svalbard. *Applied Geochemistry* **26**, S206–S209.

Leal, O.D.A., Dick, D.P., Lombardi, K.C., Maciel, V.G., González-Pérez, J.A. & Knicker, H. 2014. Soil chemical properties and organic matter composition of a subtropical Cambisol after charcoal fine residues incorporation. *Journal of Soils and Sediments* 805–815.

Martín-García, J.M., Márquez, R., Delgado, G., Sánchez-Marañón, M. & Delgado, R. 2015. Relationships between quartz weathering and soil type (Entisol, Inceptisol and Alfisol) in Sierra Nevada (southeast Spain). *European Journal of Soil Science* **66**, 179–193.

Mavris, C., Götze, J., Plötze, M. & Egli, M. 2012. Weathering and mineralogical evolution in a high Alpine soil chronosequence: A combined approach using SEM-EDX, cathodoluminescence and Nomarski DIC microscopy. *Sedimentary Geology* **18**, 1270–1284.

Pachauri, T. 2013. SEM-EDX Characterization of Individual Coarse Particles in Agra, India. *Aerosol and Air Quality Research* **13**(2), 523–536.

Rabinowicz, E., Dunn, L.A. & Russell, P.G. 1961. A study of abrasive wear under three-body conditions. *Wear* **4**(5), 345–355.

Ren, L., Cohen, D.R., Rutherford, N.F., Zissimos, A.M. & Morisseau, E.G. 2015. Reflections of the geological characteristics of Cyprus in soil rare earth element patterns. *Applied Geochemistry* **56**, 80–93.

Sabet, H., Khierandish, S., Mirdamadi, S. & Goodarzi, M. 2011. The Microstructure and Abrasive Wear Resistance of Fe–Cr–C Hardfacing Alloys with the Composition of Hypoeutectic, Eutectic, and Hypereutectic at $$ \frac{Cr}{C} = 6 $$. *Tribology Letters*, **44**(2), 237–245.

Sahin, Y., Erdogan, M. & Kilicli, V. 2007. Wear behavior of austempered ductile irons with dual matrix structures. *Materials Science and Engineering, A* **444**(1–2), 31–38.
Sánchez-Marañón, M., Romero-Freire, A. & Martín-Peinado, F.J. 2015. Soil-color changes by sulfuricization induced from a pyritic surface sediment. *CATENA* **135**, 173–183.
Sellami, A., Kchaou, M., Elleuch, R., Cristol, A.L. & Desplanques, Y. 2014. Study of the interaction between microstructure, mechanical and tribo-performance of a commercial brake lining material. *Materials and Design* **59**, 84–93.
Stachowiak, G. & Stachowiak, G. 2001a. The effects of particle characteristics on three-body abrasive wear. *Wear* **249**(3–4), 201–207.
Stachowiak, G.B. & Stachowiak, G.W. 2001b. The effects of particle characteristics on three-body abrasive wear. *Wear* **249**(3–4), 201–207.
Stachowiak, G.W. 2000. Particle angularity and its relationship to abrasive and erosive wear. *Wear* **241**, 214–219).
Taylor, E.W. 1949. Correlation of the Mohs's scale of hardness with the Vickers' s hardness numbers. *Mineralogical Magazine* **13**(4), 718–721.
Toureng, C. 1966. *Vickers hardness of minerals and rocks – a few applications*. Paris: Laboratoire Central des Ponts et Chausees (LCPC). Retrieved from http://trid.trb.org/view.aspx?id=138158
Venkatarama Reddy, B.V. & Latha, M.S. 2014. Retrieving clay minerals from stabilised soil compacts. *Applied Clay Science* **101**, 362–368.
Vodyanitskii, Y.N., Vasil'ev, A.A. & Gilev, V.Y. 2007. Iron minerals in soils on red-earth deposits in the Cis-Ural region. *Eurasian Soil Science* **40**, 432–444.
Woldman, M., Tinga, T., Van Der Heide, E. & Masen, M.A. 2015. Abrasive wear based predictive maintenance for systems operating in sandy conditions. *Wear* **338–339**, 316–324.
Woldman, M., van der Heide, E., Schipper, D.J., Tinga, T. & Masen, M.A. 2012. Investigating the influence of sand particle properties on abrasive wear behaviour. *Wear* **294–295**, 419–426.
Zimba, J., Simbi, D. & Navara, E. 2003. Austempered ductile iron: an alternative material for earth moving components. *Cement and Concrete Composites* **25**(6), 643–649.

Agronomy Research **14**(Sp.1), 984–993, 2016

Mechanical properties of polymer matrix composites filled with Jatropha Curcas L.

P. Hrabě[1,*], M. Müller[1] and Č. Mizera[2]

[1]Czech University of Life Sciences, Faculty of Engineering, Department of Material Science and Manufacturing Technology, Kamýcká 129, 165 21 Prague, Czech Republic
[2]Czech University of Life Sciences, Faculty of Engineering, Department of Mechanical Engineering, Kamýcká 129, 165 21 Prague, Czech Republic
[*]Correspondence: hrabe@tf.czu.cz

Abstract. Polymers and their composites are widely used for their specific properties. This paper deals with composite materials based on Jatropha oil cake. Seeds of Jatropha Curcas L. plant are pressed for gaining oil. A cake is a by-product.
A polymer composite was a subject of performed experiments. A continuous phase was in a form of a two-component epoxy adhesive and Jatropha oil cakes were a discontinuous phase (reinforcing particles).
Using Jatropha oil cake as the by-product after the mechanical extraction of the oil decreases a price of the composite system. Jatropha oil cake is the waste which is not further utilized.
The research was focused on various weight concentrations from 5 to 30%. The volume energy, the strength characteristics and the impact resistance were tested at these composite materials. Results were evaluated by means of the statistical program ANOVA. The filler moisture was 4.59 ± 0.22% WB. Mechanical properties were not changed using of the filler.
The negative influence of the filler was ascertained at the tensile strength. The positive influence was ascertained at the impact strength until 20 wt% of the filler concentration.
Owing to the high complexity of the failing process of the composite material the grid electron microscopy in the area of the fracture surface was used.

Key words: Adhesive, seeds, Jatropha oil cake, statistica.

INTRODUCTION

With regard to the environment and a high level of exhaustion of oil resources, biopolymers have a great scientific attention in recent years. Polymer composites reinforced with natural fibres have been developed over the last decade as sustainable alternatives of engineering applications. According to Kumar & Sharma (2008) the growing interest in the development of composites has become more effective thanks to the growing demand for low-cost renewable materials which could replace the traditional ones. In addition, the high price of synthetic fibres, the public awareness and the sensitivity to the preservation of the natural environment contribute to the development of new research activities in this area (Satheesh et al., 2009; Müller et al., 2015).

Naturally renewable energy has many advantages, such as the availability of feedstock, the environmental friendliness and the low-cost (Ahmed et al., 2001; Aigbodion & Pillai, 2001). Firstly, these products must comply with the technical and

industrial standards of a durability, an exposure stability, a chemical resistance, etc. They must also comply with all environmentally appropriate standards (Galusek et al., 2007). A number of vegetable oils were used for the synthesis of various polymer resins, such as polyester, epoxy, polyurethane, polyester amide, etc. (Herák et al., 2013; Ružbarský et al., 2014).

The reason to incorporate the filler into the polymer is dual: firstly, to improve the tribological, mechanical and thermal properties, secondly, to reduce the cost of the final composite.

Jatropha curcas L. is a versatile plant with diverse use, such as biodiesel, medicines, cosmetics, etc. Jatropha is a drought resistant bush or tree widely distributed in the wild and cultivated form in some areas of Central and South America, Africa and South-East Asia (Cano-Asseleih, 1986; Ružbarský et al., 2014). The first commercial applications of Jatropha curcas L. were in Lisbon where the oil was imported from Cape Verde. It was used for the manufacture of soaps and for lamps (Galusek et al., 2007).

Jatropha oil cake yield is approximately about 500–600 g kg^{-1} of Jatropha seeds (Syed et al., 2009). Oil cakes contain a large amount of minerals (Satheesh et al., 2009).

Shivamurthy & Murthy (2014) describe in the experiment the strength and the rigidity of the epoxy matrix, which is increased by an addition of microparticles prepared from the residues of Jatropha curcas L. seeds after pressing. It is necessary to describe the properties of composites with particles from renewable sources (biomaterials) and to determine the area of the application of these materials (Ružbarský et al., 2014).

Nanocomposites reinforced with 1 wt.% of expanded graphite showed an improvement by 15% in the module of elasticity compared to a pure epoxide (Mishra et al., 2000).

Rosso et al. (2006) evaluated the mechanical strength of epoxy resins with the addition of 5 vol.% of silicon dioxide nanoparticles. The silicon dioxide addition was able to improve the rigidity and the toughness of the polymer. As a consequence the module of elasticity was increased by 20% and the fracture toughness by 70%.

Isik et al. (2003) and Yasmin et al. (2003) studied the effects of a nanoclay added to the epoxy resin from 0 to 10 wt.%. Isik et al. found that the tensile strength was increased with the addition of 1 wt.% of the nanoclay. However, the module of elasticity was increased gradually with the addition of clay nanoparticles. Yasmin, et al. (2003) found an increase by 80% in the module of elasticity by addition of 10 wt.% of clay nanoparticles.

Subramanian & Sun (2006) examined the effect of the nanoclay with the addition of 0, 3, 5 and 8 wt.% to the epoxy resin. The compressive strength of composites was increased by 22% and 36% with the addition of 3 wt.% and 5 wt.% of the nanoclay.

This paper deals with the mechanical properties of Jatropha oil cakes, such as the tensile strength, the impact strength and the volume energy. The matrix is a two-component adhesive and a filler (discontinuous phase) is Jatropha oil cakes. The research objective was the utilization of the material waste from the Jatropha urcas L. pressing process. The secondary objective was to find an application which improves the mechanical properties of the composite.

MATERIALS AND METHODS

The object of the experiments was a particle polymer composite. A continuous phase was in the form of a two-component epoxy adhesive ChS Epoxy 324 Epoxy 1200 (hardener P11 – Diethylenediamine) and the discontinuous phase (reinforcing particles) in the form of Jatropha oil cakes (Fig. 1). The filler was obtained as a waste from the seeds of Jatropha curcas L. during the presswork process. This waste of the process (cakes) was dried to a moisture content 4.59 ± 0.22% WB and subsequently the size of the particles was adjusted by crushing. The filler thus obtained has not been further modified, e.g. fractionated.

The size of the particles was measured by means of an optical analysis at the stereoscopic microscope. A great variability of the filler in the form of the microparticles is apparent from performed 100 measurements. The dimension was 435 ± 256 μm.

The concentration of subcomponents was determined and expressed in weight percentages. Test specimens were made in the concentrations of 5, 10, 20, 30, 40 and 50 wt.% of Jatropha oil cake microparticles.

Figure 1. Jatropha oil cakes.

By mixing of the specified matrix – filler phases ratio the composite was made. It was used for the preparation of test specimens according to the specified standards.
The moulds for casting were made from the material Lukapren N using models. The form and size of moulds meet the corresponding standards.

The composite mixture was let to be fully cured under time 340 h. The secondary curing of the composite mixture was provided. The influence of the impact resistance, the tensile strength and the volume energy was experimentally investigated.
The test specimens for the tensile properties determination according to the standard CSN EN ISO 527-1 (Plastics – Determination of tensile properties – Part 1: General principles) were prepared according to the standard CSN EN ISO 3167 (Plastics – Multipurpose test specimens, Czech Standard Institution). By the destructive testing the tensile strength σ was ascertained.

To determine the relationship between a tension force and a deformation, a device (Labortech, MPTest 5.050, Czech Republic) was used to record the course of a deformation function. The tensile test was performed according to CSN EN ISO 527-2 (2012). A deformation speed at the tensile test was 6 $mm.min^{-1}$. Ascertained values of

tensile forces were transformed by means of an equation 1 to the tensile stress and deformations were transformed by means of an equation 2 to the relative deformation.

$$\sigma = \frac{F}{S} \tag{1}$$

where: σ – tensile stress in sample (MPa); F – tensile force (N); S – appropriate cross section area of sample (mm^2).

The volume deformation energy was set as an area below a curve 'stress – strain' from zero to a maximum value of the deformation according to an equation 2.

$$\lambda = \sum_{n=0}^{n=i-1}\left[\left(\frac{\sigma_{n+1}+\sigma_n}{2}\right)\cdot\left(\varepsilon_{n+1}-\varepsilon_n\right)\right] \tag{2}$$

where: λ – volume energy ($J\ m^{-3}$); i – indicates the additional amount of strain in which the stress was determined (step of measurement – 0.001 mm), -; σ_n – tension stress at appropriate strain (MPa); σ_{n+1} – tension stress at the sequential strain (MPa); ε_n – strain (-); ε_{n+1} – sequential strain (-).

The impact strength was ascertained in an apparatus Dynstat determined for the testing of plastics. The test specimen preparation and impact tests were performed according to the standard CSN 64 0611 (Determination of the impact resistance of rigid plastics by means of Dynstat apparatus). By the destructive testing the impact strength a_n was determined. The calculation was performed according to the equation (3)

$$a_n = \frac{A_n}{b.h} \tag{3}$$

where: a_n – impact strength ($kJ\ m^{-2}$); A_n – energy consumed to breaking up test specimen (kJ); b – width of test specimen (m); h – thickness of test specimen (m).

The destructive testing conducted at the laboratory temperature 22 ± 2 °C.

Statistical hypotheses were also tested at measured sets of data by means of the program STATISTICA. A validity of the zero hypothesis (H_0) shows that there is no statistically significant difference ($p > 0.05$) among tested sets of data. On the contrary, the hypothesis H_1 denies the zero hypothesis and it says that there is a statistically significant difference among tested sets of data or a dependence among variables ($p < 0.05$).

RESULTS AND DISCUSSION

Fig. 2 shows the results of the tensile strength. A negative influence of the filler based on Jatropha oil cake microparticles is visible from the results of the experiment. The fall of the tensile strength caused by the addition of Jatropha oil cake microparticles

ranged in the interval 65 to 80%. The tensile strength fall was more significant with increasing concentration of the filler.

Fig. 3 shows the results of the volume energy. A negative effect of the filler based on Jatropha oil cake microparticles is obvious from the experimental results. The fall of the module of elasticity caused by adding of Jatropha Oil Cake microparticles ranged in the interval 75 to 92%. The fall of the volume energy was more significant with increasing concentration of the filler.

Fig. 4 shows the results of the impact strength. A positive effect of the filler based on Jatropha Oil Cake microparticles till 20 wt.% is obvious from the experimental results. The increase of the impact strength was 14% at the concentration 20 wt.%. At the concentration 30 wt.% the fall of the impact strength of 21 to 37% occurred.

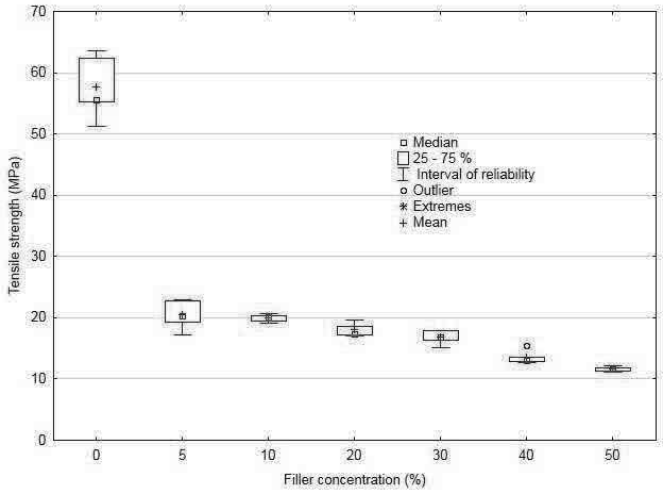

Figure 2. Effect of filler based on Jatropha oil cake microparticles on tensile strength.

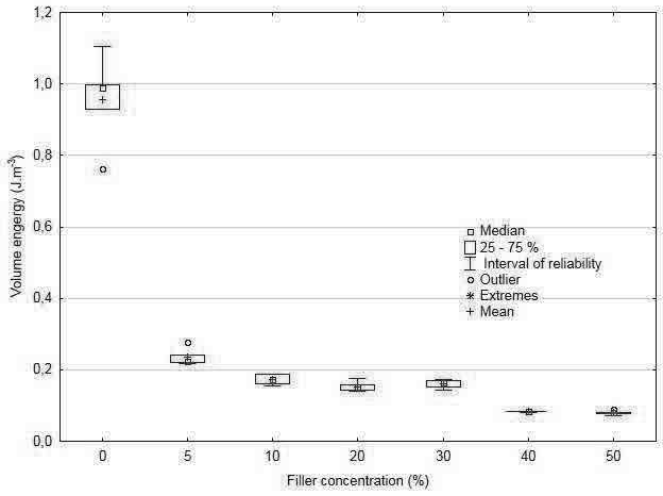

Figure 3. Effect of filler based on Jatropha oil cake microparticles on volume energy.

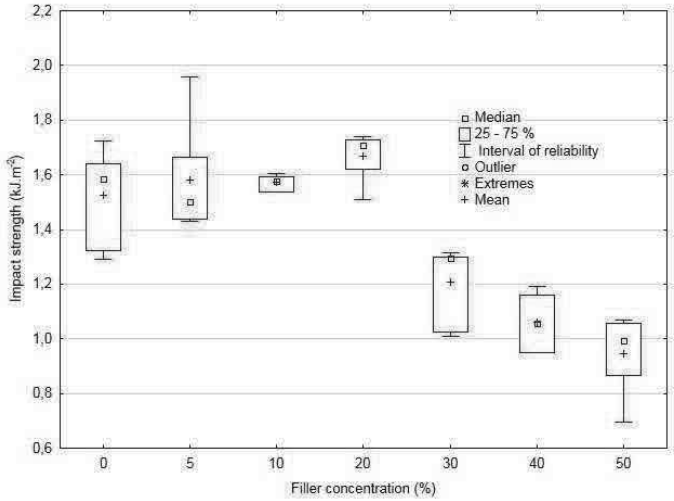

Figure 4. Effect of filler based on Jatropha oil cake microparticles on impact strength.

In terms of the filler of Jatropha oil cake influence on mechanical properties of the polymer composite material the results of ANOVA F-test are following:

- Tensile strength: at comparing all variants of the experiment the hypothesis H_0 was not certified ($p = 0.0000$), i.e. there is a difference among single tested concentrations of the filler microparticles 5, 10, 20, 30, 40 and 50 wt.% of Jatropha oil cakes and the matrix in the significance level 0.05. So, the influence of the concentration of the filler based on Jatropha oil cake microparticles on the tensile strength was statistically proved in the significance level 0.05.
- Volume energy: at comparing all variants of the experiment the hypothesis H_0 was not certified ($p = 0.0000$), i.e. there is a difference among single tested concentrations of filler microparticles 5, 10, 20, 30, 40 and 50 wt.% of Jatropha oil cakes and the matrix in the significance level 0.05. So, the influence of the concentration of the filler based on Jatropha oil cake microparticles on the volume energy was statistically proved in the significance level 0.05.
- Impact strength: at comparing all variants of the experiment the hypothesis H_0 was not certified ($p = 0.0000$), i.e. there is a difference among single tested concentrations of filler microparticles 5, 10, 20, 30, 40 and 50 wt.% of Jatropha oil cakes and the matrix in the significance level 0.05. So, the influence of the concentration of the filler based on Jatropha oil cake microparticles on the impact strength was statistically proved in the significance level 0.05.

During the experiments the assumption about the negative effect of the filler on the tensile strength was confirmed. Cho et al. (2006) indicate that the strength of the composite is reduced with increasing volume of the filler particles.

According to the research by various authors the addition of fillers to the epoxy adhesive does not produce a definite improvement or deterioration in impact strength. E.g. Dadfar & Ghadami (2013) indicate an improvement in the toughness due to the

increased content of the rubber modifier. Further, it was proved that the aluminium microparticles also increased the impact strength.

The investigation showed that the epoxy adhesive retained the adhesion of the adhesive and the filler up to 50 wt.%.

Jiang-Jhy et al. (2001) proved in their experiments that the irregular shape of the particles ensured good interaction between the matrix and the filler. Farraf et al. (2008) ascertained that the irregular shape of the particles showed reaching smaller mechanical properties probably owing to the separation between the matrix and the filler. Good interaction between the filler and the matrix is visible from Figs 5 and 6. It is obvious from the result that it did not depend on the shape of the filler.

Jatropha curcas L. seeds contain a high percentage of oil which is widely used, e.g. it is used at a production of biodiesel (Samsuri & Zoveidavianpoor, 2014). The filler based on Jatropha oil cake microparticles contains residual concentration of oil. This fact made perfect wetting of the filler surface with the matrix impossible. So, it is obvious from the results that the shape and the type of the filler are essential.

A wettability of the filler with the matrix is important at filling structural two-component epoxies with the filler. The research results confirmed also ca. 2–3% porosity of created material.

Figs 5, 6 and 7 show a fracture surface of the polymer composite based on the filler in the form of Jatropha oil cake microparticles with using the electron microscope Tescan Mira 3. Bad interaction of the filler with the matrix in the form of the epoxy was proved within the experimental research by use of the electron microscopy (Figs 5, 6). Fig. 5 shows ordering of the filler microparticles.

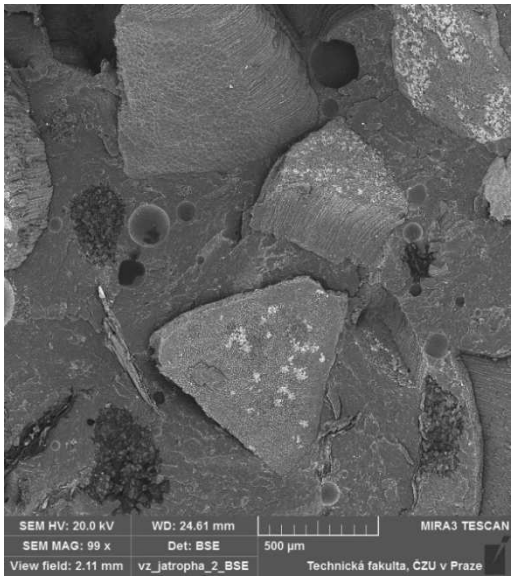

Figure 5. SEM images – fracture surface of composite based on Jatropha oil cake microparticles (composite 40 wt.% of filler).

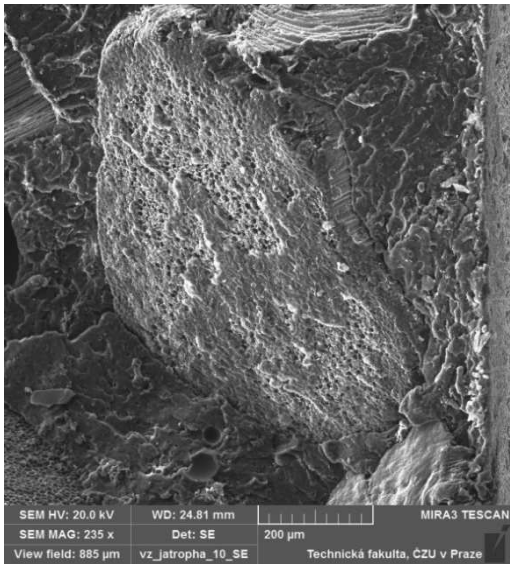

Figure 6. SEM images – fracture surface of composite based on Jatropha oil cake microparticles (filler particles in form of kernel).

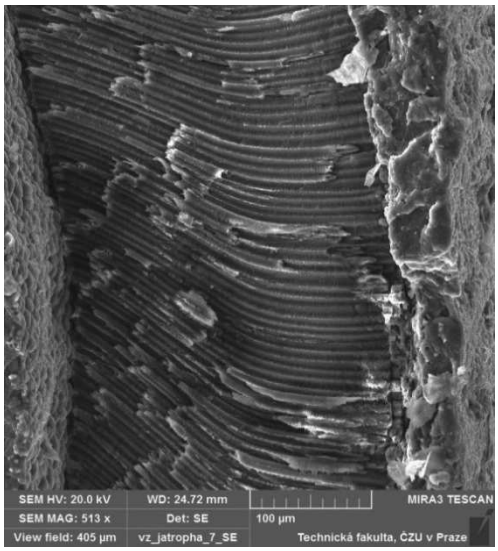

Figure 7. SEM images – fracture surface of composite based on Jatropha oil cake microparticles (filler particles in form of peel).

CONCLUSIONS

Based on the experiment it is possible to establish these conclusions:

- The results of the experiments show an obvious negative impact of the filler based on Jatropha oil cake microparticles on the tensile strength and the volume energy.

A significant decrease was of approximately 90% with increasing concentration of the filler based on Jatropha oil cake microparticles.

- The results of the experiments show an obvious positive impact of the filler based on Jatropha oil cake microparticles on the impact strength. This positive trend can be monitored up to 20 wt.%. This positive effect was due to a modification of the matrix, i.e. a structural epoxy with the filler which contained residual concentration of oil.

Increased dynamic strain resistance of the polymer particle composite system is positive. Polymer materials are characterized by reduced dynamic stress resistance. This causes problems in practice.

ACKNOWLEDGEMENT. Supported by Internal grant agency of Faculty of Engineering, Czech University of Life Sciences in Prague.

REFERENCES

Ahmad, S., Ashraf, S.M., Yadav, S. & Jamal, A. 2001. Studies on urethane-modified alumina-filled polyesteramide anticorrosive coatings cured at ambient temperature. *Journal of Applied Polymer Science* **82**, 1855–1865.

Aigbodion, A.I., Pillai, C.K.S. 2001. Synthesis and Molecular Weight Characterization of Rubber Seed Oil-Modified Alkyd Resins. *Journal of Applied Polymer Science* **79**, 2431–2438.

CSN EN ISO 527-2. 2012. Plastics – Determination of tensile properties. In: Czech Standard Institution

CSN EN ISO 178. 2011. Plastics – Determination of flexural properties. In: Czech Standard Institution

Cano-Asseleih, L.M. 1986. Chemical investigation of Jatropha curcas L. seeds, Ph.D. Thesis. University of London, U.K., 1986.

Cho, J., Joshi, M.S. & Sun, C.T. 2006. Effect of inclusion size on mechanical properties of polymeric composites with micro and nano particles. *Composites Science and Technology* **66**, 1941–1952.

Dadfar, M.R. & Ghadami, F. 2013. Effect of rubber modification on fracture toughness properties of glass reinforced hot cured epoxy. *Materials and Design* **47**, 16–20.

Farrah, N.A., Mariatti, J., Samayamutthirian, P. & Khairun, A.M.A. 2008. Effect of particle shape of silica mineral on the properties of epoxy composites. *Composites Science and Technology* **68**, 346–353.

Galusek, D, Sedláček, J. & Riedel, R., 2007. Al2O3-SiC composites prepared by warm pressing and sintering of an organosilicon polymer-coated alumina powder. *Journal of the European Ceramic Society* **27**, 2385–2392.

Herák, D., Kabutey, A. & Hrabě, P. 2013. Oil point determination of Jatropha curcas L. bulk seeds under compression loading, *Biosystems Engineering* **116**, 470–477.

Isik, I., Yilmazer, U. & Bayram, G. 2003. Impact modified epoxy/montmorillonite nanocomposites: synthesis and characterization. *Polymer*. **44**(20), 6371–6377.

Jackel, M. & Scheibner, W. 1991. Boundary layer induced modification of thermal and mechanical properties of epoxy resin composites. *Cryogenics* **31**, 269–272.

Jiang-Jhy, Ch. & Wei-Chung, Y. 2001. The effect of particle shape on bond strength improvement of epoxy particle coating composites. *Journal of Marine Science and Technology* **9**, 153–160.

Kumar, A. & Sharma, S. 2008. An evaluation of multipurpose oil seed crop for industrial uses (Jatropha curcas L.). *Industrial Crops and Products* **28**, 1–10.

Mishra, S., Naik, J.B. & Patil, Y.P. 2000. The compatibilising effect of maleic anhydride on swelling and mechanical properties of plant-fiber-reinforced novolac composites. *Compos Science Technology* **60**, 1729–1735.

Müller, M., Cidlina, J., Dědičová, K. & Krofová, A. 2015. Mechanical properties of polymeric composite based on aluminium microparticles. *Manufacturing* Technology **15**, 624–628.

Rosso, P., Ye, L., Friedrich, K. & Sprenger, S. 2006. A toughened epoxy resin by silica nanoparticle reinforcement. *Journal of Applied Polymer Science* **100**, 1849–1855.

Ružbarský, J., Müller, M. & Hrabě, P. 2014. Analysis of physical and mechanical properties and of gross calorific value of Jatropha curcas seeds and waste from pressing process. *Agronomy Research* **12**, 603–610.

Samsuri, A. & Zoveidavianpoor, M. 2014. Does the Maturity of jatropha curcas L. Affect the quality and quantity of the yield of oil for biodiesel production?. *International Journal of Green Energy* **11**, 193–205.

Satheesh, K.M.N., Yaakob, Z. & Abdulla, R.S. 2009. Applications of jatropha oil seed crop. *Recent Patents on Materials Science* **2**, 131–139.

Shivamurthy, B. & Murthy, K. 2014. Mechanical properties and sliding wear behavior of jatropha seed cake waste/epoxy composites. *Journal of Material Cycles and Waste Management* **17**, 144–156.

Subramaniyan, A.K. & Sun, C.T. 2006. Enhancing compressive strength of unidirectional polymeric composites using nanoclay. *Composites Part A Applied Science and Manufacturing* **37**, 2257–2268.

Syed, M.Z., Siddaramaiah, S.B. & Syed, A.A. 2009. Mechanical and abrasive wear behavior of coleus spent filled unsaturated polyester/polymethyl methacrylate semi interpenetrating polymer network composites. *Journal of Composite Materials* **43**, 2387–2400.

Yasmin, A., Abot, J.L. & Daniel, L.M. 2003. Processing of clay/epoxy nanocomposites by shear mixing. *Scripta Materialia* 49, 81–86.

Agronomy Research **14**(Sp.1), 994–1003, 2016

Mechanical and physical properties of thermally modified wood flour reinforced polypropylene composites

H. Kallakas[1,*], M. Martin[1], D. Goljandin[2], T. Poltimäe[1], A. Krumme[3] and J. Kers[1]

[1]Tallinn University of Technology, Faculty of Chemical and Materials Technology, Department of Polymer Materials, Chair of Woodworking, Teaduspargi 5, EE 12618 Tallinn, Estonia
[2]Tallinn University of Technology, Faculty of Mechanical Engineering, Department of Materials Engineering, Chair of Materials Science, Ehitajate tee 5, EE19086 Tallinn, Estonia
[3]Tallinn University of Technology, Faculty of Chemical and Materials Technology, Department of Polymer Materials, Ehitajate tee 5, EE 19086 Tallinn, Estonia
[*]Correspondence: heikko.kallakas@ttu.ee

Abstract. Heat treatment of wood helps to lower the hydrophilicity and polarity of wood fibres used in wood-plastic composites. By means of heat treatment it is possible to reduce the access to wood hydroxyl (OH) group, which causes hydrophilic and polarity of wood fibres. Therefore improving compatibility between the wood and polymer matrix. In this research, the effect of wood flour (WF) heat treatment and chemical modification with 3-aminopropyltriethoxysilane (APTES) were investigated. WPC test samples were prepared using alder (*Alnus incana*) WF with mesh size of 0.05 mm as a filler material and polypropylene (PP) as the matrix material. WF was chemically modified with NaOH and APTES to increase the adhesion and compatibility of WF to polymer matrix. The composites were manufactured using a twin-screw extruder and the test samples were made by injection molding. The composites mechanical properties were tested using three-point flexural test and Charpy impact test. The composite physical properties were investigated with Fourier transform infrared spectroscopy (FTIR). The effect of silane (APTES) and NaOH modification on thermally treated and untreated WF was examined with contact angle measurement. Comparisons were made between the untreated WF and thermally treated WF. Also the effect of NaOH and silane (APTES) modification on the properties of thermally modified and unmodified WF composite were investigated. Using WF as a filler material increased flexural strength, while impact strength decreased thus making the material more rigid and brittle. The test results revealed that there was no significant difference in the mechanical properties between thermally treated and untreated composites. However, chemical modification improved the mechanical properties of the composites.

Key words: wood-plastic composite, wood flour, chemical modification, thermal treatment.

INTRODUCTION

The use of lignocellulosic fillers has received considerable interest from academics and industry for its environmental and economic benefits. Natural fillers have many advantages over inorganic fillers such as: renewable nature, availability, low cost and

density, high specific strength and moduli etc. Despite many advantages they have a big disadvantage – they are incompatible with the polymer matrix due to the polarity of the natural fillers and non-polarity of the polymer matrix. Many solutions have been proposed to overcome this problem for instance adding a coupling agent has been a successful way of aiding compatibility (Krzysik & Youngquist, 1991; Gatenholm et al., 1993; Kazayawoko et al., 1999; Lu et al., 2000; Kaboorani et al., 2008). Presently, the use of coupling agents such as silane, maleic anhydride grafted polypropylene, alkali treatment, acetylation have been the most common ways to increase the compatibility of the hydrophilic natural fibers and the hydrophobic polymers (Luo et al, 2013).

Heat treatment is a relatively simple method for modifying wood. This method improves hydrophobicity, dimensional stability and biological resistance. During heat treatment, significant changes take place in the chemical composition of the wood filler including decomposition of hemicellulose which is hydrophilic. Heat treatment also has some drawbacks including the reduction of mechanical properties and unwanted color and odor (Adyembir et al., 2015). With heat treatment the adsorption of water into wood decreases which results in lowered swelling or shrinkage behavior compared to untreated wood. It is noted that moisture is absorbed by the hydrophilic wood fibers into the composite which leads to degradation of the interfacial adhesion quality and therefore decreases the strength of the composite. Thermal modification reduces the polarity of wood fibers and thereby improves their compatibility with hydrophobic thermoplastics and increases interfacial strength. Therefore, these materials provide the needed properties for such uses as decking, railing, cladding and under the hood applications in the automotive industry (Follrich et al., 2010).

Thermal treatments use no chemicals thus making it an environmentally friendly process (Eslam et al., 2011). Wood can be degraded and finally burn at high temperatures. The initial degradation can start at temperatures as low as 117 °C depending on the heating period, atmosphere and wood species. Thermal stability is a critical factor in the processing time and temperature (Kaboorani & Faezipour, 2009). In theory, adding heat treated wood in which some components have been decomposed should lead to an improvement in thermal stability (Kaboorani & Faezipour, 2009).

The aim of this research was to explore the use of thermally modified wood as a filler material for wood plastic composites as thermal treatment potentially reduces the polarity of wood and makes it more compatible with thermoplastic polymers. The task of this project is to investigate the effect of chemically treated, thermally treated and untreated wood on the mechanical and physical properties.

MATERIALS AND METHODS

Materials

In this research, PP was used as the matrix material for making WPCs. The PP (BC245MO) obtained from the Borealis Polymers OY company is a heterophasic copolymer (block copolymer) with a density of 0.905 g cm^{-3}, and melt flow index (MFI) of 3.5 g 10 min^{-1}. Thermally treated (170 °C) hardwood (alder (*Alnus incana*)) boards were supplied by HA SERV OÜ. Thermally modified boards were then comminuted into a fine flour with mesh size of 0.05 mm using a disintegrator device DS-A. As a coupling agent 3-aminopropyl-triethoxysilane (APTES) from Sigma-Aldrich was used. The molecular weight of the substance is $M_w = 221.37$ g mol^{-1} and the boiling point at

atmospheric pressure is 217 °C. A reagent grade sodium hydroxide (NaOH), 98% was also used and glycerine in some samples.

Wood flour modification

Preparation of the composites started with modification of wood flour (WF). Firstly, WF was weighed in a stainless steel vessel. According to the previous research (Gwon et al., 2010), optimum concentration of alkali for the treatment is 10 wt% and above, so that the mechanical properties may slightly decrease. Therefore, in this study a 10 wt% (based on WF mass) aqueous solution of NaOH was prepared in the laboratory by dissolving NaOH granules in water. WF was immersed in 10 wt% NaOH solution at room temperature (25 °C) for 90 min. The WF was then rinsed with distilled water to neutralise the excess NaOH and dried in the oven at 60 °C for 24 h.

WF silane modification according to a previous research (Kim et al., 2011) was used. For silane modification, 5 wt% (based on WF) APTES was taken. APTES was immersed in a solution of ethanol/distilled water (6:4 ratio) for 1 h in order for it to be hydrolized and the pH of the solution was adjusted to the value of 4–5 with acetic acid. Then silane solution was poured on the WF was left at room temperature (25 °C) for 2 h. After the silane treatment the WF was dried in the oven at 60 °C for 24 h.

The usage of glycerine in WPC-s was similar to a previous research (Sanadi & Caulfield, 2008) which showed that adding 2% glycerine resulted in the best properties. Glycerine was used as a processing aid and added to the modified WF in the amount of 2% of the mass of WF. Glycerine was weighed and 500 ml of water was added to it so that the mixing process would be easier. Table 1 illustrates the composition of the composites.

Composite processing

The test specimens were prepared in Tallinn University of Technology, Department of Polymer Materials. The first operation was the modification of WF and then the compounding and granulation of the obtained mixtures. The last step was to produce test specimens by injection molding method.

After the modification, the WF was weighed and mixed with polymer granules maintaining the ratio of 65% polymer and 35% WF for all the samples. The composition of the mixtures are shown in Table 1. The mixtures were compounded using twin-screw extruder Brabender Plast-Corder PLE651. The barrel had four heating zones. The melting zone temperatures were set at 180 °C, 185 °C and 190 °C, and 185 °C for die zone. The rotation speed of the twin-screw was 60 rpm. The extruded material was cooled with ventilators and granulated with a Brabender granulator. The test samples were made by injection moulding (Battenfeld BA 230 E) according to standard ISO 178:2010. Depending on the material the temperature and pressure was suitably adjusted. Conditions for injection moulding were: temperature: 170–185 °C from the feed zone to the die zone, injection pressure: 7 MPa, screw speed 40 rpm, cooling time 15 s. The mixture was injection moulded into bar shape specimens for flexural and impact tests. Dimensions of the specimens were 63 x 10 x 4 mm.

Table 1. Composition of the composites

Sample	PP (wt%)	WF (wt%)	NaOH (wt%)	APTES (wt%)	Glycerine (wt%)
1	100	–	–	–	–
2	65	35	–	–	–
3	65	35	10	5	–
4	65	35	10	5	2
5	65	35*	–	–	–
6	65	35*	10	5	–
7	65	35*	10	5	2

* – thermally treated WF

Mechanical properties

Flexural properties were tested by means of three-point loading system Instron 5866 according to ISO 178:2010. Testing was carried out at room temperature 20 °C, crosshead speed of 20 mm min^{-1}, test span of 60 mm. Five specimens were used for each composite. For each composite, flexural strength and modulus of elasticity (MOE) were calculated. Also, the Charpy impact strength was determined for single-notched samples according to ISO 179-1. Notched impact strength was tested with a Zwick 5102 pendulum impact tester at room temperature 20 °C and nominal pendulum energy of 4 J. The energy absorbed by breaking the test specimen was measured and Charpy impact strength was calculated.

Fourier transform infrared spectroscopy (FTIR)

The efficiency of the chemical modification was verified using Fourier transform infrared spectroscopy (FTIR). FTIR spectroscopy measurements were performed using Interspectrum FTIR spectrometer (model Interspec 200-X) with KBr disc method. The spectral resolution was 4 cm^{-1} and the spectra were recorded in the range of 1,800–800 cm^{-1} using. Thin wafers were cut from the previously produced flexural test specimens using a scalpel. The thin wafers were placed under a clamp and the spectra were measured under ambient conditions.

RESULTS AND DISCUSSION

Flexural properties

The flexural strength of WPCs with thermally treated and untreated, silane modified and unmodified WF is presented in Fig. 1 The addition of WF has increased the flexural strength by 9–21% (from 32.76 MPa to 41.47 MPa), thus making the composites more rigid and brittle. The results show very slight differences in flexural strength between different composites. In order to achieve better mechanical properties, chemical modification of WF was used to gain better adhesion and better dispersion of the filler in the composite but unfortunately the results show little difference between modified and unmodified WF based composites. Chemical modification of WF slightly decreased the flexural strength (about 10%) compared to unmodified WF based composites. The decrease of flexural strength of modified WF based composites may be due to the excessive alkali that weakens the surface of WF and causes the effect of corrosive interactions between wood fibers in the composites (John et al., 2008; Gwon et al., 2010).

However, there were no significant differences between thermally treated and untreated WF based composites. This can be explained by the fact that WF was ground to very fine flour with mesh size of 0.05 mm and therefore modifications have no effect on the composite properties anymore. WF with mesh size of 0.05 mm acts just as a filler in the PP matrix and not as a reinforcing fiber. WF with mesh size 0.05 mm was chosen to be similar with wood dust in sawmill and furniture industries and to find usage for this wood dust in WPCs. As can be seen from Fig. 1, there is almost no difference between modified, thermally treated or untreated WF used in WPCs. The differences of the results between all the composite remain fit within the boundaries of measurement uncertainty. However, previous researches have shown increase in flexural properties with APTES modified WF/PP composites (Kim et al., 2011; Kallakas et al., 2015). For some WPC samples, glycerine was used as processing aid. The results show (see Fig. 1) that there was no effect of using glycerine on the flexural properties.

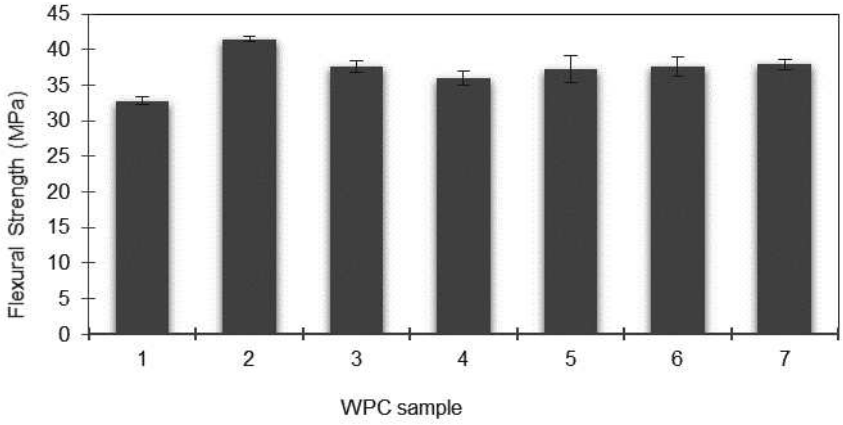

Figure 1. Flexural strength of chemically and thermally modified and unmodified WF/PP composites.

Modulus of elasticity (MOE) shows the materials ability to withstand deformation. The results derived from the flexural test show the stiffness of the composite (see Fig. 2). Comparing the results to the MOE of pure PP (1.01 GPa) the stiffness of the composite is significantly higher (over 200%). The increased stiffness can be explained by the stress transfer from the polymer matrix to the filler (Ndiaye & Tidjani, 2012). The results show that chemically unmodified composites have slightly, about 10% higher MOE values than modified composites. When comparing thermally treated and untreated WF composite, it can be seen from the results (see Fig. 2) that there is no difference. The results show a slight effect on MOE values when glycerine was used. MOE decreased by 50% with untreated WF composites where glycerine was used as a processing aid since it is likely that the small molecules of glycerine could act as a plasticizer/lubricant.

Therefore, from the flexural properties, it can be concluded that chemical or thermal modification has minimal or no effect on the flexural properties of WPCs when fine WF with mesh size of 0.05 mm is used.

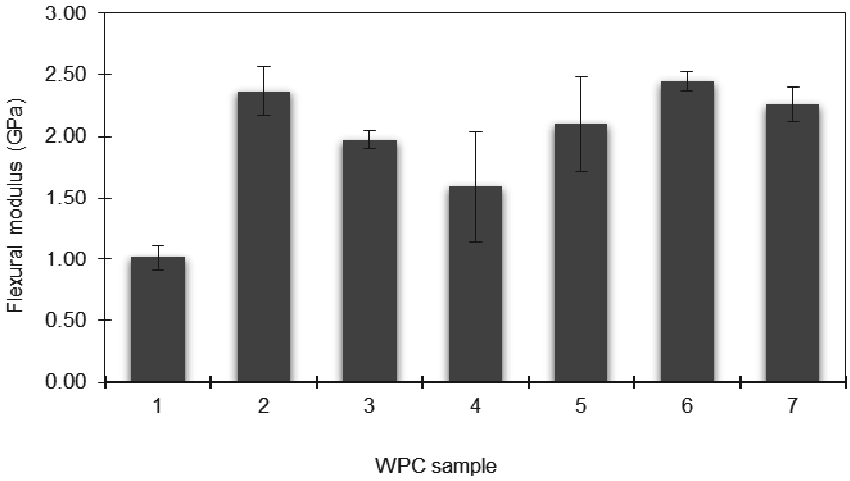

Figure 2. Flexural modulus of chemically and thermally modified and unmodified WF/PP composites.

Impact strength

Impact strength was measured by Charpy impact test of single notched specimens of unmodified and modified WPC samples. Single notched impact test was chosen because the pendulum impact tester machine did not provide sufficient energy to break un-notched PP – because PP matrix has high elasticity which is also shown by previous researches (Bledzki & Frauk, 2004; Bledzki et al., 2009).

The results of the impact test are shown in Fig. 3. From the results it can be seen that using fine WF in the PP matrix lowered the impact properties significantly (about three times) compared to pure PP (11 kJ m^{-2}) which is also shown in previous researches (Bledzki & Frauk, 2004; Bledzki et al., 2009). Using fine WF in the PP matrix reduces the impact strength because composite is more heterogenic than PP and it creates stress concentration regions in the WPC. These regions require less energy for breaking the composite under impact. Also, small WF particles are difficult to disperse due to their tendency to agglomerate which results in low impact energy therefore making the composite more brittle. The results show lower (50–100%) impact strength on chemically unmodified WF composites. The increased impact strength with chemically modified WF based composites can be explained by the fact that that alkaline treatment removes hemicelluloses, lignin and waxes which produces a rougher surface which in turn increases the length to diameter ratio or aspect ratio (L/D) thus enlarging the surface area of contact with the polymer matrix which increases the surface area of interaction at the interface (Ichazo et al., 2001). Higher impact strength on APTES modified WPC samples is also due to silanol groups in these composites that have strong bonds with hydroxyl groups of WF. These strong bonds increase interfacial adhesion between WF and the polymer matrix. It is supposed that the increased interfacial adhesion between WF and the polymer matrix is supported by the formation of siloxane by condensation reaction. (Kim et al., 2011). Therefore this impact test clearly shows the influence of chemical modification on the mechanical properties of WPC materials.

The results show (see Fig. 3) the highest impact values for WPC samples with APTES modified WF composites based on an addition of 2% glycerine (6 kJ m^{-2}). The addition of glycerine has increased impact strength by 70% due to a plasticization effect. This plasticization effect is caused by glycerine that plasticizes the amorphous components such as lignin and hemicellulose in wood by breaking some of the H-bonds present (Sanadi & Caulfield, 2008). However, there were no significant differences between thermally treated and untreated WF composite samples. Though, the impact values for thermally treated WF composites were slightly higher than those for untreated WF composites.

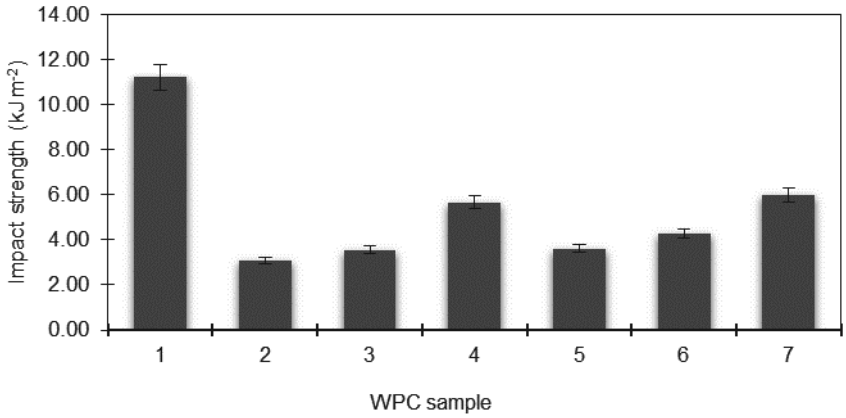

Figure 3. Impact strength of chemically and thermally modified and unmodified WF/PP composites.

Fourier transform infrared spectroscopy (FTIR)

FTIR spectra shows the changes of molecular interactions which lead to wave number shifts. The wavenumber values can be compared to multiple tables or specific software designed to give different chemical bond value range. Previous researches (Bodirlau et al., 2008; Emandi et al., 2011) show that typical wood structure has peaks 3,300–4,000 cm^{-1} indicating strong broad OH stretching and C-H stretching (2,800–3,000 cm^{-1}) in methyl and methylene groups. Specific, fingerprint area absorption in the region from 600–1,800 cm^{-1} are assigned to major cell wall components such as cellulose, hemicelluloses and lignin. (Rana et al., 2010).

In this study, FTIR spectra were collected by co-adding 32 scans at a resolution of 4 cm^{-1} in the range from 1,600–600 cm^{-1} at room temperature. It is the range of typical PP FTIR spectra which was compared to WPC samples to see any differences. FTIR spectra changes in WPC samples are demonstrated on Figs 4 and 5. There is no difference in FTIR spectra peaks between thermally modified and unmodified WF based composites. WPC samples had similar peaks to pure PP. However, there were changes in peak intensity in the range of 1,164 cm^{-1} to 1,025 cm^{-1} which are only present in WPC samples. In this region (1,164 cm^{-1} – 1,025 cm^{-1}) chemical modification of WF leads to changes of characteristic peaks and peaks changes for APTES treated samples are shown in Fig. 5. Modification with APTES showed peak changes at 1,025 cm^{-1} and 1,104 cm^{-1} assigned to Si-O-C band indicating that the coupling reaction between WF and APTES

has occurred thanks to the NaOH treatment. The signal intensity of the composite mixtures in comparison to pure PP (blue) in the range of 600–800 cm^{-1} are mostly aromatic structures example lignin molecules (Figs 4 and 5). Bands specific to PP used as the polymer matrix in WPCs are also present as shown in Table 2 and Figs 4 and 5. Peaks at 1,456 cm^{-1} represent CH_2 deformation; 1,376 cm^{-1} represent symmetric CH_3 deformation; peaks at 1,164, 998 and 974 cm^{-1} represent isotactic polypropylene band (Jordi).

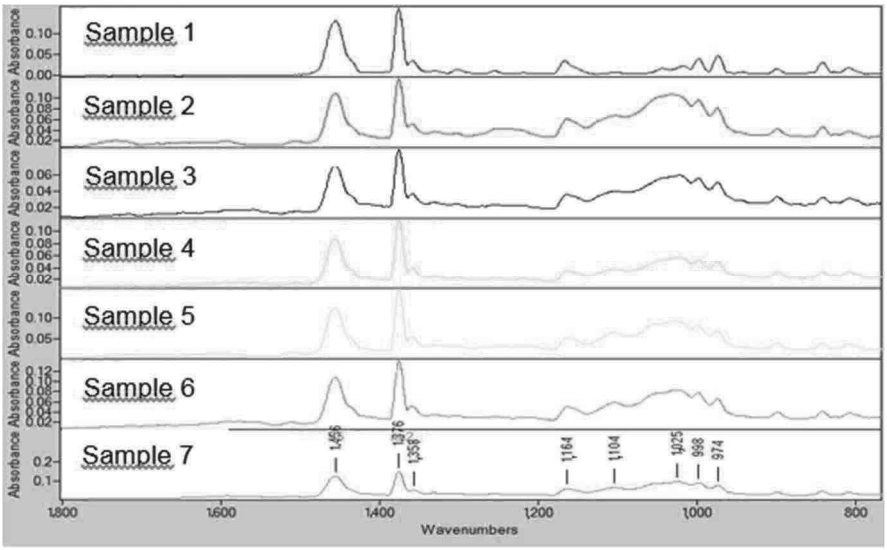

Figure 4. FTIR spectra of chemically and thermally modified and unmodified WF/PP composites.

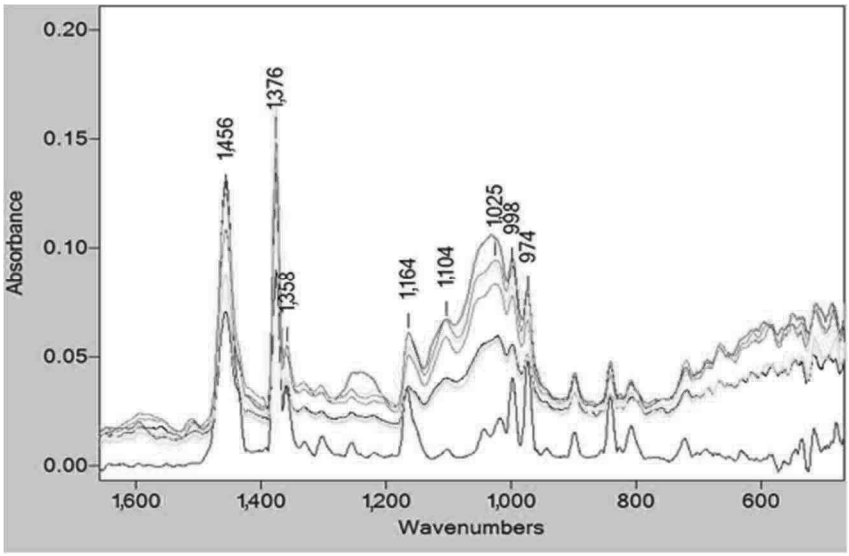

Figure 5. FTIR spectra peaks of chemically and thermally modified and unmodified WF/PP composites.

Table 2. FTIR peaks and identifications of WPC samples

Wavenumber (cm^{-1})	Frequency (cm^{-1})	Bond	Functional group
1,456	1,450–1,470	CH2 and CH3	Alkanes
1,376	1,375–1,380	CH3	Alkanes
1,358	1,350–1,370	C–H	Alkanes
1,164	1,000–1,320	RCOOR	Ester
1,104	1,000–1,100	Si–OR	Silyl ether
1,025	1,000–1,100	Si–OR	Silyl ether
998	900–1,050	P–OR	Ester
974	965–975	cis RCH=HCR	Alkene

CONCLUSIONS

This research focuses on exploring the use of thermally treated wood as a filler in thermoplastic composites. The objective was to investigate the different effects of chemically treated, thermally treated and untreated WF on the mechanical and physical properties of the obtained composites. It was found that thermally treated composite mixtures showed slightly higher MOE and flexural strength values than untreated wood mixtures thus suggesting that thermal treatment can increase the mechanical properties of the composite. However, there were no significant differences between chemically treated and thermally treated WF based composites. An addition of WF made the material more brittle as the impact strength results were lower than for pure PP. Thermally treated composite mixtures showed greater impact strength values than untreated composite mixtures. The addition of coupling agents helped to decrease the brittleness to some extent. FTIR showed that the coupling agent had reacted with the WF with the emergence of silyl ether groups (Si-OR). The addition of glycerine did not show any significant difference in the properties of the composites and may need further research. The use of thermally treated WF shows better mechanical properties than untreated WF composites. Waste materials from the timber industry can be easily used but perhaps the use of thermally treated wood may increase the price of the products.

REFERENCES

Adyembir, D., Kiziltas, A., Kiziltas, E.E., Gardner, D.J. & Gunduz, G. 2015. Heat treated wood-nylon 6 composites. *Compos. Part B. Eng*. **68,** 414–423.

Bledzki, A.K. & Frauk, O. 2004. Creep and impact properties of wood fibre–polypropylene composites: influence of temperature and moisture content. *Compos. Sci. Technol*. **64**, 693–700.

Bledzki, A.K., Jaszkiewicz, A. & Scherzer, D. 2009. Mechanical properties of PLA composites with man-made cellulose and abaca fibres. *Compos. Part A: App. Sci. Man*. **40**, 404–412.

Bodirlau, R., Teaca, A.C. & Spiridon, I. 2008. Chemical modification of beech wood: effect on thermal stability. *BioRes*. **3**, 789–800.

Emandi, A., Vasiliu, I. C., Budrugeac, P. & Stamatin, I. 2011. Quantitative investigation of wood composition by integrated FT-IR and thermogravimetric methods. *Cellulose Chem. Technol*. **45**, 579–584.

Eslam, H.K., Saieh, S.E. & Rajabi, M. 2011. Effect of steaming treatment on the physical and mechanical properties of WPC made of cotton flour and polypropylene. *Aus. J of Basic and App Sci*. **5**, 1143–1150.

Follrich, J., Müller, U., Gindl, W. & Mundigler N. 2010. Effects of long-term storage on the mechanical characteristics of wood plastic composites produced from thermally modified wood Fibers. *J. of Thermop. Comp. Mat*. **23**, 846–853.

Gatenholm, P., Bertilsson, H. & Mathiasson, A. 1993. The effect of chemical composition of interphase on dispersion of cellulose fibers in polymers. I. PVC-coated cellulose in polystyrene. *J. App. Pol. Sci.* **49**, 197–208.

Gwon, J.G., Lee, S.Y., Chun, S.J., Doh, G.H. & Kim, J.H. 2010. Effect of chemical treatments of wood fibers on the physical strength of polypropylene based composites. *Korean. J. Chem. Eng*. **27**, 651–657.

Ichazo, M.N., Albano, C., Gonzalez, J., Perera, R. & Candal, M.V. 2001. Polypropylene/wood flour composites: treatments and properties. *Comp. Struct*. **54**, 207–214.

John, M.J., Francis, B., Varughese, K.T. & Thomas, S. 2008. Effect of chemical modification on properties of hybrid fiber biocomposites. *Compos. Part A: App. Sci. Man.* **39**, 352–363.

Jordi, M. Case Study FTIR for Identification of Contamination. Jordi Labs LLC.

Kaboorani, A. & Faezipour, M. 2009. Effects of wood preheat treatment on thermal stability of HDPE composites. *J. of Rein. Plast. and Comp*. **28**, 2945–2955.

Kaboorani, A., Faezipour, M. & Ebrahimi, G. 2008. Feasibility of using heat treated wood in wood/thermoplastic composites. *J. of Reinf. Plast. and Comp*. **27**, 1689–1699.

Kallakas, H., Shamim, A. M., Olutubo, T., Poltimäe, T. Süld, M. T., Krumme, A. & Kers, J. 2015. Effect of chemical modification of wood flour on the mechanical properties of wood-plastic composites. *Agro. Res*. **13**, 639–653.

Kazayawoko, M., Balatinecz, J.M. & Matuana, L.M. 1999. Surface modification and adhesion mechanisms in woodfiber-polypropylene composites. *J. Mat. Sci*. **34**, 6189–6199.

Kim, T.W., Lee, S.Y., Chun, S.J., Doh, G.H. & Paik, K.H. 2011. Effect of silane coupling on the fundamental properties of wood flour reinforced polypropylene composites. *J. Compos. Mat*. **45**, 1595–1605.

Krzysik, A.M. & Youngquist, J.A. 1991. Bonding of air-formed wood fibre/polypropylene fibre composites. *Int. j. Adhesion and Adhesives*. **11**, 235–240.

Lu, J.Z., Wu, Q. & McNabb, H.S. 2000. Chemical coupling in wood fiber and polymer composites: a review of coupling agents and treatments. *Wood and Fiber Sci*. **32**, 88–104

Luo, S., Cao, J. & Wang, X. 2013. Investigation on the interfacial compatibility of PEG and thermally modified wood flour/polypropylene composites using the stress relaxation approach. *BioRes*. **8**, 2064–2073.

Ndiaye, D. & Tidjani, A. 2012. Effects of coupling agents on thermal behavior and mechanical properties of wood flour/polypropylene composites. *J. Compos. Mat*. **46**, 3067–3075.

Rana, R., Heyser, L.R., Finkeldey, R. & Polle, A. 2010. FTIR spectroscopy, chemical and histochemical characterisation of wood and lignin of five tropical timber wood species of the family of Dipterocarpaceae. *Wood Sci. Technol*. **44**, 225–242.

Sanadi, A.R. & Caulfield, D. 2008. Thermoplastic polyolefins as formaldehyde free binders in highly filled lignocellulosic panel boards: using glycerine as a processing aid in kenaf fibers polypropylene boards. *Mat. Res*. **11**, 487–492.

Agronomy Research **14**(Sp.1), 1004–1014, 2016

Determination of the heat flux of steel for the heat treatment model of agricultural tools

A. Kešner[1,*], R. Chotěborský[1] and M. Linda[2]

[1]Department of Material Science and Manufacturing Technology Faculty of Engineering, Czech University of Life Sciences Prague, Kamýcká 129, CZ 165 21 Prague – Suchdol, Czech Republic
[2]Department of Electrical Engineering and Automation, Faculty of Engineering, Czech University of Life Sciences Prague, Kamýcká 129, CZ 165 21 Prague – Suchdol, Czech Republic;
[*]Correspondence: kesner@tf.czu.cz

Abstract. Chisels and tines for agricultural machinery are mechanically worn. Mechanical wear depends on the microstructure of the material. The desired microstructure of the material, specifically steel is obtained by heat treatment. Microstructure after heat treatment can be determined in two ways. The first one is the experimental determination, which is time-consuming and not economically efficient. The second is to build the thermal model during the heat treatment. Microstructure is affected during the heat flux during heat treatment. This research was focused on the boundary conditions of the model heat flux during quenching. The heat flux was measured during quenching with solid cylindrical samples (ø25–50 mm) by means of two thermocouples. The first temperature was measured in the axis of the sample and the second temperature was measured near the sample surface. The results of the heat flux were appointed to the model and experimentally verified. In this way it is possible to construct a model of tines and chisels for agricultural machine, which shows the progress of the heat flux during quenching.

Key word: quenching, FEM, tool steel, heat flux.

INTRODUCTION

Mechanical properties of the surface of a product are designed microstructure (Prabhu & Prasad, 2003; Li & Wells, 2005). For this reason an estimation of the hardening course is very important (Telejko, 2004). The most important step during quenching is cooling (Li & Wells, 2005). Quenching of steel in liquid medium consists of three distinct stages of cooling: vapor phase, nucleate boiling, and convective stage. In the first stage, a vapor blanket is formed immediately upon quenching. This blanket has an insulating effect and heat transfer in this stage is slow, since it is mostly through radiation (Prabhu & Prasad, 2003; Fernandes & Prabhu, 2007). The heat flux between the surface material and the hardening medium is essential to simulate hardening. The parameters affecting the heat flux are heating temperature, the sample surface, the movement of quenching media, thermo-physical properties of the sample and quenching media. The most widely used quenching medium is readily available and cheap water. The thermophysical properties of the water also depend on the correct setting of

boundary conditions of modeling to estimate the heat flux. The choosing exact boundary conditions allows the correct choice of quenching medium (Prabhu & Prasad, 2003; Li & Wells, 2005).

Estimation of the heat flux and the heat transfer coefficient of measured temperatures is based on the inversion method (Archambault et al., 1997; Babu & Prasanna Kumar, 2009; 2014). The right method for getting the realistic metal/quenchant interfacial heat transfer properties is inverse modeling and this method allows the determination of boundary conditions by the coupling of numerical methods with simple temperature measurements inside the quench probe (Prabhu & Prasad, 2003). The inverse method consists in numeric selection of boundary heat transfer conditions providing a heat distribution in the sensor not differing, within the necessary accuracy limits, from the assumed one (Buczek & Telejko, 2004; Lu et al., 2013). Various ways of inverse method solutions are documented (Ref.). Heat flux transient technique was found to be more accurate than the Grossmann technique in assessing the severity of quenching (Prabhu & Prasad, 2003). Telejko (Telejko, 2004) applied the method of inverse thermal conductivity. Thermal conductivity computations were done using measured temperature profiles. Heat equations were compiled using the finite element method (FEM). The optimization computing has been solved by the Broyden–Fletcher–Goldfarb–Shanno (BFGS) variable metric method. (Ramesh & Narayan Prabhu, 2014) used a high performance smart camera for temperature measurement. Specifications of these methods are described for example in (Blackwell & Beck, 2010), wherein the model equation are parabolic in time, provided that the heat flux is constant over time. The predicted temperature is used to reduce errors in the estimates of heat flux measurements and also to stabilize the calculation as the time steps. The heat flux is determined so as to minimize the least squares error between the model and experimental temperatures and it is also thoroughly monitored during casting. Methods of detection also include using a 3-D inversion technique. For best detection of the temperature course thermocouples are placed in transverse and longitudinal sections, which also serve as input parameters to boundary conditions (Hebi et al., 2006).

For accurate simulation of heat treatment it is necessary to accurately estimate temperatures in the components and know the thermo-physical properties and quenching media (Archambault et al., 1997; Telejko, 2004). To predict the temperature field of the heat treatment finite element models were developed. Thermal conductivity λ can be calculated if the density ρ and specific heat capacity c_p are known (Telejko, 2004).

Babu (Babu & Prasanna Kumar, 2009) proposed description of heat flux as a function of dimensionless parameters. Boundary conditions were set in ANSYS. Their results showed that the heat flux is dependent on the initial heating temperature.

High-current cooling of the material has been shown to provide big temperature differences in the material and correct mathematical model makes it possible for it to be preceded by deformation of the material (Naceur et al., 2011). Accuracy of the FEM facilitated successful comparison of two cooling media (Buczek & Telejko, 2013).

Hardening of the material creates bainitic or martensitic structure (Fernandes & Prabhu, 2007). When creating heat equations, it is necessary to take into account the phase transformation during quenching (Telejko, 2004). Correct estimate of the course of heat treatment can predict the course of phase transformations (Babu & Prasanna Kumar, 2014).

(Prabhu & Fernandes, 2007) discovered that the surface roughness of the product has a significant effect on the flow of the thermal field and thus the final microstructure component. Grooved surface had fully martensitic structure. Smooth surface had a mixed microstructure.

The phase transformations occur during the hardening of the material. (Hernandez-Morales et al., 1992), like most authors in literature, phase transformation during heat flux is neglected. (Telejko, 2004) summed knowns temperature phase transformations and calculations divided into three steps. In the first step calculations the thermal conductivity up to temperature of phase transformation is determined on the basis of a heating test. In the second step, function for the temperatures above the phase transformation is calculated by using the temperature measurements from the cooling test. Finally, the thermal conductivity was determined using all the temperatures.

The sets of boundary conditions are crucial to model accuracy. It is necessary to use algorithm to optimization of heat treatment which their aim will be found to thermal cycle to ideal structure. The algorithm of FEM model needs a general model for a sets of Neumann conditions. Other than simple function to FEM programming increase the time calculation. Thus losing the advantage of modeling. Generalized functions can be used for creating FEM models. This function can be used, for example, to optimization of heat treatment of agricultural tools (Chotěborský & Linda, 2015).

This paper is focused onto estimate of simple equation of heat flux during quenching at different conditions of cooling and heating temperatures. The simple nonlinear function is generalized to set temperature conditions.

MATERIAL AND METHODS

The method in this work enables estimation of the heat flux on the basis of the inverse method using the FEM model. Chemical composition of tested steel is presented in Table 1.

Table 1. Chemical composition of steel 25CrMo4 in wt. %

	C	Mn	Si	P	S	Cr	Ni	Mo	Cu	V
25CrMo4	0.250	0.710	0.230	0.018	0.022	1.030	0.090	0.210	0.230	0.004

The experimental procedure consisted of a furnace for heating the samples. A container with water as cooling media was placed next to the furnace for quick transfer of samples into the bath. Eighteen samples (ø25–50mm) were used each to which was secured a pair of thermocouples (near the surface and the axis of the sample). Thermocouples were electrically isolated with a protective coating and connected to the measuring apparatus. The measuring apparatus was connected to the computer and measured temperatures were recorded during the heat treatment. The experimental system is shown in Fig. 1.

Quenching had different heating temperatures (800 °C, 900 °C and 1,000 °C), and done in a calm cooling environment (standing water) or a moving cooling medium (turbulent water). Heating holding time was 0.5 hours for each sample. Each measurement was repeated 3 times at the heating temperature (It was processed a total of 18 samples).

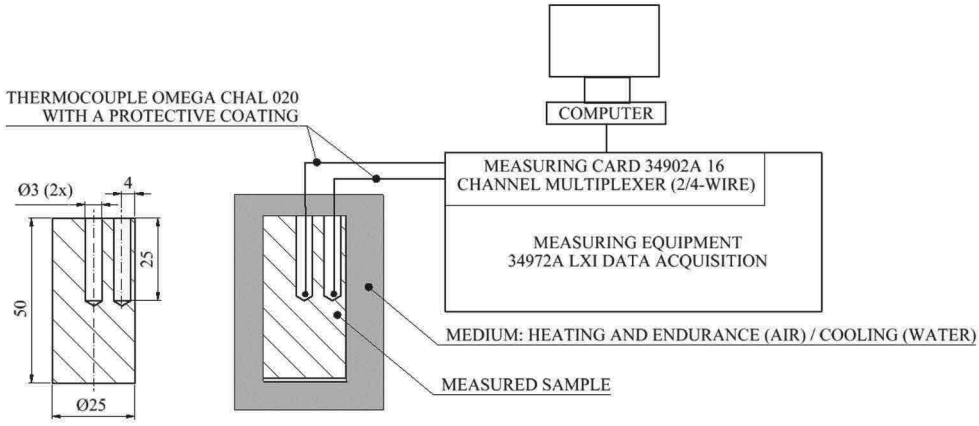

Figure 1. Scheme of measurements of heat treatment of samples.

The recorded measure data (time, temperature) were separated to a heating, holding time at heating temperature and the cooling stage. These two steps were separated by an algorithm written in SCILAB 5.5.1 – See Fig. 2.

From the cooling were obtained temperature differences of surface and core of sample. Furthermore, according to the eqn 1, absolute temperatures were transformed to the relative temperatures (dimensionless temperature-from 0 to 1).

$$r = \frac{T_K - T_{MINK}}{T_{MAXK} - T_{MINK}} (-) \tag{1}$$

where: T_K – actual surface temperature (K); T_{MINK} – minimum surface temperature (K); T_{MAXK} – maximum surface temperature (K).

Experimental heat flux was calculated from eqn 2:

$$q = \pi \cdot \lambda \cdot \frac{\Delta T}{rt} \tag{2}$$

where: q – heat flux (W m^{-2}); λ – thermal conductivity (W m^{-1} K^{-1}); ΔT – difference the measured temperature on surface and in the core of sample (K); rt – the measured distance of thermocouples (m).

The constants c_0, c_1, c_2 were determined by Levenberg-Marquardt algorithm according to eqn. 3 and 4. The constants c_1, c_2 characterize curve slope.

$$fce(r) = c_0 \cdot r^{c_1} \cdot (1 - r)^{c_2} \tag{3}$$

where: c_o – constant (boost) (-); c_1, c_2 – constants (slope from the peak) (-).

$$\sum_{i=1}^{n-1} \left(\Delta T_i \times (x_i - x_{i+1})\right) = \int_0^1 fce(r) \tag{4}$$

where: ΔT_i – difference of the cooling temperature at time (K); x_i – the absolute value of the axis x (-).

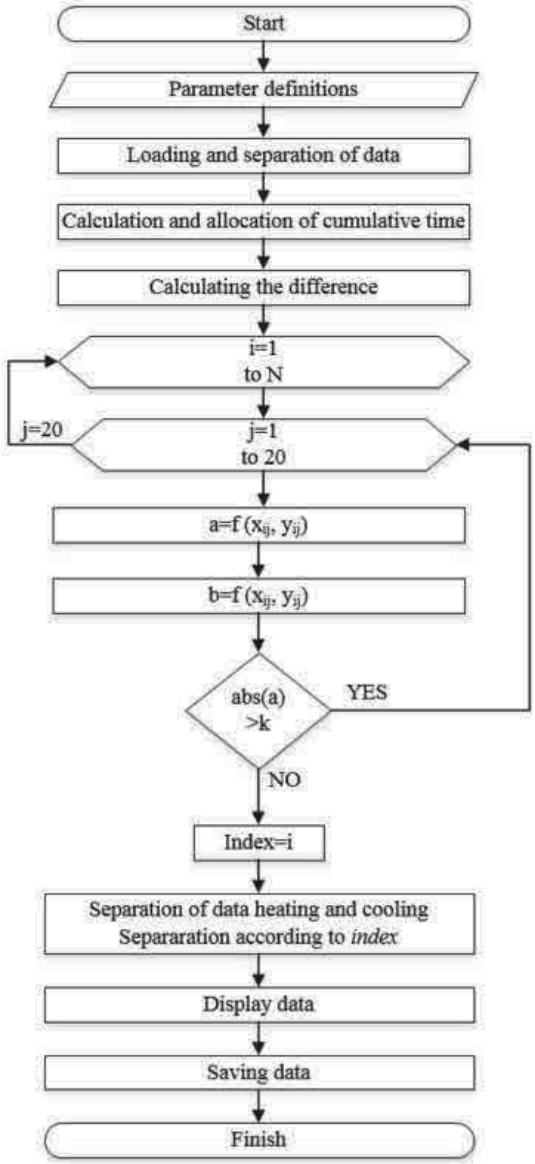

Figure 2. Flow chart for data processing, where N is number of measured data, j = 20 is set number of data for regression (fixed number of data for regression with regard to the course of the derivation measurement data – the result was affected at smaller value), a and b are the parameters functional dependency f(x) = ax+b, k is set directive for compared to with the calculated value.

These values have been transformed from relative values into absolute values for the FEM calculation using eqn 5.

$$x_i = r \cdot (T_{MAX} - x_0) + x_0 \tag{5}$$

where: x_0 – the surface temperature during cooling (K).

The course of the calculated heat flux depending on the calculated surface temperature is shown in Fig. 5. Calculated surface temperature was calculated from eqn 6.

$$\mathrm{Tpc} = \frac{\mathrm{r}^2 \cdot (\mathrm{Tp} - \mathrm{Ta})}{\mathrm{rt}^2} + \mathrm{Ta} \tag{6}$$

where: r – the radius of the sample (m); Tp – measured surface temperature (K); Ta – measured core temperature (K).

RESULTS AND DISCUSSION

Measured data of surface and core temperatures of samples were used to fit Eqn (2). The result is shown in Fig. 3. It is dependency between heat flux and dimensionless temperature for sample 25CrMo4 number 1 – cooled in calm waters at 800°C heating temperature.

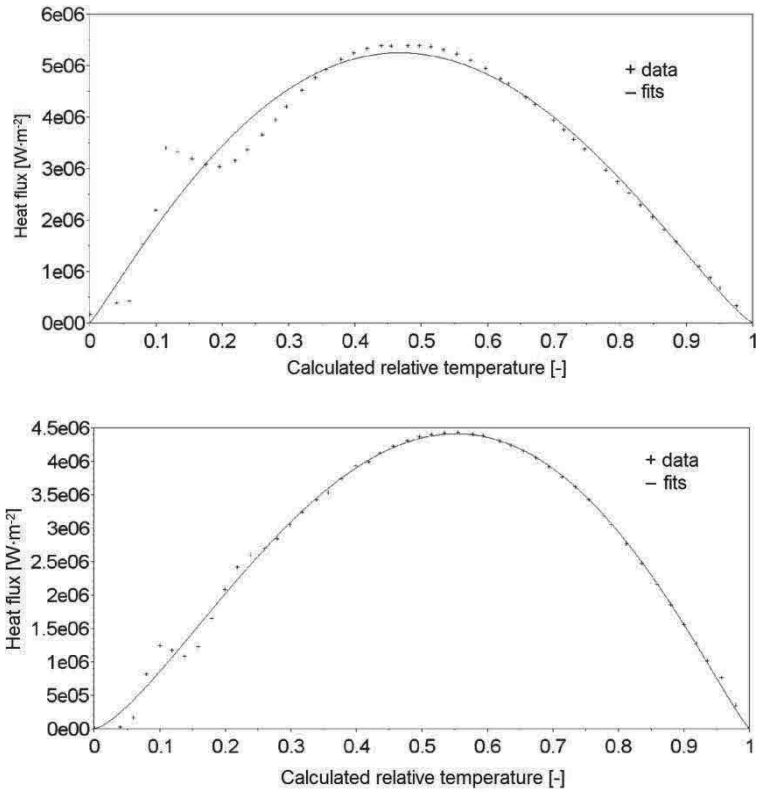

Figure 3. Dependency between heat flux and relative temperature – in the upper part is sample 25CrMo4 number 1 – cooled in calm waters at temperature of heating 800°C and in down part is sample 25CrMo4 number 14 – cooled in calm waters at temperature of heating 1,000°C.

In Figs 3–6 are shown dependency between coefficients c_0, c_1, c_2 and temperature of the heating furnace. The results show that a correlation exists between these coefficients and heating temperature. In Figs 3–6 are presented obtained coefficient from fit and heating temperatures. Obtained data can be fitted by regression, index of determination show a significant and close correlation between coefficients and heating temperature. Increasing heating temperature was observed to influence coefficients of Eqn. 3. Dependency between coefficients and heating temperature show decreasing character.

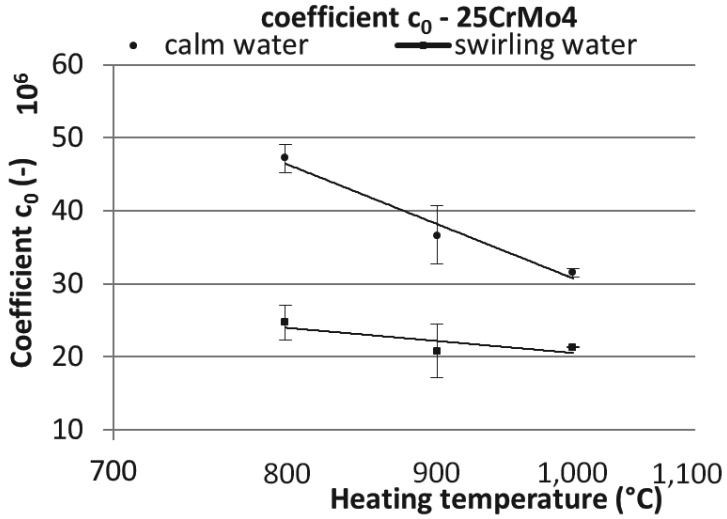

Figure 4. Dependency between coefficient c_0 and heating temperature for steel 25CrMo4.

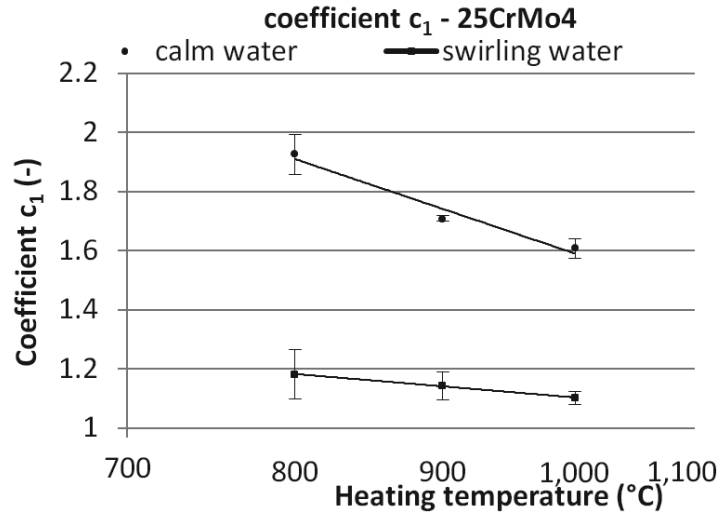

Figure 5. Dependency between coefficient c_1 and heating temperature for steel 25CrMo4.

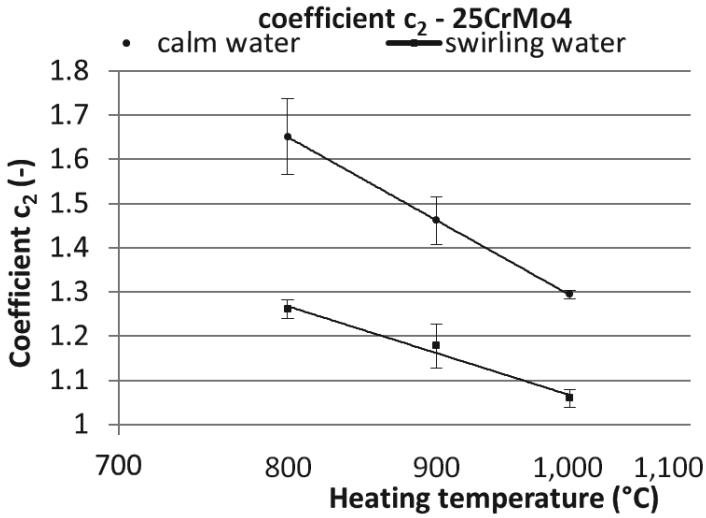

Figure 6. Dependency between coefficient c_2 and heating temperature for steel 25CrMo4 number 12 – cooled in calm waters at various heating temperature.

Eqn. 3 can be generalized if we use a temperature dependency of coefficient these equation according to regression function (Table 2). In Table 3 are presented correlation between mathematical models according to Eqn. 3. Statistical analysis show that the mathematical model is close to measured data and it can be used as a general model in the 800–1,000 °C temperature range.

Table 2. Temperature dependency of coefficient according to regression function

coefficients	calm water	swirling water
c_0	$7{,}030 \times 10^{-7} \cdot \log(T) + 5{,}164 \cdot 10^{8}$	$1{,}545 \times 10^{-7} \cdot \log(T) + 1{,}273 \cdot 10^{8}$
c_1	$-1.433 \cdot \log(T) + 11.491$	$-0.357 \cdot \log(T) + 3.566$
c_2	$-1.605 \cdot \log(T) + 12.377$	$-0.902 \cdot \log(T) + 7.299$

Table 3. Correlation between mathematical model and measured data

	800 °C	900 °C	1,000 °C
calm water	0.996118	0.983460	0.995671
swirling water	0.991619	0.990898	0.992837

Correlation between mathematical model and measured data was calculated according to Eqn. 7 (Xu et al., 2016)

$$r_{xy} = \frac{n \cdot \sum x_i.y_i - \sum x_i \cdot \sum y_i}{\sqrt{n \cdot \sum x_i^2 - (\sum x_i)^2} \cdot \sqrt{n \cdot \sum y_i^2 - (\sum y_i)^2}} \tag{7}$$

where: x are measured data (°C); y are calculated data (°C); n is number of data (pcs).

Fig. 7 shows dependency between predicted heat flux and measurement heat flux.

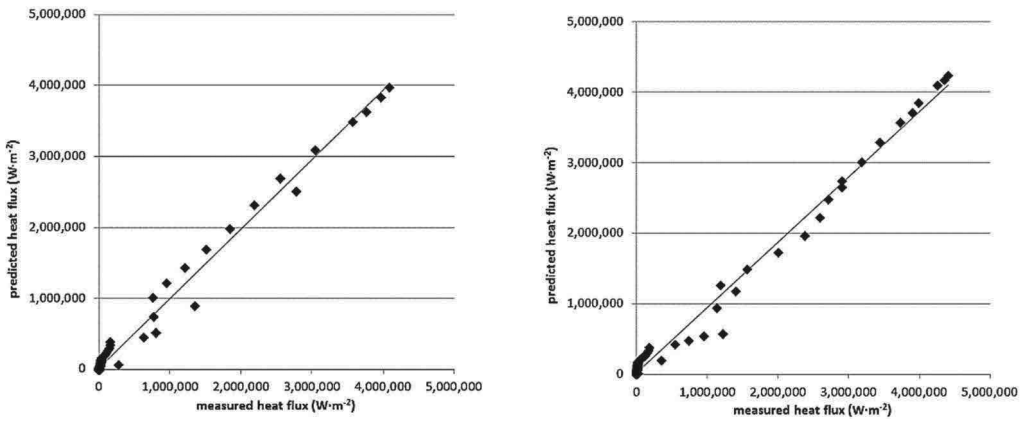

Figure 7. Dependancy between predicted heat flux and measurement heat flux – left side for sample 1 and right side for sample 14.

(Prabhu & Prasad, 2003; Li & Wells, 2005; Abishek et al., 2013;) in their articles performed similar measurements at a single heating temperature. In this study, there were three heating temperature which led to a refinement of the model.

(Prabhu & Fernandes, 2007; Babu & Prasanna Kumar, 2009; Babu & Prasanna Kumar, 2014;) in their publications took same measurements under various cooling environments and the dependencies of heat flux were described using polynomial functions. If we look at the value of function near the boundary conditions (near to maximal and minimal temperatures), polynomial function can yield fatal errors near the boundary conditions. The function presented in this article eliminates those errors and it can be generalized. The polynomial function on the other hand cannot be generalized.

For the present model, it is not necessary do experimental validation of heat fluxes at temperatures other than those listed in this article. It is possible to construct algorithms for finding optimal heat treatment parameters in order to reduce the energy and time consumption in production while maintaining or improving the mechanical properties of agricultural tools.

CONCLUSIONS

The following findings can be summarized from the experimental measurements:

- Depending on the surface temperature, the position of the maximum flux rises with increasing heating temperature,
- there is a link between the coefficients c_0, c_1 and c_2 eqn 2 and the heating temperature,
- function in this article eliminates physical errors, unlike commonly used polynomial function,
- the outcrop function of this study can be generalized,
- the process of creating FEM models used in this article enables design heat treatment without verification with the experimental treatment with different temperatures than those mentioned in this article,

- algorithms for finding optimal heat treatment parameters - while reducing energy and time consumption and maintaining or improving the mechanical properties of agricultural tools can be created for the procedure above.

ACKNOWLEDGEMENT. Supported by Internal grant 31140/1312/3105 agency of Faculty of Engineering, Czech University of Life Sciences in Prague.

REFERENCES

Abishek, S., Narayanaswamy, R. & Narayanan, V. 2013. Effect of heater size and Reynolds number on the partitioning of surface heat flux in subcooled jet impingement boiling. *International Journal of Heat and Mass Transfer* **59**, 247–261.

Archambault, P., Denis, S. & Azim, A. 1997. Inverse resolution of the heat-transfer equation with internal heat source: Application to the quenching of steels with phase transformations. *Journal of Materials Engineering and Performance* **6**(2), 240–246.

Babu, K. & Prasanna Kumar, T.S. 2009. Mathematical Modeling of Surface Heat Flux During Quenching. *Metallurgical and Materials Transactions B* **41**(1), 214–224.

Babu, K. & Prasanna Kumar, T.S. 2014. Comparison of Austenite Decomposition Models During Finite Element Simulation of Water Quenching and Air Cooling of AISI 4140 Steel. *Metallurgical and Materials Transactions B* **45**(4), 1530–1544.

Blackwell, B. & Beck, J.V. 2010. A technique for uncertainty analysis for inverse heat conduction problems. *International Journal of Heat and Mass Transfer* **53**(4), 753–759.

Buczek, A. & Telejko, T. 2004. Inverse determination of boundary conditions during boiling water heat transfer in quenching operation. *Journal of Materials Processing Technology* **155-156**, 1324–1329.

Buczek, A. & Telejko, T. 2013. Investigation of heat transfer coefficient during quenching in various cooling agents. *International Journal of Heat and Fluid Flow* **44**, 358–364.

Fernandes, P. & Prabhu, K.N. 2007. Effect of section size and agitation on heat transfer during quenching of AISI 1040 steel. *Journal of Materials Processing Technology* **183**(1), 1–5.

Hebi, Y., Man, Y. & Dacheng, F. 2006. 3-D Inverse Problem Continuous Model for Thermal Behavior of Mould Process Based on the Temperature Measurements in Plant Trial. *ISIJ International* **46**(4), 539–545.

Hernandez-Morales, B., Brimacombe, J.K. & Hawbolt, E.B. 1992. Application of inverse techniques to determine heat- transfer coefficients in heat- treating operations. *Journal of Materials Engineering and Performance* **1**(6), 763–771.

Chotěborský, R., & Linda, M. 2015. FEM based numerical simulation for heat treatment of the agricultural tools. *Agronomy Research* **13**(3), 629–638.

Li, D.I. & Wells, M.A. 2005. Effect of subsurface thermocouple installation on the discrepancy of the measured thermal history and predicted surface heat flux during a quench operation. *Metallurgical and Materials Transactions B* **36**(3), 343–354.

Lu, J.F., Bourouga, B. & Ding, J. 2013. Transient boiling heat transfer performances of subcooled water during quenching process. *International Communications in Heat and Mass Transfer* **48**, 15–21.

Naceur, I.B., Kchaou, M. & Ksibi, H. 2011. Optimization of local cooling for hot components by a water jet. *Metal Science and Heat Treatment* **53**(5–6), 233–238.

Prabhu, K.N. & Fernandes, P. 2007. Effect of surface roughness on metal/quenchant interfacial heat transfer and evolution of microstructure. *Materials & Design* **28**(2), 544–550.

Prabhu, K.N. & Prasad, A. 2003. Metal/Quenchant Interfacial Heat Flux Transients During Quenching in Conventional Quench Media and Vegetable Oils. *Journal of Materials Engineering and Performance* **12**(1), 48–55.

Ramesh, G. & Narayan Prabhu, K. 2014. Spatial Dependence of Heat Flux Transients and Wetting Behavior During Immersion Quenching of Inconel 600 Probe in Brine and Polymer Media. *Metallurgical and Materials Transactions B* **45**(4), 1355–1369.

Telejko, T. 2004. Analysis of an inverse method of simultaneous determination of thermal conductivity and heat of phase transformation in steels. *Journal of Materials Processing Technology* **155-156**, 1317–1323.

Telejko, T. 2004. Application of an inverse solution to the thermal conductivity identification using the finite element method. *Journal of Materials Processing Technology*.

Xu, W., Ma, R., Zhou, Y., Peng, S. & Hou, Y. 2016. Asymptotic properties of Pearson′s rank-variate correlation coefficient in bivariate normal model. *Signal Processing* **119**, 190–202.

Agronomy Research **14**(Sp.1), 1015–1022, 2016

Electromagnetic shielding properties of ceramic spheres coated with paramagnetic metal

T. Koppel[1,*], A. Shiskin[2], I. Hussainova[1], H. Haldre[3] and P. Tint[1]

[1]Tallinn University of Technology, Ehitajate 5, EE 12616 Tallinn, Estonia
[2]Faculty of Material Science and Applied Chemistry, Riga Technical University, 3 Paula Valdena str, LV-1048 Riga, Latvia
[3]Institute of Environmental Health and Safety, Jaam 14, EE 11615 Tallinn, Estonia
[*]Correspondence: tarmo.koppel@ttu.ee

Abstract. This study utilized a setup of radiofrequency generating and metering instruments to measure the reflective and pass-through properties of the innovative material of paramagnetic metal coated ceramic hollow spheres (MCS). The dimensions of the spherical articles reside around 50–250 μm, the thickness of metal (Cu) coating is 0.5–1.3 μm. The radiofrequency field was of 2.4 GigaHertz (GHz) frequency and radiated towards the material via a waveguide-horn antenna at 100 mWt power output. Two additional waveguide-horn antennas connected to a radiofrequency analyzer measured the reflection and pass-through characteristics of the material. Reflection and pass-through coefficients (from 0 to 1) were calculated to each tested sample. The material was tested at different thicknesses: from single – to multi (up to 5) mono-layers and 5 mm layer in bulk condition of MCS.
The measurement results show insignificant shielding characteristics for 1 to 5 layer thickness samples: pass-through coefficient from 0.96 to 0.92. Noteworthy shielding characteristics were starting to show in case of MCS mixed with graphite emulsion: transmission coefficient dropped to 0.16.
The latter sample demonstrates the prospective shielding characteristics of the material, since most of the radiofrequency radiation was not allowed to pass through the material neither to be reflected, but absorbed within the structure of the material.

Key words: electromagnetic fields, microwaves, shielding, absorption, cenospheres.

INTRODUCTION

With the emergence of new high intensity radiofrequency technologies in the workplaces has risen the workers exposure to the electromagnetic fields. Also, the modern urban environment is packed with new wireless communication protocols, because of which the environmental radiofrequency electromagnetic fields have shown abrupt rise during the last ten years. Controlling the propagation of these fields has become increasingly relevant both in living and occupational environments.

The importance of minimizing exposure to the electromagnetic fields is also stressed by the high level European bodies. Reduction of environmental risk factors, where possible, is in fact the corner stone of European occupational health legislation (EP&EC, 2013).

Electromagnetic radiation from high intensity sources may have adverse effects on human health. Development of new coating materials has become relevant in order to suppress the above mentioned fields where needed. Reducing the electromagnetic fields would allow better controlling such technologies in a way that these would not pose a risk to human health nor to other technologies in the area. The civil construction domain would gain a new material, which would allow shielding houses or rooms from high level electromagnetic fields, infrared radiation, and noise. Due to the electromagnetic shielding properties of the material, it could also be used to reduce the risk of industrial espionage from electronic eavesdropping.

Non-destructive testing using microwaves is a method used to characterize various properties of material without braking it or making it useless in another way. Mainly non-destructive testing is used for material dielectric characterization, fatigue surface crack evaluation of metals, layered composite inspection, microwave measurements and imaging.

Microwaves penetrate into dielectric materials easily. The limitation is the depth, from where useful information can be received, which is mainly a function of the loss factor of that material or testing from both sides – reflection and transmission measurements. Microwave non-destructive testing is sensitive to geometrical and dimensional properties of the given material (Zoughi, 2000).

Therefore microwaves could be used for testing density, thickness, hardness, porosity, moisture, anisotropy, chemical composition, degree of aging, presence of voids, cracks, delaminations. Tests could be made from a distance, since microwave travel relatively a long way. Therefore such tests are utilized in to determine the moisture in grains of cereals and detecting buried metal objects. Microwave techniques have proved very effective in locating delaminations in honeycomb structures and fibre composites, but they are not useful in detecting thinner cracks (Blitz, 1997).

It is expected that while hitting the material, some microwaves will bounce back (reflection) and some will penetrate the material (transmission). Another part of the microwaves gets trapped inside the material (absorption). The latter portion would desirably claim the largest part of the given three, since materials that allow the microwaves to penetrate are useless in controlling the emissions of the electromagnetic fields. From another side, reflection is also not desirable in some instances, since reflecting microwaves would just create countless reflections in the environment, therefore increasing the levels of microwave many folds or even many orders of magnitude. Each application of the microwave controlling material could have their own prescriptions on how much of the incident wave is passed, reflected or absorbed. For example, in environments where communications are done by means of wireless devices, having some transmission of microwaves could be required.

The applications of this innovative material include shielding the objects from incoming electromagnetic emissions but also from outbound electromagnetic fields. Examples of such applications may be to build casing for sensitive electronic equipment, but also to protect the environment and humans within the environment from the high intensity electromagnetic fields. Also, the radiofrequency electromagnetic fields may be shielded at their source i.e. by using the material in the construction of the equipment that generates and propagates such intense fields.

Also the current safety guidelines refer that the obligation of the employer is not only to assure the workplace's compliance with the limits but also to ensure that EMFs are reduced to the minimum. Special risk groups should also be considered – pregnant women and people wearing passive or active medical implants (EP&EC, 2013).

There are many places where people in work or in public are exposed to the EMFs. An international study done in several European countries, monitored peoples overall exposure to the EMFs, and it was found that the highest exposures were encountered in transportation vehicles (e.g. people using mobile devices simultaneously in a closed metal casket), followed by exposure in outdoor urban environments (wireless transmission antennas), and then in offices, followed by urban homes (Wout et al., 2010).

Modern office environment consists of a many EMF propagating appliances: some produce EMFs as a by-product; others use EMFs intentionally (e.g. wireless data link). Many of such types of products are new and not fully covered by compliance standards, therefore may create exposures to the EMFs that are currently unaccounted for in the guidelines (Kühn et al., 2007).

Frequencies of the electromagnetic fields produced by the laptop computers also vary from model to model. Besides typical sinusoidal waveforms, the EMFs have also an impulsive nature forming a complex waveform (Zopetti et al., 2011). Switching mode power supplies should be considered as main contributors to the impulse EMFs in the PC usage. A study by Zopetti et al. (2011) concluded that power supply units are the main source of high EMFs.

Bellieni et al. (2012) reported that next to the power supply unit, also the laptop PC's body itself (being in contact with a human body) gives off nearly the same levels of EMFs, and these can be higher than these found in the proximity of high tension power lines, transformers and domestic video screens.

This study is set to investigate shielding of paramagnetic metal material under Wi-Fi frequency microwaves.

MATERIALS AND METHODS

This study investigates electromagnetic shielding properties of ceramic hollow spheres coated with paramagnetic metal. The composite powder is a ceramic hollow sphere (cenosphere, obtained from fly ash of coal combustion at a thermal-power plant) coated with a paramagnetic metal (Cu) by magnetron sputtering. The samples MCS outer and internal structure are shown in figure 1. MCS has bulk density 0.44 ± 0.003 g cm^{-3}, metal coating has thickness 0.5–1.3 μm sphere wall thickness is 10–15 μm (Fig. 1a) and sphere diameter is 50–250 μm (Fig. 1a).

The material was tested at different thicknesses: from 1 mono-layer of ceramic hollow spheres coated with metal to a 5 mm layer in bulk condition. The sample sheet size was 270.0 x 390.0 mm.

The sheets of MCS were produced by laying down MCS on a self-adhesive polymer film (ORACAL 1640, by ORAFOL Europe GmbH). The self-adhesive film was put on a flat surface and the protective paper removed. The adhesive film was covered with 2 mm layer of MCS. The layer was applied with a pressure of 980 N m^{-2} for 1 min. The excess amount of MCS was cleaned off from the film so that a monolayer of MCS would remain attached to the film.

The outlay of ceramic hollow spheres coated with paramagnetic metal was 71.9 ± 1.2 g m^{-2} for a single sheet which was determined by weighing adhesive films before and after being covered by MCS.

The MCS bulk material of 2 to 5 mm was produced by using a radiofrequency transparent tray that was covered evenly with a specified amount of MCS.

A graphite PVA (polyvinyl alcohol) emulsion with MCS contains of 45 vol % of polyvinyl alcohol (20%), 33 vol % of MCS and 22 vol % of graphite.

An aluminium foil used in covering 5mm MCS bulk material was of thickness 100 μm.

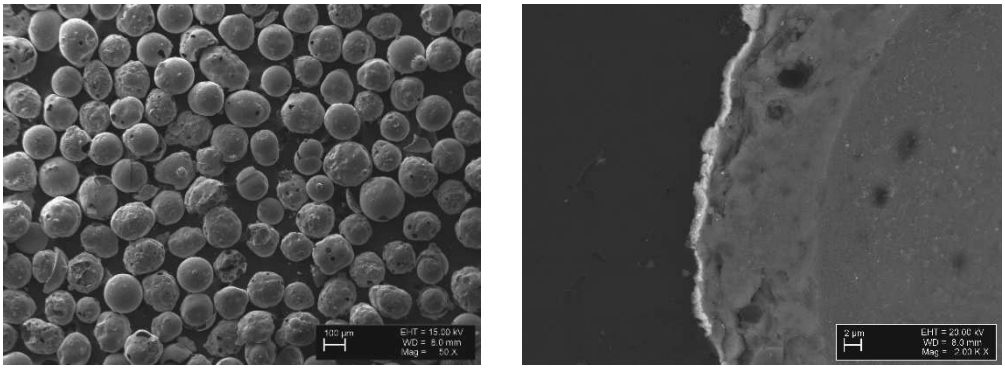

a) b)

Figure 1. Scanning electron microscope images of MCS: a) common view at magnification x 50 and b) cross section of at magnification x 2000.

The study was founded on a premise that hollow spheres absorb the electromagnetic fields. Like shown by Panigrahi & Srivasava (2015) the synthesized spherical hollow spheres act as a conducting trap in absorbing electromagnetic (EM) wave by internal reflection.

A setup of three standard gain (2.4 GHz) horn antennas were used (Fig. 2) to determine the electromagnetic properties of the materials under testing (MUT). One of the horn antennas (Tx1) acted as an irradiator radiating a microwave beam on to the tested material. The other two antennas were used for receiving and measuring the amplitude of the signal (Rx1 and Rx2). Horn Rx1 collected the signal reflected back from the material under testing. Horn Rx2 collected the signal that penetrated the material under testing. From both receiving horn antennas the signal was routed via RF switch to a Universal Protocol Test Platform Rohde & Scharz CRTU which measured the amplitude of the signal. The signal was generated by the same unit and amplified by an external amplifier (Power output-Po 100 mW). In this study the testing frequency was 2.45 GHz as the intention was to test the materials under Wi-Fi frequency. The power output was also selected to reflect the nominal irradiating power of the Wi-Fi routers.

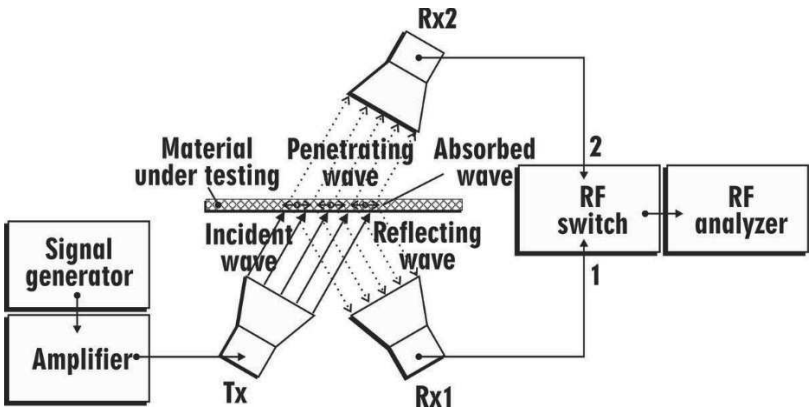

Figure 2. Material testing setup.

In case of transmitting horn antenna, the radiation emerges from the horn in a parallel beam, called near-field or Fresnel zone. Divergence of the field takes place in the so-called far-field or Fraunhöfer zone with the wave intensity decreasing by the inverse square law – the amplitude decreases in inverse proportion to distance from the opening of the horn (Blitz, 2012).

The length of the near field zone (l) in case of rectangular horn opening was considered based on the formula by Botsco et al. (1986) (formula 1), where A is the dimension of the largest side of the rectangle and λ the wavelength. The wavelength in case of 2.45GHz electromagnetic field is 0.122 m.

$$l = \frac{A^2}{2\lambda} \tag{1}$$

In making the microwave measurements where determining the amplitude and attenuation was the goal, it is important to take into account the beam propagation from the horn into the far field.

Prior to a measurement the setup was prepared by following a calibration procedure which included measuring full and zero reflection/transmission microwave levels. The full reflection was measured by placing a sample size aluminium plate to the sample tray. The full transmission was obtained by leaving the sample tray empty and measuring the detected microwaves at the transmission registering horn antenna.

Reflection and transmission coefficients (from 0 to 1) were calculated to each tested sample as a transmitted/reflected wave ratio to the full transmission/reflection.

RESULTS

Altogether nine variations of the paramagnetic metal coated ceramic spheres were investigated. The measurement results show insignificant shielding characteristics for 1 to 11 layer thickness samples: pass-through coefficient from 0.96 to 0.87 (96 to 87 per cent of the radiation passes through the material), see Table 1.

Increasing MCS thickness up to 5mm provided no satisfactory results – the thicker the sample got, the more radiation was reflected, the rest was transmitted through.

Noteworthy electromagnetic shielding characteristics were starting to show when the paramagnetic metal coated cenospheres were used in conjunction with graphite PVA emulsion: transmission coefficient only 0.16 (only 16 per cent of the radiation was passing through); the reflection coefficient rose to 0.63 (63 per cent radiation was reflected).

Cenospheres without paramagnetic coating (CS) in turn offered little reflective properties, allowing most of the radiation to pass through (transmission coefficient 0.88).

Table 1. EMF exposure and intervention scenarios investigated in this study

Sample model	Transmission coeficient	Reflection coeficient
MCS 1 monolayer	0.96	0.01
MCS 5 monolayers	0.92	0.01
MCS 11 monolayers	0.87	0.03
MCS 2 mm layer	0.76	0.03
MCS 5 mm layer	0.45	0.68
MCS 5 mm layer+Al.foil	0.01	1.00
CS 15 mm layer	0.88	0.01
Graphite PVA emulsion	0.73	0.12
MCS graphite PVA emulsion	0.16	0.63

CONCLUSIONS AND DISCUSSION

The results indicate that a significant amount of radiation was absorbed within the paramagnetic metal coated cenospheres emulsion. The latter sample demonstrates the prospective shielding characteristics of the material, since most of the radiofrequency radiation was not allowed to pass through the material neither to be reflected, but absorbed within the structure of the material.

Monolayer MCS from 1 to 11 layers did not produce any significant results because of single spheres being not connected to one and another. For the same reason, also bulk material of MCS of 2 mm thickness provided unsatisfactory shielding properties. However, starting from 5 mm bulk material thickness we see significant reflection coefficient increase due to spheres being interconnected due to increased quantity. With adding an aluminium foil sheet on the 5mm bulk material the reflection coefficient is increased to maximum due to the radiation that passes through the bulk material, reflected by the aluminium layer. By introducing PVA to the MCS bulk material the matrix material withheld some of the radiation and allowed less microwaves to be reflected.

The future research should focus on determining optimal ratio of MCS, graphite, matrix material and the quantity of these.

Absorption of the radiofrequency electromagnetic fields would allow to reduce the fields at their source and to eliminate countless reflections that would occur in case of using simple metallic reflectors in shielding applications.

Most shielding materials available on the market only reflect the electromagnetic field while creating countless reflections and increasing the field in some hotspots. The material discussed in this study would allow minimizing the reflections by attenuating the reflective properties of the material.

The new material studied in this paper would offer an alternative in shielding rooms in public and occupational environments where high intensity radiowaves are present. Such occupational environments could be: radiofrequency welding; microwave heating; radiofrequency treatments in hospitals; areas near radar, radio and television transmitters etc. Also the office environments may have an increased level of radiofrequency electromagnetic fields due to ever increasing amount of wireless protocols and transmitters positioned near the workstations.

The relevance of usage of such material is also stressed by recent developments in European legislation (Directive 2013/35/EU) which stresses the protection of risk groups. Such risk groups may include maternity hospitals, hospitals, kindergartens, schools etc. (EP&EC 2013). Besides legally binding safety limits, there are also recommendations from non-governmental sector: Bionititative working group, based on the review of the scientific literature, has suggested safety limits many orders of magnitude lower than in the European directive (Bioinitiative, 2007 and 2012). In order to achieve such low microwave levels in the urban area, as set in the Bioinitiative reports, the usage of microwave absorbing materials is inevitable. The reason for limiting exposure to electromagnetic fields is also argued as a precautionary principle (EEA, 2007).

In long-term perspective, the implementation of such shielding materials would improve environmental health conditions and result in a positive effect on population's health.

REFERENCES

Bellieni, C.V., Pinto, I., Bogi, A., Zopetti, N., Andreuccetti, D. & Buonocore, G. 2012. Exposure to Electromagnetic Fields From Laptop Use of 'Laptop' Computers. *Archives of Environmental & Occupational Health* **67**(1), 31–36.

BioInitiative Working Group. 2007. Bioinitiative report: A Rationale for a Biologically Based Public Exposure Standard for Electromagnetic Fields.

BioInitiative Working Group, Editors Cindy Sage and David O. Carpenter. 2012. BioInitiative Report: A Rationale for a Biologically-based Public Exposure Standard for Electromagnetic Radiation – http://www.bioinitiative.org

Blitz, J. 1997. Microwave methods. Chpt Electrical and Magnetic Methods of Non-destructive Testing, Vol 3 of the series Non-Destructive Evaluation Series pp. 184–213.

Blitz, J. 2012. Electrical and Magnetic Methods of Non-destructive Testing. Springer Science & Business Media.

Botsco, R.J., Cribbs, R.W., King, R.J. & McMaster, R.C. 1986. *Microwave methods and applications in nondestructive testing. In: nondestructive testing handbook—electromagnetic testing: eddy current, flux leakage, and microwave nondestructive testing*, American Society of Nondestructive Testing. 4, section 18.

EEA – European Environment Agency 2007. Radiation risk from everyday devices assessed – http://www.eea.europa.eu/highlights/radiation-risk-from-everyday-devices-assessed

EP&EC – The European Parliament and the Council 2013. Directive 2013/35/EC of the European Parliament and of the Council of 26 June 2013 on the minimum health and safety requirements regarding the exposure of workers to the risks arising from physical agents (electromagnetic fields) (20th individual Directive within the meaning of Article 16(1) of Directive 89/391/EEC). *Official Journal of the European Union* 26.06.13.

Kühn, S., Lott, U., Kramer, A. & Kuster, N. 2007. Assessment Methods for Demonstrating Compliance With Safety Limits of Wireless Devices Used in Home and Office Environments. *IEEE Transactions on Electromagnetic Compatibility* **49**(3), 519–525.

Panigrahi, R. & Srivastava, S.K. 2015. Trapping of microwave radiation in hollow polypyrrole microsphere through enhanced internal reflection: A novel approach, *Sci. Rep*. **5**, 7638.

Wout, J., Frei, P., Roösli, M., Thuróczy, G., Gajsek, P., Trcek, T., Bolte, J., Vermeeren, G., Mohler, E., Juhász, P., Finta, V. & Martens, L. 2010. Comparison of personal radio frequency electromagnetic field exposure in different urban areas across Europe. *Environmental Research* **11**0(7), 658–663.

Zopetti, N., Andreuccetti, D., Bellieni, C., Bogi, A. & Pinto, I. 2011. Evaluation and characterization of fetal exposures to low frequency magnetic fields generated by laptop computers. *Progress in Biophysics and Molecular Biology* **107**, **pp.** 456–463.

Zoughi, R. 2000. Microwave Non-Destructive Testing and Evaluation Principles. Kluwer Academic Publishers, Dordrecht/Boston/London.

Agronomy Research **14**(Sp.1), 1023–1033, 2016

Improving fretting resistance of heavily loaded friction machine parts using a modified polymer composition

V. Krasnyy[1], V. Maksarov[1,*] and J. Olt[2]

[1]Saint-Petersburg Mining University, 21st Line 2, RU 199106 St. Petersburg, Russia
[2]Institute of Technology, Estonian University of Life Sciences, Kreutzwaldi 56, EE51014 Tartu, Estonia
[*]Correspondence: maks78.54@mail.ru

Abstract. The application of coatings based on fluorocarbon polymer composition, friction-mechanical brass, fullerene C_{60} and surface treatment of vibroroling with the regular roughness for the protection of heavily loaded mating parts of machines, working in conditions of fretting-corrosion. Studied the mechanisms of friction of coating, which will considerably reduce the fretting-wear mechanisms of friction in engineering products. It is established that in all studied for the protection of heavily loaded mating parts of machines is a single mechanism of increasing wear resistance when fretting in the area of the contact layer of the fine particles through the use of thin-layer coatings. Their presence may be due to either structural self-organization material, or forming of composite structures with small wear particles when using the polymeric composition. At that the protective coating virtually eliminates component corrosion mechanism of fretting – wear.

Key words: fretting corrosion, fluorocarbon polymeric composition, friction-mechanical brass, vibroroling, fullerene C_{60}.

INTRODUCTION

Fretting corrosion is a frequent cause of breakdown of a number of critical parts of internal combustion engines, in particular, those of oversize mining trucks, drilling equipment parts and other ones operating under vibration and high subgrade stresses. Fretting is peculiar to nominally fixed structural connections (e.g., part attachment points, etc.). As a rule, it arises under vibrations that cause oscillatory relative movements and deformations of various kinds. Fretting is often accompanied by chemical processes occurring on friction surfaces (fretting corrosion). Wear caused by fretting manifests itself in 'wasting' of material at part fastening points. Unlike other types of sliding friction, a characteristic feature of fretting is small amplitude of counterbodies' relative movements comparable with the distance between tops of microroughnesses on the friction surface; therefore, removal of wear products from the contact zone is protracted. Whereupon wear products begin to act as an abrasive, causing additional wear (Ramesh & Gnanamoorthy, 2006; Kubiak et al., 2010; Huang et al., 2011).

When choosing materials for coatings protecting high-load joint parts from fretting corrosion, one should take into account not only their wear resistance, but also their shift sensitivity, i.e. the ability of a material to take shear deformation without initiating fatigue damage processes. It is known that it is a feature of sufficiently thin coatings. Those coatings have yet another advantage: they do not impede overhaulability of assemblies and permit to retain negative allowances specified during assembly in the process of operation (Drozdov et al., 2010; Garkunov et al., 2013).

Fretting corrosion is a frequent cause of reduced reliability of a number of vital parts of machines, including mining machinery (Gilev, 2011; Ostrovsky, 2011).

The purpose of this work is to study the impact of coatings based on fluorocarbon polymer compound, friction mechanical brass plating, C_{60} fullerene, as well as surface vibration knurling forming a regular microrelief on wear of heavily loaded joints of mining machinery operating under fretting corrosion conditions.

The thin-layer coatings named above, as well as surface vibration knurling, were never examined before as means of protection against fretting corrosion under high loads characteristic of a number of performance units of internal combustion engines and mining machines. The phenomena of fretting corrosion of parts made of such a widely used structural material as cast iron, as well as the prospects of using C_{60} fullerene under extreme friction conditions (including fretting corrosion) were also underexplored in the literature. The result of research performed by us expand the sphere of application of thin-layer coatings, the surface vibration knurling method and allow to obtain new data for studying the mechanisms of fretting corrosion, creating prerequisites for expansion of the range of surface protection methods in use.

MATERIALS AND EXPERIMENTAL PROCEDURE

A number of studies propose various versions of wear-resistant protection coating operating efficiently under the conditions of fretting corrosion, e.g. copper-nickel (Zhang & Xue, 2011), copper-phosphorous (Aslanyan et al., 2011) and other ones, applied electrolythically; C_{60} fullerene coating (Ginzburg et al., 1997), epilam/foleox polymer coatings and silicon-molybdenum based coatings (Potapov, 1996) and others.

In many cases, special kinds of processing, in particular, vibration knurling creating a regular microrelief on the surface prove effective in fretting control (Bulatov et al., 1997; Varenberg et al., 2002; Volcho et al., 2002).

This work studies thin-layer coatings based on fluorocarbon polymer compound, friction mechanical brass plating, C_{60} fullerene-containing additives to lubrication oil and grease, as well as using vibration knurling creating a regular microrelief when exposed to heavy contact loads peculiar of large-size joints of locomotive and marine diesel engines, mine trucks and a number of heavily loaded joints of mining machinery.

Samples were tested according to the procedure meeting GOST 23.211-80 on a special FK testing facility using the principle of a standard friction machine (Fig. 1, a &b). In all cases, coatings were applied to fixed samples and mobile counter-samples were not coated.

Fixed sample (1) was a disk 35 mm in diameter and 7.5 mm thick. Moving counter-sample (2) was a hollow cylinder whose internal and external diameters were equal, respectively, to 25 and 20 mm. Its end (ring) surface contacted with the flat surface of the sample, creating a ring contact 0.5 cm^2 in area. Eccentric (7) with eccentricity equal

to 0.1 mm and rocker arm (5) caused the cylinder to execute reciprocating rotary oscillations around its own axis. Axial loads applied to it created preset pressures acting at right angle at the contact surfaces. This research plant allowed to vary fretting amplitude at contact surfaces from 40 to 200 μm, to change pressure applied at right angles from 10 to 85 MPa and to create oscillation frequency from 200 to 1,000 cycles per minute thanks to using a friction machine drive. An eccentric was used as the top roller in the standard 'roller to roller' test procedure. This design allowed us to obtain reciprocating rotary oscillations of moving countersamples and to use measuring capabilities of the friction machine (friction moment and coefficient).

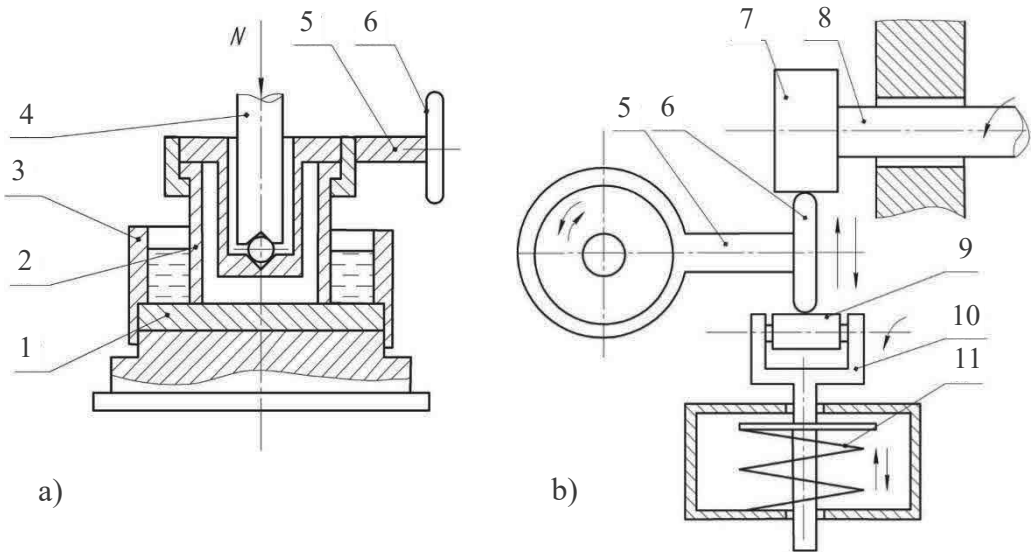

Figure 1. Friction machine FC: a) cross-section, b) top view: 1 – fixed sample, 2 – mobile sample, 3 – liquid process medium cell, 4 – thrust rod, 5 – rocker arm, 6 – roller; 7 – eccentric, 8 – drive shaft, 9 – pressure roller, 10 – fork, 11 – spring.

The linear wear of samples was measued by processing friction track profilograms otained on a standard profilograph-profilometer, mass wear was evaluated by weighing on electronic scales with an accuracy to 0.1 mg before and after tests.

The first series of samples and counter-samples made of grade 15 steel were tested by rotating and reciprocating motion with 100 μm amplitude under 25 MPa pressure and at 900 cycles min^{-1}. frequency. The second series of tests was performed on samples made of SCh 25 grade cast iron and grade 15 steel counter-samples with 20 μm displacement amplitude and at 250 cycles min^{-1} frequency under 85 MPa pressure. The number of load cycles for each pair of samples amounted to 5×10^5, at least 4 samples with each type of coating have been tested. Wear after tests were assessed by mass change of the samples within the accuracy of 0.1 mg. Linear wear was assessed by friction tracks profile diagram. Friction coefficient was determined by calibration graphs according to resistive strain gauge readings.

The third series of tests compared steel and cast iron samples machined by vibration knurling that created a regular microrelief and processed by grinding. Samples and counter-samples made of grade 20 steel were tested at 20 MPa load and 100 μm oscillation amplitude and 900 Hz oscillation frequency. Samples made of grey cast iron and counter-samples made of grade 20 steel were tested at 87 MPa load and 50 μm oscillation amplitude and 500 Hz oscillation frequency.

The fourth series of tests compared impact of C_{60} fullerene added to lubricating oil and grease in the form of powder containing 2.5% of C_{60} fullerene on fretting wear of steel and brass samples with steel counter-samples during intense mechanical agitation. Brass samples were coated with fullerene as well. Test conditions were as follows: oscillation amplitude 150 μm, oscillation frequency 500 cycles min^{-1}, normal load during tests with lubrication 4.2 MPa, during tests without lubrication 3.2 MPa.

RESULTS AND DISCUSSION

The results of tests of metal samples coated with fluorocarbon polymer compound and friction mechanical brass plating are shown in Fig. 2 in comparison with the uncoated samples data. In Fig. 2a one can see the results of fretting wear tests of metal samples (where U_l is linear wear, μm; U_m is wear measured by a sample mass change, mg), in Fig. 2b, the wear of counter-samples, and in Fig. 2c, the values of established friction coefficients μ. Steel samples were used for tests Nos. 1–3 inclusive, whereupon No. 1 is an uncoated sample, No. 2 is a sample coated with 3–5 μm thick friction mechanical brass plating , No. 3 is a ample coated with 5 μm thick fluorocarbon polymer compound. Samples Nos. 4–6 inclusive were made of cast iron, whereupon sample No. 4 was uncoated, sample No. 5 was coated with friction mechanical brass plating and sample No. 6, with fluorocarbon polymer compound.

As can be seen in Fig. 2, mass wear U_m and linear wear U_l under fretting conditions is reduced several times by all types of coatings under study. Whereupon the fretting friction coefficient values obtained during tests do not correlate to the samples wear data. In the cases under consideration, friction coefficient is even higher than the one of the reference sample. This may be caused by both specific character of strain affecting friction joints under high basic loads under fretting conditions as compared to ordinary sliding friction and the nature of microstructural changes in surface layers of the joint parts. Besides, during model tests under actual loads and displacement amplitudes relatively small contact area of samples (0.5 cm^2) brings about harder fretting conditions than in real joints. This also may increase friction coefficient several times as compared to sliding friction coefficient.

A raster electronic microscopic examination of friction surfaces has been carried out in order to detect the phenomena that reduce fretting wear when effective coatings are used (Bulatov et al., 1994; Krasnyy et al., 2013; Maksarov et al., 2015).

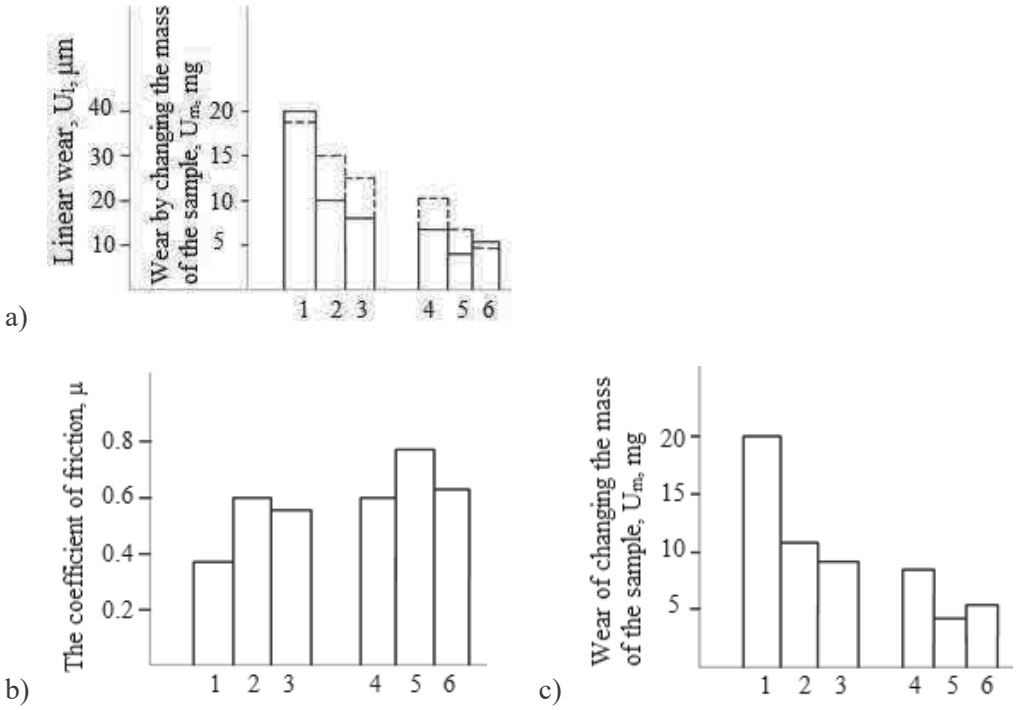

Figure 2. Fretting test results: a) – wear of samples (contour line – mass, dashed line – linear); b) – counter–samples wear; c) – established friction coefficient values; 1–3 – steel specimens: 1 – uncoated; 2 – friction mechanical brass plating, thickness 3–5 μm; 3 – fluorocarbon polymer compound, thickness 5 μm; 4–6 – cast iron samples: 4 – uncoated; 5 – friction mechanical brass plating; 6 – fluorocarbon polymer compound.

Caverns filled with oxidized wear particles observed on friction surfaces of reference steel samples are typical of fretting wear. Oxidization is evidenced by a specific effect of electric charge accumulation on low-conductivity surface of oxidized particles that reduces image contrast and creates an impression of 'fluorescence' under the impact of electron beam. Since such an effect is not observed on the rest of the friction surface, it is believed that wear particles are oxidized after they are formed as a result of interaction between oxygen and the surface of small particles that was activated in the process of friction. I.e. probably the process of corrosion is not related directly to the mechanics of fretting wear, moreover the areas with oxidized particles (Fig. 3a) occupy a comparatively small part of the total friction area. Areas covered with particles several microns in size without oxidization traces (Fig. 3b) are also encountered rather often on the 15 grade steel fretting wear tracks; brittle fracture cracks are clearly visible on them. Apparently, those particles are carbide or other inclusions characteristic of steel resulting from perlite interlayers fracture in the process of friction, etc.

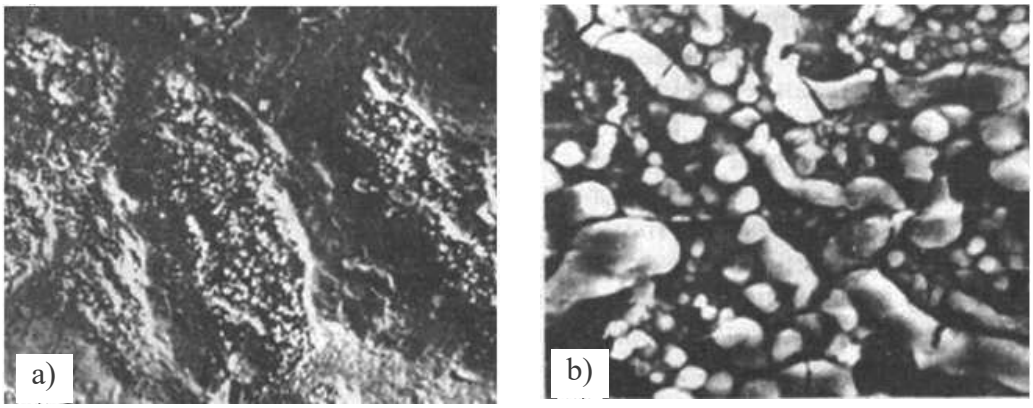

Figure 3. Fretting wear surface (steel): a) – caverns with wear particles, (x 160); b) – particles on the friction surface, (x 2,000).

Application of fluorocarbon polymer compound solution with subsequent drying creates a thin polymer film on the surface. This film protects friction surfaces from oxidization and caving (Fig. 4), a) and somewhat increases the fineness of the particles visible on the surface, preventing their brittle fracture (Fig. 4, a & b).

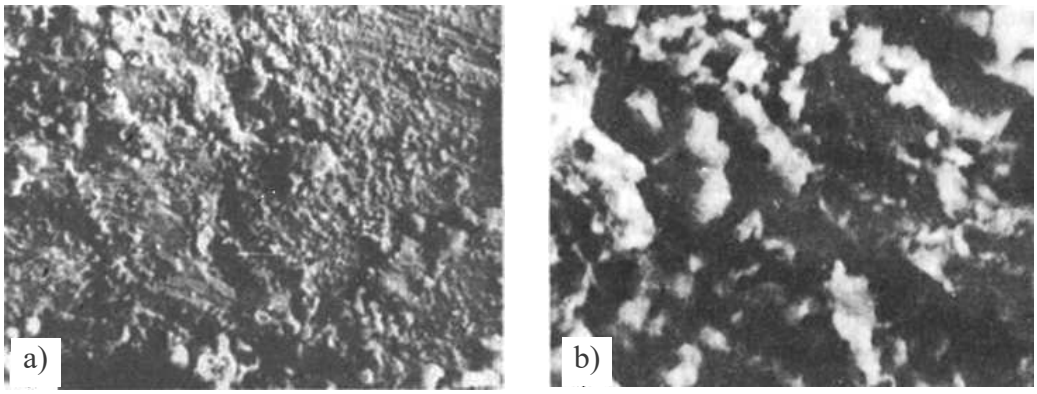

Figure 4. Fretting wear surface (fluorocarbon coated steel): a) – friction surface patch (x 200); b) – dispersed particles on friction surface, (x 2,000).

In this case, microparticles embedded in the polymer film created by the modifying agent may probably act as a fine aggregate in the polymer matrix, forming a composite coating film. Composite polymer materials have shown themselves to advantage as antiwear and antifriction coatings. It is composite coatings with a soft matrix and harder aggregate particles that reduce wear most efficiently, this phenomenon is implemented in the case under consideration as well.

Friction surfaces of friction brass plated samples look somewhat differently. Brass plating creates very smooth layers of brass on the surface of a steel sample. Their adhesion to the surface is poor in some places; there they flake on the friction track during fretting (Fig. 5a). But more frequently their adhesion is so good that even alligatoring does not bring about flaking and chipping of the brass coating (Fig. 5b); this

is probably the cause of its efficiency. In Fig. 5b steel base grains are visible on the fracture surface; they are covered with a plastic, highly porous layer of brass several microns thick. One can see at high magnification that the structure of such a layer consists of separate spherical particles approximately 1 μm large and smaller (Fig. 5d). Whereupon the highly dispersed structure of the layer created as a result of friction coating application under the impact of high tensions and sliding velocities ensure deformation under the impact of shear stress during fretting by means of mutual rotation and slipping of fine structural elements. Probably, this permits to deform thin subsurface layers of materials without dislocation causing fracture and wear. Implementation of such friction mechanics even at some areas of the contact surface may reduce total wear.

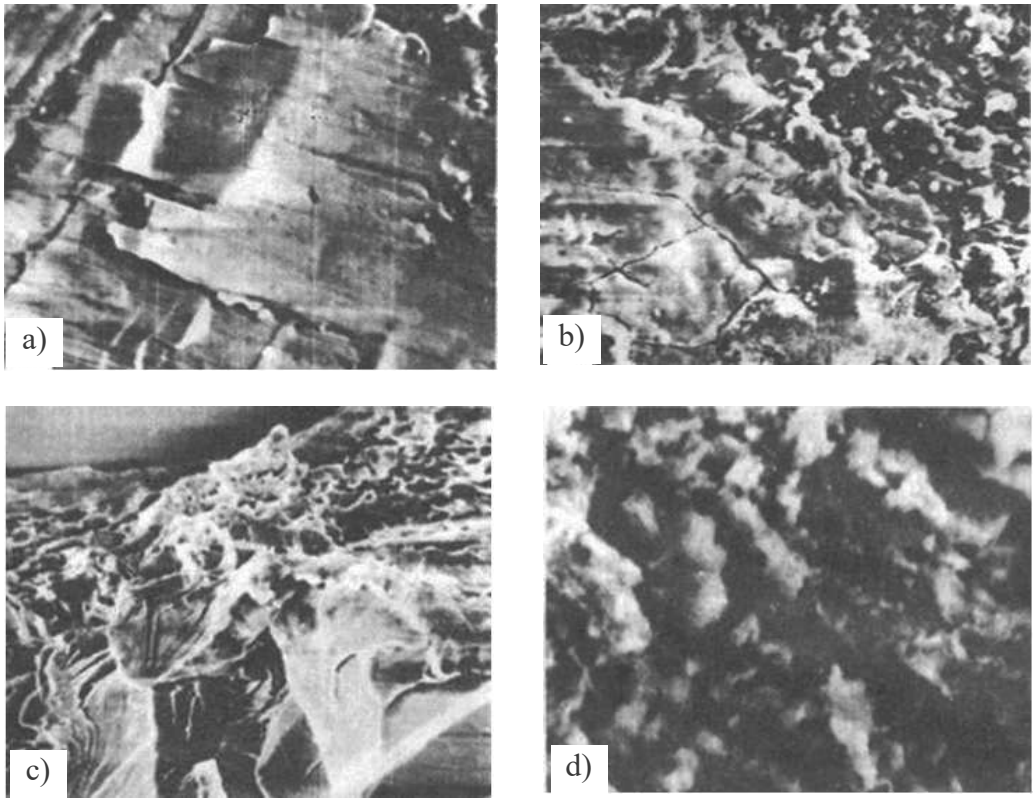

Figure 5. Fretting wear surface (friction mechanical brass plated steel): a) – a layer of brass plating on the friction surface (x 150); b) – alligatored brass plating after fretting (x 300); c) – transverse fracture surface of a plated sample in liquid nitrogen – loose porous brass coating on coarse grain steel base (x 400); d) – a fragment of low-temperature fracture of brass plating with a finely dispersed structure (x 7,000).

Comparative results of tests of vibration knurled and ground samples (in respect of mass and volume wear) after 500,000 cycles are shown in Fig. 6 (1, 2 – steel/steel couple; 3, 4 – cast iron/steel couple; 1, 3 – grinding, 2, 4 – vibration knurling). Vibration knurled samples have shown 30–35% less fretting wear resistance than the ground ones, after lubrication this difference amounts to 25–30% (Bulatov et al., 1994).

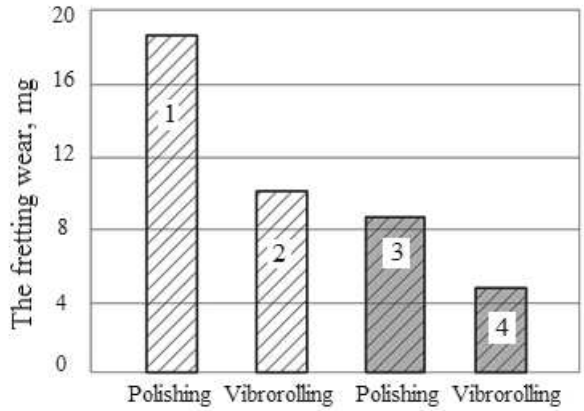

Figure 6. Fretting wear dependence on processing type: 1, 2 – steel samples and counter-samples; 3, 4 – cast iron samples, steel counter-samples; 1, 3 – after grinding; 2, 4 – after vibration knurling.

Vibration knurled samples with a regular microrelief surface have a different wear resistance improvement mechanics. In Fig. 7b one can see that the friction track surface is broken down into separate facets whose dimensions are comparable with fretting displacement amplitude. No specific surface layers with a structure different from the original steel structure are visible within the borders of single facets, except usual grooves in the sliding direction. Probably, such a faceted nature of the friction tracks bears record to the process of splitting of strain and deformation waves on the surface with a regular microrelief. This process contributes significantly to the fretting effects hardening.

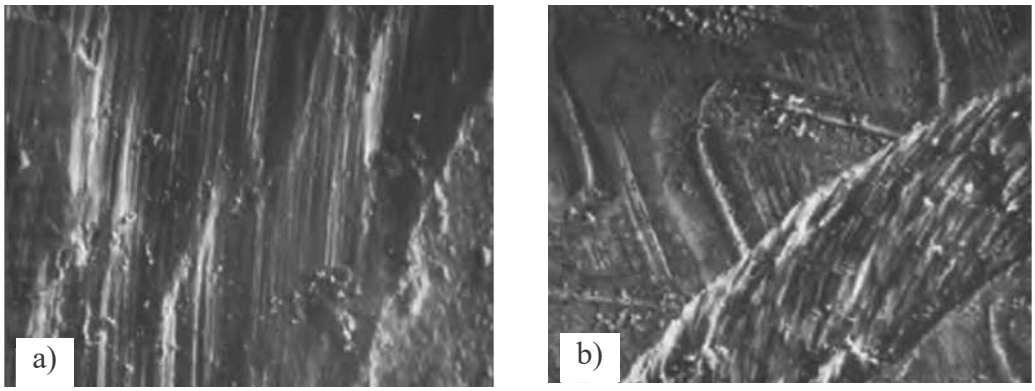

Figure 7. Fretting friction track on steel surface: a) – grinding; b) – vibration knurling.

A combination of the above describe method with application of thin-layer coatings capable of reducing fretting wear even more may be of interest.

The results of tests of C_{60} fullerene additive to lubricating oil and grease presented in Fig. 8 (steel samples and counter-samples) and in Fig. 9 (brass samples and steel counter-samples) demonstrate that introduction of 2.5% powder into lubricating oil reduces fretting wear significantly.

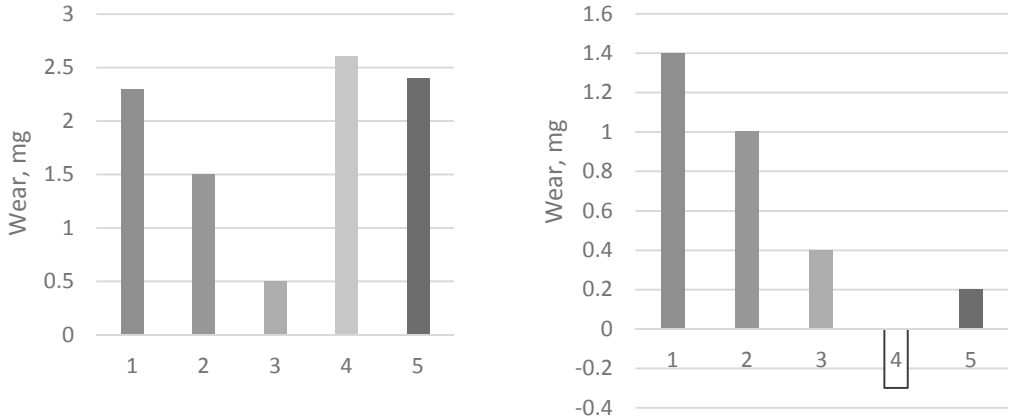

Figure 8. Wear of steel samples and counter-samples: 1 – unlubricated; 2 – VITREA 68 (SCHELL) oil; 3 – VITREA 68 (SCHELL) oil with 2.5% C_{60}; 4 – ALVANIA EP2 (SCHELL) grease; 5 – ALVANIA EP2 (SCHELL) grease with 2.5% C_{60}.

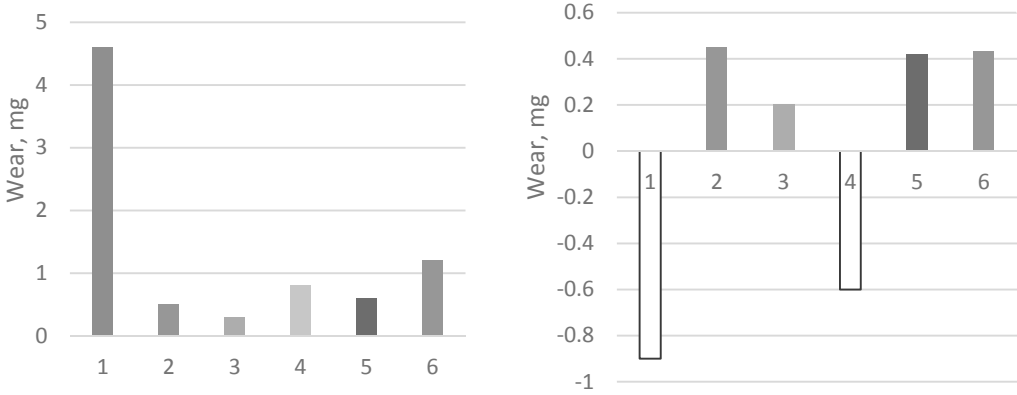

Figure 9. Wear of brass samples and counter-samples: 1 – unlubricated; 2 – VITREA 68 (SCHELL) oil; 3 – VITREA 68 (SCHELL) oil with 2.5% C_{60}; 4 – ALVANIA EP2 (SCHELL) grease; 5 – ALVANIA EP2 (SCHELL) grease with 2.5% C_{60}; 6 – C_{60} coating on a brass sample, dry friction.

Whereupon introduction of analogous powder to lubricating grease proved to be effective only in respect of a combination of brass and steel samples, this is probably caused by high viscosity of grease and its insufficient mechanical stability under shear deformations. In a number of cases wear particles were transferred to the counter-body under study; negative wear values bear witness to that. However, even for such type of

lubrication introduction of C_{60} reduced wear as compared to oil without additives (Ginzburg et al., 1997).

Tests of brass samples coated with C_{60} demonstrated that under normal pressure amounting to 4.2 MPa uncoated and unlubricated samples seized and the counter-sample rotation visibly slowed down. Therefore, it was required to reduce load to 3.2 MPa. Rotation slowdown was not observed when a coated brass sample was used. The wear of a coated brass sample was 3 times less than that of an uncoated and unlubricated one, there was no transfer of copper onto the counter-sample. Therefore, it is possible to make a preliminary conclusion that it is effective to use such kind of coatings as a solid lubricant, especially when supplying the friction unit with a liquid lubricant is structurally complex.

CONCLUSIONS

1. As a result of studies of heavily loaded machine part mating protection by fluorocarbon polymer compound, friction mechanical brass plating, it was established that such coatings have the same mechanics of fretting wear resistance improvement in the zone of contact layer of finely dispersed particles thanks to using thin-layer coatings. The presence of such particles may be caused either by structural self-organization of the coating material in the process of friction brass plating, or by creation of a composite polymer coating with fine wear particles when a polymer compound is used. Whereupon the protective coatings considered above virtually exclude the corrosion component of fretting wear.

2. The presence of a regular microrelief improves load-bearing capacity of the surface, facilitates preservation of lubricant in the contact area and removal of wear products. Under the conditions of fretting, regular microrelief facilitates splitting of strain and deformation waves on the surface, improving shear sensitivity and preventing fatigue damage development.

3. Using F_{60} as an additive to lubricating oil and grease, as well as for coating samples facilitates reduction of fretting wear of steel and brass samples, although its use under high contact loads may be only limited.

4. The research performed by us established additional areas of application of thin-layer coatings, including modified polymer compounds and surface vibration knurling method as means of protection against fretting of high-load friction assemblies of machinery. The results of the research may be widely used in production and repair of internal combustion engines, mining machinery, farm equipment and a number of other areas.

REFERENCES

Aslanyan, I.R. Celis, J.P. & Shuster, L.S. 2011. Fretting-corrosion of electrolytic NiP coatings. *Friction and wear* **32**(6), 556–561. (in Russian).

Bulatov, V.P., Krasnyy, V.A. & Shneider, Y.G. 1997. Basics of machining methods to yield wear- and fretting-resistive surfaces, having regular roughness pattern. *Wear* **208**, 132–137.

Bulatov, V.P., Krasnyy, V.A., Kireenko, O.F. & Popov, I.N. 1994. The study of fretting-corrosion under conditions of high contact loads. *The friction and wear* **15**(1), 101–108. (in Russian).

Drozdov, Yu. N., Yudin, E.G. & Belov, A.I. 2010. *Applied tribology (friction, wear and lubrication).* Moscow: EKO-Press, 604 pp. (in Russian).

Ostrovsky, M.S. 2011. Fretting as a cause of reduced reliability of mining machines. *Mining information and analytical Bulletin* **12**(3), 315–331. (in Russian).

Garkunov, D.N., Melnikov, E.L. & Gavrilyuk, V.S. 2013. *Tribotechnics*. McGraw-hill, 408 pp.

Gilev, A.V. 2011. *Basic maintenance of mining machines and equipment*. Krasnoyarsk, Sib. Feder. University, 276 pp. (in Russian).

Ginzburg, B.M., Krasnyy, V.A., Kozyrev, Yu.P. & Bulatov, V.P. 1997. The decrease in the fretting-wear of metals under the action of fullerene C60. *Friction and wear* **18**(4), 523–526. (in Russian).

GOST 23.211-80. Maintenance of wear resistance of products. Method of testing materials for wear under fretting and the fretting. (in Russian).

Huang, D., Li, R., Huang, L., Ji, V. & Zhang, T. 2011. Fretting wear behavior of bulk amorphous steel. *Intermetallics* **19**(10), 1385–1389.

Krasnyy, V.A., Maksarov, V.V. & Busin, R.V. 2013. The effect of thin nano-coatings on the fretting corrosion high load of mates of large machine parts. *Metalworking* **5–6**, 63–67. (in Russian).

Kubiak, K.J., Mathia, T.G. & Fouvry, S. 2010. Interface roughness effect on friction map under fretting contact conditions. *Tribology International* **43**(8), 1500–1507.

Maksarov, V.V. & Krasnyy, V.A. 2015. Mechanisms of friction of thin coatings in the conditions of fretting. *Scientific and technical Gazette of St. Petersburg GPU* **226**(3), 111–120. (in Russian).

Potapov, S.I. 1996. The application of thin polymer coatings for protection against fretting of the main bearing caps of the engine. *The engine* **2**, 31–33. (in Russian).

Ramesh, R. &, Gnanamoorthy, R. 2006. Development of a fretting wear test rig and preliminary studies for understanding the fretting wear properties of steels. *Materials and Design* **27**(2), 141–146.

Varenberg, M., Halperin, G. & Etsion, I. 2002. Different aspects of the role of wear debris in fretting wear. *Wear* **252**(11), 902–910.

Volchok, A., Volchok, A., Halperin, G. & Etsion, I. 2002.The effect of surface regular microtopography on fretting fatigue life. *Wear* **253**(3–4), 509–515.

Zhang, W. & Xue, Q. 2011. Fretting wear characteristics of Ni/Cu multilayers electrodeposited on beryllium bronze substrate. *Friction and wear* **32**(2), 74–78.

Agronomy Research **14**(Sp.1), 1034–1042, 2016

Influence of dust pollution in the laboratory on the strength of adhesive bond

A. Krofová[1,*], P. Kic[2] and M. Müller[1]

[1]Czech University of Life Sciences Prague, Faculty of Engineering, Department Material Science and Manufacturing Technology, Kamýcká 129, CZ 165 21, Czech Republic
[2]Czech University of Life Sciences Prague, Faculty of Engineering, Department of Technological Equipment of Buildings, Kamýcká 129, CZ 165 21, Czech Republic
[*]Correspondence: kofovaa@tf.czu.cz

Abstract. The main aim of this paper is to evaluate the influence of microclimate conditions on the bond strength in the research laboratory in the Faculty of Engineering at the Czech University of Life Sciences Prague. The main attention is paid especially to the contamination of the working environment with dust particles. In the frame of this research the concentration and size of dust particles in the air was measured by the aerosol monitor DustTRAK II Model 8530 with impactors for measurement of size fractions PM_1, $PM_{2.5}$, PM_4 and PM_{10}. The adhesive bonds were created according to the ISO standards from Duralumin material specimens with different type of two-component epoxy adhesives under different conditions of ventilation (0%, 50% and 100% of ventilation rate). The tensile strength of created specimens was measured by universal testing machine for tensile strength measurement – LABTest 5.50ST. The results of measurement were evaluated by statistical methods and summarized in the conclusions. There is no significant difference in the strength of the bond when applied various performance of ventilation.

Key words: adhesive bond, contamination, dust, ventilation.

INTRODUCTION

Adhesive bonding technology is very important for many structural joints and connections. Different bodies made from different materials can be combined on the contact surfaces with adhesive bonding. There is a better adhesion between the surfaces of liquid and solids than the adhesion between two surfaces of solid substances, and therefore the adhesives (adhesives) are used to bond components. The adhesive penetrates into the inequalities between the bonded materials (adherents) and expels from the micro pores majority of the absorbed gases and vapours.

In this method of adhesive bonding the important terms are the adhesion and cohesion. The glued joint consists of two adherents, two adhesive layers and a one cohesive layer. Adhesion indicates the adhesion of the adhesive to the glued material and indicates cohesion consistency between the particles of adhesive. An equally important factor affecting the quality of the adhesive bonding is wettability that is mainly dependent on the surface tension of both adhesives and adhesive materials (Peterka, 1980).

Currently, the adhesive bonding is used in almost all fields of technology, e.g. automobile industry, aerospace and shipping industries, mechanical engineering, civil engineering, but also in electrical engineering, healthcare and many other branches of industry. This method is suitable for mass production operations. However, the theory still lags behind practice. Many research papers solved the preparation of bonded joints, degrading aspects etc. The area that is currently not properly investigated is an effect of contamination of bonded joints with microparticles such as dust in the air, e.g. from ventilation or halls, workshops, etc.

The research was focused on the evaluation of the impact of contamination by dust microparticles in a two component epoxy adhesive during the hardening process.

Dust is a significant source of the risk in working environment that can be found everywhere in the air. It is a limitation, which cannot be avoided in common practice. In the past many studies on research air quality in various environments have been carried out (Di Giorgio et al., 1996; Jones, 1999), there were also studied problems of special rooms in which the people are working performing various work activities (Bluyssen, 1996; Karwowska, 2003; Kic & Chladek, 2010; Kic & Růžek, 2014), or in agricultural buildings for poultry housing (Karwowska, 2005; Kic et al., 2007; Nimmermark et al., 2009; Kic et al., 2012).

Dust is a common name for solid particles of diameter less than 0.075 mm. It contains human skin cells, a small amount of plant pollen, human and animal hair, textile fibres, paper fibres and many other materials that may be present in the air and which depend on the particular environment (Nou & Viljasoo, 2011).

During the hardening e.g. two-component epoxy adhesives, epoxy resins react with hardeners to form macromolecules (Krofova & Müller, 2015a; Krofova & Müller, 2015b). New methods of bonding and sticking the new adhesives are tested in the laboratory under prescribed conditions. Different chemicals and adhesives containing various chemical components are used during these activities. This creates a very intensive contamination by pollutants that must be removed. The quality of indoor environment must be maintained within the prescribed limits, which are especially the air temperature, humidity, concentration of chemical pollutants and dust environment.

The polymerization process affects the resulting strength of the bonded joint. It can be assumed that the contamination of the bond during the hardening process (polymerization) can cause changes in the chemical process (chain), which depends on polymer properties. This means that the change in the molecular weight of macromolecular substances may result in a reduction or in some cases even in an increase of the resulting adhesive strength (Mleziva, 2008).

The aim of this research was to carry out laboratory experiments on bond strength contaminated by dust during mechanical ventilation in working areas, using information obtained from literature and using recommendations for standard procedures. The results should be used for evaluation of the impact of two-component epoxy adhesive contaminated by dust with microparticles on the bonded joint.

Adhesively bonded single-lap joints are from point of manufacturing view less expensive and in many cases they satisfy strength requirements, while in situations, where there is a requirement of higher strength of adhesively bonded joints, the special construction modifications are applied. These modifications however, require higher expenses and they are more difficult from the technology point of view (Valášek & Müller, 2015).

When the adhesively bonded joints are created, the negative part is a significant consumption of expensive adhesives. One option is adding the filler into the adhesive.

Significant factor for manufacturing expenses is also treatment of surface (Novak, 2012; Hricova, 2013). Nevertheless, recent researches show, that effectiveness of mechanical and chemical treatments is not that principal for strength of adhesively bonded joint (Bockenheimer et al., 2002). The reason is particularly the development of 'new' adhesives.

Adding the filler into reactoplastics matrix on the base of epoxies influences the mechanical properties of resulting composite (Fu et al., 2008; Kim & Khamis, 2001; Kejval & Müller, 2013).

MATERIALS AND METHODS

The research was focused on evaluate the effect of contamination of the environment from ventilation system on the structural joints glued with two-component epoxy adhesives. Used adhesives are showed at the Table 1.

Table 1. Used adhesives

Ozn.	Adhesive	Filler
A	UHU PLUS ENDFEST	-
B	BISON EPOXY METAL	-
C	GLUE EPOX RAPID SINCOLOR	20%$_{vol}$ of Al microparticles (about 90% of the particles < 45 μm)
D	CHS EPOXY 324 EPOXY 1200	20%$_{vol}$ of Al microparticles (about 90% of the particles < 45 μm)

The total concentration of air dust was measured by special exact instrument the Dust-Track™ II Aerosol Monitor 8530 (Fig. 1). After installation of different impactors the PM_{10}, PM_4, $PM_{2.5}$ and PM_1 (Fig. 2) size fractions of dust were also measured. There were measured and evaluated 90 data of total dust concentrations, as well as 90 data of each size fraction.

Figure 1. The DustTrak™ II Aerosol Monitor 8530.

Figure 2. Impactors for PM_{10}, PM_4, $PM_{2.5}$, PM_1 measurement.

The failure type according to ISO 10365 was determined at the adhesives bonds. The tensile strength and the elongation test were performed using the universal tensile strength testing machine LABTest 5.50ST (a sensing unit AST type KAF 50 kN, an evaluating software Test&Motion). A speed of the deformation corresponded to 6 mm min^{-1}. Tests were performed on normalized testing samples 100 x 25 x 1.5 mm of alloy AlCu4Mg, prepared under standard ČSN EN 1465 by cutting the metallurgical semi-finished product in form of metal sheet. An even thickness of the adhesive layer was reached by a constant pressure 0.5 MPa. The lapping was according to the standard 12.5 ± 0.25 mm. The adhesive bonds were hardened at the laboratory temperature 21 ± 2 °C.

The testing samples without mechanical treatment of surface were used for adhesive bonding. Adhesively bonded surface was chemically treated – degreased with Acetone before its own process of adhesive bonding. The untreated samples were used due to minimizing the factors effecting the preparation of bonded surface. This trend is significant particularly in operations, where the automation is implemented.

The roughness parameters Ra and Rz were measured on the adherent's surface designated for adhesive bonding. Roughness parameters were measured with portable profilometer Mitutoyo Surftest 301. Boundary wave length of cut-off was placed to 0.8 mm. Using the profilograph Surftest 301 following values were determined: Ra 0.34 ± 0.07 μm, Rz 2.38 ± 0.38 μm.

Structural epoxy adhesives were used in experiments. There can be added different fractions into the adhesives, with the aim to reduce the final cost of the adhesive (Müller et al., 2015).

- Adhesive A: Design a two-component adhesive Uhu Plus Endfest (transparent),
- Adhesive B: Bison epoxy metal (filled by the manufacturer, unknown filler and concentration),
- Adhesive C: Two-component epoxy adhesive Glue Epoxy Rapid Sincolor and discontinuous phase (reinforcing particles) was in the form of aluminum microparticles (about 90% of the particles are smaller than 45 μm). In this research experiments the filling was 20%vol of aluminium microparticles,
- Adhesive D: Two-component epoxy adhesive ChS Epoxy Epoxy 324 1200 (hardener P11 – Diethylenediamine) and discontinuous phase (reinforcing particles) was in the form of aluminium microparticles (about 90% of the particles are smaller than 45 μm). In this research experiments the filling was 20%vol of aluminium microparticles.

Statistical hypotheses were also tested at measured sets of data by means of the program STATISTICA. A validity of the zero hypothesis (H_0) shows that there is no statistically significant difference ($p > 0.05$) among tested sets of data. On the contrary, the hypothesis H_1 denies the zero hypothesis and it says that there is a statistically significant difference among tested sets of data or dependence among variables ($p < 0.05$).

RESULTS AND DISCUSSION

The bond strength of adhesive C (without filler) was 3.59 ± 0.37 MPa, and the adhesive D (without filler) had the bond strength of 0.20 ± 3.03 MPa. Glued joints C and D without fillers were glued at 0% capacity of air conditioning. By adding the filler in the form of aluminium powder the bonding strength was increased by 14 and 26%.

A substantial change in mechanical properties can be achieved by adding an optimum volume of filler i.e. reinforcement (Ramazan et al., 2008; Miroslav & Valášek, 2012). Optimum utility properties of these composites are limited primarily by risk of cohesive damage caused by improper concentrations and the material of filler.

One example is in research by Ramazan et al. (2008), who found that adding aluminium microparticles increased the bonding strength. Ramazan et al. (2008) used for bonding a composite mixture of aluminium-based microparticles.

Results of experiments showed a positive effect of aluminium microparticles on the increase of the strength of the adhesive (Müller et al., 2015).

Fig. 3 shows the influence of ventilation performance in the hall used for adhesive bonding on the bonding strength. Based on the results of experiments there is not a clear trend of influence of ventilation equipment on the bond strength. Decline and increase of the bond strength, depending on the performance of ventilation equipment moved in the interval from – 9 to 27%. Coefficient of variation ranged from 7 to 25%.

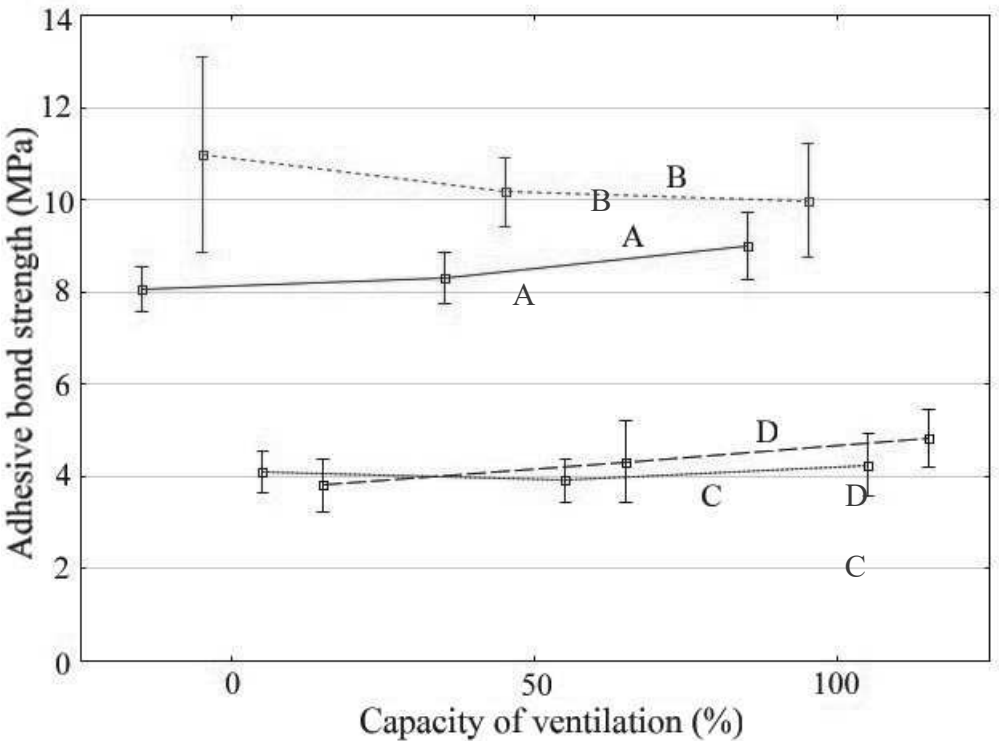

Figure 3. Influence of capacity of ventilation in hall determined for adhesive bonding on adhesive bond strength.

The total concentration and size of dust particles in the laboratory of adhesive bonding measured with a special exact instrument The DustTrak ™ II Aerosol Monitor 8530 are shown in the Fig. 4.

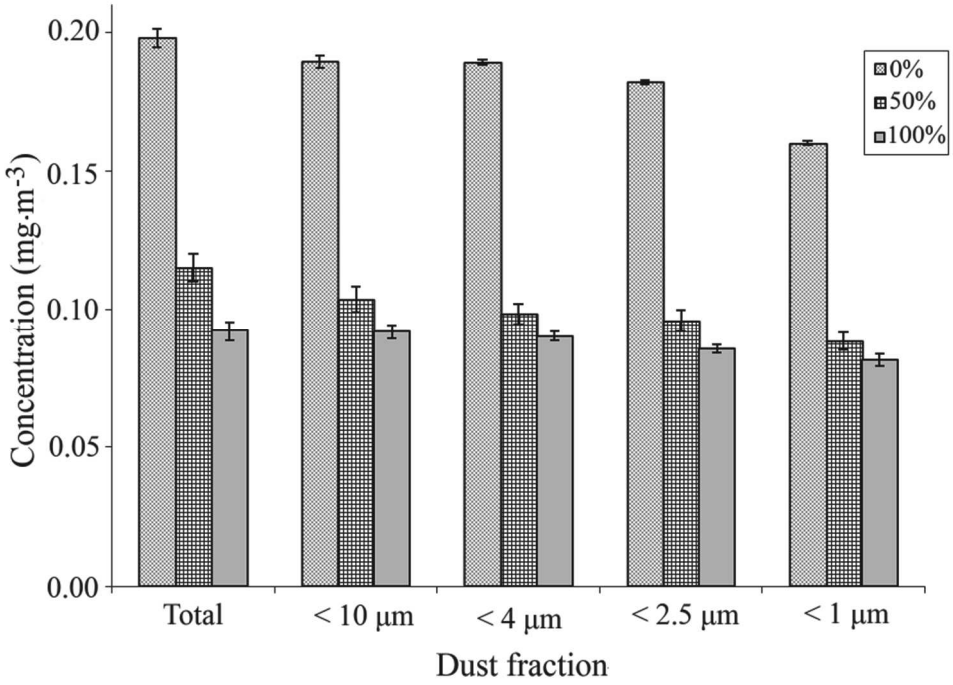

Figure 4. The total concentration and size of dust particles in the laboratory of adhesive bonding.

Based on the statistical analysis of influence of different performance of ventilation on bond strength, it is possible to state that there are statistically homogeneous groups, i.e. there is no difference between the tested adhesives A ($p = 0.0524$), B ($p = 0.5236$), C ($p = 0.6071$) and D ($p = 0.0799$). H_0 hypothesis was confirmed, i.e. there is no difference in the adhesive strength at a significance level of 0.05 between various performance of ventilation, i.e. between 0, 50 and 100%.

Bonded joints A and B showed an adhesive type of fracture surfaces.

Bonded joints C and D showed a special type of cohesive fracture surface. Addition of the filler in the form of microparticles of aluminium not changes breach in comparison with adhesives without filler. Therefore is not possible to agree with the statement of Ramazan et al. (2008) that filled epoxy adhesive has improved adhesion to the glued surface, i.e. there were not cohesive breach of the bond.

Due to different ventilation performance there were not changes of the fracture surface.

Using electron microscopy (SEM) in the frame of the experimental research of the contamination of the adhesive due to the surrounding environment has been confirmed. The back-scattered electrons (BSE) was used in this research analysis. An example of that is a fracture surface of adhesive B on Fig. 5.

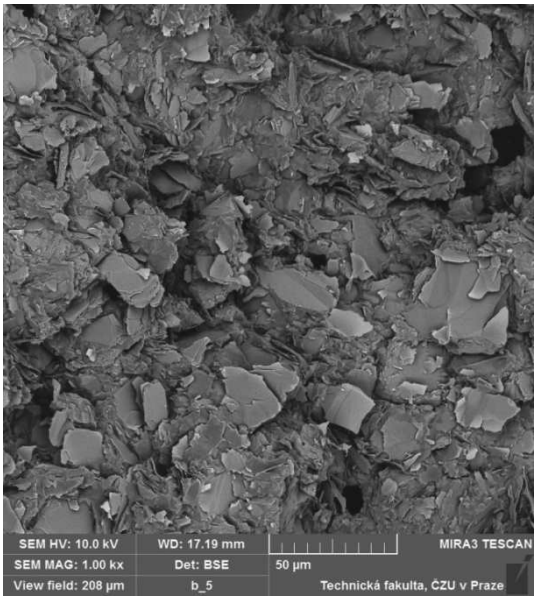

Figure 5. SEM images of fracture surface of sample – Back-scattered electrons (BSE).

CONCLUSIONS

Following conclusions can be deduced from the research focused on the influence of dust pollution in the laboratory on the strength of adhesive bond:

- Bond strength of adhesive C (unfilled) was 3.59 ± 0.37 MPa.
- Bond strength of adhesive D (unfilled) was 3.03 ± 0.20 MPa.
- By addition of filler in the form of aluminium powder was increased bonding strength by 14 and 26%.
- There is no significant difference in the strength of the bond in level of significance 0.05 when applied various performance of ventilation, i.e. 0, 50 and 100%.
- The decline or increase strength of the bond, depending on the performance of ventilation equipment moved in the interval from – 9 to 27%. Coefficient of variation ranged from 7 to 25%.
- The failure area did not change owing to the contamination of the adhesive bond with the dust pollution.

ACKNOWLEDGEMENT. Supported by Internal grant agency of Faculty of Engineering, Czech University of Life Sciences in Prague no: 2015:31140/1312/3106 and Research on mechanical properties of multi-component polymer systems during their preparation, processing and application.

REFERENCES

Bluyssen, P.M. 1996. European indoor air quality audit project in 56 office buildings. *Indoor Air*. **6**(4), 221–238.

Bockenheimer, C., Bernd, V. & Wulff, P. 2002. Network structure in epoxy aluminium bonds after mechanical treatment. *International Journal of Adhesion and Adhesives* [online]. 1., **22**(5), 349–356.

Di Giorgio, C., Krempff, A., Guiraud, H., Binder, P., Tiret, C. & Dumenil, G. 1996. Atmospheric pollution by airborne microorganisms in the city of Marseilles. *Atmospheric Environment* [online]. 1., **30**(1), 155–160.

Fu, Shao-Yun, Xi-Qiao Feng, Bernd Lauke & Yiu-Wing Mai. 2008. Effects of particle size, particle/matrix interface adhesion and particle loading on mechanical properties of particulate–polymer composites. *Composites Part B: Engineering* [online]. 9, **39**(6), 933–961.

Hricova, J. 2013. Environmentally Conscious Manufacturing: The Effect of Metalworking Fluid in High Speed Machining. *Key Engineering Materials* [online]. 10, **581**, 89–94.

Jones, A.P. 1999. Indoor air quality and health. *Atmospheric Environment* [online]. 12, **33**(28), 4535–4564.

Karwowska, E. 2003. Microbiological air contamination in some educational settings. *Polish Journal of Environmental Studies* **12**(2), 181–185.

Karwowska, E. 2005. Microbiological air contamination in farming environment. *Polish Journal of Environmental Studies* **14**(4), 445–449.

Kic, P., Hubeny, M., Ledvinka, Z., Tumova, E., Giner, C.C. & Torres, C.M. 2007. Control of indoor environment in housing of laying hens. *Conference Proceedings – 3rd International Conference, TAE 2007: Trends in Agricultural Engineering 2007.* CULS, Prague, 212–214.

Kic, P. & Chladek, L. 2010. Microclimate in tutorial and research brewery during winter season. *Conference Proceeding – 4th International Conference, TAE 2010: Trends in Agricultural Engineering 2010*. CULS, Prague, 311–315.

Kic, P. & Růžek, L. 2014. The microbiological environment in specific rooms of a university campus. *Agronomy Research* **12**(3), 837–842.

Kic, P., Růžek, L., Ledvinka, Z., Zita, L. & Gardianoba, I. 2012. Pollution of indoor environment in poultry housing. *Engineering for Rural Development* **11**, 480–483.

Kim, Ho Sung & KHAMIS, Mohammad Azhar. 2001. Fracture and impact behaviours of hollow micro-sphere/epoxy resin composites. *Composites Part A: Applied Science and Manufacturing* [online]. 9, **32**(9), 1311–1317.

Krofová, A. & Müller, M. 2015a. Influence of dusty micro-particles contamination on adhesive bond strength. *Agronomy Research* **13**(3), 654–661.

Krofová, A. & Müller, M. 2015b. Research in mechanical properties of adhesive contaminated with dusty micro-particles from production process. In 14th International Scientific Conference on *Engineering for Rural Development* 20.05.2015, Jelgava: Latvia University of Agriculture, 806–809.

Mleziva, J. 2008. *Polymers – Production, Structure, Properties and Applications* (1st ed.). Prague: Czech Technical University Publishing House. (in Czech)

Müller, M. & Valásek, P. 2012. Abrasive wear effect on Polyethylene, Polyamide 6 and polymeric particle composites. *Manufacturing Technology* **12**, 55–59.

Müller, M., Cidlina, J., Dědičová, K. & Krofová, A. 2015. Mechanical properties of polymeric composite based on aluminium microparticles. *Manufacturing Technology*. B.m.: Univerzita J.E. Purkyne, **15**(4), 624–628.

Nimmermark, S., Vonne, L., Gösta, G. & Wijnand, E. 2009. Ammonia, dust and bacteria in welfare-oriented systems for laying hens. *Annals of Agricultural and Environmental Medicine* **16**(1), 103–113.

Nou, T. & Viljasoo, V. 2011. The effect of heating systems on dust, an indoor climate factor. *Agronomy Research* **9**(1), 165–174.

Novak, M. 2012. Surfaces with high precision of roughness after grinding. *Manufacturing Technology* **12**, 66–70.

Peterka, J. 1980. Adhesive bonding of structural materials in engineering. Prague, SNTL 1980, 792 pp. (in Czech)

Ramazan, K., Mehmet, S. & Bekir, Y. 2008. Influence of adhesive thickness and filler content on the mechanical performance of aluminum single-lap joints bonded with aluminum powder filled epoxy adhesive. *Journal of Materials Processing Technology* [online]. 8., **205**(1–3), 183–189.

Valášek, P. & Müller, M. 2015. Properties of Adhesives Used for Connecting in Automotive Industry. *Acta Universitatis Agriculturae et Silviculturae Mendelianae Brunensis*. Mendel University of Agriculture and Forestry Brno, 11.5, **63**(2), 463–470.

Agronomy Research **14**(Sp.1), 1043–1052, 2016

Effect of porosity on the performance of cutting ceramics

V. Maksarov[1,*], A. Khalimonenko[1] and J. Olt[2]

[1]Saint-Petersburg Mining University, 21st Line 2, 199106 St. Petersburg, Russia
[2]Institute of Technology, Estonian University of Life Sciences, Kreutzwaldi 56, EE51014 Tartu, Estonia
[*]Correspondence: maks78.54@mail.ru

Abstract. The article examines the forecasting performance of the cutting tool equipped with interchangeable plates of carbide oxide ceramics (A_2 – mixed ceramic), by definition porous ceramic tool material affecting its cutting properties. Set correlation of porosity ceramic tools from electrical resistivity removable ceramic plates. Cutting tools having larger electrical resistivity values and, respectively, smaller porosity percentages should be used for machining the most precise components of machine part blanks, since their performance will be better than that of the tools whose ceramic bits have small electrical resistivity values. Based on the established correlation selects ceramic plates for the required machining conditions.

Keywords: cutting ceramics , the strength, the porosity of the material, operation tools, electrical resistivity.

INTRODUCTION

Ceramic cutting tools find ever-widening applications in industrial production; they are used for finishing precision components of machine parts. The number of ceramic materials used for making tools is quite large. This work focuses on carbide oxide ceramics, a material that is used extensively at machine-building enterprises and therefore can be used as a reference point for studying the performance of other ceramic cutting materials.

In spite of the fact that ceramic tools performance depends, first and foremost, on their hardness, apart from other factors, ceramic materials porosity has a sizable effect on it. It is known that the less is the porosity of a tool material, the better are the cutting property and performance of a tool manufactured with the help of powder metallurgy (Margules, 1980; Maksarov et al., 2014). Whereupon this factor virtually does not depend on the method of tool material manufacture – hot pressing, sintering, etc. – a material porosity percentage may be reduced but it is not yet possible to eliminate it altogether. This is equally applicable to all tools made of ceramics, irrespective of its components and structural composition.

Thereby, determining functional relationship between cutting properties of ceramics (e.g., its strength) and its material porosity can be considered as a solution of the problem of forecasting ceramic tools performance.

As a rule, any ceramic material, including carbide oxide cutting tools is solid substance with cavities (pores). The volume of pores, their distribution and dimensions

have a sizable effect on a number of properties of ceramic articles and material. E.g., strength of ceramics does not only depend on total porosity but on the sizes of pores and evenness of their distribution throughout the area of the surface under study.

As porosity increases, ceramics strength deteriorates through increased defectiveness of its structure and reduced strength of its bonds. Pores in ceramics have various shapes and outlines, they are unevenly distributed in its volume. Therefore, it is hard to obtain a complete characteristic of porosity. In spite of variety of their shapes, pores can be subdivided into closed ones (impermeable for liquids and gases) and open ones that are in their turn subdivided into dead-end ones (fillable by liquids and gases but not affecting ceramics permeability) and canal-forming ones (open from both ends and creating pore channels).

There are several principal approaches to measuring porosity and analyzing the surface structure of the material under study. The principal methods are the gas absorption one (physical and chemical), mercury injection porosimetry, the gas-dynamic method, etc. Each of those methods proves as the most efficient when measuring material porosity within a strictly defined range (Fig. 1). Therefore, the choice of analysis technique depends very heavily on the presumed structure of material, as well as the types and shapes of the pores.

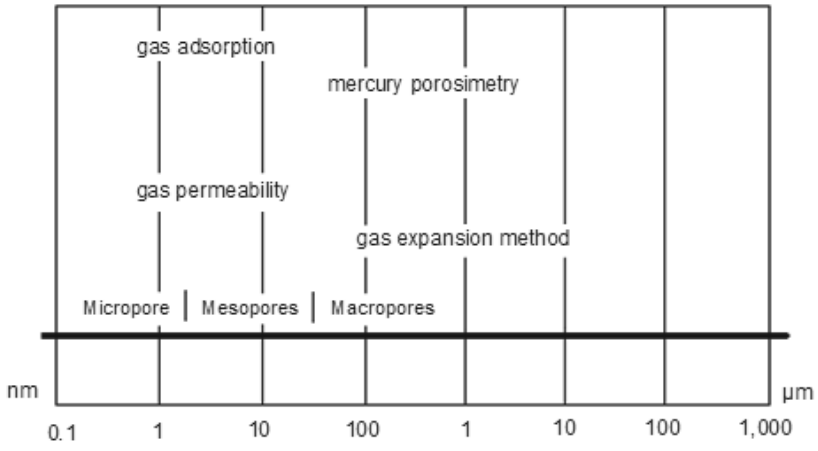

Figure 1. Measuring methods of material porosity depending on the sizes of pores.

Since direct methods of material porosity measurement are extremely complicated and measuring equipment is rather expensive, in ceramics technology this indicator is often assessed by determining other properties directly depending on porosity. We propose to assess material porosity by its correlation dependence on the electrical resistivity of ceramic cutting bits.

MATERIALS AND METHODS

At the beginning of the studies performed in order to determine carbide oxide ceramics strength it was necessary to carry out metallographic surveys that would elicit the structural composition of ceramics, determine the presence of pores and their number.

Metallographic survey data (Fig. 2) permitted us to establish that modern VOK63 type carbide oxide ceramics contain Al_2O_3 - 75% + (Ti, W, Mo)C - 25% (Wittenauer, 1995; Borovskii, 2007).

	A	B	C	D	E	F	G	H
1	Objekt 1	valge faas						
2								
3	All results in weight%							
4								
5	Spectrum	In stats.	C	Al	Ti	W	Total	
6								
7	1	Yes	8,27	0,81	17,77	73,15	100	
8	2	Yes	7,93	2,94	19,28	69,84	100	
9	3	Yes	9,45	0,67	20,25	69,63	100	
10								
11	Mean		8,55	1,47	19,1	70,87	100	
12	Std. deviation		0,8	1,28	1,25	1,97		
13	Max.		9,45	2,94	20,25	73,15		
14	Min.		7,93	0,67	17,77	69,63		

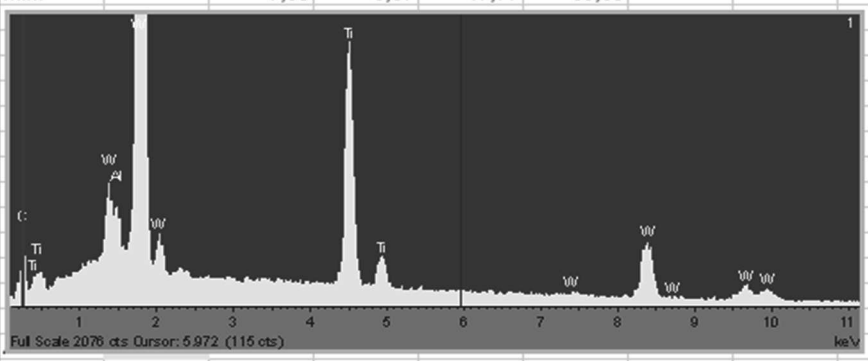

Figure 2. Percentage ratio between carbide oxide ceramics phases.

The structure of cutting ceramics was studied with the help of a scanning electron microscope in order to confirm the extent of porosity. The photos of the front surface of a ceramic cutting tool are presented in Fig. 3. As it can be seen in this picture, the sample under study has pores of different sizes and structures. It is known that more porous ceramics has a coarser grain size (about 3–4 μm) as compared to ordinary ceramic (having no pores) (about 1–2 μm). The data of the sample of ceramic under study coincide with a number of literature ceramic data (Dunand & Grabowski, 2000; Maksarov et al., 2014).

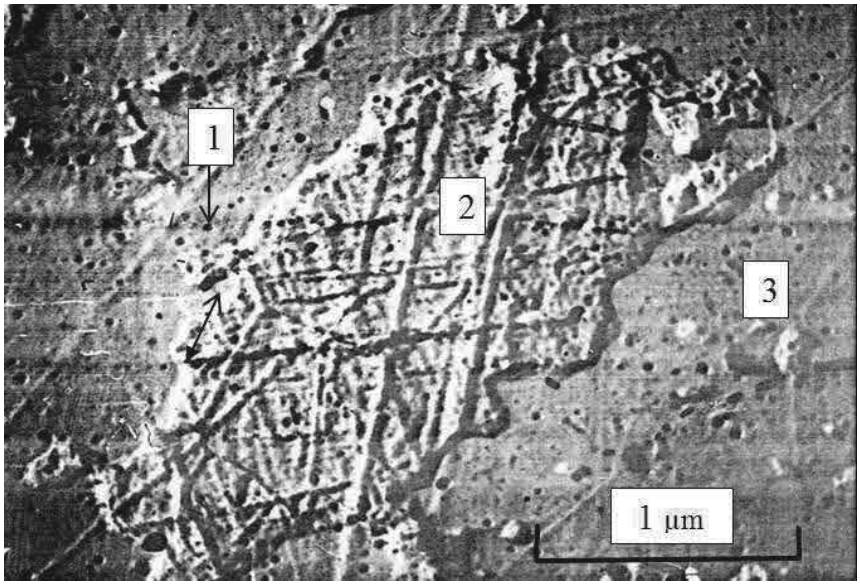

Figure 3. Carbide oxide ceramics pores: 1 – pores, 2 – (Ti, W, Mo)C, 3 – Al_2O_3.

It is difficult to use on the shop floor the methods ordinarily used for determining the number of pores whose size amounts to 0.1–10 nm Ceramics porosity can only be assessed with the help of electronic microscope and the ceramic bit must be thoroughly prepared for survey in a special way; it is a time-consuming process.

We propose to solve the above problem using correlation dependence between cutting ceramics porosity and its strength determined as a function of the ceramic bit material electrical resistivity.

RESULTS AND THEIR DISCUSSION

Several samples of replaceable multifaceted cutting bits made of the same grade cutting ceramics (VOK63) were selected for determining strength of ceramic cutting bits having a certain porosity percentage. Each of them had a different electrical resistivity value. The samples of ceramic bits were divided into two groups. The samples having electrical resistivity parameters $R \approx 10$ Ω were included into the first group, the samples having electrical resistivity parameters $R \approx 100$ Ω were included into the second group.

Electrical resistivity parameters were determined with high precision with the help of a mercury contact gauge (Margules, 1980; Maksarov et al., 2014).

The ceramic bits chosen for further tests were specially prepared. The front surfaces of ceramic cutting bits were thoroughly polished in order to determine the state of microstructure parameters.

Each sample of ceramic bits was subjected to an effect simulating the processes that accompany metal cutting.

The samples of ceramic bits were subjected to mechanical loads equal to $P = 3 \cdot 10^4$ N, simulating the state of a cutting bit subjected to compression deformation.

After load exposure, the ceramic cutting bit samples were exposed to thermal action equal to $T = 600$ °C, simulating heating of ceramic cutting tools during machining of workpieces. The ceramic samples were heated in thermal jacket. A chromel-copel thermocouple installed on its border contract permitted to assess the thermal effect on the material of the cutting bit under study precisely enough.

We propose to assess strength of ceramic bits through its relationship with porosity using a formula proposed by M.Yu. Balshin (Balshin, 1972):

$$\sigma = \sigma_c \left(1 - \phi\right)^{\lambda} , \qquad (1)$$

where: σ_c is the strength of non-porous or semi-porous body, for VOK63 carbide oxide cutting ceramic the value of $\sigma_c = 322$ MPa, T is the exponent, for the conditions under study $\lambda = 3$, ϕ is porosity, %. The results of ceramic tool cutting process simulation can be seen in Table 1.

Table 1. The results of ceramic tool cutting process simulation

The initial state of the sample			The condition of the sample under load				The condition of the sample under the influence of temperature			
R, Ω	ϕ, %	σ, MPa	R, Ω	P, N	ϕ, %	σ, MPa	R, Ω	T, °C	ϕ, %	σ, MPa
10	12	218	12	$3 \cdot 10^4$	16	190	11	600	14	202
100	8	240	103	$3 \cdot 10^4$	11	236	102	600	10	238

The obtained results permitted us to create characteristic curves linking electrical resistivity parameters of ceramic cutting bits to porosity (ϕ) and strength (σ) of the ceramic material. The electrical resistivity-vs-porosity and strength curves for carbide oxide cutting ceramic whose electrical resistivity values are approximately 100 Ω in the initial state $R_0 = f(\phi, \sigma)$, after exposure to load $R_P = f(\phi, \sigma)$ and after thermal exposure $R_T = f(\phi, \sigma)$ are shown in Figs 4 and 5.

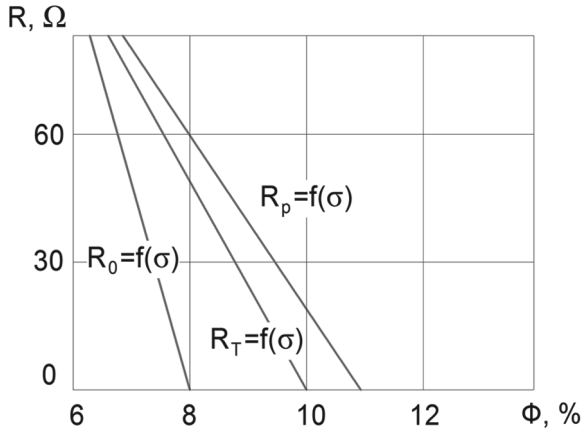

Figure 4. Ceramics electrical resistivity vs. porosity curves in the initial state $R_0 = f(\phi)$, after exposure to load $R_P = f(\phi)$ and after thermal exposure $R_T = f(\phi)$.

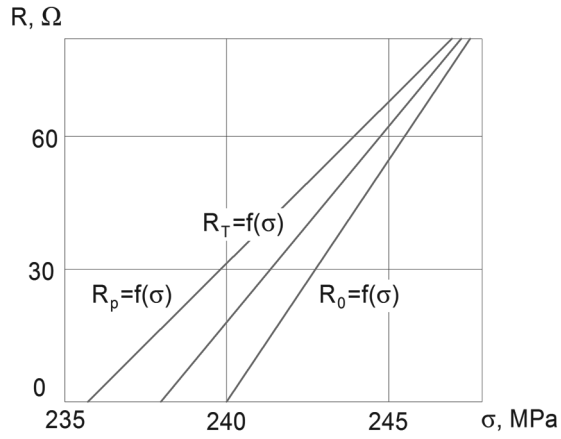

Figure 5. Ceramics electrical resistivity vs. strength curves in the initial state $R_0 = f(\sigma)$ after exposure to load $R_P = f(\sigma)$ and after thermal exposure $R_T = f(\sigma)$.

We have constructed a $R = f(\phi, \sigma, K)$ functional relationship where K is a coefficient replacing load and temperature values during cutting process simulation in order to determine generalized relationship between electrical resistivity of ceramic material and the porosity and strength values of ceramic cutting bits.

In the process of experimental studies, we have obtained $R = f(\phi)$ and $R = f(\sigma)$ characteristic curves that permitted us the shape a 3D area and to demonstrate the existence of a relationship between electrical resistivity of a ceramic material, its strength and porosity percentage (Fig. 6).

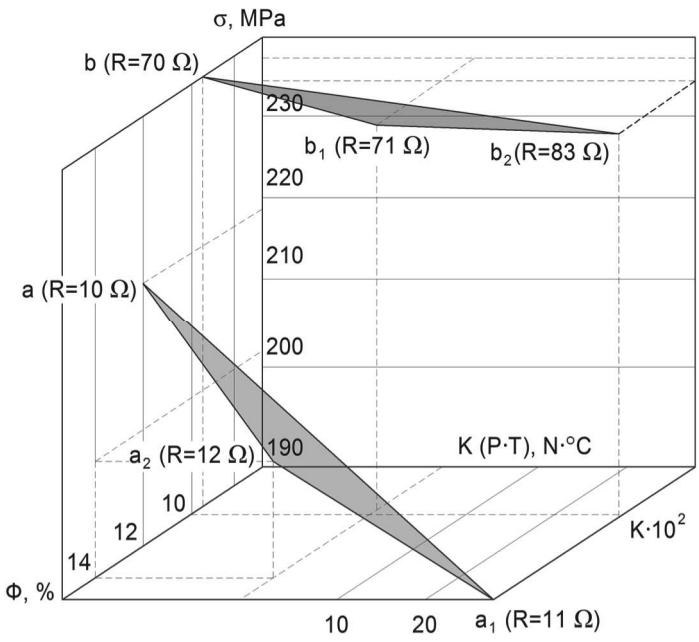

Figure 6. 3D curve $R = f(\phi, \sigma, K)$ constructed on the basis of experimental data.

Force actions created in the process of cutting bring about an increase in electrical resistivity of ceramic material and its porosity percentage.

Changes accompanying the cutting process (thermal heating) also slightly increase the electrical resistivity of ceramic material and its porosity percentage, but to a lesser extent than under load.

All samples of ceramic cutting bits underwent similar strength and porosity changes, irrespective of the value of their electrical resistivity. However, under identical external impacts the samples of ceramic bits whose electrical resistivity values were approximately equal to 10 Ω demonstrated greater quantitative differences.

The ceramic bits whose electrical resistivity values were approximately equal to 100 Ω have relatively small porosity percentage, and under temperature and force impacts accompanying the cutting process their strength is higher than that of ceramic bits with relatively small electrical resistivity values approximately equal to 10 Ω.

A detailed survey of ceramic cutting bit samples' microstructure was carried out in order to determine strength parameters of the same grade ceramics having different electrical resistivity values.

The ceramic samples were specially prepared according to the procedure described in works (Vaidyanathan et al., 1999; Matryona, 2004).

After that, the average diameter of carbide grains was determined with the help of computer software determining the parameters of structural components of the ceramic material under study chosen in the microscope field of view. The cross dimension of a grain L taken at certain increments (0–1 μm, 1–2 μm, 2–3 μm) chosen accepted as the parameter value. In its turn, the number of grains of each size within a preset range can be used as a basis for obtaining relative frequency values, i.e. the numbers of occurrences of each variant of the chosen parameter.

Relative frequency was determined by the formula:

$$F = \frac{A}{200}, \% \tag{2}$$

where: A is absolute frequency, i.e. the number of carbine grains of a given size in a certain range; 200 is the total number of grains under survey within the chosen range.

Mathematical statistics method permitted us to obtain precise measurements whose results were used to determine other values.

The average diameter of a carbide grain was determined by the formula:

$$D_{av.} = \frac{\sum m \cdot x}{\sum m}, \ \mu\text{m}, \tag{3}$$

where x is the diameter of carbide grains in each group, m is the frequency of a group occurrence.

The absolute value of a carbide grain diameter $D_{av.abs.}$ was determined by multiplying the obtained value of average diameter of carbide grains $D_{av.}$ by the microscope eyepiece division value used by the software E:

$$D_{av.abs.} = D_{av.} \cdot E, \tag{4}$$

Strength characteristics depending on grain size $\sigma = f(L)$ were determined by formula (Zhukov, 2011):

$$\sigma = 0{,}37 L^{-\frac{1}{2}}, \text{ MPa}, \tag{5}$$

where L is the average grain size, μm.

The data permitting to construct characteristic curves for ceramics having different electrical resistivity values (porosity changes vs. strength characteristics and even grain size changes vs. relative occurrence frequency and strength value) were obtained by formula (1) (Fig. 7).

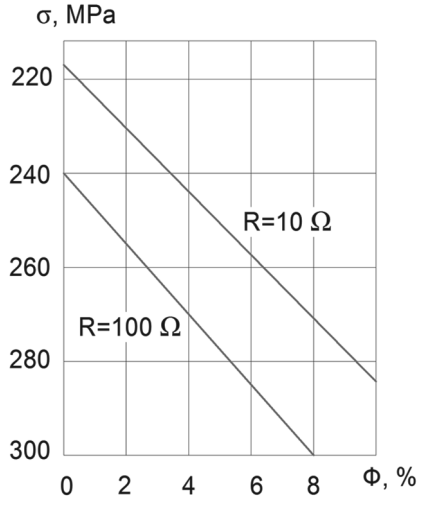

Figure 7. Porosity change vs. strength characteristics and even carbide grain size changes vs. occurrence frequency and strength value curves.

Determined strength values of ceramic material with different electrical resistivity parameters depending on carbide grain sizes demonstrated that all the cutting ceramic bit samples under study demonstrated nearly the same carbide grain occurrence frequency density. However, at the same time grain size fluctuation ranges were different. Ceramic bits with electrical resistivity $R \approx 10\ \Omega$ had a wider grain size fluctuation range.

The root-mean-square values of strength parameters of the ceramic bits under survey are tabulated in Table 2.

Table 2. The RMS values of the strength characteristics of ceramics

R, Ω	D_{CP}, μm	$\sigma = 0.37L^{-\frac{1}{2}}$, MPa	ϕ,%	$\sigma = \sigma_c (1 - \phi)^T$, MPa
10	2,2	171	12	218
100	1,5	232	8	240

The resulting relationships confirm again that ceramics strength characteristics improve as porosity decreases, whereupon ceramics whose electrical resistivity $R \approx 100$ Ω was significantly stronger than that with electrical resistivity $R \approx 10$ Ω because it had a finer structure and a smaller porosity percentage.

Structural parameters of ceramic plates have a great influence on the working ability of cutting tool equipped with them and on the processing quality. The smaller the carbide grain size, larger the cumulative line of carbide grain boundary extension, lower the percentage of material porosity, and more the quantity of carbide grain in the definite bulk of material, the higher the wear-resistance of the cutting tool (Maksarov et al., 2014). Influence of the value of electrical resistance on the wear of clearance face of ceramic plate (h_3) and thus on the working ability of tool is also specified by the structural parameters of the sample. The more the value of the electrical resistance of ceramic plate is, the better microstructural parameters are. According to them, the tool performance time under the constant processing modes (t, S, v) rises considerably, that is the tool life period (T) increases or cutting distance, which allows us to correct essentially the processing speed increasingly and thus to increase the working ability of tool on the preservation of standard wear value (q.v. Table 3).

Table 3. Cutting distance with wear h_3 = 0.5 mm of rear surface

Φ, %	R, Ом	Cutting distance with wear h_3 = 0.5 mm of rear surface, m		
		V = 1,64 m s^{-1}	V = 2.35 m s^{-1}	V = 3.14 m s^{-1}
12	10	26,282	25,641	20,512
8	100	41,000	40,000	32,000

Comparison test showed that the wear-resistance of ceramics of grade VOK63 with R = 100 Ω is 1.56 times high in comparison with VOK63 ceramics with R = 10 Ω on steel cutting under the same parameters of cutting modes v, S, t.

CONCLUSIONS

The estimation of influence of porosity is conducted on specific electric resistance of ceramic material at the simulation of cutting process.

It was found that in the initial state a structure and porosity of cutting ceramics can be estimated on the size of specific electric resistance.

Dependence was set between durability and specific conductivity of ceramic material.

Comparison test showed that the wear-resistance of ceramics of grade VOK63 with electrical resistivity R = 100 Ω is 1.56 times high in comparison with VOK63 ceramics with R = 10 Ω on steel cutting under the same parameters of cutting modes.

Thereby, we can conclude that the greater is the electrical resistivity value of a ceramic cutting tool, the better that tool will perform.

Cutting tools having larger electrical resistivity values and, respectively, smaller porosity percentages should be used for machining the most precise components of machine part blanks, since their performance will be better than that of the tools whose ceramic bits have small electrical resistivity values.

Simulation of cutting process by application to the cutting of ceramics of different load and temperature also demonstrated the existence of a relationship the preservation of the specific conductivity with porosity and strength of ceramics.

REFERENCES

Balshin, M.Yu. 1972. *Scientific foundations of powder metallurgy and fiber metallurgy*. Metallurgy. Moscow. 336 pp. (in Russian).

Borovskii, G.V., Grigoriev, S.N., Maslov, A.R. 2007. *Handbook of toolmaker*. Mashinostroenie. Moskva, 464 pp. (in Russian).

Dunand, D.C, Grabowski, J. 2000. Tensile Transformation-Mismatch Plasticity of Bismuth Sesquioxide. *J. Amer. Ceram. Soc*. **83**(10), pp. 2521–2528.

Maksarov, V., Khalimonenko, A., Timofeev, D. 2014. Machining quality when lathing blanks with ceramic cutting tools. *Agronomy Research* **12**(1), 269–278.

Margules, A.U. 1980. *Cutting metals cermets*. Machine building. Moskva, 160 pp. (in Russian).

Matryona, C.V. 2004. *Technical ceramics*. Tomsk: Publishing house TPU, 751 pp. (in Russian).

Wittenauer, J. 1995. Superplastic forming of zirconia. In: *Plastic Deformation of Ceramics*, eds. Plenum, New York, pp. 321–331.

Vaidyanathan, R., Bourke, M.A., Dunand, D.C. 1999. Analysis of Neutron Diffraction Spectra Acquired In-Situ During Stress-Induced Transformations in Superelastic NiTi. *Journal of Applied Physics A*. **86**(6), 3020–3029.

Zhukov, I.A. 2011. Structure and properties of porous ceramics Zr02-Al203. *Izv. Universities. Physics*. **54**(9), 120–124. (in Russian).

Agronomy Research **14**(Sp.1), 1053–1062, 2016

Cellular tubular structures from perforated metallic tape and its application

V. Mironovs[1], I. Boiko[2,*], T. Koppel[3] and M. Lisicins[1]

[1]Riga Technical university, Faculty of Civil Engineering, Institute of Building Production, Azenes street 16/20–331, LV-1048 Riga, Latvia
[2]Riga Technical University, Faculty of Mechanical Engineering, Transport and Aeronautics, Institute of Mechanical Engineering, Ezermalas street 6k, LV-1006 Riga, Latvia
[3]Tallinn University of Technology, Department of Labor Environment and Safety, SOC351, Ehitajate tee 5, EE19086 Tallinn, Estonia
[*]Correspondence: irina.boiko@rtu.lv

Abstract. The objectives of performed research were the following: 1) check out the possibility of effective formation of the tubular and planar structures from the perforated steel tapes, which were obtained as a waste during stamping of fine-sized details, by cutting and bending; 2) testing of achieved tubular and annular structures for fixing up of the electrical cables and as electromagnetic shielding solutions; 3) analysis of achieved results and elaboration of the recommendations for using of lightweight tubular shields for the electrical cables. The actuality of research is connected with the re-using of metallic wastes and shielding solutions against electromagnetic fields. All objectives were reached successfully using bending for formation of the tubular structures. The bending strength of achieved structures and the shielding efficiency in a controlled environment was examined. The measurement results have shown that perforated steel will exhibit noticeable shielding properties against both the electric and magnetic field. Such results open up wide possible application of the planar and cellular tubular structures from perforated metallic tapes.

Key words: perforated metallic waste, tubular structures, electromagnetic fields, shielding.

INTRODUCTION

During last years the perforated metallic materials (PMM) become more used in building industry and mechanical engineering. For example, such materials are widely used as spacers for wall and floor constructions, for containing walls or sandwich wall structures (Lisicins et al., 2015). Another popular application of PMM is using as reinforcement material in concrete works and brickworks (Kalva, 2011), as well as fixtures and connectors for nodes of wooden constructions (Ozola, 2011). The support structures consisting of an annular or tubular casing, which cavity is arranged with reinforcing member and filled with the infill material were proposed by Mironovs & Lisicins (2015). Due to light weight and decorative behaviour PMM also used for producing the elements of ventilation devices, filters, channels and heating systems. In such applications the tubular structures are usually used (Perforated metal, 2016). Also

PMM have been actively used in the construction of cladding panels in residential housing or as so called thermoprofiles (Garifullin et al., 2015).

Nowadays it is possible to produce the tubular structures from the PMM in wide diapason of the diameters (from few mm to one and more meters) with length up to 10 meters and larger according to application (Wadley et al., 2003; Perforated metal, 2016). The choice of manufacturing method for producing tubular structures from PMM is based on the tube diameter and length, material thickness, mechanical properties of the material etc. Mostly the welded tubular structures are used, which were produced from the PMM tape by spiral twisting, winding, stretching and profiling (Wadley et al., 2003; Wadley, 2006; Mironovs et al., 2013).

Mironovs et al. (2014) have shown the possibility of application of cellular structures from perforated metallic tape for electromagnetic solutions, in particular shields for electrical cables (Fig. 1). It should be mentioned, that it is necessary to analyze the mechanical properties of PMM and achieved structures using appropriate simulation and/or experimental evaluation methods (Ochsner et al., 2001; Vaz et al., 2011; Bhavitha et al., 2015).

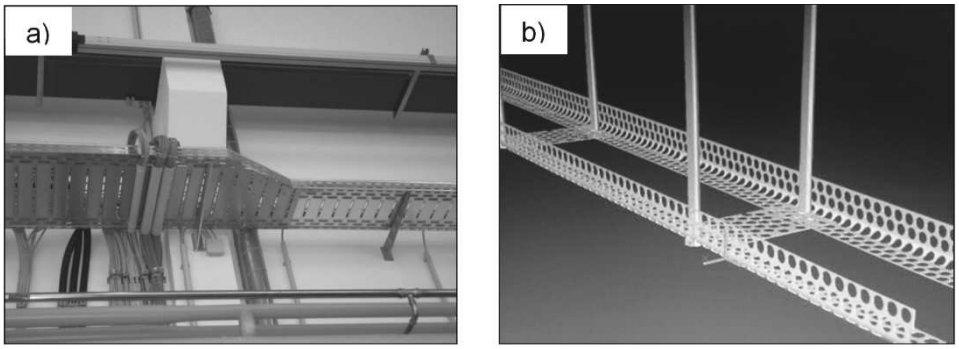

Figure 1. Application of cellular structures from MPP for placing of suspended cables in closed construction (a) and open construction (b).

Mostly for manufacturing cellular structures the specially produced PMM are used. More effective way is to use the perforated steel tapes, which are obtained as a waste during stamping of fine-sized details, for example, elements of the leaf chain (Mironovs et al., 2014). Since the base material usually is the structural steel with relative high carbon content such metallic waste is characterized by high strength.

The main objective of performed research was the testing of tubular and annular structures achieved by bending for fixing up of the electrical cables and as electromagnetic shielding solutions. The actuality of research is connected with the re-using of metallic wastes and shielding solutions against electromagnetic fields.

The necessity of shielding electromagnetic fields may be presented in many forms (Borner et al., 2011; Koppel et al., 2013). In telecommunications shielding devices and cables is aimed at preventing crosstalk and interference from a device to another. Such interference or crosstalk may emanate from the cables that carry some sort of communication signal. Even cables that just pass on a significant amount of the electrical current may affect sensitive nearby electronic devices. In such case a shielding of the cables is sought for.

In this paper electromagnetic field measurements were conducted to determine the shielding effectiveness of perforated steel elements placed around or next to the power cables that irradiate extremely low frequency (power frequency 50 Hz) magnetic and electric fields.

MATERIALS AND METHODS

Usually, the cable packages at a great length have a significant weight. Therefore in case of placing those into suspended perforated metallic constructions under ceilings the mechanical properties (especially bending strength) of perforated tubes are of great importance. Mechanical and geometrical parameters of PST-2 type perforated steel tape (trade mark of JSC 'DITTON Driving Chain Factory', Latvia), which was used for producing of perforated steel tubes for supporting and shielding of the cable packages are shown in Table 1. This tape is achieved as a technological waste during stamping of the elements of driving chains which are used in motor industry.

Table 1. Mechanical and geometrical parameters of PST-2 type perforated steel tape, which was used for producing of perforated steel tubes for supporting and shielding of the cable packages.

Parameter	Value	Tape representation	Tape geometry
designation	PST-2	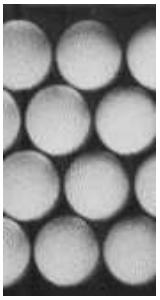	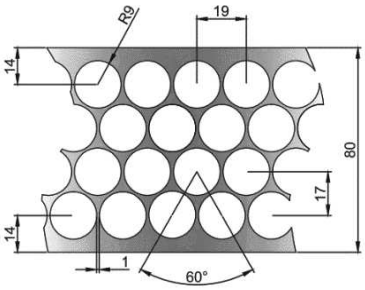
mark of steel	08пс-ОМ-Т-2-К		
standard	GOST 503-81		
thickness, mm	1.50		
width, mm	80		
permeable area, %	69.10		
effective cross-sectional area, mm^2	25.13		
tensile load bearing capacity, kN	5.54		
tensile strength, MPa	220.65		
displacement, mm	6.54		
strain, %	3.93		

For research the samples of cellular tubular structures (tubes) with diameter 27 mm and length 1 m were produced by bending. View of the perforated steel tube is shown on Fig. 2, but the three-point bending testing process of the perforated steel tube is shown on Fig. 3. The span between supports was 350 mm. Loadings rate was 30 mm/min, air temperature: +24 °C. The loading was performed by Instron 10000 (Instron, USA) testing machine.

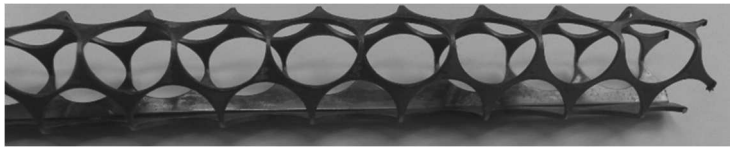

Figure 2. View of the perforated steel tube (fragment).

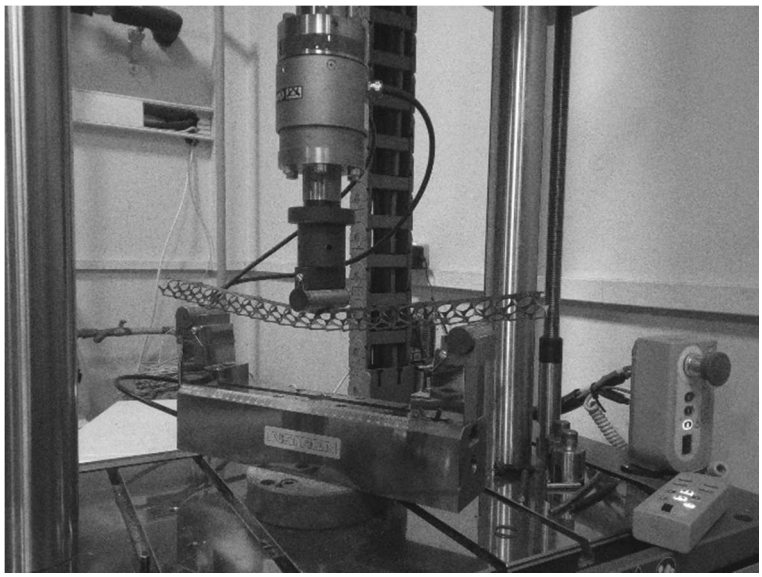

Figure 3. Testing process of perforated steel tube made by Instron 10000 testing machine.

Fig. 4. shows the relationship between flexural stress and strain of perforated steel tube made of material described in Table 1. As shown three-point bending testing proves the possibility to use such tubular structures for fixing up of the electrical cables and cable packages.

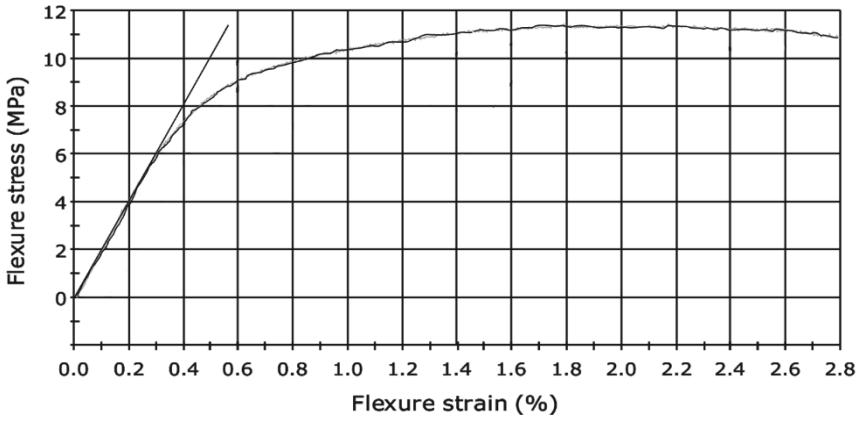

Figure 4. The relationship between flexure stress and flexure strain of perforated steel tube, the straight line reflects the modulus of elasticity in shear.

In order to test the shielding effectiveness of perforated steel structures against electromagnetic field, two forms of samples were produced: 1) a tube as was mentioned above and 2) a planar strip. Both were of a length of one meter. Power cables were positioned in the center of the tubular sample and in the center of the side of the planar sample (Figs 5, 6).

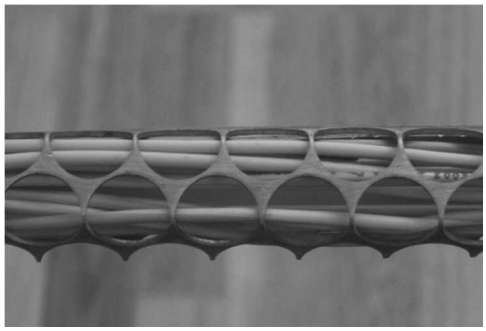

Figure 5. Perforated steel tube shielding with the power cable package.

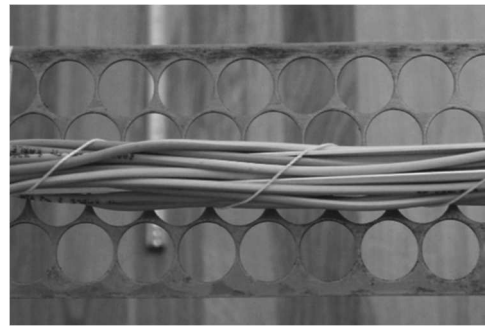

Figure 6. Perforated steel strip sheet shielding with the power cable package.

A high current was run through 14 isolated copper cables (1.5 mm²). When an electromagnetic field hits another material than the one it travels within, some of the energy may be reflected and the rest transmitted through. In this study the effectiveness of the shielding intervention is determined by measuring the electromagnetic field before and after the intervention. The shielding articles are meant for power cables meaning the frequency of 50 Hz.

The measurement device used was Gigahertz Solutions NFA400 (Langenzenn, Germany). In order to guarantee the reliability of the measurement results the area was constantly monitored for background electromagnetic fields, which topped at 9 nT (nanoTeslas) for magnetic field and 5 V m^{-1} (Volts per meter) for electric field. It was also controlled that no other electromagnetic field sources were nearby that would affect the reading.

The cables were positioned horizontally to the height of 1 m from the floor. The measurement readings were taken from the same height at 12 different distances from the cable: starting from 0.05 and ending with 2.5 m. The range of interventions applied included (Fig. 7): A) unshielded wire bundle, B) application of tubular shield, C) application of grounded tubular shield, D) application of planar shield, E) application of grounded tubular shield. In case of magnetic field, the shielding of course makes no difference, measurements were conducted only for the scenarios A, B and D.

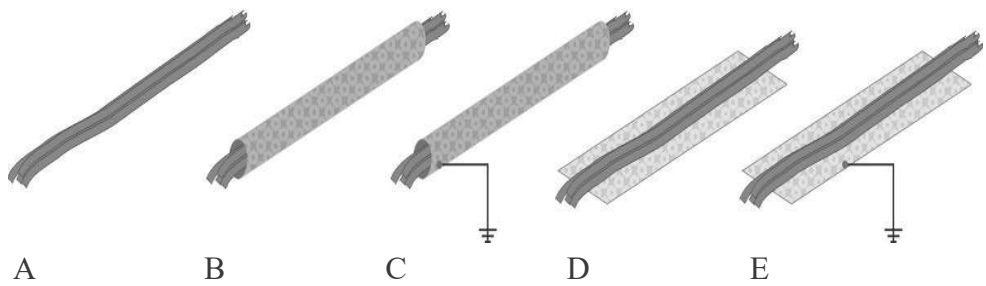

Figure 7. The investigated electromagnetic irradiation scenarios: A) unshielded wire bundle, B) application of tubular shield, C) application of grounded tubular shield, D) application of planar shield, E) application of grounded tubular shield.

In order to conduct measurements one must note the different field propagation principles of electric and magnetic fields. In Fig. 8 the propagation path is pictured by arrows. Whereas electric shielding is easier to achieve due to straightforward path of the electric field lines. The magnetic field lines always need to finish the loop, making encapsulating this more complex task.

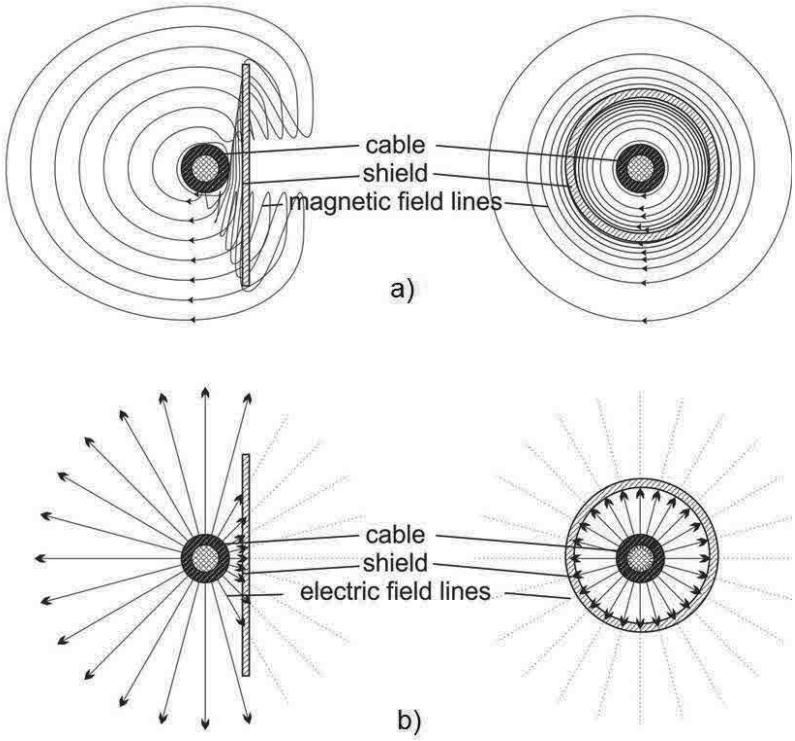

Figure 8. A principal field propagation of magnetic (a) and electric (b) field in respect to the planar and tubular shielding measures.

RESULTS AND DISCUSSION

For the electric field, the measurements clearly indicate the importance of grounding the shield. Without the grounding, at 0.5 m the 100% of the planar shield and 78% of the tubular shield electric field passed through. While grounding the shield, at 0.5 m the transmission of the electric field was retained at 28% for the planar shield and 30% for the tubular shield (Fig. 9 and Table 2).

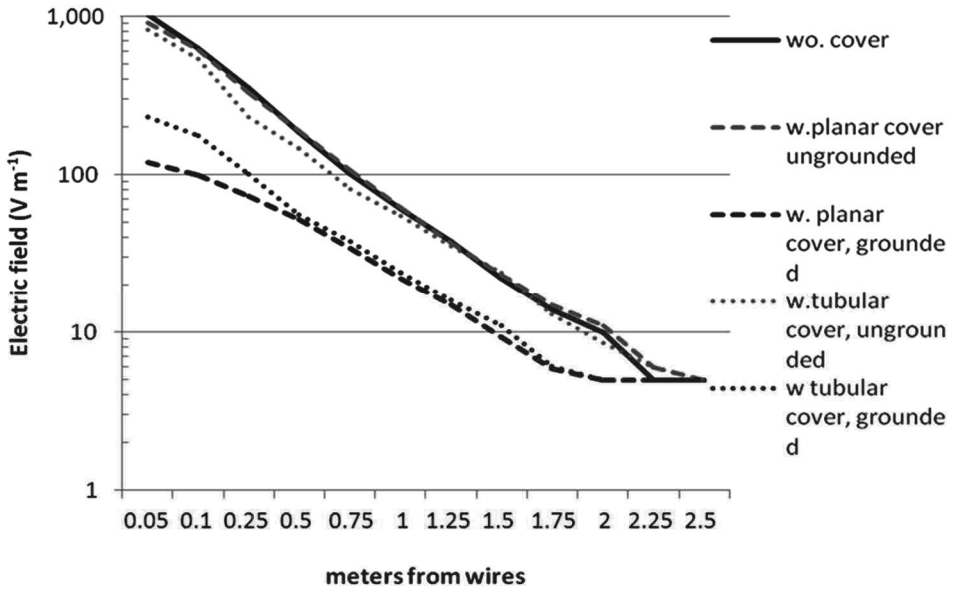

Figure 9. Electric field strength for a wire bundle with (w.) and without (wo.) a perforated steel cover.

Table 2. Electric field strength (V/m) for a wire bundle with and without a perforated steel cover: A) unshielded wire bundle, B) application of tubular shield, C) application of grounded tubular shield, D) application of planar shield (see Fig. 7)

Distance from the wires, m	A	B	C	D	E
0.05	1,016	906	120	821	230
0.1	628	614	99	536	175
0.25	354	326	73	231	101
0.5	185	187	52	145	56
0.75	100	105	34	81	38
1	61	62	22	55	24
1.25	38	37	15	35	16
1.5	22	23	9.3	24	11
1.75	14	15	5.9	13	6.1
2	10	11	5	8.5	5
2.25	5	6	5	6	5
2.5	5	5	5	5	5

In case of magnetic field the shielding effectiveness was less than compared to the electric field attenuation. At 0.5 m distance 74% of the magnetic field passed through the planar shield and 78% from the tubular shield (Fig. 10 and Table 3). In average the transmission across all measurement distances was 77% for the planar shield and 67% for the tubular shield.

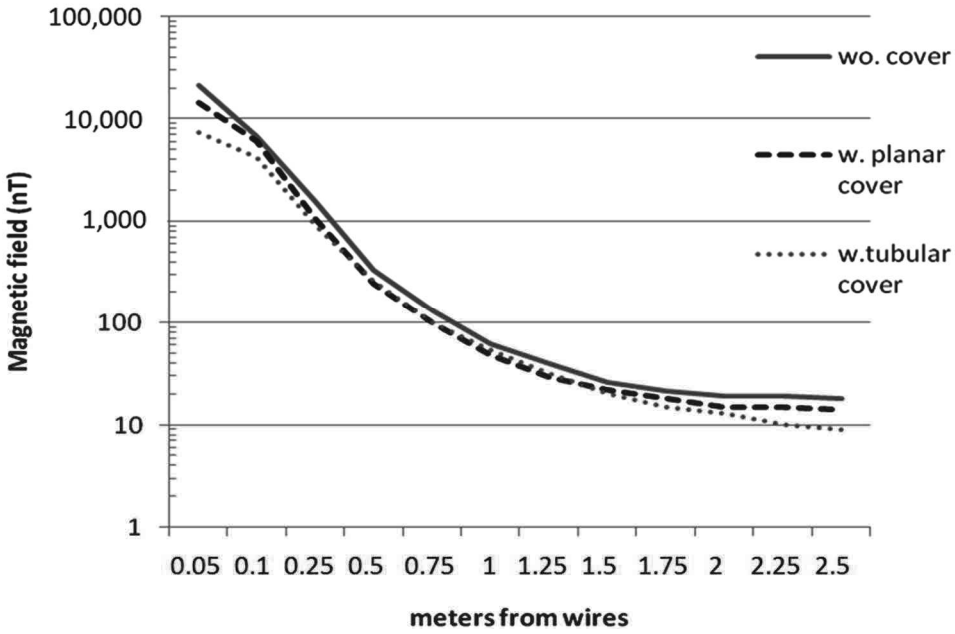

Figure 10. Magnetic field flux density for a wire bundle with (w.) and without (wo.) a perforated steel cover.

Table 3. Magnetic field flux density for a wire bundle with and without a perforated steel cover: A) unshielded wire bundle, B) application of tubular shield, D) application of planar shield (see Fig. 7)

Distance from the wires, m	A	D	B
0.05	21,300	14,290	7,346
0.1	6,857	6,050	4,194
0.25	1,540	1,021	892
0.5	332	245	260
0.75	130	98	100
1	61	48	54
1.25	39	29	32
1.5	26	22	20
1.75	21	18	15
2	19	15	13
2.25	19	15	10
2.5	18	14	9

The measurement results have shown that perforated steel will exhibit noticeable shielding properties against both the electric and magnetic field. Considering that the tested perforated shields are a manufacturing waste product, the surface of the shield is tightly packed with holes. In cases where only moderate shielding attenuation is required, the usage of the studied material may very well be justified. The application is likely to include cable pathways such us catwalks in the ceiling or inside the walls.

It should be mentioned that according to the information of the JSC 'Ditton Driving Chain Factory' (Latvia) only this enterprise produces about 500 tons of the perforated steel waste per year. The 'Ditton Driving Chain Factory' specializes in a wide range of roller-, bush-, leaf and other chains (Ditton Driving Chain Factory, 2016). Nowadays the waste obtained during cold stamping of the elements of driving chains of the motors is sold out as a metallic scrap in spite of the fact that the perforated tape is practically ready raw material that may be directed for processing without any significant preparation. That's why the recycling of such waste is actual and needed to be implemented.

Besides the noticeable shielding properties against both the electric and magnetic field the main advantage of the perforated steel tape is the smaller weight in comparison with the unperforated tape (0.21 kg against 0.29 kg of the 1 m of the tape). Such difference (28%) is significant taking into the mind the planned application of perforated steel tape for fixing up of the electrical cables and cable packages. At that the tensile strength of the perforated tape (220.65 MPa) is reduced only by 18% in comparison with the unnperforated conventional steel tape (270.00 MPa). Another important advantage is the lower cost of the perforated steel tape in comparison with the unperforated tape (0.041 EUR against 0.057 EUR of the 1 m of the tape) and decorative value of the perforated shield. These aspects as well as results of given research prove the economic and technological effect of the offered recycling of the perforated steel waste by application as shielding against electromagnetic field and fixing solution for the cables.

CONCLUSIONS

The new promising direction for recycling of the technological waste is offered. The plannar and tubular shields against electromagnetic fields were produced by cutting and bending from the perforated steel tapes, which were obtained as a waste during cold stamping of fine-sized details particularly elements of driving chains of the motors. Such manufacturing method not complicated, nor special equipment is needed, which together with waste as a base material allows to conclude that it is economically and technologically effectvie way to recycle the technological waste.

Achieved tubular and planar structures were tested for fixing up of the electrical cables and as electromagnetic shielding solutions. Bending test proves the possibility to use such structures for fixing up of the electrical cables and cable packages. From the other hand, testing of the shielding efficiency has shown that perforated steel will exhibit noticeable shielding properties against both the electric and magnetic field. It should be mentioned, that better results were achieved for the electric field shielding in the case of grounding the shield. Without the grounding, at 0.5 m the 100% of the planar shield and 78% of the tubular shield electric field passed through. While grounding the shield, at 0.5 m the transmission of the electric field was retained at 28% for the planar shield and 30% for the tubular shield.

Such results open up wide possible application of the cellular tubular and planar structures from perforated metallic tapes for fixing up of the electrical cable packages and as electromagnetic shielding solutions in cases where only moderate shielding attenuation is required. The application is likely to include cable pathways such us catwalks in the ceiling or inside the walls.

REFERENCES

Accurate Perforating Company, Inc: Perforated metal technical information 2016. *http://accurateperforating.com/resources/perforated-metal-technical-information.* Accessed 07.01.2016.

Bhavitha, E.B., Rosemol, K.G. & Teena, J. 2015. Comparative study on moment connections in cold formed steel sections with and without perforations. *International Journal of Innovative Science, Engineering & Technology* **21**, 478–481.

Borner, F., Bruggermeyer, H., Eggert, S., Fisher, M., Heinrich, H., Hentschel, K. & Neuschulz, H. 2011. *Electromagnetic fields at workplaces: A new scientific approach to occupational health and safety, Elektromagnetische Felder am Arbeitsplatz.* Bundesministerium fur Arbeit und Soziales, Bonn, 46 pp.

Ditton Driving Chain Factory: Company. 2016. *http://www.dpr.lv/en/about-us/about-us/.* Accessed 10.01.2016.

Garifullin, M. Sinelnikov, A., Bronzova, M. & Vatin, N. 2015, Buckling behavior of perforated cold-formed columns. In: *The knowledge-based innovation network METNET seminar*, HAMK, Budapest, pp. 112–123.

Kalva, L. 2011. *Metallic perforated materials in concrete works.* Riga Technical University, Riga, Latvia, 87 pp. (in Latvian).

Koppel, T., Tasa, T. & Tint, P. 2013. Electromagnetic fields in contemporary office workplaces. *Agronomy Research* **11**, 421–434.

Lisicins, M., Mironovs, V., Boiko, I. & Lapkovskis, V. 2015. Sandwich wall constructions made of perforated metallic materials. *Agronomy Research* **13**, 662–670.

Mironovs, V., Lisicins M., Boiko, I. & Zemchenkovs, V. 2013. Manufacturing of the cellular structures from the perforated metallic materials. *Agronomy Research* **11**, 139–146.

Mironovs, V., Lisicins, M. & Boiko, I. 2014. Cellular structures from perforated metallic tape and its application for electromagnetic shielding solutions. *Agronomy Research* **12**, 279–284.

Mironovs, V. & Lisicins, M. 2015. *Perforated metallic materials and their application possibilities.* Riga Technical University, Riga, Latvia, 159 pp. (in Latvian).

Ochsner, A., Winter, W. & Kuhn, G. 2001. Elastic-plastic behaviour of perforated aluminum under tension and compression. *Technische Mechanik* **21**, 101–108.

Ozola, L. 2011. Connections with perforated metallic plates. In: *Estimation and design of timber constructions II: Application of Eurocode 1 and Eurocode 5 in construction design.* Latvia University of Agriculture, Jelgava, Latvia, pp. 89–91 (in Latvian).

Vaz, M., Eduardo, A., De Souza, N. & Munoz-Rojas, P. 2011. Materials Modelling-Chalenges and Perspectives. In Vaz, M. et al. (ed): *Advaced Computatinal Materials Modelling: From Classical to Milti-Scale Techniques*, pp.1–21.

Wadley, H.N.G, Fleck, N.A. & Evans, A.G. 2003. Fabrication and structural performance of periodic cellular metal sandwich structures. *Composites Science and Technology* **63**, 2331–2343.

Wadley, H.N.G. Multifunctional periodic cellular metals. 2006. *Phil. Trans. R. Soc. A.* **364**, 31–68.

Agronomy Research **14**(Sp.1), 1063–1068, 2016

Production of Crumb Ruber – Iron Powder Mixture for perspective synthesis of Carbon-Iron powder sorbent

V. Mironovs[1], O. Ozernovs[1], V. Lapkovskis[1,*] and D. Golyandin[2]

[1]Riga Technical University, Laboratory of Powder Materials, Kipsalas Str. 6, LV-1048 Riga, Latvia
[2]Tallinn Technical University, Tallinn University of Technology, Ehitajate tee 5, EE 19086, Tallinn, Estonia
[*]Correspondence: lap911@latnet.lv

Abstract. A sustainable technique for conversion of end-of-life tyres (ELTs) to products with added value is of a great importance for resource-efficient circular economy. However, obtaining products with added value often requires multi-stage procedures, which include traditional and emerging technological approaches. In current paper, the authors suggest an efficient approach for recycling of ELT tyres, obtaining products which can be subsequently used for environmental applications. This approach introduces a synthesis path for new materials by transformation of industrial wastes i.e. ELT rubber wastes to crumb rubber and further mixing with iron powder. Particular attention is driven to perspective processing of obtained crumb rubber-iron powder mixture by means of microwave pyrolysis for synthesis of carbon-iron powder mixture and its use as a composite absorbent material along with emerging application for electromagnetic and microwave irradiation protection.

Key words: crumb rubber, iron powder, high pressure grinding rolls, disintegrator, microwave pyrolysis.

INTRODUCTION

The European Union recognises end-of-life tyres as a valuable resource with growing potential (ETRMA, 2011). A significant amount of ELTs in the European Union 220 million/year rises an up-to-date agenda for research of effective ELTs treatment methods with the aim of producing final treatment/recycling products with added value by means of sustainable treatment processes (Lam et al., 2010).

In current paper, the authors suggest an efficient approach for recycling of ELT tyres, obtaining products which can be subsequently used for environmental applications. The suggested approach represents a synthesis path for new materials by transformation of industrial wastes i.e. ELT rubber wastes to crumb rubber and further mixing with iron powder, describing processing stages 1, 2 (Fig. 1) for preparation of crumb rubber-iron powder mixture. Thus, producing a 'crumb rubber-iron powder mixture' for further processing by pyrolysis (microwave), facilitating a preheating of crumb rubber by means of iron particles incorporated into milled crumb rubber granules.

Pyrolysis processes are widely used for treatment of end-of-life shredded or granulated (particles size range: 0.5 mm – 3 cm) tyres (Athanassiades, 2013). However, applying a microwave heating brings an additional advantage, leading to devulcanisation (Ramos et al., 2011) of rubber material (i.e. ELTs), hence producing higher quality carbon particles. Iron powders, having distinct absorbing properties (An et al., 2008), influences on microwave treatment, acting as an absorber in microwave-range wave band. In case of solid waste processing, application of iron powder as a microwave absorber agent increases an effectiveness of material degradation, meanwhile decreasing a treatment residence time (Gedam & Regupathi, 2012). In case of rubber-iron mixture, particles of iron powder can be rapidly heated by microwave irradiation up to 700 °C (Yoshikawa et al., 2006), accelerating pyrolysis of rubber along with formation of carbon-iron powder mixture. Obtained carbon-iron powder mixture can be directly used as a composite absorbent material with distinctive magnetic properties (Shishkin et al., 2014) Additionally, there could be several emerging applications of fine carbon-iron powder as a raw material for catalyst applications (Xiao et al., 2012), as well as for electromagnetic and microwave irradiation shielding (Sano et al., 2007; Micheli et al., 2011).

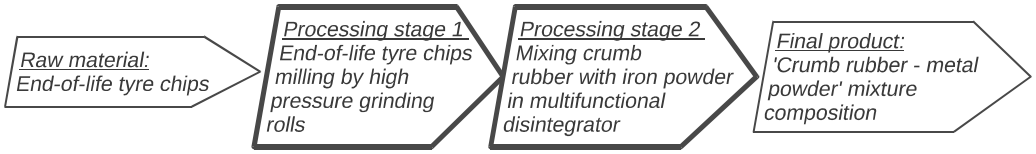

Figure 1. ELT rubber wastes transformation stages from tyre chips to 'Crumb rubber – metal powder' mixture composition.

MATERIALS AND METHODS

High pressure grinding rolls (HPGR) is known as milling technique for mineral processing (Ozcan et al., 2015). However, HPGR can be considered as a perspective technological approach for ELT disintegration (Fig. 1, Processing stage 1.) (Jevmenovs, 2015), competing to widely-used shredding (ETRMA & Chemrisk, 2009). In order to obtain crumb rubber granulate suitable for further mixing with iron powder, an experimental studies of rubber chips disintegration process in high pressure grinding rolls have been performed by means of industrial HPGR schematically shown in (Fig. 2). Further mixing of crumb rubber with iron powder (Fig. 1, Processing stage 2) has been performed by means of multifunctional disintegrator developed in Tallinn University of Technology (Estonia) Fig. 3 (Tumanok et al., 1997). The disintegrator operates in direct, separation and selective milling modes (Tumanok & Kulu, 1999) reaching maximum rotation speed up to 12,000 rpm.

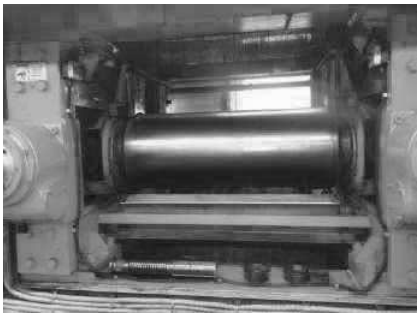

Figure 2. Experimental setup for the study of the ELT chips disintegration process (in partnership with Rubber Products Llc (Latvia)).

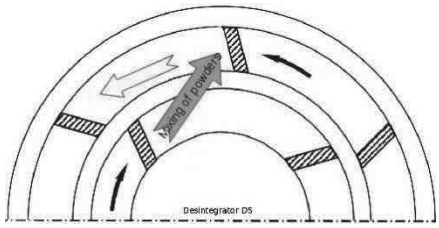

Figure 3. Multifunctional disintegrator: mixing process schematics (Tallinn University of Technology).

RESULTS AND DISCUSSION

ELTs rubber chips before disintegration in HPGR and a final product after HPGR processing have shown in Fig. 4, a, b. It is evident that treatment in HPGR has leaded to comminution of rubber chips up to 0.1–1.0 mm. After HPGR treatment, obtained rubber particles (or granules) were processed in multifunctional disintegrator for mixing with iron powder.

a) 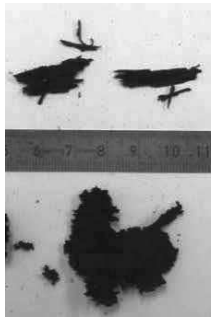

b) 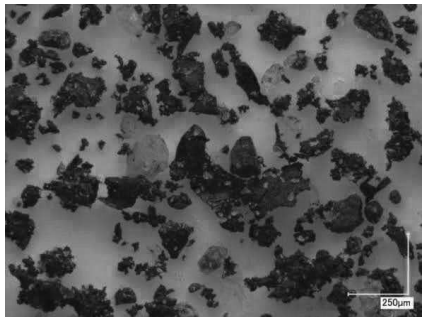

Figure 4. Optical microscopy of a crumb rubber before (a) and after (b) HPGR (Fig. 2) processing.

Iron powder is composed mainly of metal with insignificant impurities in form of scale and rust. Particle size distribution of iron powder and crumb rubber used for experimental mixing (Processing stage 2, (Fig. 1)) in multifunctional disintegrator (Fig. 3) is shown in (Fig. 5). Volumetric mixing ratio of crumb rubber with iron powder is 1:3. The final product – 'crumb rubber – iron powder mixture' was prepared by applying a single direct grinding mode.

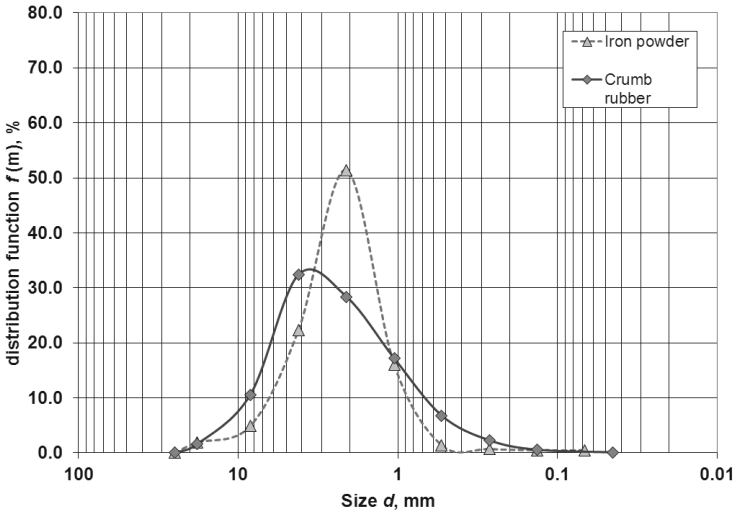

Figure 5. Crumb rubber and iron powder particles size distribution (Equipment: Analysette 22) used for feeding of multifunctional disintegrator (Processing stage 2, Fig. 1.).

During the high-energy processing of mixture in disintegrator, iron particles (Fig. 7) were incorporating to the surface of rubber granules, forming a stable rubber-iron composition with granule size up to 500 μm (Fig. 6).

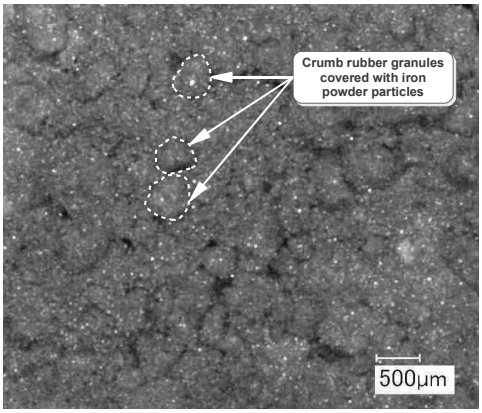

Figure 6. Crumb rubber granules covered with iron powder (Equipment: Keyence VHX-2000).

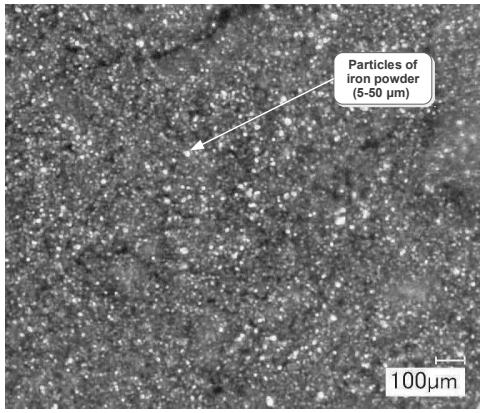

Figure 7. Iron powder particles after processing in disintegrator (Equipment: Keyence VHX-2000).

As it follows from (Fig. 1), the obtained rubber-iron mixture will be subsequently processed by pyrolysis for carbon-iron powders composition recovering. Further research activities will cover several emerging applications of carbon-iron powder composition, such as composite absorbent material with distinctive magnetic properties for spilled oil collection (Treijs et al., 2013), and as a material for electromagnetic/microwave irradiation shielding.

CONCLUSIONS

Two-stage processing approach for conversion of ELTs rubber into 'Crumb rubber - metal powder' mixture has been proposed and tested. Application of high pressure grinding rolls along with disintegrator has proven a concept of developing a new raw material based on crumb rubber and iron powder.

A disintegrator has been used for mixing rather than for comminution process. As a process product, a stable composition of crumb rubber with iron powder has been obtained, with granule size up to 500 μm (Fig. 6).

The obtained 'Crumb rubber – metal powder' composition will be subsequently processed by pyrolysis for synthesis of new composite absorbent material based on carbon-iron powders composition.

REFERENCES

An, Y.J. Nishida, K., Yamamoto, T., Ueda, S. & Deguchi, T. 2008. Characteristic evaluations of microwave absorbers using dielectric and magnetic composite materials. *Journal of Ceramic Processing Research* **9**(4), 430–436.

Athanassiades, E. 2013. Waste tyre pyrolysis : Sustainable recovery and reuse of a valuable resource. Imperial College London.

ETRMA. 2011. End of life tyres – A valuable resource with growing potential, Available at: http://www.wastexchange.co.uk/documenti/tyres/ETRMA_ELTs_report_2006.pdf.

Gedam, V.V. & Regupathi, I. 2012. Pyrolysis of Municipal Solid Waste for Syngas Production by Microwave Irradiation. *Natural Resources Research* **21**(1), 75–82.

Jevmenovs, I. 2015. 'Method for Devulcanization of Rubber and Devulcanization Catalyst for Such Purpose. Patent Application PCT/IB2014/066580'. WIPO. http://www.google.com/patents/WO2015083109A1?cl=en.

Lam, S.S., Russell, A.D. & Chase, H.A. 2010. Pyrolysis using microwave heating: A sustainable process for recycling used car engine oil. *Industrial and Engineering Chemistry Research*, **49**(21), 10845–10851.

Micheli, D. Apollo, C., Pastore, R., Morles, R.B., Marchetti, M. & Gradoni, G, 2011. Electromagnetic Characterization of Composite Materials and Microwave Absorbing Modeling. Advances in Nanocomposites – Synthesis, Characterization and Industrial Applications, pp. 360–384. Available at: http://www.intechopen.com/source/pdfs/15412/InTech-Electromagnetic_characterization_of_composite_materials_and_microwave_absorbing_modeling.pdf.

Ozcan, O., Aydogan, N.A. & Benzer, H. 2015. Effect of operational parameters and recycling load on the high pressure grinding rolls (HPGR) performance. *International Journal of Mineral Processing* **136**, 20–25.

Ramos, G., Alguacil, F.J. & López, F.A. 2011. The recycling of end-of-life tyres. Technological review. *Revista de Metalurgia* **47**(3), 273–284.

Sano, S. Takayama, S., Takao, Y., Tsuzuki, A. & Makino, Y. 2007. Microwave Absorption Behavior of Iron – Alumina Mixed Powder. *ISIJ International* **47**(4), 588–591.

Shishkin, A. Mironovs, V., Lapkovskis, V., Treijs, J. & Korjakins, A. 2014. Ferromagnetic Sorbents For Collection and Utilization of Oil Products. *Key Engineering Materials* **604**, 122–125.

Treijs, J. Teirumnieks, E., Mironovs, V., Lapkovskis, V. & Shishkin, A. 2013. Investigations of Properties of Powdered Ferromagnetic Sorbents. In *Proceedings of the 9th International*

Scientific and Practical Conference: Environment. Technology. Resources, Volume 1. Rezekne (Latvia), pp. 95–100.
Tumanok, A. & Kulu, P. 1999. Treatement of different materials by disintegrator systems. *Estonian Acad. Sci. Eng*. **5**(3), 222–242.
Tumanok, A. Kulu, P., Goljandin, D. & Roštšin, D. 1997. Disintergator as a machine for utilizing of metal chips to metal powder. *In III ASM International Conference and Exhibition*. The Recycling of Metals, 513–522.
Xiao, L., Wen, Z., Ci, S., Chen, J. & He, Z. 2012. 'Carbon/iron-Based Nanorod Catalysts for Hydrogen Production in Microbial Electrolysis Cells'. *Nano Energy* **1**(5), 751–56. doi:10.1016/j.nanoen.2012.06.002.
Yoshikawa, N., Ishizuka, E. & Taniguchi, S. 2006. Heating of Metal Particles in a Single-Mode Microwave Applicator. *Materials Transactions* **47**(3), 898–902.

Agronomy Research **14**(Sp.1), 1069–1077, 2016

Relaxation and creep behaviour of false banana's fibre (*Ensete ventricosum*)

Č. Mizera[1,*], D. Herák[2] and P. Hrabě[3]

[1,2]Czech University of Life Sciences Prague, Faculty of Engineering, Department of Mechanical Engineering, Kamýcká 129, CZ 165 21 Praha 6 Suchdol, Czech Republic
[3]Czech University of Life Sciences Prague, Faculty of Engineering, Department of Material Science and Manufacturing Technology, Kamýcká 129, CZ 165 21 Praha 6 Suchdol, Czech Republic
[*]Correspondence: mizera@tf.czu.cz

Abstract. This study was focused on the analysis of viscoelastic behaviour of fibres of false banana (*Ensete ventricosum*). The aim of the experiment was to describe the short term creep and relaxation behaviour under tension loading. The fibers of *Ensete ventricosum*, originally from Ethiopian region Hawasa, were used in this experiment. Moisture content $Mc = 8.40 \pm 0.67\%$ (d. b.) and true density $\rho_t = 668 \pm 44$ kg m^{-3} of the samples were determined. The specimens had initial gauge length of $L_0 = 100 \pm 1$ mm and the average yarn breaking load (YBL) after 20 tests was $\sigma_r = 14.3 \pm 1.7$ N. To determine the relationship between tension force and deformation, tension device (Labortech, MPTest 5.050, Czech Republic) was used to record the course of deformation function. All tests were performed using a constant rate $\alpha = 3.1$ N s^{-1}. The short term creep tests were performed using constant loads of 30%, 60% and 90% of the average YBL. The short term relaxation tests were performed using constant strain of 30%, 60% and 90% of maximal strain. Measured data were analysed by computer software Mathcad 14. Experimental creep and stress relaxation curves at different load levels were determined. Experimental creep lifetimes t_r for different load levels: 24,311 ± 7,489 s (30% YBL), 1,831 ± 462 s (60% YBL) and 17.6 ± 5.5 s (90% YBL) were determined. Initial modulus of elasticity, finite modulus of elasticity and initial energy of stress relaxation and creep of Ensete fibres were determined.

Key words: agriculture, initial modulus, tensile test.

INTRODUCTION

The design of new materials based on natural reseurces is essential for both environmental and economical analyses (Alves et al., 2010). Currently, there has been great attention on the application of natural fibres as a substitute for synthetic fibres. The natural fibres are environmentally friendly, biodegradable and recyclable, and also they can help in the reduction of waste and environmental pollution (Kalia et al., 2013). Natural fibres can be a suitable substitute of synthetic fibres because they are available in a fibre form at low costs (Aseer et al., 2013). Literature indicate that natural fibres such as flax, jute, hemp, sisal and pineapple have significant advantages in comparison with conventional fibres (Rao et al., 2007; Silva et al., 2008; Alves et al., 2010; Faruk et al., 2012). They reach relatively high specific strength and a rigidity owing to their low density. Another suitable plant with great potential for the production of natural fibers is

Ensete (*Ensete ventricosum*) also known as false banana (Tsehaye & Kebebew, 2006; Yemataw et al., 2014). The Ensete plant do not bear edible fruits and it is not categorized as usual banana plants (genera Musa). It is a perennial herbaceous plant that grows in Ethiopia and it is primarily intended for human consumption and animal feeding (Vincent et al., 2013; Herak et al., 2014). Over centuries the Ensete fibres have been extracted from the leaves of this plant as major material for the weaving, ropes and cord production, as well as for baskets production (Diriba et al., 2013; Yirmaga 2013). Ensete fibres as reinforcement in composite materials researched Mizera et al., 2015. One of the most important considerations using natural fibres in engineering applications is the relaxation and creep behaviour. Creep and relaxation measurements are of interest to chemists and engineers in any application where the material must sustain loads for long periods (Sedlachek, 1989). However, currently, in terms of creep and relaxation behaviour the Ensete fiber are not adequately described. Previously published scientific work focused specifically on Ensete plant deal with chemical and physical properties (Nurfeta et al., 2008). The aim of this experiment was to describe creep and relaxation behavior of *Ensete ventricosum* fiber under tension loading and to determine the initial modulus of elasticity, finite modulus of elasticity and initial energy of relaxation and creep behaviour.

MATERIALS AND METHODS

Sample

Samples of fibres produced from *Ensete ventricosum*, obtained from Hawassa region, Ethiopia were used for the experiment. The moisture content $M_c = 8.40 \pm 0.67\%$ *(d. b.)* of the samples was determined using standard oven method, ASAE method (ASAE S410.1 DEC97, ASAE, 1998). Samples of 100 g mass from a batch of Ensete fibres were randomly selected for the moisture content determination. The mass of each sample m_s (g) was determined using an electronic balance (Kern 440–35, Kern & Sohn GmbH, Balingen, Germany). The true fibre density $\rho_t = 668 \pm 44$ kg m^{-3} was determined gravimetrically (Blahovec, 2008). This means that the mass of individual samples from a batch of fibres, randomly selected and measured using an electronic balance (Kern 440–35, Kern & Sohn GmbH, Balingen, Germany), was divided by the volume of sample. The volume of the individual sample was determined by weighing the sample in toluene and applying the principle of buoyancy (Kim et al., 2012). The results obtained were expressed as mean of three replicates. The morphologies of fibres were studied using a scanning electron microscope (Tescan Mira3, Czech Republic). The samples were covered with a thin layer of gold using a sputter coater (Quorum Q150R ES, United Kingdom) before SEM observation. The observation was prepared in the secondary electron mode with an accelerating voltage of 5 kV.

Tensile rupture test

To determine the relationship between tension force and deformation, tensile device (Labortech, MPTest 5.050, Czech Republic) was used to record the course of deformation function. All tests were performed using a constant rate of $\alpha = 3.1$ N s^{-1} under following conditions: 23 ± 2 °C of temperature and $51 \pm 2\%$ of humidity. The specimens had initial gauge length of $L_0 = 100 \pm 1$ mm. The average yarn breaking load (YBL) after 20 tests was 14.3 ± 1.7 N.

The stress σ at a given instant t can be defined as the rate between the applied tensile force $F(t)$ and the average yarn fibre area A_0 (Eqn. 1).

$$\sigma(t) = \frac{F(t)}{S_0}; S_0 = \frac{\rho_l}{\rho} \Rightarrow \sigma(t) = F(t) \cdot \left(\frac{\rho}{\rho_l} \right) \tag{1}$$

where: ρ_l – mass of fibre per unit length, tex, ρ – mass density of fibre material, mg m^{-3}. The rupture stress of fibre σ_r can be defined after that as:

$$\sigma_r(t) = \frac{\sigma(t)}{\rho} = \frac{F_r}{\rho_l} \tag{2}$$

where: σ_r – rupture stress of fibre, N tex^{-1}; F_r – rupture force, N; ρ_l – mass of fibre per unit length, tex.

The natural fibres have different average diameters, it was necessary to normalise the load data to obtain comparable values. In the textile industry, normalisation is generally done using the linear mass of the material, in tex (1 tex = 1g km). Ensete fibres applied in this study have linear weight ρ_l = 118.4 dtex (where 1dtex = 1g 10,000 m^{-1}). Hence the average rupture stress σ_r for fibres is given by (F_r/ρ_l) = 14.3/118.4 ≈ 0.12 N dtex^{-1}.

Short term creep test

Each sample with initial length L_0 = 100 ± 1 mm was initially loaded at a rate of α = 3.1 N s^{-1} until a limit constant load F_0. The tests were performed using constant loads of 30%, 60% and 90% of the average YBL (15 times per load levels). Fig. 1 shows the typical loading history the samples in a creep test.

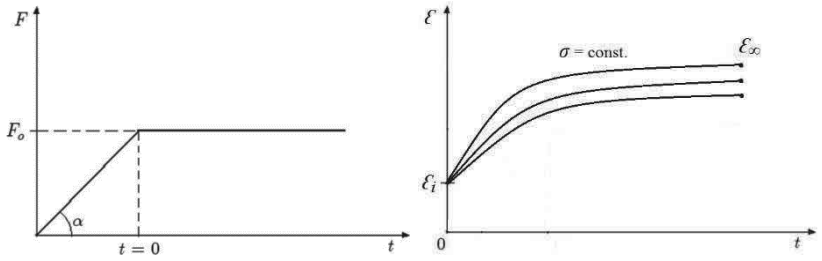

Figure 1. Typical loading history (left) and measured curves (right) in a creep test.

The tests were conducted until the fibre failure. The initial modulus of elasticity for creep E_{Ci} and finite modulus of elasticity $E_{C\infty}$ were calculated using Eqn. 3 and Eqn. 4:

$$E_{Ci} = \frac{\sigma}{\varepsilon_i} \tag{3}$$

where: E_{Ci} – initial modulus of elasticity for creep, N tex^{-1}; σ – stress of fibre, N tex^{-1}; ε_i – initial strain of fibre, –,

$$E_{C\infty} = \frac{\sigma}{\varepsilon_\infty} \tag{4}$$

where: $E_{C\infty}$ – finite modulus of elasticity for creep, N tex^{-1}; σ – stress of fibre, N tex^{-1}; $\mathcal{E}_\infty$ – finite strain of fibre, –.

The energy of creep test was calculated as an area below a curve 'stress – strain' from zero to a maximum value of the deformation according to an Eqn. 5:

$$W_{Ci} = \frac{1}{2}\sigma\varepsilon_i + \sigma(\varepsilon_\infty - \varepsilon_i) \tag{5}$$

where: W_{Ci} – energy of creep test, N tex^{-1}; σ – stress of fibre, N tex^{-1}; $\mathcal{E}_i$ – initial strain of fibre, –, $\mathcal{E}_\infty$ – finite strain of fibre, –.

Short term stress relaxation

The stress relaxation experiments were performed on tensile device (Labortech, MPTest 5.050, Czech Republic). The samples with initial length L_0 = 100 ± 1 mm was initially loaded at a rate α = 3.1 N s^{-1} until a limit constant deformation $\mathcal{E}_0$, which corresponded to the loads of 30%, 60% and 90% of the average YBL (15 times per load levels).

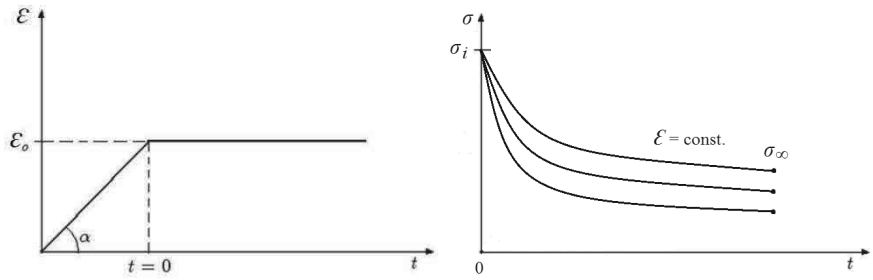

Figure 2. Typical loading history (left) and measured curves (right) in a stress relaxation test.

The tests until the run-out time of 1,000 s were conducted. The initial modulus of elasticity for relaxation E_{Ri} and finite modulus of elasticity $E_{R\infty}$ were calculated using Eqn. 6 and Eqn. 7:

$$E_{Ri} = \frac{\sigma_i}{\varepsilon} \tag{6}$$

where: E_{Ri} – initial modulus of elasticity for relaxation, N tex^{-1}; σ_i – initial stress of fibre, N tex^{-1}; $\mathcal{E}$ – strain of fibre, –,

$$E_{R\infty} = \frac{\sigma_\infty}{\varepsilon} \tag{7}$$

where: $E_{R\infty}$ – finite modulus of elasticity for relaxation, N tex^{-1}; σ_∞ – finite stress of fibre, N tex^{-1}; $\mathcal{E}$ – strain of fibre, –.

The initial energy of relaxation test was calculated as an area below a curve 'stress – strain' from zero to a maximum value of the deformation according to an Eqn. 5:

$$W_{Ri} = \frac{1}{2}\sigma_i \varepsilon \tag{8}$$

where: W_{Ri} – initial energy of relaxation test, N tex^{-1}; σ_i – initial stress of fibre, N tex^{-1}; $\mathcal{E}$ – strain of fibre, –.

RESULTS AND DISCUSSION

SEM image of cross-section of Ensete fibre which was used in this study can be seen in Fig. 3. Fig. 4 shows the creep strain as a function of time under tensile stress at different load levels (level 1: $F_0 = 4.3$ N; level 2: $F_0 = 8.6$N; level 3: $F_0 = 12.9$ N). The rupture force in a tensile test with prescribed load history $F(t) = \alpha t$ is dependet of the rate α (Mattos & Chimisso, 2011). For the rate $\alpha = 3.1$ N s^{-1}, the average YBL obtained in the tensile tests was 14.3 ± 1.7 N. Very similar values were determined also in polyethylene fibres (Lechat et al., 2011).

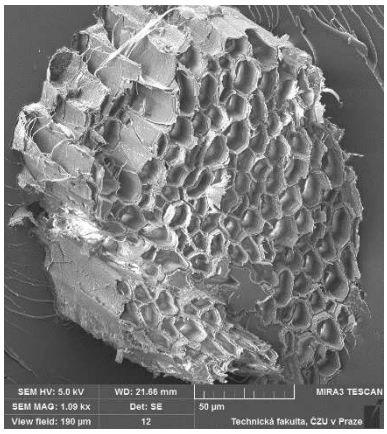

Figure 3. SEM image of Ensete fibre.

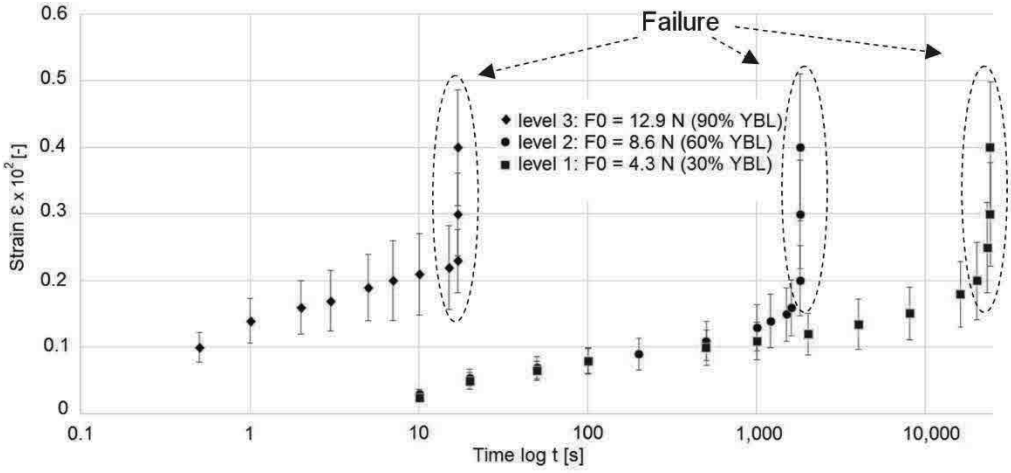

Figure 4. Measured creep curves of Ensete fibres.

From Fig. 4 it is possible to observe that a typical experimental curve of natural fibres shows three stages: (i) a 'primary creep' phase during hardening of material leads to a decrease in the rate of flow which is initially very high. Primary creep is the time-dependent recoverable portion of the delayed deformation. This response of viscoelastic materials is thought to be due primarily to configurational changes in molecular structure produced by the applied load. Alfrey discusses the mechanisms of such molecular movement.; (ii) a 'secondary creep' phase is a portion of the total sample deformation which is nonrecoverable at the test conditions after removal of the load. Permanent deformation is caused by viscous flow, irreversible crystallization, and molecular chain rupture (Ferry, 1961). In this phase is the rate of flow almost constant. ; (iii) a 'tertiary creep' phase during which the strain rate increases up to failure. It can be verified that the load level strongly affects the creep deformation rate and creep lifetime (Mattos & Chimisso, 2011). Table 1 shows the experimental lifetimes t_r of Ensete fibres obtained for different load levels.

Table 1. Experimental creep lifetimes for different load levels

F_0 (N)	t_r (s)
4.3	24,311 ± 7,489
8.6	1,831 ± 462
12.9	17.6 ± 5.5

From the creep curves (Fig. 4) the modulus of elasticity using Eqn. 3 and Eqn. 4 for different load level were calculated. Table 2 presents initial modulus of elasticity, finite modulus of elasticity and creep energy of Ensete fibres for different load levels.

Table 2. Initial modulus of elasticity, finite modulus of elasticity and creep energy of Ensete fibres

F_0 (N)	E_{Ci} (N tex^{-1})	$E_{C\infty}$ (N tex^{-1})	W_{Ci} (mN tex^{-1})
4.3 (30% YBL)	12.23 ± 3.18	11.46 ± 2.54	6.0913 ± 1.1574
8.6 (60% YBL)	20.08 ± 5.83	19.22 ± 3.44	14.2348 ± 3.4151
12.9 (90% YBL)	18.58 ± 4.11	17.91 ± 3.22	34.1797 ± 6.4929

Similar values of initial modulus of elasticity was shown also in jute fibre (Kozlowski, 2012). From Table 2 it is evident that the difference between the initial modulus and finite modulus of elasticity reaches low values. This is due to a very small value of strain of natural fibres in tensile loading (Kozlowski, 2012). In natural fibre the cellulose chains lie approximately parallel to the long axis of the fibre.When load is applied on a fibre, the stress is transmitted from one chain to its neighbour by means of intermolecular forces. These forces are strongest in the crystalline areas, where the chains lie in closest proximity to each other (Ray et al., 2009). The creep depends on the fibre mobility in the stress concentration region. Therefore, closer arrangement of the molecular chains (higher crystallinity) reduces the creep deformation (O´Shaughnessy, 1948).

Fig. 5 shows stress relaxation curves for different load levels. The test rate α and the deformation rate are affect the failure pattern of the fibres and thereby, the relaxation mechanism. Table 3 presents initial modulus of elasticity, finite modulus of elasticity and initial energy of stress relaxation of Ensete fibres for different load levels.

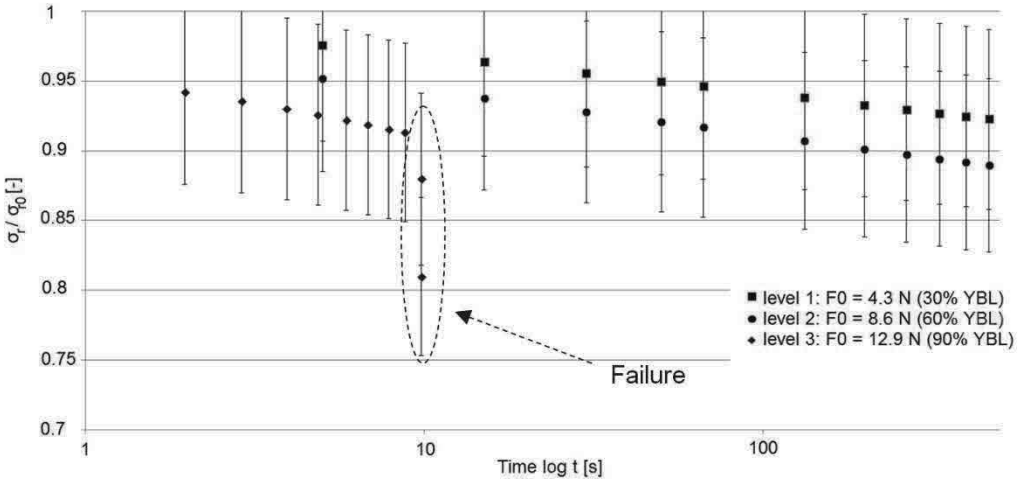

Figure 5. Measured stress relaxation curves of Ensete fibres.

Table 3. Initial modulus of elasticity, finite modulus of elasticity and initial energy of stress relaxation of Ensete fibres

F_0 (N)	E_{Ri} (N tex^{-1})	$E_{R\infty}$ (N tex^{-1})	W_{Ri} (mN tex^{-1})
4.3 (30% YBL)	12.35 ± 3.11	11.13 ± 2.21	5.3667 ± 1.1497
8.6 (60% YBL)	20.64 ± 6.04	17.67 ± 3.68	13.0754 ± 3.2217
12.9 (90% YBL)	17.98 ± 3.97	16.31 ± 3.18	31.7886 ± 5.7811

The stress relaxation curves at 30%, 60% and 90% load levels were given in Fig. 5. The extent of fibre failure accurrence will differ at different strains. On application of stress, physical and chemical rearrangements may occur but on relaxation, the mechanism is only physical. At higher strain levels, the highly fractured portions of the fibre leads to higher relaxation, owing to its physical rearrangement at long duration (Sreekala et al., 2001). The rate of relaxation becomes higher for high strain strain levels at long durations. At very low strain levels, commendable failure of fibre does not happen. In such a system, the relaxation rate will be very low. At very high strain levels, there is also the possibility for a slow relaxation as the failure has already occurred. Nonetheless, a medium-strained fibre passes through complicated failure mechanisms. Hence, the major relaxation takes place and a higher rate will be recorded. From Fig. 5 is vissible, that the general trends are the same for all three, however, maintaining higher strain level brings about higher relaxation. The values of stress relaxation of Ensete fibres are lower than in the case of oil palm fibres. Higher values of stress relaxation reached also the fibres from Jute and Sisal (Gaston et al., 2010).

CONCLUSIONS

The aim of this study was to describe the creep and stress relaxation behaviour of the fibres from the plant false banana *Ensete Ventricosum*. It was ascertained following:

- The average yarn breaking load (YBL) of Ensete fibres after 20 tests was 14.3 ± 1.7 N.
- The short term creep curves of Ensete fibre under tensile stress at different load levels (30% YBL: F_0 = 4.3 N; 60% YBL: F_0 = 8.6N and 90% YBL: F_0 = 12.9 N) were determined. Experimental creep lifetimes for different load levels: 24,311 ± 7 489 s (30% YBL), 1,831 ± 462 s (60% YBL) and 17.6 ± 5.5 s (90% YBL) were determined. Initial modulus of elasticity, finite modulus of elasticity and creep energy at different load levels were also determined.
- The short term stress relaxation curves of Ensete fibre under tensile stress at different strain levels (30% of maximal strain; 60% of maximal strain and 90% maximal strain) for time of 1,000 s were determined. Initial modulus of elasticity, finite modulus of elasticity and initial energy of relaxation of Ensete fibres were also determined.

ACKNOWLEDGEMENT. This paper has been made with the assistance of the grant IGA TF CZU No. 2015:31130/1312/3104.

REFERENCES

Alves, C., Ferrao, P.M.C., Silva, A.J., Reis, L.G., Freitas, M. & Rodrigues, L.B. 2010. Ecodesign of automotive components making use of natural jute fiber composites. *Journal of Cleaner Production* **18**, 313–327.

Aseer, J.R., Sankaranarayanasamy, K., Jayabalan, P., Natarajan, R., Dasan, K.P. 2013. Morphological, Physical and Thermal Properties of Chemically Treated Banana Fiber. *Journal of Natural Fibers* **10**, 365–380.

ASAE S410.1 DEC97. 1998. Moisture measurement of peanut. In: ASAE standards, 45th edition. 560–561.

Blahovec, J. 2008. Agromaterials – study Guide. *Czech University of Life Sciences Prague*, Prague.

Diriba, H.D., Mazancová, J., Rušarová, K. & Havrland, B. 2013. Possibilities and Acceptance of Alternative Energies from Farm Solid Waste Material (Kocho): Case Study from Kembata Tenbaro Zone. *EthiopiaTropentag 2013 International Research on Food Security, Natural Resource Management and Rural Development Agricultural development within the rural-urban continuum*, Gottingen.

Faruk, O., Bledzki, A. K., Fink, H.-P. & Sain, M. 2012. Biocomposites reinforced with natural fibers: 2000–2010. *Progress in Polymer Science* **37**, 1552–1596.

Ferry, J.D. 1961. Viscoelastic Properties of Polymers. *John Wiley and Sons, Inc.*, New York.

Gaston, M.F., Rodriguez, E.S. & Vázquez, A. 2010. Study of the Compaction Behavior of Natural Fiber Reinforcements in Liquid Composite Molding Processes. *The 10th International Conference on Flow Processes in Composite Materials*. Ascona.

Herák, D., Hrabě, P., Kabutey, A., Jaweso, D.E. & Diriba, H.D. 2014. Mechanical behavior of enset (ensete ventricosum) pulp under compression loading – A multipurpose product in Ethiopia. *Journal of Food Process Engineering* **37**, 588–595.

Kalia, S., Thakur, K., Celli, A., Kiechel, M.A., & Schauer, C.L. 2013. Surface modification of plant fibers using environment friendly methods for their application in polymer

composites, textile industry and antimicrobial activities. *Journal of Environmental Chemical Engineering* **1**, 97–112.

Kim, J.H., Lee, H.J., Lee, H.S., Lim, E.J., Imm, J.Y., Suh, H.J. 2012. Physical and sensory characteristics of fibre – enriched sponge cakes made with Opuntia humifusa. *Food Science and Technology* **47**, 478–484.

Kozlowski, R.M. 2012. Handbook of Natural Fibres, 1st Edition, *Woodhead Publishing*, Cambridge.

Lechat, C., Bunsell, A.R. & Davies, P. 2011. Tensile and creep behaviour of polyethylene terephthalate and polyethylene naphthalate fibres. *Journal of Materials Science* **46**, 528–533.

Mattos, H.S. da C. & Chimisso, F.E.G. 2011. Modelling creep tests in HMPE fibres used in ultra-deep-sea mooring ropes. *International Journal of Solids and Structures* **48**, 144–152.

Mizera, Č., Herák, D., Müller, M. & Hrabě, P. 2015. Mechanical behaviour of polymeric composite with fibres of false banana (Ensete ventricosum). *Agronomy Research* **13**, 680–689.

Nurfeta, A., Eik, L.O., Tolera, A. & Sundstol, F. 2008. Chemical composition and in sacco dry matter degradability of different morphological fractions of 10 enset (Ensete ventricosum) varieties. *Animal Feed Science and Technology* **146**, 55–73.

O´Shaughnessy, M.T. 1948. An Experimental Study of the Creep of Rayon. Textile Research Journal 18, 263–280.

Rao, K.M.M., & Rao, K.M. 2007. Extraction and tensile properties of natural fibers: Vakka, date and bamboo. *Composite Structures* **77**, 288–295.

Ray, D., Das, M. & Mitra, D. 2009. Influence of Alkali Treatment on Creep Properties and Crystallininity of Jute Fibres. *BioResources* **4**, 730–739.

Sedlachek, K.M. 1989. The Effect of Hemicelluloses and Cyclic Humidity on the Creep of Single Fibres. *Institute of Paper Science and Technology*, Atlanta.

Silva, F. de A., Chawla, N. & Toledo Filho, R.D. 2008. Tensile behavior of high performance natural (sisal) fibers. *Composites Science and Technology* **68**, 3438–3443.

Sreekala, M.S., Kumaran, M.G. & Thomas, S. 2001. Stress relaxation behaviour in oil palm fibres. *Materials Letters* **50**, 263–273.

Tsehaye, Y. & Kebebew, F. 2006. Diversity and cultural use of Enset (Enset ventricosum (Welw.) Cheesman) in Bonga in situ Conservation Site, Ethiopia. *Ethnobotany Research and Applications* **4**, 147–157.

Vincent, H., Wiersama, J., Kell, S., Fielder, H., Dobbie, S., Castaneda-Alvarez, N.P., Guarino, L., Eastwood, R., Leon, B. & Maxted, N. 2013. A prioritized crop wild relative inventory to help underpin global food security. *Biological Conservation* **167**, 265–275.

Yirmaga, M.T. 2013. Improving the Indigenous Processing of Kocho, an Ethiopian Traditional Fermented Food. *Journal of Nurition and Food Science* **3**, 1–6.

Yemataw, Z., Mohamed, H. & Yeshitla, M. 2013. Assessment of phenotypic variability in Enset (Ensete ventricosum (Welw.) Cheesman) accessions using multivariate analysis. *International Journal of Natural Sciences Research* **7**, 50–59.

Agronomy Research **14**(Sp.1), 1078–1087, 2016

Impact strength behaviour of structural adhesives

M. Müller* and R. Chotěborský

[1]Department of Material Science and Manufacturing Technology, Faculty of Engineering, Czech University of Life Sciences, Kamýcká 129, CZ 165 21 Prague, Czech Republic
*Correspondence: muller@tf.czu.cz

Abstract. A cohesive force at an adhesive bond is one of the limit for a strength of an adhesive bonding. This study is focused on an impact force of an adhesive. Samples without a notch were cast in the casting mould at a laboratory temperature with a normal pressure. The instrumentation microcharpy test equipment was used for the evaluation of the impact force. The samples were tempered at a laboratory temperature, 40 °C and 60 °C. Results showed that the temperature of the specimens influenced the impact strength, the toughness and the maximum deformation of the adhesives. Higher temperature decreased the impact force but it increased the toughness. The hardness Shore D of commercial filled two-component epoxies is comparable. A non-homogeneity of adhesives distinguished for a porosity was found by the investigation of a fracture surface.

Keyword: Deformation, hardness, impact force, impact energy, microcharpy test, temperature.

INTRODUCTION

The production process in various industrial sectors divers, but it usually has one common element and that is forming a bond (Müller, 2011). One of important requirements is, that the products have to reach a sufficient resistance to the dynamic load (Hayashida et al., 2015).

A promising method of creating the bond is the adhesive bonding technology. This technology is often used as a complementary method of joining (Müller, 2013).

According to Messler (2004), the bonding is a process of joining materials with the aid of acting of a chemical agent which is able to keep together these materials via surface attractive forces. Materials which are joined are called adherents, while the bonding factor is an adhesive. The forces, which allow the surface attraction, arise from one or more sources, mostly chemical, but some may be mechanical or even electrostatic. These forces give rise to that what is called an adhesion, i.e. bonding of different materials together (Messler, 2004). The adhesive layer forms the cohesive strength. A summary of forces can be considered as the cohesion. They bind the adhesive particles to each other by a valence mutual action and molecular forces of an attraction (Müller, 2013).

The environmental temperature is a significant factor which influences the behaviour of the adhesive, i.e. polymer (Müller & Valášek, 2012; Messler, 2004). An effective application of adhesive bonds depends also on their resistance to an effect of

different temperatures. This means, that their ability to retain their properties during the long-term exposure to increased or decreased temperature is significant for the practical application.

It is not possible to perform a general evaluation of the temperature influence on the adhesive strength and adhesive bonds. The critical decrease of the strength of all adhesives is usually in the range from 60 to 100 °C (Messler, 2004). Hu et al. (2013) discovered, that the long-term exposure of adhesive bonds to increased temperature causes a decrease in the strength.

The temperature is a significant factor which affects the mechanical properties of the adhesive. Influencing of the adhesive occurs already during a storage, a transportation or an application on the adhesive bonded material (Valášek & Müller, 2015). The impact resistance is another significant limit of the effective application of adhesive bonds.

In spite of the increasing use of adhesives in the aircraft and automotive industries the crashworthiness of structures joined with adhesives is still a challenging subject.

Following considerations are made for adhesive bonded structures:

- The impact performance of the bond and whether it is different from the quasi-static performance.
- The capability of any energy absorption of the adhesives can contribute to the impacted system.
- Understanding of the impact loading of the bonds so that they can be designed for such conditions (Hayashida et al., 2015).

There are several dynamic tests enable to simulate the impact force. These dynamics tests are mainly based on the principle of tests according to Izod and Charpy.

Adhesives are sensitive to the dynamic loading and it is proved that the strength decreases with the temperature (Adamvalli & Parameswaran, 2008).

The adhesives filled with a filler are used in the automotive industry. The reason is particularly the decrease of a price and the increase of the impact strength (Valášek & Müller, 2015).

A substantial change in mechanical properties can be achieved by adding an optimum volume of the filler i.e. the reinforcement (Kahramana et al., 2008). Optimum utility properties of these composites are limited primarily by a risk of a cohesive failure caused by an improper amount and the material of the filler.

Composites can include a reinforcing phase in various sizes. The reinforcement in a form of hard and thermodynamically stable chemical compounds produced primarily as a filler is used for particle composites.

The addition of fillers to the epoxy adhesive does not produce a definite improvement or deterioration in the impact strength according to the research of various authors. E.g. Dadfar & Ghadami (2013) indicate an improvement in the toughness due to the increased content of the rubber modifier. Furthermore, the addition of aluminium oxide fillers has on the contrary a negative effect (Kejval & Müller, 2013).

Another feasible method for the elimination of the brittleness of polymers (reactoplastics) is the waste utilization from the process of tyre recovery (Müller, 2015).

The polyamide fibres from the process of the tyres recovery are recommended to remove the brittleness of the materials (Parres et al., 2009). This assumption was

certified within the research. The impact strength significantly increased when adding the filler.

The aim of this research was to evaluate mechanical properties of structural adhesives used in the automotive industry.

MATERIALS AND METHODS

As adhesives two-component, epoxy and methylmetacrylate based adhesives especially developed for the body shop were used. The adhesives are used in the car to increase the operation durability and the body car stiffness. As a matter of the fact following adhesives which were hardened at increased temperature according to requirements of the producer were used:

- Bison metal epoxy (marked BM) – Two-component epoxy adhesive filled with metal microparticles, temperature range -60 to 100 °C.
- Alteco 3 Ton epoxy adhesive (marked A30M) – Two-component epoxy adhesive filled with metal microparticles, temperature range -20 to 120 °C.
- Alteco 3 Ton quick adhesive (marked A4M) – Two-component epoxy adhesive filled with metal microparticles, temperature range -20 to 120 °C.
- Perma oxy 5 minutes (marked PA) – Two-component methylmetacrylate adhesive, temperature range -50 to 120 °C.

Mechanical properties of adhesives evaluated in this paper were – impact force, elongation, hardness.

The experimental procedure of the microcharpy test contains a few steps: Making samples of the microcharpy type – width 5 mm, height 5 mm and length 27 mm, specimens for the impact test are without a notch. The samples were cast in a casting mould which was made from Lukapren N.

Samples without the notch were cast in the casting mould at a laboratory temperature with a normal pressure. The instrumentation microcharpy test equipment was used for the evaluation of the impact force. The samples were tempered at laboratory temperature 22 ± 2 °C, 40 ± 2 °C and 60 ± 2 °C. Test specimens were tempered for 60 minutes to achieve required temperature in the laboratory chamber Memmert UF55 before own testing process.

Instrumented microcharpy tester (Fig. 1) with the nominal energy 25 J was used for the evaluation of the impact force and the impact toughness of adhesives. An instrumental edge with a semiconductor strain gauge was jointed to PCI 1716 card with a maximum samples rate 200k per second (Advantech Company), the software was developed with using Microsoft Visual Basic Express 2010.

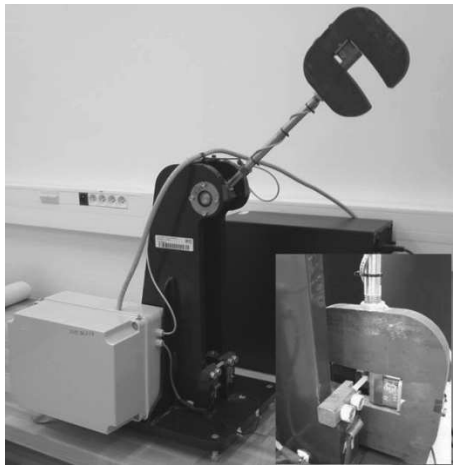

Figure 1. Instrumented Microcharpy test.

The impact energy was determined from discrete output data. The deflection was calculated from Eq. 1:

$$s(t) = v_0.t - \frac{L_p.g}{M_H}\int_0^{t_1}\int_0^{t} F(t)dtdt_1 \quad (1)$$

where: v_0 – impact velocity (m s^{-1}); t – time after impact (s) when deflection is calculated; L_p – length of pendulum (m); M_H – horizontal pendulum moment (N.m); $F(t$ – force (N) at time after impact; $s(t)$ – deflection of sample (m) at time after impact; g – gravitation accelerate (m s^{-2}).

The impact energy (W) was calculated from Eq. 2:

$$W = \sum_{i=0}^{t}\left(\frac{F_i + F_{i+1}}{2}\right).(s_{i+1} - s_i) \quad (2)$$

where: W – impact energy (J); F – force (N); s – deflection (m); t – time (s).

Five samples were used for each of the temperature. Their mean value is presented in the results.

Hardness SHORE D: The material hardness was measured by Shore D i.e. by pressing the tip of the instrument durometer Shito HT. The hardness SHORE D was measured according to the standard CSN EN ISO 868. Test specimens were 5 mm high.

The statistical survey was used for the evaluation – ANOVA F-test in the level of significance $\alpha = 0.05$. As the null hypothesis H_0 it was determined the state, when there is not a statistically significant difference among each comparing data sets in term of their mean values: $p > 0.05$. A coefficient of the variation is defined as a ratio of the standard deviation and the arithmetic mean.

RESULTS AND DISCUSSION

The results focused on the evaluation of the impact force are evident in Fig. 2. The coefficient of the variation among particular tested adhesives at the evaluation of the impact force was in the interval from 1.5 to 18.0%.

It can be stated on the basis of the statistical testing that tested adhesives are statistically non-homogeneous, i.e. there is a difference among tested temperatures which have the influence on the impact force. For adhesives A4M $p = 0.0318$, A30M $p = 0.0000$, BM $p = 0.0023$ and PA $p = 0.0046$. The hypothesis H_0 was not confirmed, i.e. there is a difference in the level of significance 0.05 among particular tested temperatures 20, 40 and 60 °C.

An increase of the average value of the impact force was measured at the temperature 40 °C for adhesives A4M, BM and PA. All adhesives showed a decrease of the impact force at the temperature 60 °C. There was a decrease in the impact force for the adhesive BM due to the increased temperature.

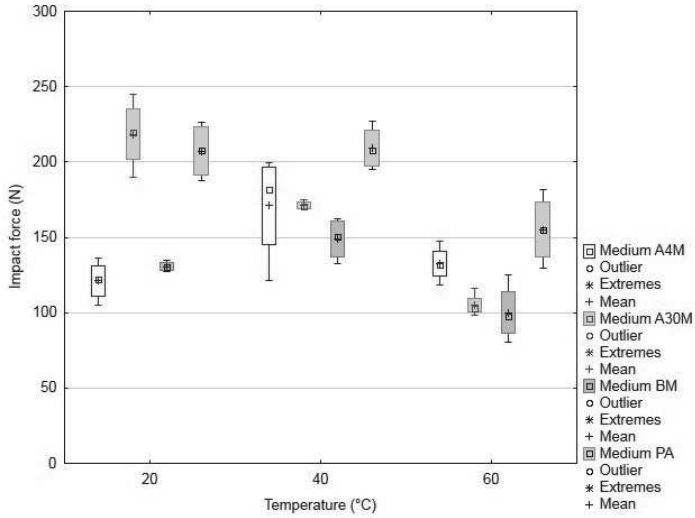

Figure 2. Effect of environmental temperature on impact force for tested adhesives.

Results of the tests focused on the evaluation of the impact energy are evident from Fig. 3. The coefficient of the variation for particular tested adhesives during the evaluation of the impact energy ranged in the interval 7.2 to 23.1%.

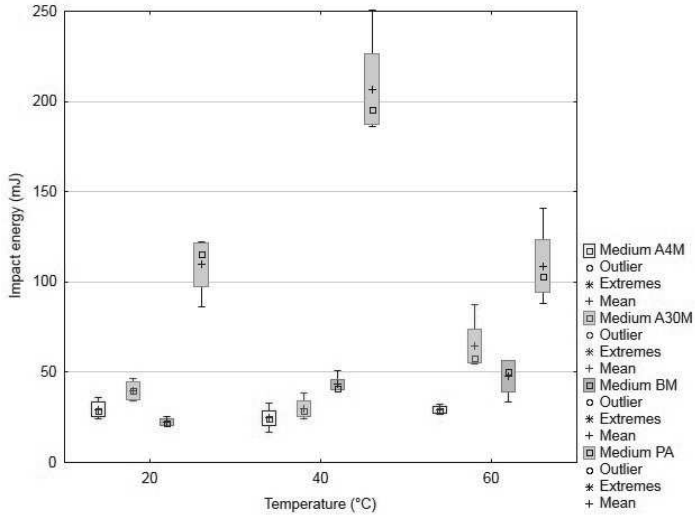

Figure 3. Effect of environmental temperature on impact energy of tested adhesives.

It can be stated from the statistical survey point of view that adhesives A30M, BM and PA are non-homogeneous, i.e. there is a difference among tested temperatures influencing the impact energy. For adhesives A30M $p = 0.0029$, BM $p = 0.0015$ and PA $p = 0.0003$. The hypothesis H_0 was not confirmed, i.e. there is a difference in the level of significance 0.05 among particular temperatures 20, 40 and 60 °C.

The difference in the impact energy due to the different temperature was not statistically proved for the adhesive A4M ($p = 0.3711$). The hypothesis H_0 was confirmed, i.e. there is not a difference in the level of significance 0.05 among particular tested temperatures 20, 40 and 60 °C. It is possible to state with a respect to the statistical testing that tested adhesives are statistically homogeneous groups.

The increase of values of the impact energy was measured for adhesives A30M, A4M and BM due to the effect of the temperature. The increase of the impact energy was measured for the adhesive PA (methylmetacrylate adhesive) at the temperature 40 °C and a subsequent decrease followed at the temperature 60 °C.

Tested samples evince a behaviour common for the brittle material, i.e. reactoplastics at the laboratory temperature and at the temperature 40 °. Spreading of an unstable crack propagation in a cross-section of the sample occurred after reaching the maximum impact force. There was an increase of deformation values in the interval from 47 to 80% for the testing temperature 60 °C (for tested adhesives with the filler, i.e. A4M and A30). There was also a significant decrease of values of the impact force.

There is evident an effect of the impact force and the time of different tested adhesives in the Figs 4, 5, 6 and 7. The laminating is also evident in particular layers of the tested sample from the progress of the graphic dependence visible from Figs 4, 5, 6 and 7. After the failure of one layer the following layer deforms until the failure occurs in the whole cross-section. It is possible to characterise the whole process as a failure of first layer distinguished by a decrease and subsequent increase of the impact force in the deflection. This state repeats until reaching the local maximum. A typical course of given dependence is presented in Figs 6 and 7.

The significance of the temperature factor at the application of the adhesive bonds was certified (Messler, 2004). Increased temperature influences not only the fall of the adhesive strength, but it also decreases the impact force (Hu et al., 2013). The conclusions of authors Müller et al. (2015) on the sensitivity of adhesives to the dynamic loading were also confirmed. It is also possible to agree with their results stating that the force decreases owing to the increased temperature (Adamvalli & Parameswaran, 2008).

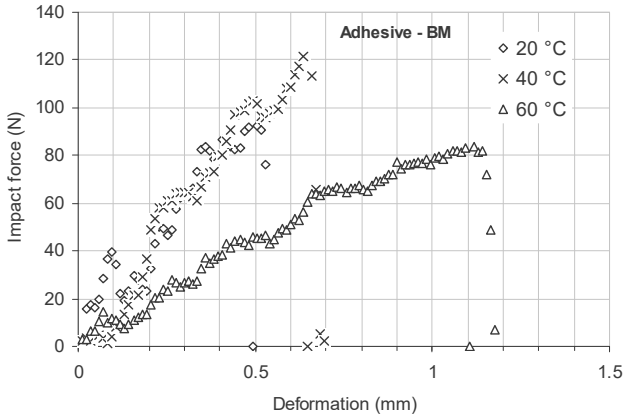

Figure 4. Dependence between impact force and deflection of tested adhesive BM at various temperatures.

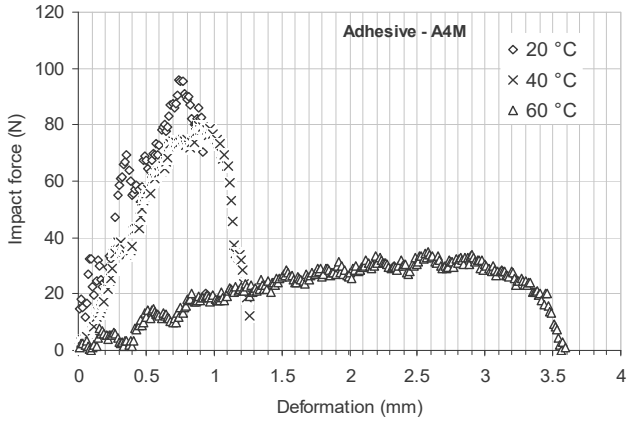

Figure 5. Dependence between impact force and deflection of tested adhesive A4M at various temperatures.

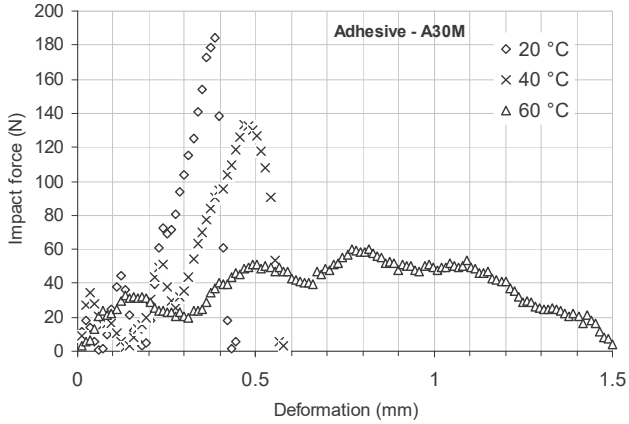

Figure 6. Dependence between impact force and deflection of tested adhesive A30M at various temperatures.

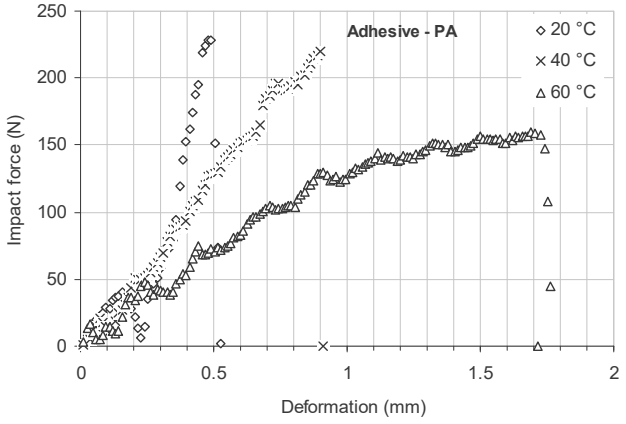

Figure 7. Dependence between impact force and deflection of tested adhesive PA at various temperatures.

The results of this experiment confirmed the assumption that the decrease of mechanical properties of adhesive bonds occurs with the increasing temperature, i.e. mainly the decrease of the strength of the adhesive bond occurs. The instrumental Charpy test has shown that the comparison of adhesives from the point of view of values of the impact energy can be deceptive. But if it is compared with the impact strength, we can obtain significant data for an engineering.

Fig. 8 shows the results of the adhesive hardness measured at the laboratory temperature 20 °C. Two-component epoxy adhesives (A30M, A4M and BM) reached higher values of the hardness Shore D comparing to the methylmetacrylate adhesive PA. The difference was 41.3 to 43.4%. The reason is, that two-component epoxy adhesives are filled with filler.

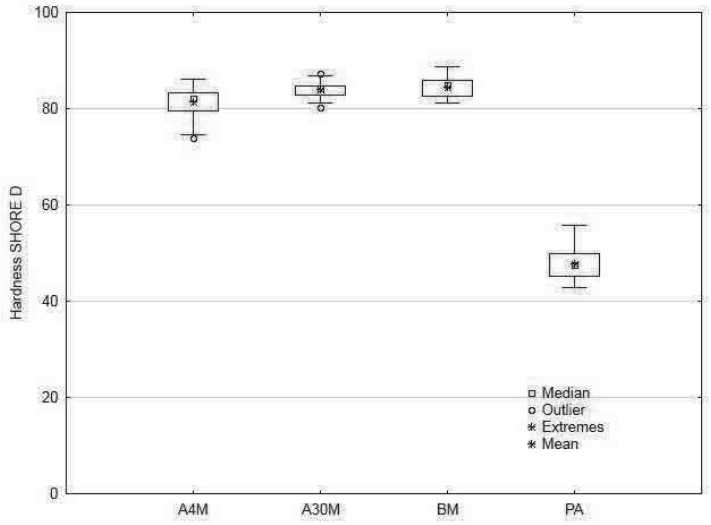

Figure 8. Hardness of tested adhesives at laboratory temperature.

When comparing the results of the hardness Shore D and the impact force it is apparent, that the adhesive with smaller hardness reached higher values of the impact strength. Similar results were observed also when adhesives were tested on the machine Dynstat characterized by an analogous principle of testing as according to Charpy.

Considering the higher complexity of the failure process during the Charpy test of adhesives the scanning electron microscopy was used in the fracture surface. From the picture of the fracture surface of the filled two-component epoxy adhesive it is possible to indicate a correct connection between the adhesive and the filler (Figs 9 and 10). It was found, that the fracture surface is rough and irregular. Also the non-homogeneity of the adhesive, which is distinguished for its spherical shape, is evident from the fracture surface. These are air bubbles which came into being during a process of mixing of the two-component epoxy adhesive and during a curing process (Fig. 9).

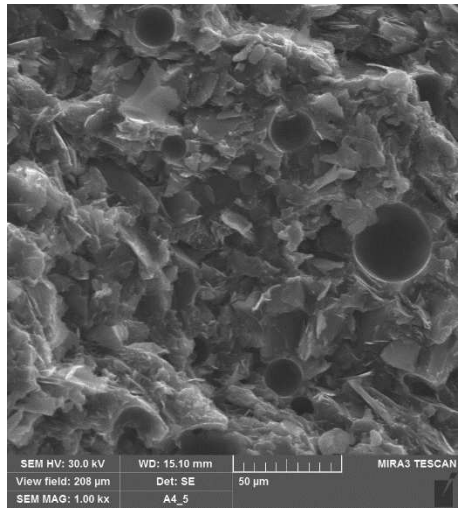

Figure 9. Fracture surface of sample – adhesive A30M, secondary electrons.

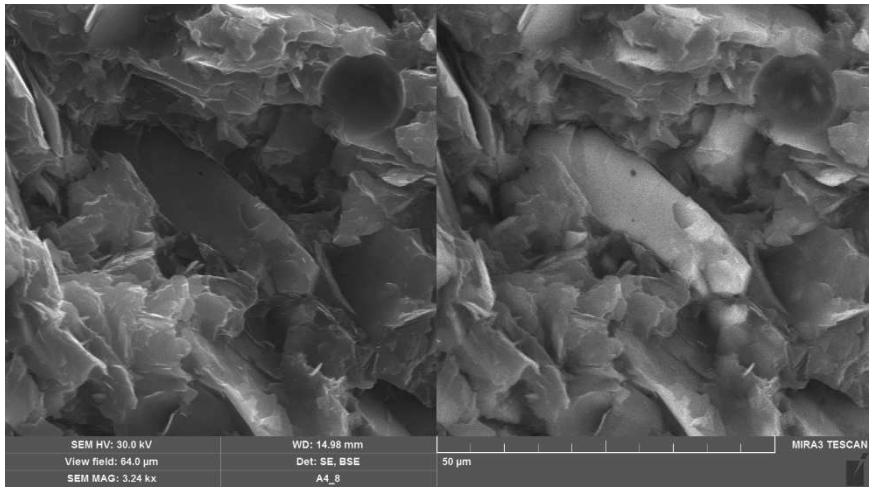

Figure 10. Fracture surface of sample – adhesive A4M, left-secondary electrons, right-back scattered electrons.

CONCLUSIONS

Results of measurements were obtained at the device Microcharpy test which is visible in Fig. 1. It is a suitable method for a characterisation of the dynamic loading of adhesives. It is possible to state these conclusions on the basis of obtained data:

- results showed that the temperature of the specimens influenced the impact force, the toughness and the maximum deformation of the adhesives. Higher temperature decreased the impact force but it increased the toughness. This result should be taken in account at the structure, i.e. in the real application of adhesive bonds,
- the hardness Shore D of commercial filled two-component epoxies is comparable,

- the non-homogeneity of adhesives distinguished for a porosity was found by the investigation of the fracture surface.

ACKNOWLEDGEMENT. Supported by Internal grant agency of Faculty of Engineering, Czech University of Life Sciences in Prague (Research on mechanical properties of multi-component polymer systems during their preparation, processing and application).

REFERENCES

Adamvalli, M. & Parameswaran, V. 2008. Dynamic strength of adhesive single lap joints at high temperature. *International Journal of Adhesion & Adhesives* **28**, 321–327.

Dadfar, M.R. & Ghadami, F. 2013. Effect of rubber modification on fracture toughness properties of glass reinforced hot cured epoxy. *Materials and Design* **47**, 16–20.

Hayashida, S., Sugaya, T., Kuramoto, S., Sato, Ch., Mihara, A. & Onumac, T. 2015. Impact strength of joints bonded with high-strength pressure-sensitive adhesive. *International Journal of Adhesion and Adhesives* **56**, 61–72.

Hu, P., Han, X. Li, W.D., Li, L. & Shao, Q. 2013. Research on the static strength performace of adhesive single lap joints subjected to extreme temperature environment for automotive industry. *International Journal of Adhesion and Adhesives* **41**, 119–126.

Kahramana, R., Sunarb, M. & Yilbas, B. 2008. Influence of adhesive thickness and filler content on the mechanical performance of aluminium single-lap joints bonded with aluminium powder filled epoxy adhesive. *Journal of materials processing technology* **205**, 183–189.

Kejval, J. & Müller, M. 2013. Mechanical properties of multi-component polymeric composite with particles of Al2O3/SiC. *Scienty Agriculturae Bohemica* **44**(4), 237–242.

Messler, R.W. 2004. Joining *of materials and structures from pragmatic process to enabling technology*. Burlington: Elsevier, 790 pp.

Müller, M. 2011. Influence of surface integrity on bonding process. *Research in Agricultural Engineering* **57**(4), 153–162.

Müller, M. 2013. Research of renovation possibility of machine tools damage by adhesive bonding technology. *Manufacturing Technology* **13**(4), 504–509.

Müller, M. 2015. Hybrid composite materials on basis of reactoplastic matrix reinforced with textile fibres from process of tyres recyclation. *Agronomy Research*, **13**(3), 700–708.

Müller, M. & Valášek, P. 2013. The logistics aspects influencing the resultant strength of adhesives at practical application. *Agronomy Research* **12**(1), 285–290.

Müller, M. & Valášek, P. 2012. Abrasive wear effect on Polyethylene, Polyamide 6 and polymeric particle composites. *Manufacturing Technology* **12**(12), 55–59.

Müller, M., Cidlina, J., Dědičová, K. & Krofová, A. 2015. Mechanical properties of polymeric composite based on aluminium microparticles. *Manufacturing Technology* **15**(4), 624–628.

Parres, F., Crespo-Amorós, J.E. & Nadal-Gisbert, A. 2009. Mechanical properties analysis of plaster reinforced with fiber and microfiber obtained from shredded tires. *Construction and Building Materials* **23**, 3182–3188.

Valášek, P. & Müller, M. 2015. Properties of adhesives used for connecting in automotive industry. *Manufacturing Technology* **15**(2), 232–237.

Agronomy Research **14**(Sp.1), 1088–1098, 2016

Electrical field based detection of fruits and vegetables for robotized horticulture

V. Osadcuks* and A. Pecka

Latvia University of Agriculture, Faculty of Engineering, Department of Energetics, Cakstes blvd. 5, LV-3001 Jelgava, Latvia; *Correspondence: vtl@tvnet.lv

Abstract. In this research authors study possibilities of using transmitting-type electric field based sensors for recognition of fruits and vegetables. The main idea is to detect distortions of electrical field between electrodes of sensors by measuring capacitance changes for these electrodes. Electrical field is strongly affected by relative permittivity of medium, which is several times larger for fruits and vegetables consisting mainly of water than for surrounding air, leaves and other low-mass non-conductive objects. This could help to develop electrical field sensing device with number of electrodes for detection of fruits or vegetables and determining their position thus serving as additional sensor in multi sensor system with optical camera or as stand alone device. The research covers both theoretical aspect of proposed approach and experimental evaluation of prototype device based on mixed signal controller MGC3130 originally intended for electrical field based gesture sensing periphery for consumer electronics. Main results show that in worst condition when an electrode is fully covered with a physical model of leaf 43% of signal value in comparison to sensor output without obstacle is still usable. Thus this type of sensors potentially can be an integral part of complex fruit or vegetable recognition system in robotized horticulture applications.

Key words: electrical field, sensor, horticulture, fruit and vegetable recognition.

INTRODUCTION

Reliable, fast and energy-efficient recognition and determination of spatial position and orientation of fruits and vegetables is one of key tasks for agricultural robots to be technically and economically efficient in precision application of plant protection products and harvesting tasks. In majority of experimental agricultural robots prototypes and solutions this task is accomplished by using computer vision systems in various spectral ranges. Main drawbacks of this approach are computational power and recognition speed tradeoffs, sensitivity to changes in ambient lighting, necessity of readjustment for various species and even degrees of ripeness, difficulties to recognize objects of interest in heavy foliage and affection by atmospheric conditions (for, rain, dust etc.) (Cohen et al., 2011) as well as difficulties to select proper recognition algorithm for these changing conditions (Fernández et al., 2014).

Capacitive sensing is used very widely nowadays. Beginning from automation applications in industrial environment (Taghinezhad et al., 2012) to power saving using human body detection in appliances and smart homes and consumer electronics (Villiers, 2012) with focus on various types of HMI.

Mainly there are three modes of capacitive sensing: loading mode, shunt mode and transmit mode, in this study the latter one is used, which gives the longest sensing range. Transmit mode uses a transmitting electrode that is coupled to a conductive object. The properties of an alternating electric field generated with respect to a receiving electrode will therefore depend on the distance of this body, thus extending the achievable range (Smith, 1996; Brauna et al., 2015).

This type of sensing technology could hypothetically substitute or supplement computer vision based sensors in situations where they fail to recognize fruit or vegetable under canopy, in adverse conditions for optical systems or when processing power and optical equipment necessary for successful completion of the task makes them economically and practically ineffective. Electrical field is strongly affected by relative permittivity of medium, which is several times larger for fruits and vegetables consisting mainly of water than for surrounding air, leaves and other low-mass non-conductive objects. This could help to develop electrical field sensing device with number of electrodes for detection of fruits or vegetables and determining their position.

The aim of the study is to find if it is practically possible to use transmitter-receiver type electrical field based sensor for detection and position measurement of fruits and vegetables under cover by surrounding canopy.

In this study authors use integrated mixed signal chip manufactured by Microchip Inc. MGC3130 which uses manufacturers proprietary GestIC technology to give the proof of concept for near E-field sensing of vegetables and fruits in robotized horticulture applications. The experiments consisted of positioning a detectable object over the sensor with and without obstacles and measuring field strength. Positioning was automated using V-plotter type CNC machine.

MATERIALS AND METHODS

Equivalent circuit for MGC3130 chip based E-field sensing electrode system is given in Fig. 1. It consists of transmitting and receiving electrodes E_{Tx}, E_{Rx}, ground plane, capacitances between electrodes and ground plane, transmitting driver and receiving buffer.

The sensing system operates by measuring voltage on capacitance voltage divider formed by C_{RxTx}, C_L as upper side and C_{RxG}, C_{Obj}, C_{Buf} as lower side. Transmitter provides square wave signal U_{Tx} at frequencies 44–115 kHz (can be changed depending on external noise conditions) to transmitting electrode, and after division it is measured at receiver as U_{Rx}. Magnitude of signal can be expressed according to voltage divider equation (1) (Microchip Inc., 2013a).

$$U_{Rx} = \frac{U_{Tx}}{1 + \frac{C_{RxG} + C_{Buf} + C_{Obj}}{C_{RxTx} + C_L}}. \quad (1)$$

When there is no object in vicinity C_{Obj} approaches to zero. Receiver should be capable to detect voltage changes on divider when object distorts electrical field and changes C_{Obj}. Because input buffer load is too high to measure U_{Rx} voltage directly without specific parameterisation procedures, receiver simply measures the difference

of signal ΔS when $C_{Obj} = 0$ and when it changes assuming that C_{Obj} is much smaller than electrode mutual and ground capacitances (Microchip Inc., 2013a):

$$\Delta S = U_{Rx}\left(C_{Obj} = 0\right) - U_{Rx}\left(C_{Obj} > 0\right) = \\ = \frac{U_{Tx} C_{Obj}}{C_{RxTx} + C_L + 2\left(C_{RxG} + C_{Buf}\right) + \frac{\left(C_{RxG} + C_{Buf}\right)^2}{C_{RxTx} + C_L}}. \quad (2)$$

Signal value when $C_{Obj} = 0$ is obtained by reading and storing U_{Rx} when there is no object in vicinity, thus calibration is performed.

End signal after amplification and preprocessing which is carried out by MGC3130 built-in DSP is defined as signal deviation S_D, which relates to gain of 10 times, measurement voltage range of 3 V and half of ADC resolution and is given as 16 bit signed dimensionless integer value (Microchip Inc., 2013a):

$$S_D = 10 \cdot \frac{2^{15}}{3\text{V}} \Delta S . \quad (3)$$

This value is used as signal relative strength in measurements of object's approach to the sensor.

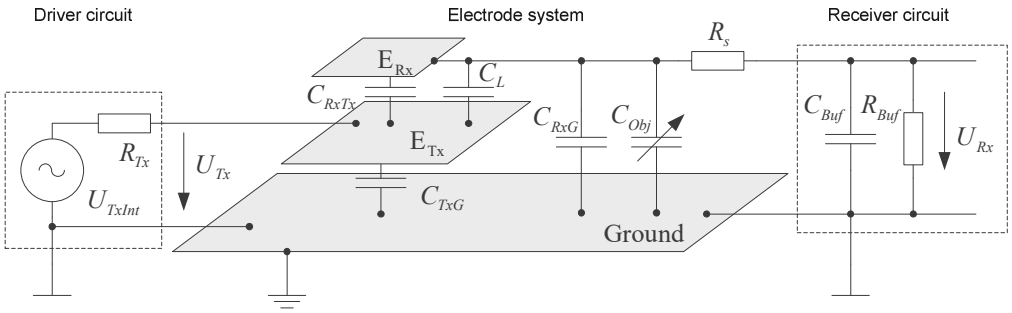

Figure 1. Equivalent circuit of single electrode and MGC3130 output driver and inpud buffer: E_{Rx} – receiver electrode; E_{Tx} – transmitter electrode; U_{TxInt} – internal transmitter signal; U_{Tx} – signal on driver's output pin; U_{Rx} – received signal; R_{Tx} – driver source resistance; R_{Buf} – resistance of MGC3130 input buffer; R_s – series resistance between E_{Rx} and MGC3130 input pin, can be increased for high frequency noise suppression (1 kΩ on evaluation board); C_{TxG} – capacitance from transmitter to ground; C_{RxTx} – capacitance between E_{Tx} and E_{Rx} electrodes; C_L – receivers interconnection wire's capacitance to transmitter electrode; C_{RxG} – capacitance from receiver to ground; C_{Obj} – capacitance between sensed object and ground; C_{Buf} – capacitance of MGC3130 input buffer (Microchip Inc., 2013a).

In experiments MGC3130 Sabrewing evaluation board was used, which has 5 electrodes, E-field sensing chip and USB interface for connection to PC (Microchip Inc., 2013b), physical configuration and dimensions of electrodes are given in Fig. 2.

The electrode system is built in 4-layer 1.5 mm receiving electrode on top of the stacks, transmitting electrode and interconnection wires for receivers at 3rd layer and ground plane at the bottom layer. Transmitting electrode is formed as mesh and covers

all board's sensing area. Receiving electrodes at the edges of board are made as solid copper, but large centre electrode is formed as a mesh in order to make signal level approximately equal to those on edges of sensor board. Interconnection wires between receivers are built in between transmitter wiring in 3rd layer thus improving noise immunity.

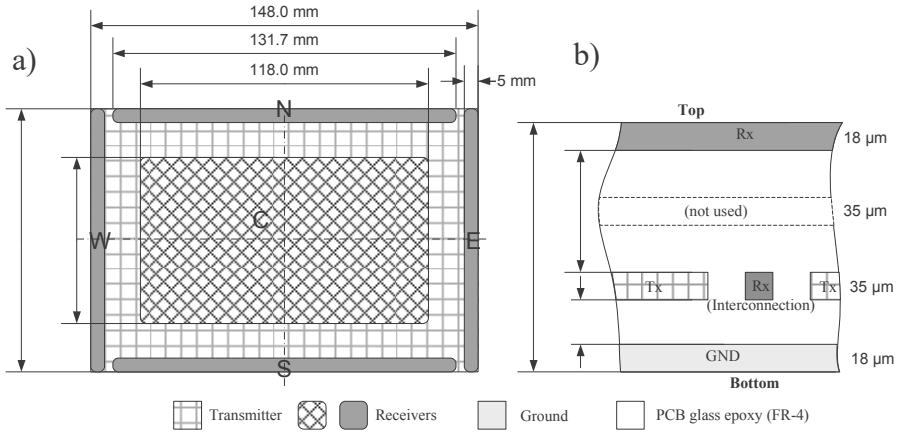

Figure 2. Physical configuration and dimensions of electrodes in evaluation board: a – top view (ground plane not seen); b – cross section of PCB layers (Microchip Inc., 2013b).

Experimental setup (Fig. 3) consists of sensor (GestIC evaluation board), CNC positioning mechanism and controlling computer with two interfaces for sensor and motor control running ungrounded on batteries. Grounded shielding plate is placed under the sensor board. Arrangement of the setup was chosen to minimise unwanted electrical fields and charge build-ups on sensed object.

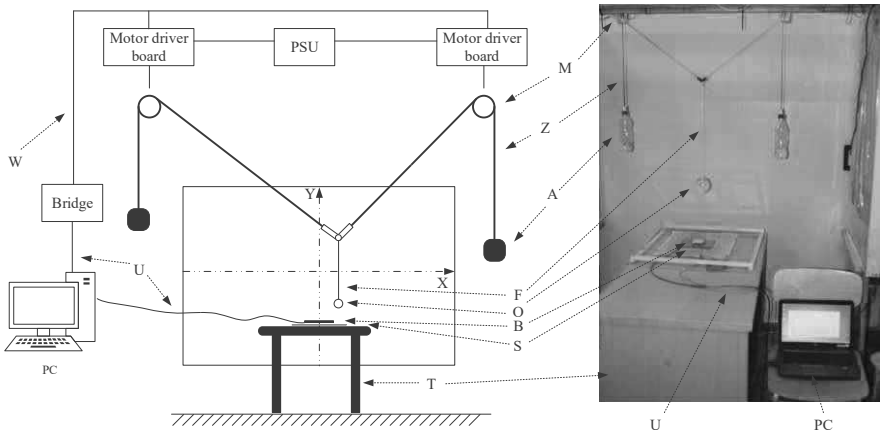

Figure 3. Experimental setup: A – balance weight; B – evaluation board; F – fishing lines; M – steper motor; O – object to sense; S – ground shield; T – table; U – USB cable; W – UART cable; Z – toothed belts.

Plastic sphere with 80 mm external diameter filled with mains water was used as a detectable object. Total mass of plastic – 32 g, water – 230 g. Positioning precision for all experiments was 0.5 mm.

Three types of experiments with approaching object were performed (see Fig. 4). The detectable object was moved near to and away from the sensor by 0.5 mm for vertical and 0.2 mm steps for horizontal movement every 100 ms. Step size and time was chosen to minimise unwanted oscillations of sphere due to its inertia. Signal deviation signal for all electrodes was measured before each step. MGC3130 chip can perform and report up to 200 measurements per second thus experimental data is fully static.

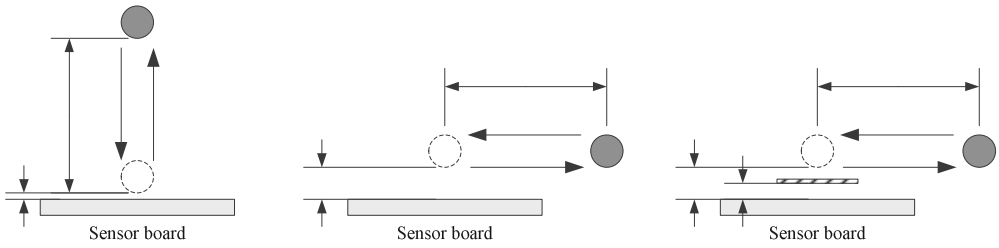

Figure 4. Types of experiments: a – object approaching from top; b – object approaching from side; c – object approaching from side with obstacle between detectable object and sensor.

Experiment 'a' was intended to evaluate signal produced by approaching object at various distances. Starting position for object was 201 mm above sensor i.e. distance between sensor and bottom of the sphere. Then sphere was moved down (direction D1) down to 1 mm above sensor then back up to the same position (direction D2) thus performing one test run.

At the same time during the experiment type 'a' influence of sensing frequency was evaluated. As external noise was minimum during experiments (see the Results section), significant differences in sensing distances for various operating frequencies were not observed. Therefore all available frequencies (44 kHz, 67 kHz, 88 kHz, 103 kHz and 115 kHz) were allowed for MGC3130 to automatically select to minimize existing external noise effect during rest of the experiments.

Experiments 'b' and 'c' were performed at constant distance between sensor and object – 21 mm to compare performance of object sensing with and without obstacles.

Obstacle in experiment 'c' was placed to demonstrate possible system performance in real life situation when detectable object (fruit or vegetable) is covered by plant's canopy. To model obstacle – plant's leave with some content of water and non-transparent, standard 80 g m^{-2} office paper sheet was saturated with mains water and placed in hermetic plastic bag to prevent evaporation. Two sizes of sheets were used: 60 x 60 mm and 120 x 70 mm, sheets were placed at 10 mm distance at the centre of the sensor board. Sizes were selected to cover Centre electrode partially and fully and to approximately reflect typical dimensions of plant leaves. Fishing lines were used to position paper sheets to minimise influence on sensor.

In experiment ‘a’ for signal strength measurement 12 test runs were performed; and one test run for each measurement frequency (5 in total). For each experiment ‘b’ and ‘c’ 4 test runs were made.

Calibration of signal (measurement of ambient signal without test object in vicinity) was carried out before each test run in direction D1. With exceptions for experiment ‘c’ where calibration was done without obstacle prior to all test runs to avoid calibrating on obstacle’s distortions in E-field.

RESULTS AND DISCUSSION

Results of the experiments as S_D signals as functions of distance from detectable object to sensor are presented in Figs 5–12. Detectable object movement from and to sensor is shown in separate graphs and the object’s closest point to the sensor (1 mm above sensor for experiment ‘a’ and 21 mm above in the centre position of sensor for experiments ‘b’ and ‘c’) is shown on both graphs.

For vertical object approach (Fig. 5) it can be seen that S_D is increasing exponentially and object’s presence can be detected already at distance of 90 mm where it rises over noise RMS level 5.6 without object in vicinity (dashed line).

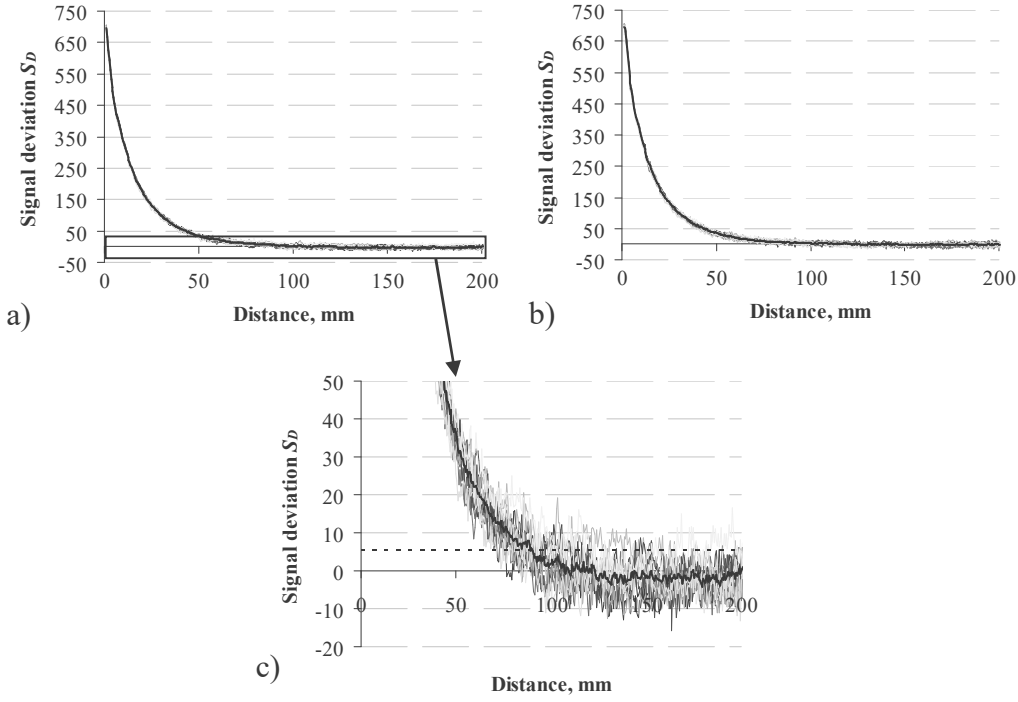

Figure 5. Results of experiment ‘a’ for centre electrode, 12 runs and average line in bold: a – direction D1 (moving to sensor); b – direction D2 (moving away from sensor); c – zoom of detection signal area.

Electrodes on the edges of the sensor were also affected, which is shown on distance's logarithmic scale for better visibility in Fig. 6. As the object approaches S_D for edge electrodes at first increased then started to fall below noise level, the explanation could be that object with larger than air permittivity attracted majority of electrical field lines. Thus field strength over edges of the sensors and consequently received signal U_{Rx} felt.

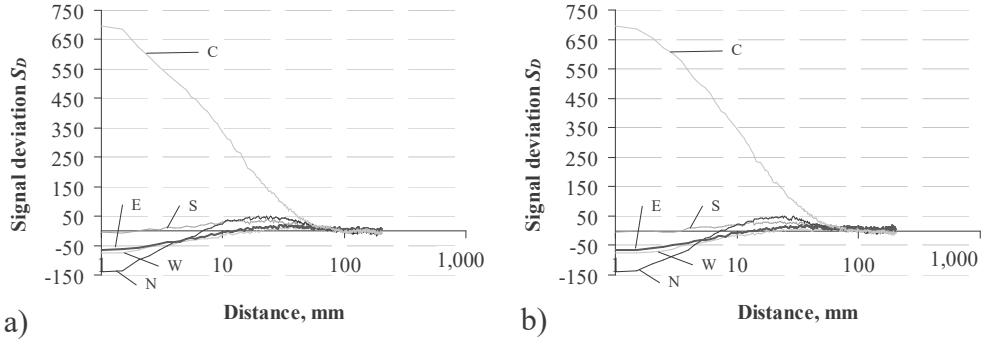

Figure 6. Results of a single run in experiment 'a' for all electrodes (in logartihmic scale): a – direction D1; b – direction D2.

Altogh effect of signal frequency was insignificant (Fig. 7) a trend could be observed that signal strength slightly increases proportionally to frequency. This can be better seen at close distances, and frequency has no effect on noise level when there is no object nearby.

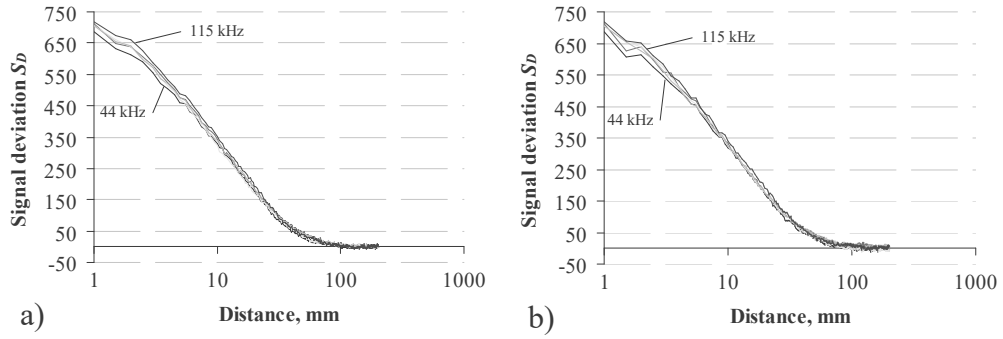

Figure 7. Effect of transmitting signal frequency for experiment 'a' (in logartihmic scale): a – direction D1; b – direction D2.

Experiment ‘b’ (see Fig. 8 for average values of center electrode and 9 for a single run and all electrodes) demonstrates performance of sensor in a fixed height over sensor and approachment of the object form electrode E side.

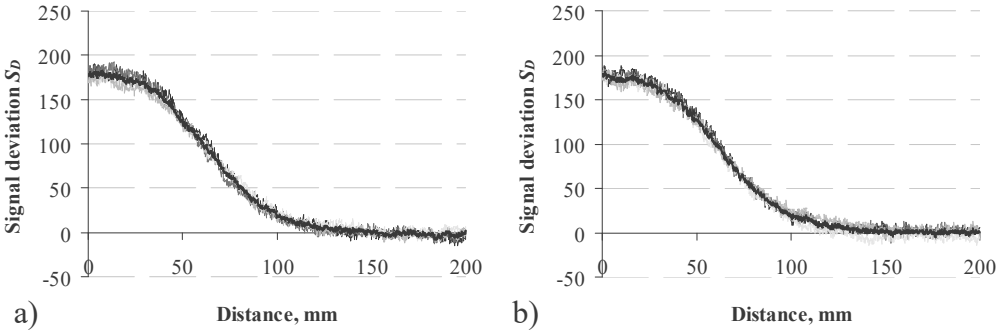

Figure 8. Results of experiment ‘b’, 4 runs and average line in bold: a – direction D1; b – direction D2.

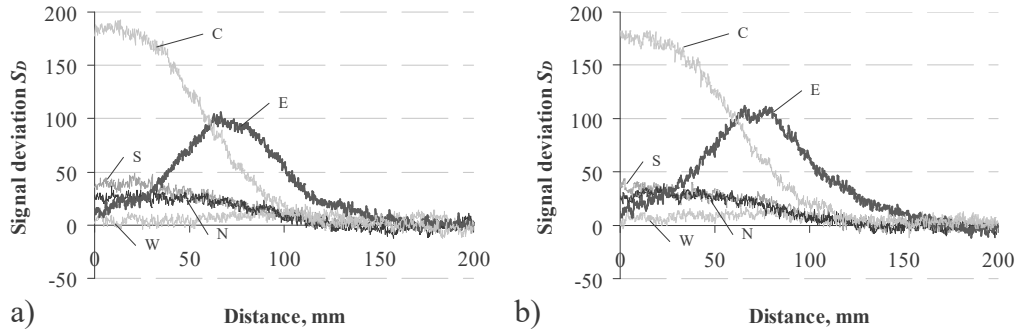

Figure 9. Results of a single run in experiment ‘b’ for all electrodes: a – direction D1; b – direction D2.

Graph for all elctrodes shows how signals are changing when the detectable object passes over. Sequential change in signal levels allows to determine position of the masss centre of the object. In original application of the sensor board this is used to detect hand gestures and determine the position of hand relative to sensor, the same approach potentially could also be used for determination of fruit’s or vegetable’s position. This data is used to compare how sensor will react if it is covered by obstacle in experiment ‘c’ (Figs 10–12).

When obstacle was placed 10 mm above sensor, S_D increased proportionally to size of the obstacle. Similarly as it was to spherical object signal of Centre electrode in comparison to ambient noise increased, but on the edges – decreased, thus signal with no object is grater than 0 (Figs 10, 11). Difference of S_D maximum level when detectable object reached central position of sensor and ambient level decreased with increase of obstacle's area – 180 without obstacle, 162 for 60 x 60 mm obstacle and 77 for 120 x 70 mm obstacle. Thus in the worst condition when the central electrode was fully covered with a "leaf" we got 43% of usable signal value of S_D without obstacle.

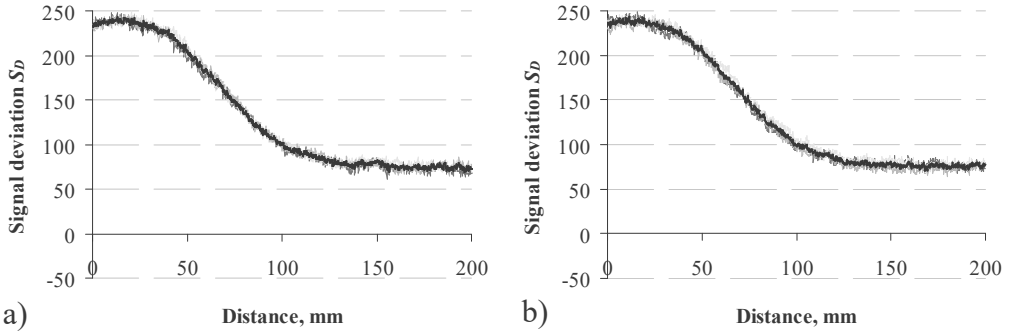

Figure 10. Results of experiment 'c' with 60 x 60 mm obstacle at the centre of electrode C, 4 runs and average line in bold: a – direction D1; b – direction D2.

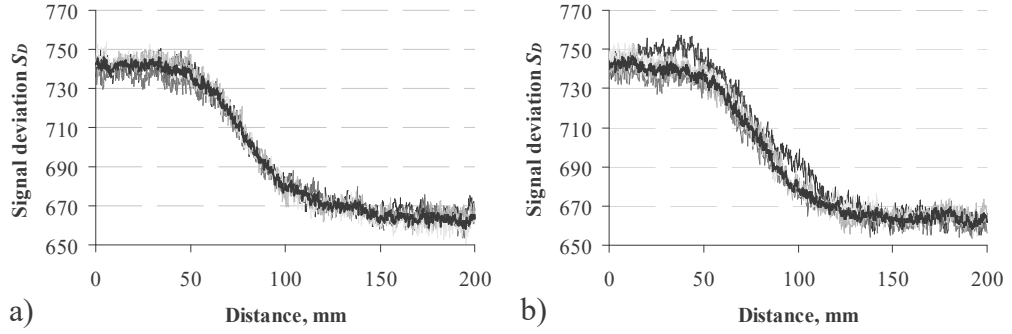

Figure 11. Results of experiment 'c' with 120 x 70 mm obstacle at the central electrode, 4 runs and average line in bold: a – direction D1; b – direction D2.

Fig. 12 shows development of S_D signal on East and Centre electrodes where detectable object passed over with obstacle between it and the sensor. The rest of electrodes are not shown, because their S_D values were out of range in comparison to Centre and East electrodes. Although change between minimum and maximum levels decreases with size of the obstacle (note the scales of Y axis in figures) it is still possible to determine transitions of signal level on both electrodes and thus to determine position of detectable object.

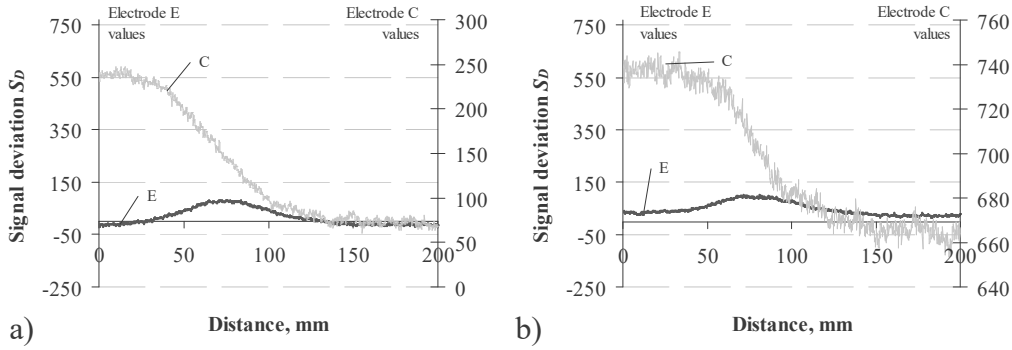

Figure 12. Signal strength on C and E electrodes for a single test in experiment 'c': a – for 60x60 mm obstacle; b – for 120 x 70 mm obstacle.

It is clear that in real life situations in horticulture and other biological applications for robotized automation to be cost-effective and reliable it is necessary to combine various types of sensors (Zujevs et al., 2015).

Object detection when direct visual contact with object of interest is not needed allows to apply the proposed electrical field based sensing as a supplement of computational vision in such use cases as:

- pre-operation – identifying areas for subsequent precise vision-based examination of vegetables to decrease necessary computing power for image processing and increasing recognition speed;
- post-operation – increasing recognition system reliability by distinguishing of vegetables or fruits between other objects if partially covered or in adverse optical conditions such as dust, direct or shadow-casting illumination, humidity etc.;
- fine adjustment of manipulator position for plant treatment or harvesting.

In order to evaluate the possibilities of application of E-field based sensing in these areas in further research it is necessary to build simulation model of the sensor, design electrode layout and finding optimum transmitting signal parameters, to develop the prototype and perform experimental testing in real-life conditions.

CONCLUSIONS

1. The main idea of the study was to show that it is practically possible to use transmitter-receiver type electrical field based sensor for detection and position measurement of fruits and vegetables under cover by surrounding canopy.

2. Development board based on Microchip GestIC technology and MGC3130 mixed signal controller was used in this study as a sensor. The board is originally intended as a gesture detection and recognition device for data input in PCs.

3. Experiments show that despite of decrease in signal to noise ratio when detection electrode is fully covered, position of detectable object is still determinable. In worst condition when an electrode is fully covered with a physical model of leaf 43% of signal value in comparison to sensor output without obstacle is still usable.

4. Changes in transmitting signal frequency in laboratory conditions had no significant results, but there was a trend in increase of detectable signal strength with increase of frequency.

5. Electrical field based sensors in essence have no limitations distinctive for optical computer vision systems as these detect only object's mass with different permittivity, but also doubtless have own drawbacks – they need frequent calibration without any objects in vicinity as electrical charges my build up on them during operation, they cannot be used for fine quality control and for recognition of relatively small objects. Thus this type of sensors potentially can be an integral part of complex fruit or vegetable recognition system in robotized horticulture applications.

REFERENCES

Villiers, G. 2012. How capacitive sensing can reduce standby power in household appliances. Embedded. [online][15.01.2016.] http://www.embedded.com/print/4395685.

Taghinezhad, J., Alimardani, R. & Jafari, A. 2012. Development of a Capacitive Sensing Device for Prediction of Water Content inSugarcanes Stalks. *International Journal of Advanced Science and Technology* **44**, 61–68.

Zujevs, A., Osadcuks, V. & Ahrendt, P. 2015. Trends in Robotic Sensor Technologies for Fruit Harvesting: 2010–2015. *Procedia Computer Science* **77**, 227–233.

Brauna, A., Wicherta, R., Kuijpera, A. & Fellner, D.W. 2015. Capacitive proximity sensing in smart environments. *Journal of Ambient Intelligence and Smart Environments* **7**(4), 483–510.

Microchip Inc. 2013. Application note DS40001716A, 82 p.

Microchip Inc. 2013. Application note DS41685A, 34 p.

Smith, J.R. 1996. Field mice: Extracting hand geometry from electric field measurements. *IBM Syst. J*. **35**(3.4), pp. 587–608.

Cohen, O., Linker, R. & Naor, A. 2011. *Estimation of the Number of Apples in Color Images Recorded in Orchards. Computer and Computing Technologies in Agriculture IV*. **344**, 630–642.

Fernández, R., Salinas, C., Montes, H. & Sarria, J. 2014. Multisensory System for Fruit Harvesting Robots. Experimental Testing in Natural Scenarios and with Different Kinds of Crops. *Sensors* **14**(12), 23885–23904.

Agronomy Research **14**(Sp.1), 1099–1106, 2016

Use of spiral conveyor in the processing of granular waste materials

J. Sander[1*] and T. Jehlička[2]

[1]Czech University of Life Sciences Prague, Faculty of Engineering, Department of Technological Equipment of Buildings, Kamýcká 129, CZ 165 21 Prague 6 – Suchdol, Czech Republic
[2]Czech University of Life Sciences Prague, Faculty of Engineering, Department of Technological Equipment of Buildings, Kamýcká 129, CZ 165 21 Prague 6 – Suchdol, Czech Republic
[*]Correspondence: sander@tf.czu.cz

Abstract. The work presents a construction solution, verification of operation function and evaluation of the efficiency of a spiral separator in processing of agricultural, food industry and other granular waste. The common method of processing waste is based on crushing and subsequent sorting by various physical and mechanical properties. Crushing waste results in a heterogeneous mix of particles with a substantial size and weight difference and major share of dangerous powder particles. Thus, specific requirements are put on the conveying and manipulation of the mixture. The solution is using pneumatic conveying and closed sub-pressure separators. Under laboratory pilot conditions a sub-pressure spiral separator was designed and tested. The separator is designed as an immobile drum sieve in which a rotating axis-free helix is inserted. The inside space of the drum sieve is linked axially to the sub-pressure pipe of the combined conveyor. A light aspiration proportion (dust particles) are carried by the air flow while the granular particles with big specific weight and specified size make the sieve fraction. The particles larger than the separation apertures of the sieve are carried mechanically by the helix. The separating efficiency was observed on a mix of granular materials at same operation conditions. The contents of the mix of granular materials varied in size, specific weight and in the proportion of dust particles. Evaluation of the separating possibilities of the spiral separator verified the operation applicability of the system for separation and conveying of various agricultural, food and other granular materials.

Key words: pneumatic conveying, mechanical conveying, granular waste, separation, combined transport materials

INTRODUCTION

Conveying and sorting granular materials is a frequently applied technological process in agriculture, food industry but even in waste management. Systems using gravitation, mechanical conveyors or pneumatic or fluid equipment are employed. The use of a particular equipment is always linked to conveying conditions and to properties of the material conveyed.

Products of variable physical and chemical properties originate during waste processing. Such products result from crushing. In practical application it is a mixture of

substances of different specific weight, granuity, or extremely dusty materials which are contaminated microbially, or are toxic. This provides elementary requirements for transport and further processing of such products. Conveying facilities must allow for both vertical and horizontal directions. They must be airtight due to dust and they must be able to convey granular material with high difference in specific weight at minimum energy requirements. Equal conditions apply for separating and sorting processes which are an inseparable part of waste processing. Pneumatic conveying in the form of closed pipelines is applied in waste processing where the material is conveyed by overpressure or by sub-pressure of the air sucked and then released into the conveyor environment. With materials of high difference in specific weight such conveying has its limits. Practically it entails the necessity to use lower pressure and smaller flow of the air volume which result in shortening the conveying distance, lowering the conveying elevation, reducing efficiency or to limiting the different in the material thus conveyed.

There is a variety of ways how to reduce the indicated shortcomings of low-pressure pneumatic conveying with maintaining the project requirements of the function of the processing lines. There is a possibility to change the properties of the material conveyed (pre-sorting and reducing the size and weight difference of the conveyed particles) or to adjust the parameters of the conveying system (increasing the volume of the air flow and pressure). Changing the material properties or adjusting the parameters of the conveying system can be used only to a relatively limited extent in the low-pressure pneumatic conveying and at the cost of a relatively higher energy requirements (Yan et. al., 2012). For this reason a solution based on combination of separated pneumatic and mechanical conveying hereinafter combined conveying was suggested. The mechanical part of the conveying deals with the higher weight and volume of the materials, with the conveying elevation and it lowers the energy requirements and technical limitations of pneumatic conveying. It has, however, greater requirements of space, the wear is quicker and there is a necessity of tuning together the pneumatic and mechanical part of the conveying path.

Operational tests of the suggested construction of a combined conveying of granular materials have confirmed the expected construction insufficiencies – namely the mechanical wear of the combined conveyor in a long-term operation. One of the reasons of the wear were the solid particles of higher weight with size close to the difference between the inside diameter of the conveyor pipeline and the outside diameter of the axis-less helix. The particles were further crushed inside the conveying path and the load of the mechanical part of the conveying path increased due to higher friction. The newly designed construction suggests to incorporate a mesh separator at the beginning of the conveying path of the body of the combined conveyor which will pre-sort the material conveyed. The design uses a part of the conveyor to be used for pushing the material through the mesh separator. The aim was to preserve every advantage of the combined conveying and increase the conveyor capacity, efficiency and reliability without any further space requirements of the line construction (Mills, 2004).

The present work follows the design of the construction of combined conveying (pneumatic and mechanical) in processing granular materials. It complements the equipment with a possibility of separation of a part of the conveyed mix as early as at the conveying and it verifies the operational functions of the separator while maintaining the operational properties of the combined conveyor.

MATERIALS AND METHODS

A mesh separator prepositioned and mechanically linked with a combined separator was designed and tested under laboratory pilot conditions. Conveying possibilities of this combined conveyor for granular waste materials with various specific weight and size of the particles have been evaluated.

The work has been carried out on the pilot line for electrical waste processing. The line was situated in the laboratories of the Czech University of Life Sciences Prague.

Brief description of arrangement and function of the line for electrical waste processing

The electrical waste is crushed in the bi-rotor crusher and further in a knife-mill. The crushed material and the dust are carried into the following conveyor pipeline of the combined conveyor where the small particles of higher weight (the medium fraction) are separated on the mesh separator. The larger particles and the dust are further conveyed by a combined conveyor into the dust separator where the dust is removed. The dust-free material is transported via a magnetic separator onto the fluid table where it is sorted by its specific weight. The spiral separator then pre-sorts the conveyed material by the set size depending on the mesh used. After magnetic separation this medium fraction is moved for further processing outside the line depending on the character of the material processed.

Design and execution of combined (pneumatic and mechanical) conveyor system

The construction is a conveying pipeline of circular diameter at 150 mm for low-pressure pneumatic conveying inserted into the inside of the pipeline in combination with the mechanical driving element in the form of an axis-free helix. Within such space the material is transported as a result of the dynamic effects of the flowing medium and at the same time it is driven mechanically by the rotating axis-free helix. A radial ventilator URBAN Technik, Type VE-6000 A is the source of negative pressure with an output of 4,500 m^3 h^{-1} and with operating negative pressure of 400 Pa. This technical solution allows for pneumatic and mechanical conveying in a single conveying space (conveyor pipeline).

Particles with lower specific weight and with greater aerodynamic resistance are carried by the airflow mainly through the centre of the pipeline. High specific weight particles are moved mechanically by the energy of the axis-free helix. Such construction of the conveyor pneumatic pipeline can be used on short distances both horizontally and obliquely (Jehlička & Sander, 2015).

Spiral separator description

A mesh with pre-defined apertures was placed on the bottom of the combined conveyor 50 cm from the opening of the combined conveyor pipeline. During the movement of the granular mix carried from the opening of the combined conveyor the separation of a part of the conveyed granular material with higher mass occurs according to the size of the mesh apertures.

Particles with lower mass and larger size and the dust particles are moved by the combined conveyor further to the dust separator. Mesh made from perforated metal sheets with circular openings at 6 and 8 mm was used for separation. The minimum size of the mesh apertures must be larger than the difference between the inner diameter of the pipeline and the outer diameter of the axis-less helix. A simple diagram of the separator is in Fig. 1.

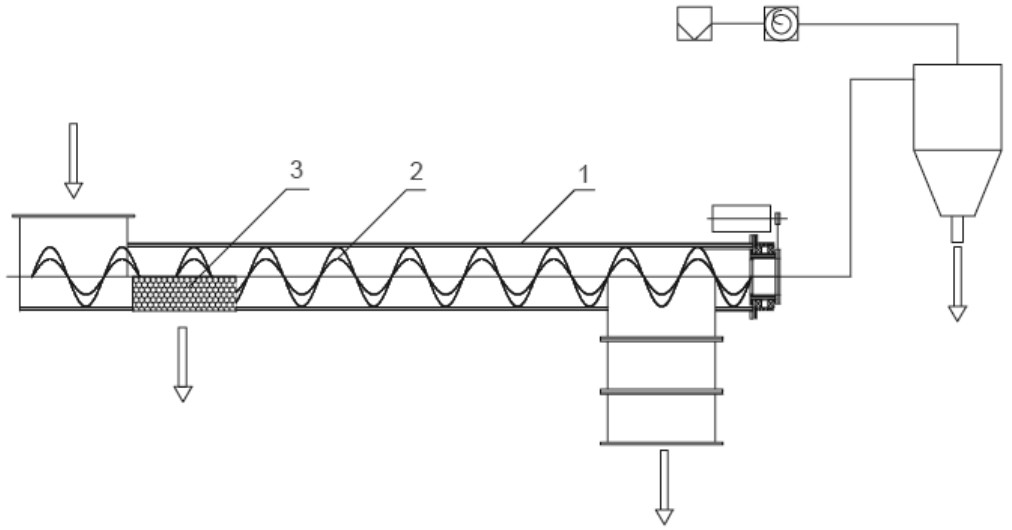

1 – pipeline; 2 – axis-less helix; 3 – mesh

Figure 1. Schematic diagram of the spiral separator.

Spiral separator operation function verification

Verification of operational function (efficiency of the separation process) was carried out by a comparison of the percentage of the volume of separated particles of the material conveyed on the mesh separator with the volume of particles of the same size in the outlet of the combined conveyor. The efficiency of the process of separation (ability to separate the material of the given physical properties at the operational conditions thus set) used in combined conveying of granular materials is affected by a number of factors. The pneumatic part of the conveyor is affected considerably by the gravitation effect during the adherence of the air through the mesh apertures. Reverse adherence of the air into the conveying path affects the function of the pneumatic part of the conveyor in front of the separator. Therefore the measuring was first carried out while the pneumatic conveying was turned off. The size of the separator mesh was by experimentation set so as, with minimum size of the mesh, the separation efficiency was maximum at the atmospheric pressure.

With the pneumatic section on, the pressure was gradually set to values which were used in the reliability measuring of the pneumatic conveying without the mechanical conveyor, including the pressure which secured conveying reliability of the combined conveying of the granular materials used without inserted separator in previous measurements (Mallick & Wypych, 2009).

The dry crushed mix used in the measurement consisted of two kinds of granular material which differed in granularity and specific weight. The same mixture was used in the measurement of reliability of the pneumatic and mechanical conveying. The mixture was created by the crushing and sorting of electric cables (electrical waste). The former material was metal (electric conductor) sorted into several groups by grain size. The other material was the share of plastics (electrical insulators). Efficiency of the separation process was observed for particles with higher mass (electric conductor) and the size coming close to the difference between the inner diameter of the conveying pipeline and the outer diameter of the axis-free helix, in this case 4 to 6 mm (the size of the apertures 6 and 8 mm). Operational conditions were set by the pressure in the conveyor pipeline according to the previous measurements on the combined conveyor less the separator. The pressure was changed step by step by setting the ventilator revs. The operational pressure was measured by a measurement device Testo 521-1 (equipped with external piezoresistive probe of 0 to 2,000 hPa; labelled 0638 1847) with a pressure sensor located in the conveying pipeline at 1.9 m from the separator (constant air flow) (Baker & Klinzing, 1999). The atmospheric pressure at the time of measurement was 1,015 hPa. The weighting method was selected for the evaluation of the separation efficiency. The measured mixture was weighted in front of the conveyor, after the mesh separator and at the exit of the combined conveyor.

RESULTS AND DISCUSSION

The measuring is always carried out repeatedly for separate values of operation pressure. The percentage of separated particles with set operating pressure within the conveying pipeline at constant conveying reliability of the combined conveyor i.e. reliable conveying of the remaining part of measuring mixture was observed. The average values of repeated measuring of the separation are recorded in Table 1 and 2. The size of separated particles was 4 and 6 mm of metallic fraction (electric conductor). Table 1 for mesh apertures of 6 mm. Table 2 for mesh apertures of 8mm.

Table 1. Operation pressure values of 4 and 6 mm particles separation, mesh 6 mm

	Granuity of mixture 4 mm	Granuity of mixture 6 mm
Pressure [hPa]	% separation	% separation
1,015	95	83
980	94	81
970	94	79
955	93	77
940	92	76
930	90	75
920	87	74
900	85	72

Table 2. Operation pressure values of 4 and 6 mm particles separation, mesh 8 mm

	Granuity of mixture 4 mm	Granuity of mixture 6 mm
Pressure [hPa]	% separation	% separation
1,015	95	95
980	94	94
970	93	93
955	92	92
940	90	91
930	89	90
920	89	90
900	87	88

The correlation of observed factors are brought into figures and interspersed with trend line. Fig. 2 represents the values of Table. 1. The Fig. 3 represents the values of Table 2.

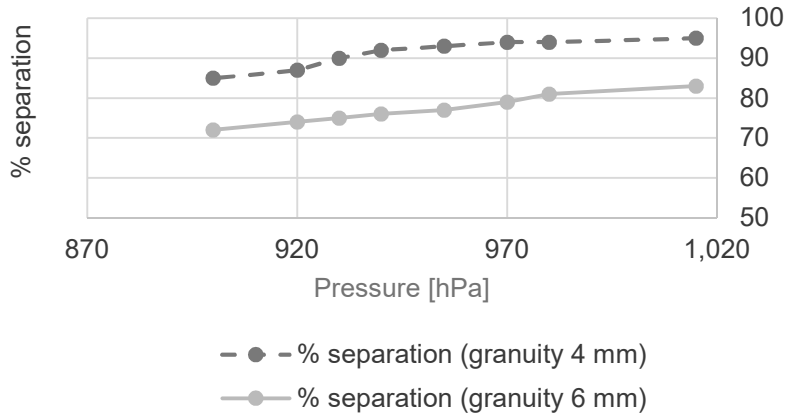

Figure 2. The dependence of separation efficiency on the operating pressure 6 mm mesh.

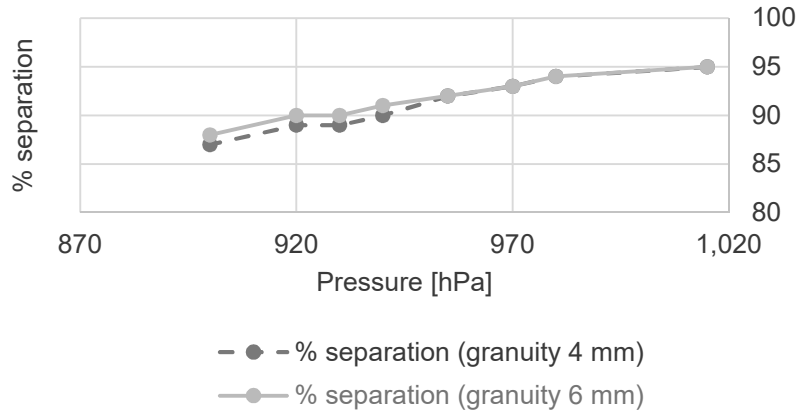

Figure 3. The dependence of separation efficiency on the operating pressure, 8 mm mesh.

The progress of separation efficiency within the range of pressure values, at which the conveying reliability of the combined conveyor without separator was verified, is apparent from acquired curves.

Given pressure value corresponds always corresponds to minimum at which the material particles were reliably conveyed. Pre-sorted mixture of crushed conductors with granuity of 4 and 6 mm was used due to the measuring accuracy of the separation mesh effectiveness.

Conclusions of measurement:

– A slight shift in the direction of the spiral rotation occurs during the movement of the measured mixture. Therefore, the mesh was placed with shift of 25 degrees from the vertical axis in order to increase the separation efficiency.

– Variable size of the mesh for assorted types of separated mixture will be required in operation conditions. The cylindrical mesh with variable aperture would be the solution.

– The measurement of efficiency at 6 mm granuity in mesh with 6 mm aperture – hexagonal apertures of the mesh will improve the separation efficiency for particles of the mixture with size close to the aperture size.

The verification of energy consumption was carried out by measuring the power input at the clamps of the electric motor of the traction spiral drive. The power input was measured with covered and exposed mesh. This method is purely orientational n dis dependent on sub-pressure and the amount of separated mixture. Therefore the measured values are not presented here. Solely the reduction of energy consumption was verified. Used method is sufficient for the verification of presumptive energy influence of mesh separator introduced into the conveyor (Hilgraf, 1998).

The measuring was carried out at laboratory equipment, therefore it largely applied only to the verification of the function. With industry prototype it would be possible to carry out more accurate measurements of properties and regulation options of the spiral separator system. Various problems can be presumed in case of real operation.

CONCLUSIONS

Constructional solution, which is proposed and verifies by the paper, is a reaction to conveying difficulties in long-term operation of combined conveyor for dry loose mixtures with high difference in mass. The operational wear of the conveyor and the operational vibrations were eliminated using the mesh separator with the combined conveyor in combination and simultaneously the premise of energy consumption reduction was proven. Elevated friction and further crushing of conveyed material due to particles the size of which is close to the gap size between the circumference of the conveying spiral and the conveyor tube were eliminated. All premises were verified by operation test and measuring.

The combined conveyor accompanied by mesh separator became a separation equipment with conveying of material. By its functional principle it divides conveyed material into three fractions. The fraction of light particles is separated by pneumatic conveying (light fraction). Whereas the fraction of particles with mass higher than the carrying force of the pneumatic conveying was mechanically separated by the conveying spiral (heavy fraction). The divide between these fractions varied according to the setting of production parameters of the pneumatic conveying and according to the nature of

conveyed mixture. A third (medium fraction) was created by insertion of mesh separator. Thus the equipment was transformed into pneumatic spiral separator with separation of three fractions the function of which was verified by measuring and pilot production using the mixture of electric waste. With measured mixture, the interaction of pneumatic conveying and mesh separation was minimal and it may be adjusted by proposed means.

The separation of medium fraction itself eliminated the sensitivity of the pneumatic conveying setting. By simple overlaying of the mesh the equipment can then serve as a conveyor or separator. Proposed combined conveying with separation is structurally simple, reduces total energy used for material conveying, has minimal built-up area requirements (tension member is inside the conveying pipeline) and low number of moving parts.

REFERENCES

Baker, J.D. & Klinzing, G.E. 1999. Optimal performance of pneumatic transport systems. *Powder Technology* **104**(3), 240–247

Hilgraf, P., 1998. Energy consumption for pneumatic conveying compared with mechanical conveying. *ZKG INTERNATIONAL* **51**(12), 660–673.

Jenlička, T., Sander, J. 2015. Use of combined pneumatic conveying in the processing of granular waste materials. *Agronomy Research* **13**(1), 83–88.

Mallick, S.S. & Wypych, P.W. 2009. Minimum transport boundaries for pneumatic conveying of powders. *Powder Technology* **194**(3), 181–186.

Mills, D. 2004. *Pneumatic conveying design guide*. Butterworth-Heinemann, London, 629 pp.

Yan, F., Rinoshika, A., Nonaka, H. 2012. An experimental study on a horizontal energy-saving pneumatic conveying system with soft fins. *Powder Technology* **217**, 516–522.

Agronomy Research **14**(Sp.1), 1107–1115, 2016

Water vapour transmission properties of linseed oil paint

R. Šemjakin, A. Ruus*, K. Kirtsi and E. Tungel

Tallinn University of Technology, Tartu College, Department of Technology, Puiestee 78, EE 51008 Tartu, Estonia; *Correspondence: aime.ruus@ttu.ee

Abstract. Linseed oil paint has been in use in indoor and outdoor decorating for a long period of time. It is not easy to date the first findings but there are signs of using linseed paint at least in V-IX century in some areas of Afghanistan and during the renaissance period in Europe. It is also known as a good preservative material for wood. Indoor finishing materials considerably influence the indoor climate (temperature, RH, ventilation rate) because of their moisture buffering ability. Moisture buffering occurs because of the sorption and diffusion properties of materials (wood, plaster, gypsum board etc.). As paint is a cover for those materials, the knowledge about material water vapour transmission properties is essential for evaluating hygrothermal properties of boarders and the co-action of paint and substrate (plaster). There could be products with different properties referred to as 'linseed oil paint'.

In the current study six handmade paints with different recipes including two primers and two commercial paints were under investigation. As for interior works, one layer of paint could be used as well therefore the samples were covered with both – one and two layers of paint. The thickness of paint layers varied from 0.8 and 6.2 μm for one-layer primers, from 11.3 to 26.9 μm for one-layer paints and from 17.8 to 40.7 μm for two-layer paints. Water vapour transmission properties were determined by using EVS-EN ISO 7783 standard.

Water vapour diffusion equivalent air layer thickness s_d was estimated as 0.1 and 0.2 m for 1-layer primers, 0.2 to 0.9 m for 1-layer paints and 0.4 to 0.9 m for 2-layer paints. The information gathered from the experiment enables to get an overview of the different properties of 'the same product" and use the data in hygrothermal calculations.

Key words: linseed oil paint, water vapour transmission, water vapour permeation coefficient, water vapour diffusion equivalent thickness, water vapour resistance factor.

INTRODUCTION

The study focuses on water vapour transmission properties of different linseed oil paints.

Linseed oil paint has been in use in indoor and outdoor decorating for a long period of time. It is not easy to date the first findings but there are signs of using linseed paint at least from V–IX century in some areas of Afghanistan (History of Linseed oil Painting…; Secrets of Bamiyan Buddhas.).

Linseed oil paint was used for interior works in the XVI century in painting art and room decorating earlier as can be read from Theophilius tractate 'Schedula Diversarum Artium' (Using of linseed oil …).

Also, it is known as the oldest timber paint for outdoor use in Central Europe in the Renaissance period already. The oldest written data about outdoor use of paint in Sweden

and Finland indicate that linseed oil as a binder in different mixtures was used already in XVI century. In the 1950–60s alcyd paints were taken into intensive use but oil paints did not disappear and today they have made comeback (Kaila, 1999).

Natural and traditional paints are quite popular in the restoration of buildings and in designing new interior as well. Compared with frequently used traditional paints like casein paint and egg tempera, and commercial alcyd paint, linseed oil paint has water vapour transmission rate more or less equal to alcyd paints (Ruus et al., 2011).

Linseed oil is also known as a good preservative material for wood.

Besides temperature, relative humidity (RH) is one of the key parameters of indoor climate and can be determined by measuring indoor moisture generation, air-change rate, and the release or uptake of moisture by hygroscopic surface materials as well as moisture flow through structures (Kurnistki et al., 2007.)

There is a need for deeper and more exact information about the the behaviour of indoor paints as a part of wall in diffusion calculations and coating of hygroscopic materials offering moisture buffering values (MBV).

The influence of different paints depending on time was studied by Minke (2006). It can be seen (Fig. 1) that on silty loam substrate the lime (KQ), casein and cellulose glue paint (KL) only slightly reduce the absorption (after a sudden increasing RH from 50–80%), whereas double latex (LX) and single linseed oil (LE) coating can reduce absorption rates to 38% and 50% respectively.

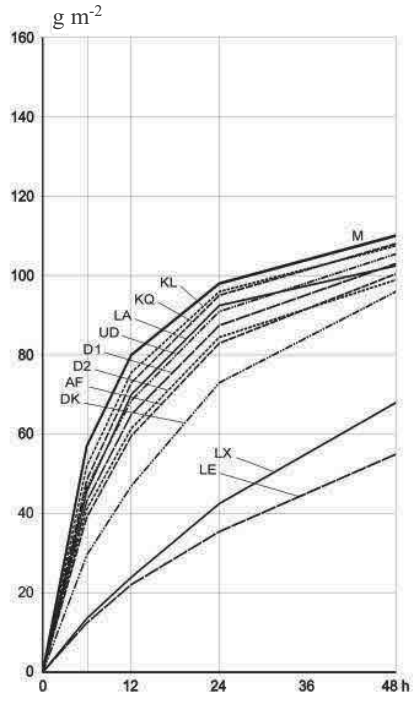

M – Silty loam without coating;
KQ – 2x Lime paint;
KL – 2x Chalk cellulose glue paint;
LE – 1x Double-boiled linseed oil;
D2 – 2x Biofa dispersible paint
LA – 1x Biofa glaze with primer;
AF – 2x Acrylic paint;
DK – 2x Synthetic dispersion paint exterior;
LX – 2x Latex;
UD – 2x Dispersion paint without solvent;
D1 – 2x Dispersion paint for interio.

Figure 1. Influence of coatings on 1.5 cm-thick one-side exposed loam plasters at temperature of 21 °C (Minke, 2006).

The influence of coating on vapour diffusion thickness could depend on using or not using the primer under paint (primer + 2 layers of paint) and on the base material also (Ramos et al, 2010). Using primer for vinyl paint increased S_D (RH = 54%) value 7.1 times on base material of gypsum board, 4.4 times for gypsum plaster and 1.5 times for gypsum + lime plaster.

Brachaczek (2014) proposed statistical models for the optimization of the recipe configurations for silicone coatings. Combining the analysis of physical parameters determining the quality of the coatings (hydrophobicity, resistance to wet scrubbing and the ability to diffuse water vapour through the coatings), the results enabled the selection of the optimal ranges of values for the analysed factors, from a physical as well as an economic point of view.

In the study paint samples as non-self-supporting systems were prepared. Thickness and water vapour transmission rate were estimated to get an idea about the differences. Afterwards numerical values derived for the water vapour permeation coefficient δ_c, water vapour diffusion equivalent thickness, s_d and water vapour resistance factor μ for different linseed oil paints and primers.

MATERIALS AND METHODS

In the current study six handmade paints with different recipes including two primers and two commercial paints were under investigation. Standard EVS-EN ISO 7783:2011 was followed in the testing procedure. Standard methodology was chosen for making results comparable and more clearly understandable.

As for interior works, one layer of paint could be used also therefore samples with both, one and two paint layers (three test pieces of each) were studied.

Recipes used for handmade paints are the following:

I – primer: varnish 0.2 l, turpentine 0.2 l, zinc oxide ~100 g, titanium dioxide ~100 g, chalk 80 g;
II – paint: varnish ~0.30 l, zinc oxide ~50 g, titanium dioxide ~200 g, kaolin 50 g;
III – paint: varnish 0.25 l, titanium dioxide ~175 g, zinc oxide 25 g, kaolin 75g;
IV – paint: varnish 0.25 l, red pigment (iron oxide) ~200g, kaolin 25 g;
V – primer: varnish 0.2 l, turpentine 0.2 l, titanium dioxide 100 g;
VI – paint: varnish 0.16 l, titanium dioxide 200 g, zinc oxide 100 g.

Another group is presenting commercial paints:
X – commercial paint of large enterprise;
XI and XII – commercial paint from a small enterprise;
XII – has some defects – includes pieces.

Turpentine was used as a solvent for primers. For both primers the amount of solvent was equal with binder. Traditional recipe for one primer (mixture I) was modified by increasing amount of solid powder part twice. That enables to satiate the substrate surface not just cover. Another primer (mixture V) was made on the basis of a traditional primer recipe.

Mixtures II, III, IV are VI present different recipes of paints in use. Mixtures II, III and IV have similar proportions of liquid binder as varnish and solid powder as pigment

plus filler (approx. 0.1 l liquid + 100 g of solid). In the recipe VI the proportion is approx. 0.1 l of liquid and 200 g of solid powder.

The samples with one-layer paints were dried for 5 and two-layer paints for 8 days in the room with natural air circulation and air temperature of 20 ± 2 °C and relative humidity of 35 ± 5%. From each sample three test pieces were cut out. 36 paint test pieces in total and three for carton as substrate were tested in RUMED 4101 climate chamber affording RH of 20–95%, with accuracy of ±2–3% and temperature of 0–+60 °C with accuracy of ±0,5 °C (Fig. 2).

Air temperature was maintained at 23 °C and relative humidity at 50% in the climate chamber (according to standard methodology). In the vessel the relative humidity was kept at 93% using ammonium dihydrogen phosphate ($NH_4H_2PO_4$) saturated solution. The test pieces were weighed once a day until weight loss speed was stabilizing using Mettler PC440 Delta Range weight, providing test area of 0.5–400 g and accuracy of 0.01 g not exactly meeting standard requirements. The accuracy of 0.01 g is suitable for pieces with areas 50 cm^2 and larger. In the current study the testing area was 42 cm^2. An interval of 24 hours was chosen for linseed oil paint which is known as a material with low water vapour permeability. In all cases the change of mass was higher than 50 mg as described in the standard procedure.

Figure 2. Test pieces sealed on vessels.

The thickness of the coating was estimated with micrometer. The total thickness of substrate plus coating and carton were measured. Thickness of paint was calculated.

Water vapour transmission rate of the coating can be expressed with the formula

$$\frac{1}{V} = \frac{1}{V_{cs}} - \frac{1}{V_s} \tag{1}$$

$$V = \frac{V_{cs} \times V_s}{V_s - V_{cs}} \tag{2}$$

where: V – water-vapour transmission rate, g $(m^2\ d)^{-1}$; V_{cs} – water vapour transmission rate of the substrate plus coating, g $(m^2\ d)^{-1}$; V_s – water-vapour transmission rate of the substrate, g $(m^2\ d)^{-1}$.

The water vapour permeation coefficient of the coating δ_c, [g (m d Pa)$^{-1}$] can be found using the formula:

$$\delta_c = \frac{V \times d}{\Delta_{pV}} \quad (3)$$

where: d – thickness of coating, m; Δp_V – the water-vapour partial pressure between two sides of the coating, Pa.

Water vapour diffusion equivalent thickness s_d, (m), can be calculated with the formula

$$s_d = \frac{\delta_a \times \Delta_{pV}}{V} \quad (4)$$

where: δ_a – water vapour permeation coefficient of the air at standard temperature and pressure 0.016 g (m d Pa)$^{-1}$

Water vapour resistance factor μ (–), can be calculated with the formula

$$\mu = \frac{s_d}{d} \times 10^6 \quad (5)$$

RESULTS AND DISCUSSION

The thickness of carton was 28.6±0.7 μm. Water-vapour transmission rate for carton was 627.6±104.8 g (m^2 d)$^{-1}$. Water vapour transmission rate for paint layers was calculated with the formula 2 (see Table 1). The water vapour permeation coefficient of air δ_a = 0.016 g (m d Pa)$^{-1}$ was used in the calculations.

Three test pieces is the minimum amount required in standard but causes too large variability in results and it makes comparison difficult. The data presented in Table 1 gives some overview of possible values and variability of data.

Table 1. Thickness of coating and water vapour transmission rate of linseed oil paint

Sample	One-layer coating		Two-layer coating	
	d, μm	*V*, g (m^2 d)$^{-1}$	d, μm	*V*, g (m^2 d)$^{-1}$
I	6.2 ± 3.4	90 ± 58.5	15.7 ± 7.1	55.4 ± 8.4
II	11.3 ± 7.4	27.3 ± 7.5	33.3 ± 7.8	33.7 ± 14.5
III	19.0 ± 4.4	29.5 ± 11.6	40.7 ± 9.1	24.9 ± 21.4
IV	12.2 ± 4.9	43.8 ± 14.4	32.0 ± 4.0	27.9 ± 7.2
V	0.77 ± 0.7	209,1 ± 2.7	7.5 ± 6.1	101.2 ± 4.1
VI	26.9 ± 23.3	20.3 ± 6.7	39.8 ± 20.4	21.9 ± 14.0
X	12.6 ± 3.3	73.2 ± 37.8	17.8 ± 6.7	46.9 ± 29.0
XI	15.5 ± 2.7	82.1 ± 63.8	24.9 ± 1.4	42.6 ± 16.9
XII	17.0 ± 9.2	83.1 ± 35.7	29.2 ± 9.8	53.2 ± 49.3

The thickness of one-layer samples was from 0.77–26.9 μm on average. For two layers thickness of 7.5–40.7 μm was measured. The thickness of traditional primers (V) was under 1 μm for one-layer and 7.5 μm for two-layer samples. The difference occurred probably because liquid mixture was absorbed by porous surface.

According to the average it can be seen that traditional primer has also the highest water vapour transmission rate – 209.1 for one-layer and 101.2 g (m^2 d)$^{-1}$ for two layers.

Paint having proportionally the largest solid powder content ratio (sample VI) gives almost highest results in thickness (26.9 and 39.8 μm) and lowest in water vapour transmission rate 20.3 and 21.9 g $(m^2\ d)^{-1}$.

Paints with the same recipe and technology (XI and XII) seems to give similar results, but in most cases variability seems to be higher for the paint with defects.

As the variability of results is large, *t-test* was chosen to analyse the results of water vapour transmission rate as a first result derived from the measurements.

T-test ($P < 0.05$) shows that one-layer paints sample V (traditional primer) has statistically significant difference compared to all others. Sample VI has also statistically significant difference compared to others. For example compared with Sample II $P = 0.04$. For other samples differences can be seen in some cases: I–II $P = 0.04$, I-IV $P = 0.02$, III–IV $P = 0.03$, XII–IV $P = 0.02$.

Using *t-test* for two-layer paints indicated that Sample V has statistically significant difference from other paints except Sample XII, where variability is too large to show any difference. The primer with modified recipe (Sample I) differs from other paint samples like II ($P = 0.01$), III, IV and VI.

The classification given in the mentioned standard (EN ISO 7783-2 2001) determines that most samples are classified as medium II class (medium) V = 15–150 g $(m^2\ d)^{-1}$ and only one-layer primer (sample V) is in class I (high) > 150 g $(m^2\ d)^{-1}$. Water-vapour partial pressure between two sides of the sample Δ_{pV} was calculated at 2 °C and saturated water vapour pressure of 2,643 Pa (Hutcheon & Handegord, 1984) and found to be (0.93–0.5)*2,643 = 1,136.5 Pa.

The water vapour permeation coefficient of the coating δ_c [g $(m\ d\ Pa)^{-1}$], water vapour diffusion equivalent thickness s_d (m) and water vapour resistance factor μ (m) were calculated with the help of the formulas 3, 4, 5 for each test piece and the results are presented in Table 2 and Figs 3–5.

The maximum and minimum values calculated are used hereby to present the range of values. For Water vapour resistance factor μ values are rounded to the nearest 100.

Table 2. The water vapour permeation coefficient of the coating δ_c [g $(m\ d\ Pa)^{-1}$,], water vapour diffusion equivalent thickness, s_d (m) and water vapour resistance factor μ (–) for samples of linseed oil paint

Sample	δ_c *10^{-7} g $(m\ d\ Pa)^{-1}$	s_d, m		μ, –
		One-layer	Two layers	
I	3.4–9.2	0.16–0.26	0.31–0.35	17,400–46,600
II	2.3–13.1	0.60–0.75	0.45–0.62	12,200–70,000
III	4.2–12.0	0.52–0.70	0.58–1.20	13,300–38,100
IV	3.8–9.0	0.37–0.49	0.60–0.73	17,800–42,000
V	1.0–8.3	0.09	0.18	19,300–39,100*
VI	3.3–7.7	0.78–1.00	0.66–1.13	20,800–48,400
X	4.6–8.9	0.21–0.32	0.32–0.53	18,000–35,000
XI	4.8–16.9	0.17–0.32	0.38–0.52	9,500–33,100
XII	7.7–20.7	0.20–0.27	0.25–0.54	7,700–20,900

*only two-layers have been taken into account.

The water vapour permeation coefficient of the coating δ_c g (m d Pa)$^{-1}$ (Fig. 3) and water vapour resistance factor μ (–) (Fig. 5), which are material properties, have to be similar not depending whether they are estimated by one or two layers. In some cases (Sample II, IV, V) μ-value has clearly lower value for two layers. That is probably because of substrate adsorption and indicates that micrometer is not the best tool for measuring the thickness of paint layer and calculation based on the application rate recommended in the standard is more reliable.

It is exceptional that s_d values for two layers have to be twice as much as for one layer paint (Fig. 4). Actually, it can be seen very clearly only on traditional primer s_d = 0.09 for one layer and 0.18 m for two layers. Compared with the sample VI, the paint with the highest percentage of solid powder (s_d = 0.66–1.13 m), the difference is clearly noticeable.

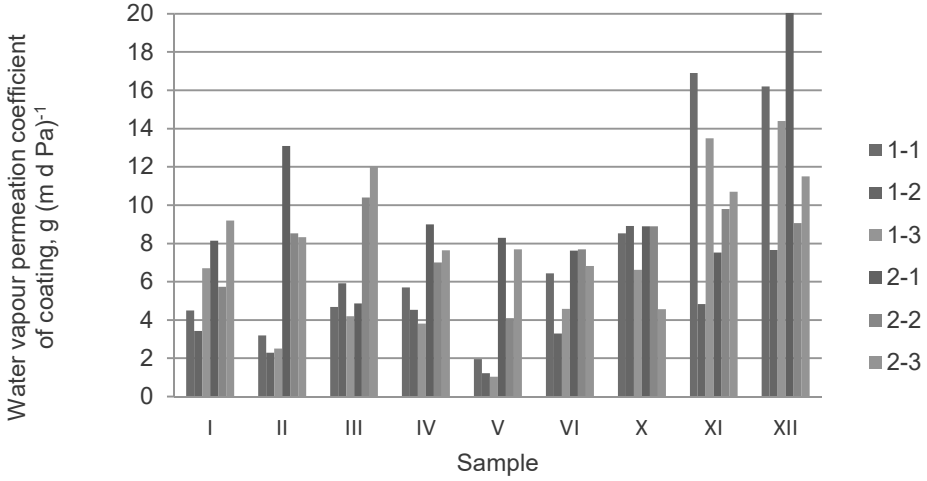

Figure 3. The water vapour permeation coefficient of the coating δ_c [g (m d Pa)$^{-1}$].

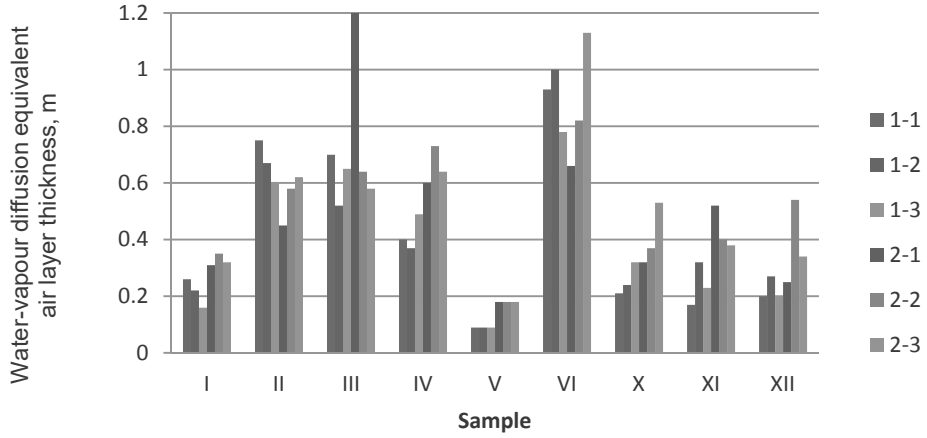

Figure 4. Water vapour diffusion equivalent thickness s_d (m).

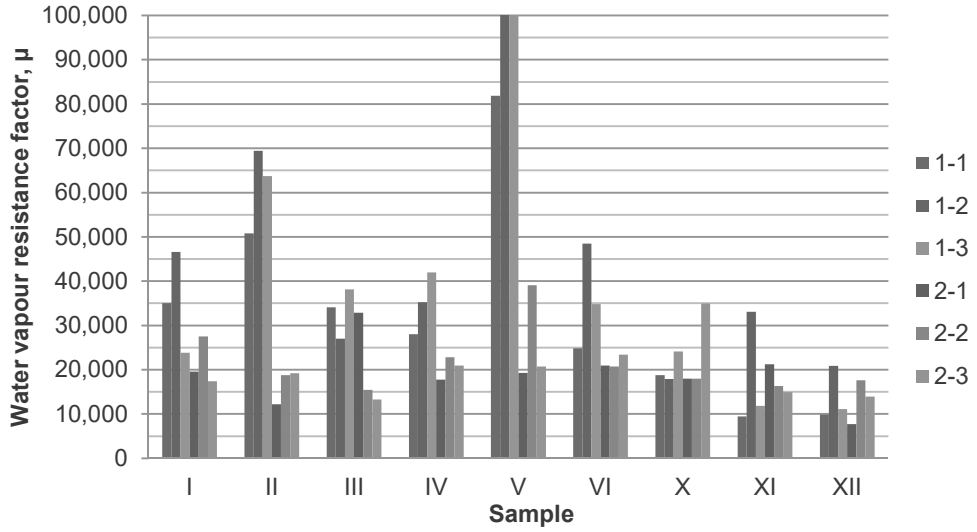

Figure 5. Water vapour resistance factor μ (–).

From the data presented in Table 2 s_d values are most reliably usable, while vapour permeation coefficient and water vapour resistance factor can be more tested with a larger number of test pieces to reduce the variability. For comparison in standard EVS EN ISO 10456:2008 presenting hygrothermal properties of building materials and products next values are can be found: emulsion paints s_d = 0.1 m, gloss paints s_d = 3.0 m and vinyl wallpaper s_d = 2.0 m.

CONCLUSIONS

Today energy efficiency or hygrothermal calculations are becoming more and more detailed and are performed with computer software enabling monthly, daily or hourly data based modelling. For the calculations of such accuracy, a detailed input of material data is needed.

The information gathered from the experiment enables to get an overview of the different properties of 'the same product' and use the data in hygrothermal calculations.

In the current study the data is presented in two ways:

1) thickness and water vapour transmission rate i.e .practical values giving an overview of the real situation,

2) material parameters for diffusion calculations in building physics.

Three test pieces is a minimum amount required in standard but causes too large variability of results and makes comparison difficult. In the further studies more test pieces have to be used.

The results of the water vapour permeation coefficient of the coating δ_c, water vapour diffusion equivalent thickness, s_d and water vapour resistance factor μ could be useful in hygrothermal calculation.

ACKNOWLEDGEMENTS. This study was supported by Tartu College of Tallinn University of Technology. Special thanks to Helgi Muoni for her kind help and support.

REFERENCES

Brachaczek, W. 2014 The modelling technology of protective silicone coatings in terms of selected physical properties: Hydrophobicity, scrub resistance and water vapour diffusion. *Progress in Organic Coatings* **77**, 859–867.

EVS-EN ISO 7783:2011. Paints and varnishes – Determination of water-vapour transmission properties – Cup method (ISO 7783:2011). Estonian Centre for Standardisation, 18 pp.

EVS EN ISO 10456:2008. Building materials and products – Hygrothermal properties – Tabulated design values and procedures for determining declared and design thermal values. Estonian Centre for Standardisation, 29 pp.(In Estonian)

EN ISO 7783-2 2001. Paints and Varnishes – Coating materials and coating systems for Exterior masonry and concrete – Part 2: determination and classification of water-vapour transmission. Estonian Centre for Standardisation, 8 pp.

History of oil painting. *http://www.antiquity.tv/episode-3-the-history-of-oil-paint/.* Accessed 30.01.2016.

Hutcheon, N.B. & Handegord G.O. 1995. *Building Science for a Cold Climate*. NRC-IRC, 440 pp.

Kaila, Panu. 1999. *House Doctor* - VI. Viplala, Tallinn, 136 pp. (In Estonian).

Kurnitski, J. Kalamees, T. Palonen, J. Eskola, L. & Seppänen, O. 2007. Potential effects of permeable and hygroscopic lightweight structures on thermal comfort and perceived IAQ in a cold climate. *Indoor Air* **17**(1), 37–49.

Minke, G. 2006. *Building with Earth – Design and Technology of a Sustainable Architecture*. Birkhäuser publisher, Basel, 200 pp.

Ramos, N.M.M., Delgado, J.M.P.Q. & Freitas, V.P. 2010. Influence of finishing coatings on hygroscopic moisture buffering in building elements. *Construction and Building Materials* **24**, 2590–2597.

Ruus, A., Peetsalu, P., Tohvri, E., Lepasaar, T., Kirtsi, K., Muoni, H., Resev, J., Tungel, E. & Kabanen, T. 2011. Water vapour transmission properties of natural paints. *Agronomy Research* **9 (**Special Issue I), 195–201.

Secrets of the Bamiyan Buddhas. *http://www2.cnrs.fr/en/1345.htm.* Accessed 24.01.2016.

Using of linseed oil on wooden surfaces. Comp. Mari Loit *http://muinas.ee/files/16.%20linaolivarv.pdf. A*ccess 30.01.2016

Agronomy Research **14**(Sp.1), 1116–1122, 2016

Study on impact strength of sisal fibers reinforced epoxy composites using experimental methods

P. Valášek

Department of Material Science and Manufacturing Technology, Faculty of Engineering, Czech University of Life Sciences Prague, Kamýcká 129, CZ 165 21 Prague; e-mail: valasekp@tf.czu.cz

Abstract. Among the advantages of composite materials is their ability to exploit the properties of partial phases that creates the composite. Common materials used as matrix materials include polymeric composites. The properties of these matrices can be optimized by using synthetic or also natural fibers. Natural fibers are inexpensive, ranks among renewable resources and when respecting their biological nature, they can replace synthetic fibers in many applications. This paper describes the impact strength of epoxy resins filled with unordered short sisal fibers with a length of 2–6 mm. From the experimental results it is evident that the presence of fibers of sisal examined as epoxy resins, increases the impact strength, up to 143%. SEM (scanning electron microscopy) was used to assess the failure of mechanism of these composites.

Key words: Agave Sisalana, fiber composite, mechanical properties, porosity.

INTRODUCTION

Composite materials are materials that use the synergy effect of its individual components. Composites with fiber reinforcement are among the frequently used materials that play an indispensable role in a wide range of industrial applications. As the matrix fiber but also particles composites may be used polymer materials, such as epoxy resin, which have excellent mechanical properties (Valasek & Muller, 2013a, Muller, 2014; Ruggiero et al., 2015a).

Still increasing interest in environmentalism, increasing fears concerning the greenhouse effect instigated various industrial fields – for instance building industry, motoring and packaging industry, to find the sustainable materials which can substitute common synthetic polymer fibers (Silva et al., 2008). Sustainable substitute can be natural fibers, which are accessible, inexpensive and it is possible to consider them as a sustainable source (Mizera et al., 2015). Environmentally friendly may also be composites filled with waste, these primarily particles composites can optimize some mechanical properties like hardness, abrasive wear etc. (Valasek & Muller, 2013b, Valasek & Muller, 2012, Ruggiero et al., 2015b). Sisal fibers are in the area of composite systems according to Li et al. (2000) very perspective due to its low price, low density, and high specific strength and due to module of elasticity. Stated are also the absence of health risk in case of utilizing these fibers, easy accessibility and renewability. Besides advantages of natural materials it is essential to concern also their limits – thus is primarily natural substance of these materials, where for example the constant

mechanical properties do not have to be maintained. Boopalan et al. (2012) indicates as a disadvantage the soaking of fibers, thereby reducing the mechanical properties in interaction with the polymer matrix.

Impact strength described in this paper ranks among important mechanical characteristic of composite systems. As it is stated by Chandramohan & Bharanichandar (2013) for optimization of impact strength can be used natural fibers of banana (Musa Sepientum), Roselle (Hibiscus Sabdariffa) but also sisal (Agave Sisalana) or their combination. For improving the impact strength of composite materials can be used short fibers, but significant improvement of epoxy matrices filled with long oriented fibers is described by Monteiro et al. (2014). Similar increase of impact strength of polymer matrix by inclusion of sisal fibers is also described by Li et al. (2015).

The aim of this experiment is to identify the change of impact strength of epoxy resins caused by the presence of short unorganized sisal fibres – confirm the hypothesis about positive influence of fibers presence on the impact strength of resins and primarily quantify the magnitude of this change. To confirm this hypothesis the common statistical surveys, i.e. ANOVA and T-test were used.

MATERIALS AND METHODS

Preparation of test samples

Matrix of composites was formed by two epoxy resins Glue Epox Rapid and Glue Epox Rapid F (these resins differ in viscosity).

The sisal fibers are extracted from the leaves of Agave Sisalana, which is mainly grown in tropical and subtropical zone – the untreated sisal fibers were used in this experiment. Country of origin: China. The fibers are obtained from the leaves of plants, each sheet weighing up to 1.5 kg and contains up to 7% fibers (see Fig. 1).

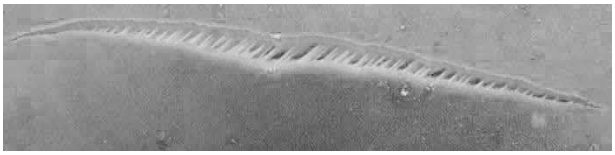

Figure 1. Fibers in the sheet of agave Sisalana plant.

The length of the fibers ranged from 80 to 100 mm. The length of the fibers was cut into short fibers having a length of 2 mm, 4 mm and 6 mm. The length of fibers after cutting did not correspond to determined length (2 mm, 4 mm and 6 mm) in all cases, therefore their concrete length was defined with stereoscopic microscope, where the real length was measured. By using this procedure, the value 1.9 ± 0.4 mm was determined for 2 mm, value 4.0 ± 0.5 mm for 4 mm, and the real length corresponded to 6.1 ± 0.5 mm length for 6 mm. Fundamental mechanical properties of these fibers shows Table 1.

Table 1. Mechanical properties of sisal fibers (Mieck et al., 1994)

Density (g cm^{-3})	Tensile strength (MPa)	Young´s modulus (GPa)	Elongation at break (%)
1.45	468–640	9.4–22.0	3–7

The preparation of composites was performed by mechanical mixing of short sisal fibers and the epoxy resins. The testing samples were consequently cast to the moulds prepared from two component silicon rubber. Concentration of the filler in the matrix was expressed with volume percentages, fiber systems with 1%, 2.5%, 5% and 10% were prepared. Casted testing samples were subjected to density control, where the deviation of real and theoretical density was measured – porosity and also the impact strength was evaluated.

The impact strength was evaluated based on the norm CSN 64 0611 (Determination of the impact resistance of rigid plastics by means of Dynstat apparatus). In these destructive tests, the Dynstat device nr. 283 stated impact strength a_n, which expresses kinetic energy the hammer needed to crush the tested object without notches in relation to the surface of its diagonal cut, as expressed by the following formula (1):

$$a_n = \frac{A_n}{b \cdot h} \tag{1}$$

where: a_n – impact strength [kJ m^{-2}]; A_n – energy required to shift the specimen [kJ]; b – width of the test specimen [m]; h – thickness of the test specimen [m].

RESULTS DISCUSSION

Among significant properties determining the qualitative indicator of composite systems ranks the porosity. Fig. 2 compares the porosity of casted fiber systems based on comparison of real and theoretical density. Theoretical density was calculated according to volume concentration of fibers in the epoxy resin, namely based on density of resin stated by the manufacturer 1.15 g cm^{-3} and density of sisal fibers 1.45 g cm^{-3}.

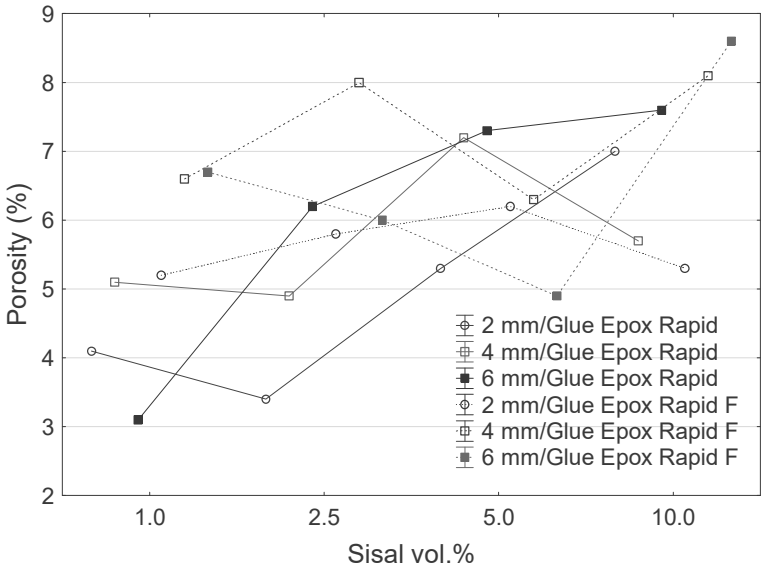

Figure 2. Porosity of Epoxy/Sisal composites.

As apparent from Fig. 3 the presence of sisal fibers in the resin Glue Epox Rapid significantly increased the values of impact strength. From the progress of the curves it is evident, that the increasing concentration has unequivocal effect on the increase of values of impact strength. With increasing length of fiber was not confirmed the effect on increase of impact strength of these cast composite systems. Impact strength of unfilled resin Glue Epox Rapid reached the value 3.24 ± 1.11 kJ m^{-2}. Significant values of dispersion were recorded when measuring the impact strength. The coefficient of variation of measurement was up to 39%. This fact can be attribute to increased porosity of cast composite systems as well as to disorder of fibers in the matrix. The highest value of impact strength 7.97 ± 2.30 kJ m^{-2} was measured in the system with fiber length 2 mm and concentration 10%.

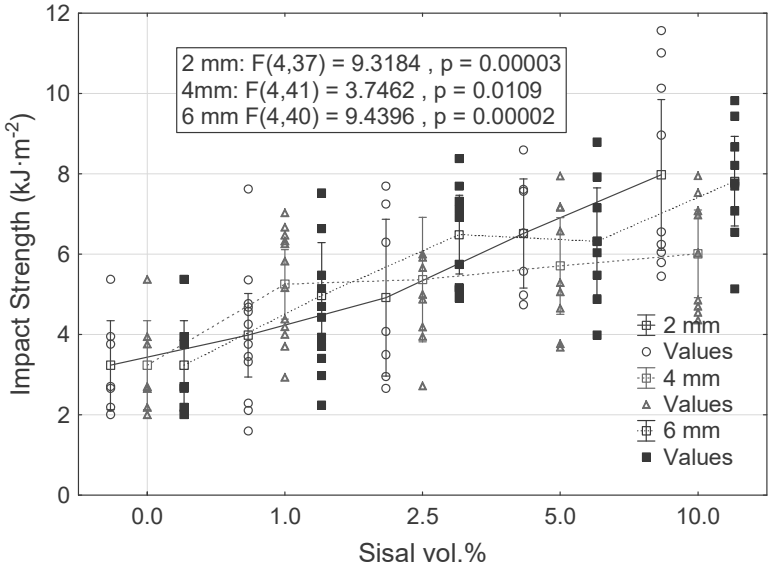

Figure 3. Impact strength of composites with matrix Glue Epox Rapid.

Average impact strength of resin Glue Epox Rapid F reached the value 3.67 ± 1.01 kJ m^{-2}. Presence of sisal fibers analogously as for other assessed resin increased impact strength proportionally with the increasing concentration of fibers in the matrix. The highest value was reached at fiber length 6 mm and concentration 10%, that was 8.91 ± 1.37 kJ m^{-2} (see Fig. 4 the results of ANOVA analysis). During measurement were recorded high coefficients of variation, which reached up to 30%.

From the Fig. 3 and Fig. 4 follows, that is possible to describe the dependence between increase of impact strength and increase of sisal fibers as a linear dependence, see equation in Table 2.

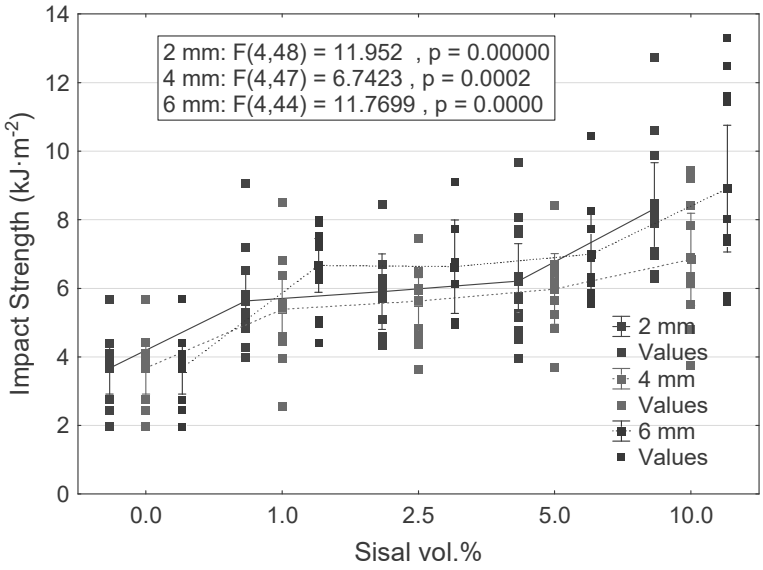

Figure 4. Impact strength of composites with matrix Glue Epox Rapid F.

Table 2. Description of increase of impact strength – linear trends

Composite	2 mm		4 mm		6 mm	
	equation	R^2	equation	R^2	equation	R^2
Glue Epox Rapid	y = 0.7864x + 3.24	0.84	y = 0.6191x + 3.24	0.76	y = 0.88x + 3.24	0.89
Glue Epox Rapid F	y = 0.8004x + 3.67	0.84	y = 0.6256x + 3.67	0.88	y = 0.9884x + 3.67	0.82

Electron microscopy confirmed sufficient wetting of fibers with resins, see fracture areas Fig. 5. From the Fig. 5 it is obvious fibers plucking during matrix failure and the presence of air bubbles, which were demonstrated by porosity as well.

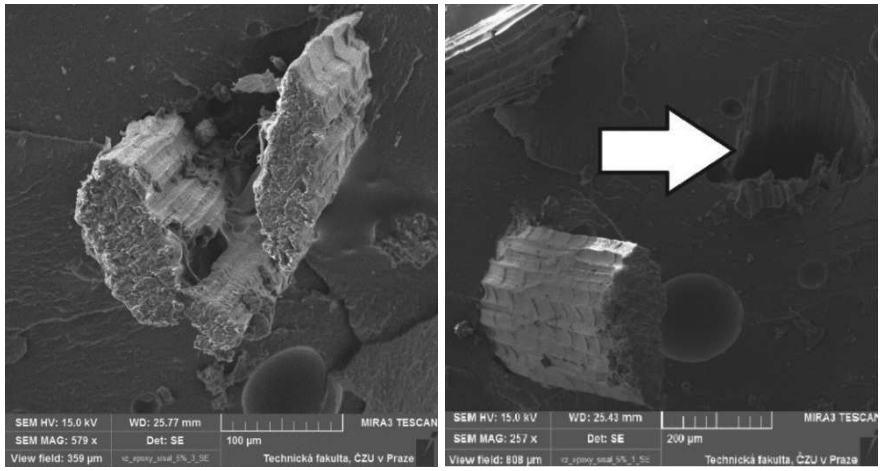

Figure 5. Fracture areas of sisal composites systems (SEM).

CONCLUSIONS

From the point of view of the coefficients of variation, which occurred at both unfilled resin and composite systems, it is necessary to analyze the measured data with statistical surveys in such way, that it was possible to statistically prove the influence of fiber inclusion on values of impact strength. To confirm the hypothesis about statistical significant effect of inclusion on the examined mechanical characteristic was chosen T-test in the level of significance $\alpha = 0.95$. If $p < 0.05$ the increase of impact strength is statistically proven, see Table 3 ($\mu 1 \neq \mu 2$), which compares low fiber concentrations with unfilled resin, that is up to moment of demonstrable increase of impact strength.

Table 3. T-test comparison of unfilled resin with low concentrations

H: $\mu 1 \neq \mu 2$	Glue Epox Rapid			Glue Epox Rapid F		
($p < 0.05$)	2 mm	4 mm	6 mm	2 mm	4 mm	6 mm
0 :1%	0.30	0.00	0.06	0.00	0.00	0.00
0 : 2.5%	0.09	-	0.00	-	-	-
0 : 5%	0.00	-	-	-	-	-

Statistical survey proved that for resin Glue Epox Rapid is possible to state the statistical increase of impact strength from 5% (2 mm) and from 2.5% (6 mm). In all other cases the increase occurs already from the lowest concentration of sisal fibers in the matrix, i.e. 1%.

The results confirm conclusions of Ashok Kumar et al. (2010), who describes the increase of impact strength for composites with epoxy matrix and fibers length 1 cm, 2 cm and 3 cm. Author recorded the highest mechanical properties for composites with fiber length 2 cm, while the experiment described in this paper unequivocally do not determine optimal fiber length from the lengths 2, 4 and 6 mm. The experiment confirmed also the conclusions about increase of impact strength of resins with sisal fibers, which were formulated by Li e al. (2015).

It is possible to agree with conclusions of Dharmalingam et al. (2015), who states, that the composite materials with sisal fibers have higher impact strength and it is possible to combine them with synthetic fibers, which could be object for further experiments in the area of evaluation of impact strength of short Sisal/Epoxy systems.

Adding the short sisal fibers has as the result the unequivocal improvement of absorption the energy of composites. Experimental values were loaded with big coefficients of variation. Impact strength did not evince demonstrable dependence on the fiber length. Increase of values of impact strength, achieved by inclusion of sisal fibers, reached up to 143% for Glue Epox Rapid F and 142% for Glue Epox Rapid.

ACKNOWLEDGEMENT. This paper has been made with the assistance of the grant CULS – IGA TF 2016: Research on mechanical properties of multi-component polymer systems during their preparation and application.

REFERENCES

Ashok Kumar, M. Reddy, G., Bharathi, Y., Naidu, S. & Naidu, V. 2010. Frictional coefficient, hardness, impact strength, and chemical resistance of reinforced sisal-glass fiber epoxy hybrid composites. *Journal of Composite*, *Materials* **44**(26), 3195–3202.

Boopalan, M., Umapathy, M.J. & Jenyfer, P. 2012. A Comparative Study on the Mechanical Properties of Jute and Sisal Fiber Reinforced Polymer Composites. *Silicon* 145–149.

Dharmalingam, G., Thirunavukkarasu, V., Mallela, G., Sriram, V. & Jayavelu, S. 2015. Study on mechanical properties of natural fiber reinforced sisal-coir-glass hybrid epoxy composites using experimental method. *International Journal of Applied Engineering Research* **10**(10), 27283–27299.

Chandramohan, D. & Bharanichandar, J. 2013. Impact text on natural fiber reinforced polymer composite materials. In: *Carbon - Science and Technology* **5**(3), 314–320.

Mieck, K.P., Nechwatal, A., & Knobelsdore, C. 1994. Potential applications of natural fibres in composite materials. In: *Melliand Textilberichte* **75**(11), 892–898.

Mizera, C., Herák, D., Müller, M. & Hrabě, P. 2015. Mechanical behaviour of polymeric composite with fibres of false banana. *Agronomy Research* **13**(3), 680–689.

Monteiro, S.N., Margem, F.M., Camposo Pereira, A., Simonassi, N. & Oliveira, M.P. 2014. Charpy impact tests in epoxy matrix composites reinforced with continuous sisal fiber. In: *Materials Science Forum* **775–776**, 290–295.

Müller, M. 2014. Influence of adhesives storing temperature on adhesive bond strength. *Manufacturing Technology* **14**(1), 71–75.

Li, Y., Mai, Y.-W. & Ye, L. 2000. Sisal fibre and its composites: A review of recent developments. In: *Composites Science and Technology* **60**(11), 2037–2055.

Li, Y., Ma, H., Shen, Y., Li, Q. & Zheng, Z. 2015. Effects of resin inside fiber lumen on the mechanical properties of sisal fiber reinforced composites. In: *Composites Science and Technology* **108**, 32–40.

Ruggiero, A. Merola, M., Carlone, P., & Archodoulaki, V.-M. 2015a. Engineering Tribo-mechanical characterization of reinforced epoxy resin under dry and lubricated contact conditions. In: *Composites Part B*, **79**(4), 595–603.

Ruggiero, A. Valášek, P. & Merola, M 2015b. Friction and wear behaviors of Al/Epoxy Composites during Reciprocating Sliding tests. In: Manufacturing technology, **15**(4), 684–689.

Silva, F.A., Chawla, N. & Filho, R.D. 2008. Tensile behavior of high performance natural (sisal) fibers. In: *Composites Science and Technology*, **68**(15–16), 3438–3443.

Valasek, P. & Muller, M. 2012. Impact strength of polymer particle composites with filler on the basis of corundum waste. *Engineering for Rural Development, 11th International Scientific Conference on Engineering for Rural Development*; Jelgava; **11**, 304–308.

Valasek, P. & Muller, M. 2013a. Polymeric composite based on glass powder – usage possibilities in agrocomplex. In: *Scientia Agriculturae Bohemica*, **2**, 107–112.

Valasek, P. & Müller, M. 2013b. Composite based on hard-cast irons utilized on functional parts of tools in agrocomplex. In: *Scientia Agriculturae Bohemica*, **3**, 172–177.

Agronomy Research **14**(Sp.1), 1123–1129, 2016

Effect of conductive ink on transfer characteristics of pressure into electric signal for tactile sensors

J. Volf*, V. Novák and V. Ryzhenko

Czech University of Life Sciences Prague, Faculty of Engineering, Kamýcká 129, CZ165 21 Prague, Czech Republic
*Correspondence: volf@tf.czu.cz

Abstract. The article deals with tactile sensors with circular electrodes in which conductive ink was used as a converter converting pressure into an electric signal. The article briefly describes theoretical background of this issue and presents several appropriate converters, from which the tested ink was selected. The measurement process is described in detail, and subsequently the dependence of resistivity on the thickness of the deposited ink layer is studied and the properties of various setups were compared. Finally, the results are summarized and the main issues are pointed out.

Key words: Conductive elastomer, conductive ink, tactile sensors and transducers.

INTRODUCTION

Up till now the conductive elastomer Yokohama rubber CS57-7RSC was used in the production of tactile sensors (Volf et al., 2009; Trinkl, 2011; Volf et al., 2012). Properties of different polymers are described in (Souza et al., 2005; Soares, 2006). Due to some of its negative properties, such as excessive hysteresis, and due to changes in the design of the Plantograf measuring system, we searched for another type of material for the conversion of the imposed pressure into an electric signal. The decision was to use conductive ink. Conductive inks consist of ink filled with small pieces of conductive particles; we tested inks containing graphite and silver particles. For testing, we obtained four types of conductive inks: KH WS SWCNT (KH Chemicals, Korea) Luxor (Luxor, Taiwan), NGAP FI Ag-4101 (NANOGAP, Spain) and DZT-3K (DZP Technologies, United Kingdom). After preliminary evaluations, the ink DZT-3K has been chosen and used in the measurements since owing to its composition. It could form a relatively high-quality conductive layer. The other inks did not meet the requirements, either they were too thin and they did not form a continuous layer, or they did not adhere to the substrate (first two, both water-based inks) or they were excessively conductive – as the third ink with silver particles as a filler – the resistance of the ink was only in units of Ω. The selected ink uses carbon particles as filler. A possible disadvantage of the conductive ink might be the difficulty to create a compact and stable layer, compared to the conductive rubber (Volf et al., 2006, Trinkl, 2011; Lufinka, 2014).

MATERIALS AND METHODS

Production of DZT-3K ink specimen

The former aim was to apply the ink layer on the electrodes directly. However, the selected ink DZT-3K was unable to create a coherent conductive layer, i.e. to sustain its integrity. Any negligible mechanical load caused the separation of the ink from the electrodes' surface. The measuring method – pushing with a force sensor tip on the ink layer – would not be applicable in this case. Additionally, we observed a certain deformation of the ink layer between the inner and outer electrode.

As this setup proved not to be utilizable, we proceeded to an alternative layout: the selected DZT-3K ink was deposited on the surface of a PET foil and applied to the electrodes similarly as the conductive elastomer. The thickness of the selected PET foil was 0.3 mm. The ink was deposited on the foil by a TG 130 spray gun, which can spray very low amounts of ink and enables fine control of spraying. A unique 12V Škoda 8P0012615A compressor originally used for inflating tyres was used as a compressor. Three thicknesses were selected of the deposited ink layer: 7 μm, 15 μm and 23 μm. The thicknesses were obtained by 6-fold, 12-fold and 18-fold repeated application. The spray applications were performed through a template made of the same foil with 3 mm holes in view of the 2.5 mm outer diameter of the circular electrodes. The thickness of the deposited ink layer was measured with a Mitutoyo SR44x1 digital micrometer with a measuring range of 0–25 mm and accuracy of 0.001 mm.

Shape of the measured electrodes

The dimensions of the measured electrodes are depicted in Fig. 1. The measurements were performed on a scanning matrix comprising circular electrodes with a 2.5 mm diameter. The electrodes were placed on a Cuflex printed circuit board. Conductors were soldered to the outlets of lines and columns which enabled easy choice of a particular electrode. The electrodes are denoted accordingly to their marking 'PD': ØE = 2.5 mm, Ød = 0.1 mm, M = 0.1 mm.

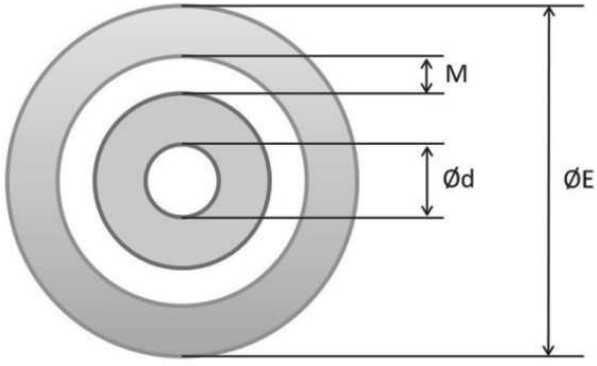

Figure 1. Dimensions of the measured electrodes.

Determination of electrical resistance of the ink

The measurement circuit scheme is shown in Fig. 2. It consists of a stabilized circuit, that supplies a voltage divider, wherein one resistor is constant and the other one, represented by the resistance of the conductive ink, is variable. The supply circuit is formed by LM317 voltage stabilizer, which enables setting of the supply voltage to 2 V and its fine adjustment. The value of the supply voltage has been chosen so that only a small current flows through the circuit. This prevents excessive heating of the conductive ink. Electrical resistance of the constant resistor in the divider is 10 kΩ, to ensure a constant current in the divider circuit. The electrical resistance of the ink was calculated using the formula (1):

$$R_{INK} = \frac{R_{CONST} \cdot U_{INK}}{U_{NAP} - U_{INK}} \tag{1}$$

where: R_{INK} – electrical resistance of the ink; R_{CONST} – constant electrical resistance 10 kΩ; U_{INK} – measured voltage; U_{NAP} – stabilized voltage – power supply for sensors.

The measurement of the voltage on the conductive ink – needed to calculate the resistance values in the divider – was performed by the DAQ device NI 6008. The measured voltage U_{INK} from the sensor was connected to an analog input of the DAQ card and it was measured by RSE method (Reference Single Ended) against ground potential. Voltage U_{NAP} from the stabilizer supplies the voltage divider R_{konst} and R_{ink} attached to DAQ card, where R_{ink} means the measured resistivity of the sensor. The output of the DAQ card was connected to a PC via USB. The entire measuring station was controlled by the NI LabView program. A LabView application was also created, which enables the recording and the calculation of the electrical resistance of the conductive ink.

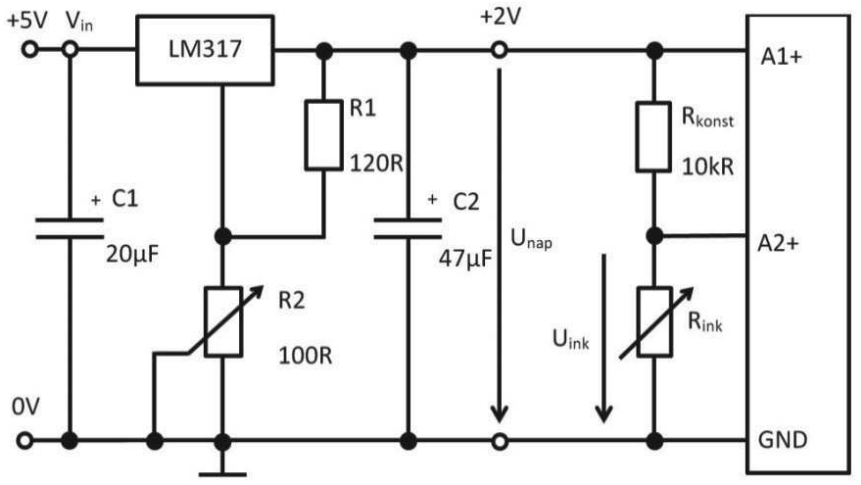

Figure 2. Circuit scheme for measuring of the resistance of the conductive ink.

Measurement method

Measurements of the properties of conductive ink were performed at a robotized workplace equipped with a Turbo Scara SR60 robot. The basic step of vertical motion of the robot's arm is 0.025 mm with a 0.01 mm resolution. The resolution caused some problems while setting the force value during the measurements of the hysteresis, as it was not possible to set exactly the same force as while loading. The pressure was imposed by means of the vertical motion of the robot's arm. A Hottinger DF2S-3 tensometer force sensor with a measuring tip with a Ø 3 mm circular surface was fixed to the end of the robot's arm. This force sensor was chosen because of its high sensitivity and appropriate range. The accuracy of the force sensor is 0.03%, its maximum permissible load is 200 N and its nonlinearity is 0.03%. The sensor is calibrated in the way that 1 gram corresponds to an output voltage change of 1 μV. The control unit is set up to display the values in grams; the conversion into the pressure values was made subsequently. The pressure imposed on the electrodes was calculated from the known area of the surface of the measuring tip and the exerted force. This resulted in the measured range of pressure values ca. from 100 kPa up to 2,200 kPa for the particular measuring tip.

The foil with the deposited ink was placed on the electrode field. The measuring tip with its circular Ø 3 mm surface, which is larger than the diameter of the electrodes, touched down on the surface of one tactile point and pressed on the conductive ink deposited on the foil against the circular electrodes, via which the electric resistance of the conductive ink was measured. The pressure imposed on the electrodes was calculated from the known area of the surface of the measuring tip and the exerted force. The output voltage of the type DF2S-3 tensometer force sensor was measured by an Almemo 2890-9 Data Logger (Lufinka, 2014). In (Pavlovkin & Novák, 2012) is outlined the possibility of measuring of tactile sensors' frequency properties.

Fig. 3(a) shows the detailed view on the measuring head: (1) is for the conductive ink deposited on a foil, (2) indicates the measuring tip, (3) is the force sensor DF2S-3 and (4) indicates the robot's head. Fig. 3(b) presents the overall layout of the measuring post.

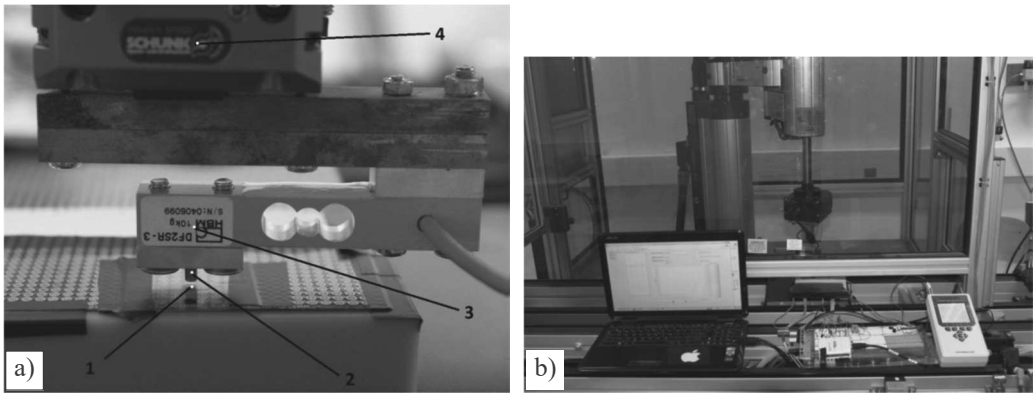

Figure 3. a) Detailed view on the measuring head, b) Layout of the robotized measuring post.

Loading and unloading procedures were performed to measure the hysteresis of the conductive ink. After each shift, the corresponding resistance and pressure values were logged by the NI LabView program. One measurement cycle thus contained 37 values. Between the individual measurement cycles, the electrodes were fully unloaded and there was a five-minute brake, so that the material could relax. The measurements were repeated 10 times for each ink layer thickness.

RESULTS AND DISCUSSION

The measured electrical resistance in dependence on applied pressure for PD-type electrodes for a particular ink layer of 7 μm are represented graphically in Fig. 4. All measurements were repeated 10x and the total (combined) measurement uncertainty was calculated and graphically represented by respective intervals for each measured value. In the diagram both the loading cycle (triangle points) and the unloading cycle (round points) are depicted.

Hysteresis (i.e. a different shape of the curve in the loading and unloading cycle) is apparent, similarly as in the case when a conductive elastic material was used, however, it is much lower (Trinkl, 2011), which makes this transducer more suitable to measure the absolute pressure than elastic materials. Initial insensitivity is apparent in all electrodes, which is obviously caused by the force necessary for the touch-down of the foil with the deposited ink on the electrodes.

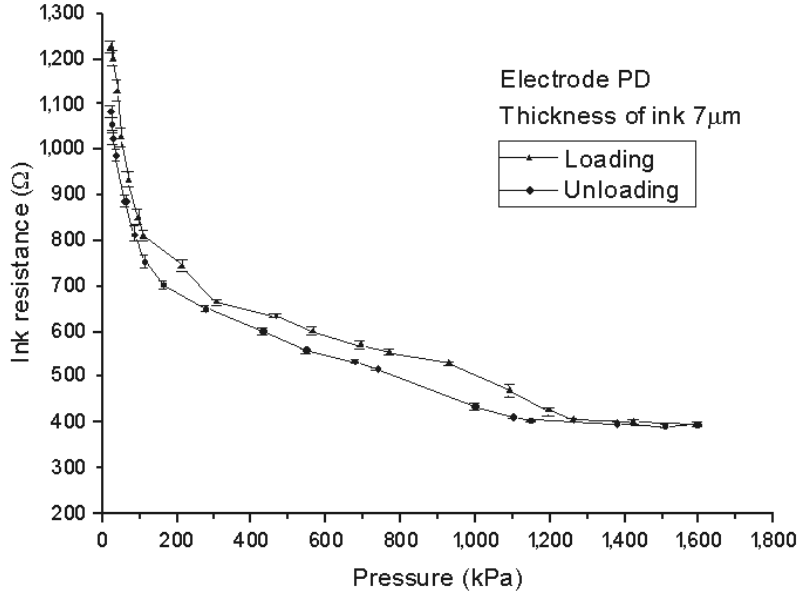

Figure 4. Dependence of resistance of a 7 μm thick ink layer on the pressure for an PD-type electrode (loading and unloading).

Fig. 5 presents the comparison of the dependence of the variation of resistance on the pressure during loading of PD-type electrodes for various thicknesses of the deposited ink layer.

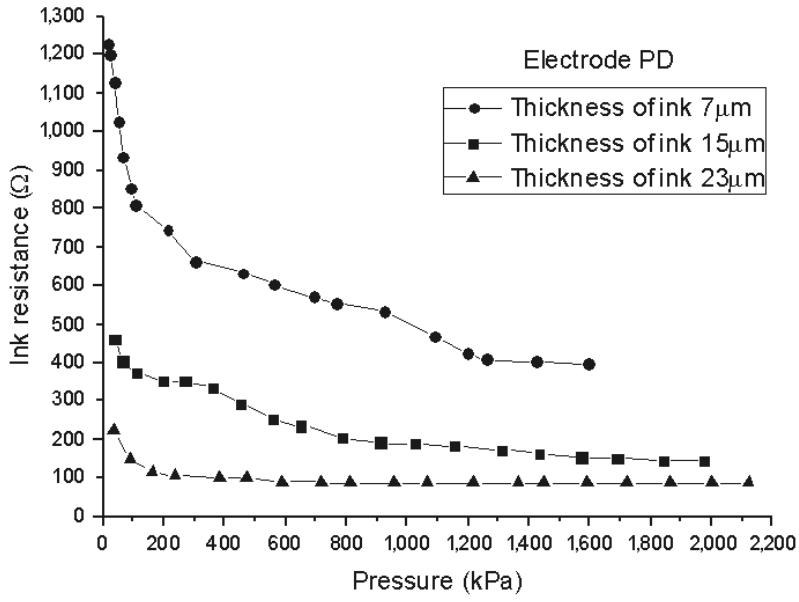

Figure 5. Comparison of PD-type electrodes with ink layers 7 μm, 15 μm and 23 μm.

From the diagram it is apparent that maximum sensitivity is achieved for a 7 μm thickness of the deposited ink; thicker ink layers exhibit only a small change in the ink's resistivity for pressures of ca. 600 kPa and above and thus they are not suitable to measure higher pressure loads, as the resistivity changes only insignificantly which degrades the resolution of the transducer. The curve associated to the 7 μm ink layer is sufficiently smooth, with nearly linear dependency in the range from 300 kPa to 1,400 kPa.

Within a limited pressure range, the setup with a 7 μm ink layer and on a PD electrode was assessed as the best transducer within the experiment. Higher thicknesses increased the conductivity of the sensor and consequently decreased its resolution. All measurements showed some hysteresis caused predominantly by the inaccuracy of positioning of the robot and relaxation of the ink and foil.

CONCLUSIONS

Measurements proved that conductive ink could act as a force transducer converting force to electric resistance. Satisfactory results were obtained for DZT-3K conductive ink in a 7 μm layer; thicker ink layers degraded the resolution of the transducer.

However, during the measurements we found out some limitations of this type of conductive ink, namely limited resistance of the ink to mechanical stress and its little adherence to the surface of the electrodes. Since the tested ink is a water based one and

thus it exhibits little adherence to the electrodes, we had to select an alternative procedure by spraying the ink on the foil. To allow a direct application of the ink to the electrodes, it would be necessary to use another type of ink – a polymer based one. We will continue the measurements with these types of inks in the future.

ACKNOWLEDGEMENTS. The measurements were carried out within the IGA project of the Faculty of Engineering, Czech University of Life Sciences in Prague.

REFERENCES

Lufinka, J. 2014. *Effect of Conductive Ink on Properties of Tactile Transducers.* Diploma thesis, CULS, Prague (in Czech).

Pavlovkin, J. & Novák, D. 2012. Messung der Frequenzcharakteristiken von Passivfilter mittels des Systems rc2000. *Edukacja–Technika–Informatyka* **3**(2), 257–264.

Souza, F.G., Michel, R.C. & Soares, B.G. 2005. A methodology for studying the dependence of electrical resistivity with pressure in conducting composites. *Polymer Testing,* **24**(8), 998–1004.

Soares, B.G., Amorim, G.S., Souza, F.G., Oliveira, M.G. & Pereira da Silva, J.E. 2006. The in situ polymerization of aniline in nitrile rubber. In: *SYNTHETIC METALS,* **156**(2–4), 91–98.

Trinkl, A. 2011. *Optimization of Design of Flat Tactile Transducers.* Dissertation, CULS, Prague, (in Czech).

Volf, J., Trinkl, A., Novák, M., Bílek, J., Prikner, P. & Neuberger, P. 2012. Plantograf V12 with Optimal Size Determination Sensor Electrodes and its Using for Pressure Distribution Between Tire and Road. In: *XX World Congress IMEKO*. IMEKO, Busan. ISBN 978-89-950000-5-2 95400.

Volf, J., Trinkl, A., Růžička, M. & Novák, M. 2009. Optimal Size Determination of Tactile Sensor Plantograf V08 and its Electrodes. In: *26th Symposium on Advances in Experimental Mechanics,* Leoben, Austria. ISBN: 978-3-902544-025.

Volf, J., Vlček, J., Papežová, S. & Novák, P. 2006. Orthopaedic Investigation System For Medical Non-Invasive Diagnostics. In: *IMEKO – XVIII World Congress and IV. Brazilian Congress of Metrology*. IMEKO, Rio de Janeiro.

Agronomy Research **14**(Sp.1), 1130–1137, 2016

Production and characterization of Ni-Co (WC) composites materials

A. Yonetken[1,*] and A. Erol[2]

[1]University of Afyon Kocatepe, Faculty of Engineering, Department of Electrical Engineering, ANS Campus, TR 03200 Afyonkarahisar, Turkey
[2]University of Afyon Kocatepe, Faculty of Technology, Department of Metallurgy and Materials Engineering, ANS Campus, TR 03200 Afyonkarahisar, Turkey
[*]Correspondence: yonetken@aku.edu.tr

Abstract. Ceramic-Metal Composite such as NiWC, CoWC are among advanced technology materials that have outstanding mechanical and physical properties for high temperature applications. Especially low density and high hardness properties stand out in such ceramic-metal composite. The microstructure, mechanical properties of %60Ni, %20Co and %20WC powders have been sintered by using tube furnace at 1,000–1,100–1,200–1,300–1,400 °C temperature. Mecahnical proporties and metalograhphic analysis were investigated after sintering. NiCo phases observed after metallographic analaysis. XRD, SEM (Scanning Electron Microscope)results showed us best microhardness of composites 174.16 HV, 8,563 g cm^{-3} density were obtained at 1,400 °C sintering tempareture.

Key words: ceramic-metal composite, powder metallurgy, sintering and high temperature.

INTRODUCTION

Electroless nickel plating is a chemical reduction process which depends upon the catalytic reduction process of nickel ions in an aqueous solution (containing a chemical reducing agent) and the subsequent deposition of nickel metal without the use of electrical energy. Several advantages like low cost, easy formation of a continuous and uniform coating on the surface of substrate with complex shape, and capability of depositing on either conductive or nonconductive parts have attracted a lot of interests from the academy and the industry (Zang et al. 2005).

WC-Co cermet is used in a wide range of hard metal manufacturing practices. Cutting tools, dies and drilling edges can be given as a couple of examples for its application. WC-Co composites are currently produced by various sintering techniques. Conventional production of powder metallurgy with thermochemical techniques still continues (Ma et al., 1996; McCandlish et al., 1992; Koc et al., 2000; Liu et al., 2008; Xiong et al., 2008;). Tungsten carbide-cobalt (WC-Co) ceramic metals have wide application due to their superior properties of high hardness and wear resistance (Nassaj & Mirhosseini, 2003; Upadhyaya & Bhaumik, 2003). Therefore, they are used in various branches of the manufacturing industry. The oxidation of WC-Co cermets was studied by many investigators (Gavriliu & Calu, 1979; Kang & Fromm, 1981; Shmatko et al., 1989). Oxidation of tungsten carbide, which is a base of hard metals, was studied with

the use of both powders and sintered samples (Kieffer & Kolbl, 1950; Shmatko et al., 1956; Webb et al., 1981). In the temperature range 500–1,200 °C. Intensive oxidation of WC starts at temperatures of at least 500 °C. Oxidation follows a parabolic law (Ekemar et al., 1982; Kovalchenko et al., 1991). At the initial stage, after which oxidation proceeds by a linear law '43'. At temperatures up to 700 °C. At 800 °C oxidation is governed by a linear law. The scale becomes porous at 600 °C. With further temperature rise up to 800 °C cracking and spalling of scale were observed. XRD-data show that the scale is composed of W03-oxide (Voitovich & Pugach, 1973; Voitovich, 1981).

The purpose of this study was to braze Ni-Co-WC powder mixtures sintered in traditional tube furnaces at 1,000–1,400 °C for 2 hours. Hardness and Maximum shear strength behaviour of the as powder metallurgy Ni–Co–WC composites would be evaluated with a hope of developing an alloy suitable for biomedical application.

MATERIAL-METHOD AND PREPARATION OF SAMPLE

Starting powders employed in this study were as follows: the purity of 99.8% for Ni powders with a particle size lower than -325Mesh, the purity of 99.9% for Co powders a particle size lower than 150 µm and the purity of 99.9% for WC powders with a particle size lower than 50 µm. The composition of (%60Ni-%20Co-%20WC) powders specimens was prepared in 5 g cylindrical compressed pre-form. They were mixed homogenously for 24 hours in a mixer following the weighing. The mixture was shaped by single axis cold hydraulic pressing using high strength steel die. A pressure of 300 Bar was used for the compacting all the powder mixtures. The cold pressed samples underwent for a sintering at 1,000, 1,100, 1,200, 1,300, and 1,400 °C for 2 hours in a traditional tube furnace using Argon gas atmosphere. The specimens were cooled in the furnace after sintering and their micro hardness and shear strengths measurements were carried out using METTEST-HT (Vickers) micro hardness tester machine, respectively.

Shimadzu XRD-6000 X-Ray Diffraction analyzer was operated with Cu K alpha radiation at the scanning rate of 2 degree per minute. LEO 1430 VP model Scanning Electron Microscope fitted with Oxford EDX analyzer was used for micro structural and EDX compositional analysis.

The volumetric changes of (%60Ni-%20Co-%20WC) composites material after sintering were calculated by using ($d = m\ V^{-1}$) formula (Fig. 1). The volume of post-sintered samples was measured with Archimedes principle

EXPERIMENTAL RESULTS AND DISCUSSION

Characterization of specimens

In the study, the samples prepared and shape were sintered at temperatures ranging from 1,000, 1,100, 1,200, 1,300 and 1,400 °C in conventional furnace. And made ready for physical, mechanical and metallographic analyses. Density-temperature change curve is shown in Fig. 1. The composition of (%60Ni-%20Co-%20WC) highest sintered density was achieved at 1,400 °C as 8,563 g cm^{-3}.

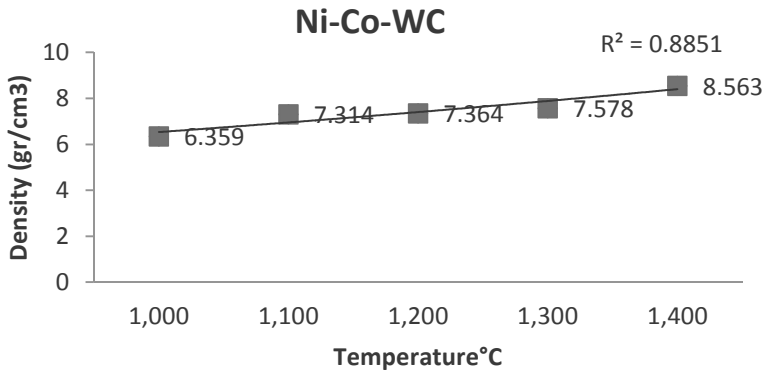

Figure 1. The density change with respect to sintering temperature.

The micro hardness-temperature change diagram is shown in Fig. 2. The micro hardness values of the composite samples produced using conventional sintering technique within the temperature range 1,000 1,200, 1,300 and 1,400 °C. According to this, the highest micro hardness value in the composite samples of (%60Ni-%20Co-%20WC) produced using powder metallurgy method was observed to be 174.16HV at 1,400 °C.

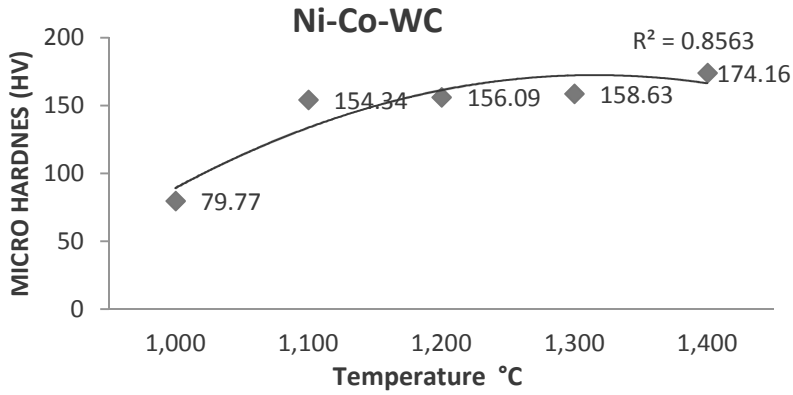

Figure 2. The micro hardness tests results from sintered specimens treated at various temperatures.

The Shear strength and hardness of the metal-matrix composite specimens were also determined. The relation between the sintering temperatures and Shear strength values is shown in Fig. 3. The shear strength value in the composite samples was observed to be 85,51MPa at 1,400 °C.

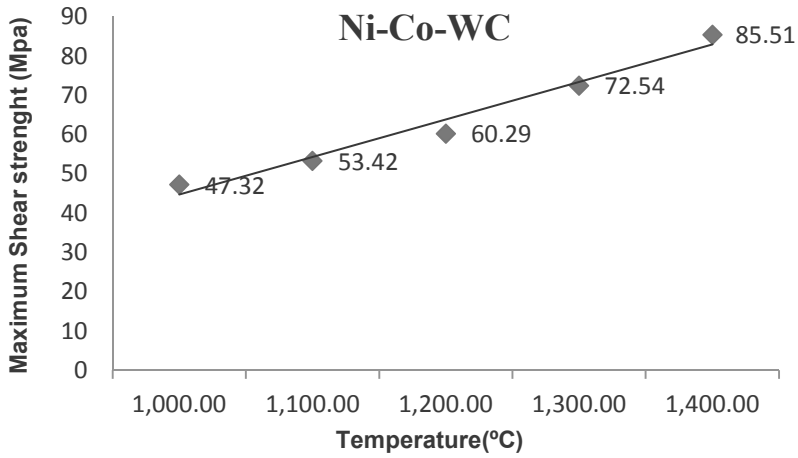

Figure 3. Shear strength results from specimens sintered at different temperatures.

Metallographic Analysis

The SEM analysis result of the metal matrix composite specimen obtained from (%60Ni-%20Co-%20WC) powders sintered at 1,400 °C is shown in Fig. 4 grain growth is observed and a homogeneous structure and grain boundaries can be seen that the pores very smaller and different shapes. (%60Ni-%20Co-%20WC) powders sintered at 1,400 °C is shown In Fig. 4, 1,400 °C to become apparent degree of grain boundaries and Sintering is not better understood at (%60Ni-%20Co-%20WC) composition at 1,400 °C temperature. This density, and hardness values are confirmed (Figs 1 and 2).

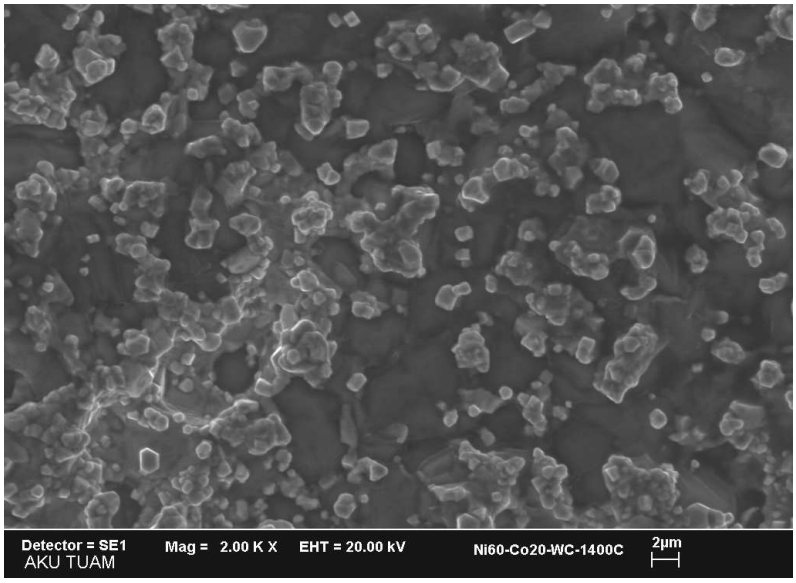

Figure 4. SEM view of (Ni-Co-WC) composite 1,400 °C.

The SEM picture(can be seen Fig. 5) is shown there are some little limitted porous, which comparing samples produced at 1,000 °C, 1,100 °C, 1,200 °C. Grain boundry can be seen also clearly in Fig. 5.

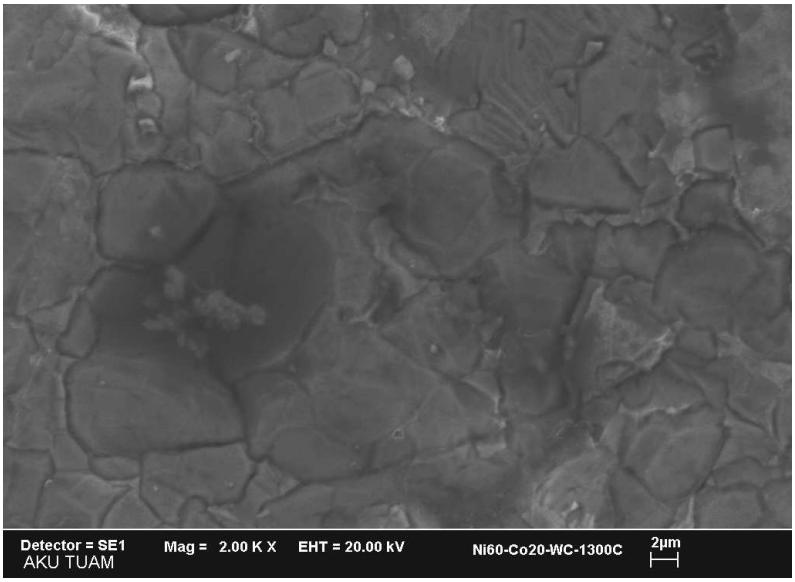

Figure 5. SEM view of (Ni-Co-WC) composite 1,300 °C.

At 1,200 °C, sintered samples SEM pictures shown there are porous which are homogeniusly distrubuted can be seen in Fig. 6. This picture also seems 1,200 °C is not good temperature for sintering.

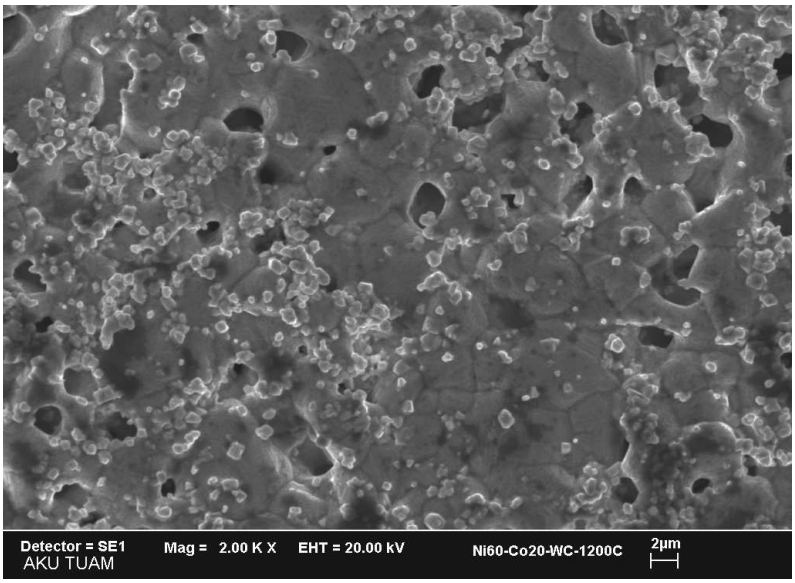

Figure 6. SEM view of (Ni-Co-WC) composite 1,200 °C.

Ni-Co, WC composites are sintered at 1,000 °C , 1,100 °C. The SEM picture Fig. 7 shown some porous unclear phases.

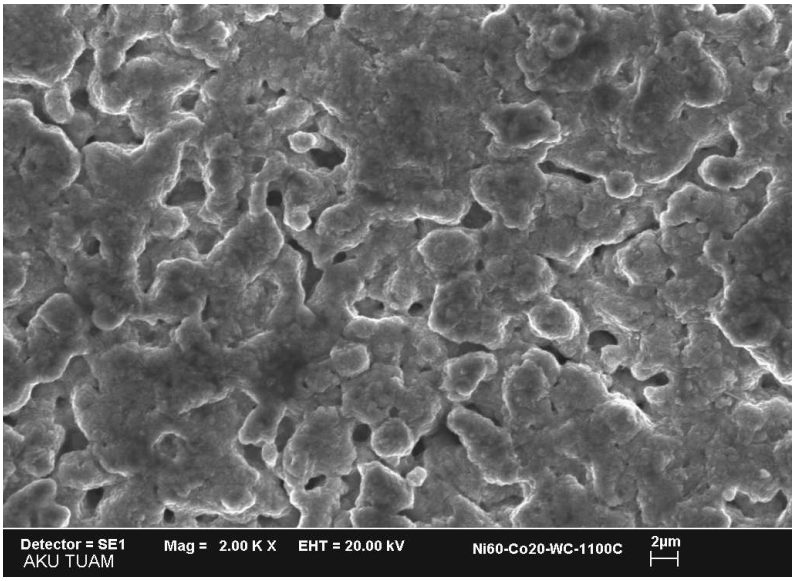

Figure 7. SEM view of (Ni-Co-WC) composite 1,100 °C.

Fig. 8 is a SEM photograph taken at 1,000 °C of the produced sample. It shows the start of the neck formation between particles. Porosity is the moment the samples are more. Grain boundaries are unclear. The density and hardness of samples are the lowest.

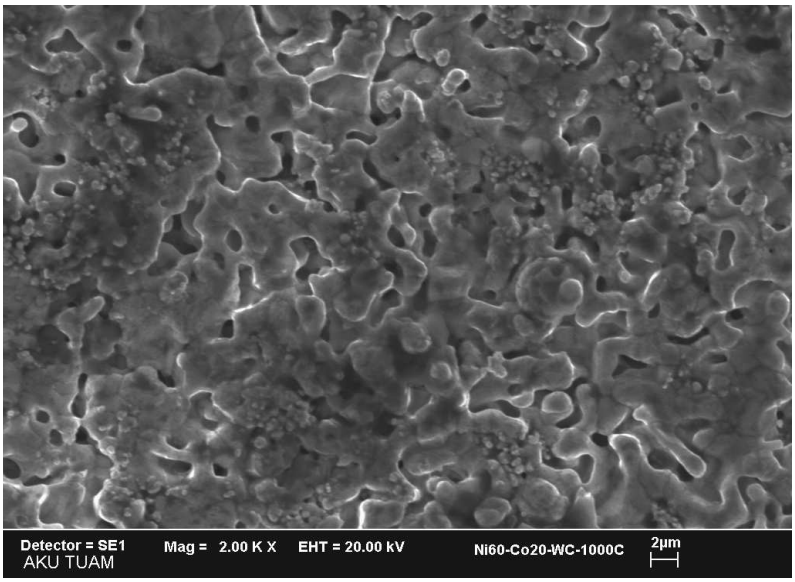

Figure 8. SEM view of (Ni-Co-WC) composite 1,000 °C.

XRD Analysis

After SEM analysis of specimens which are produced at 1,000, 1,100, 1,200, 1,300 and 1,400 °C. It will decide to X-ray analysis taken sample from sintered at 1,400 °C According to the X-ray analysissome pics are determined belong to Ni, NiCo, and WC. It can be seen Fig. 9 The Fig. 9 also shown WC reinforced to NiCo metallic phases.

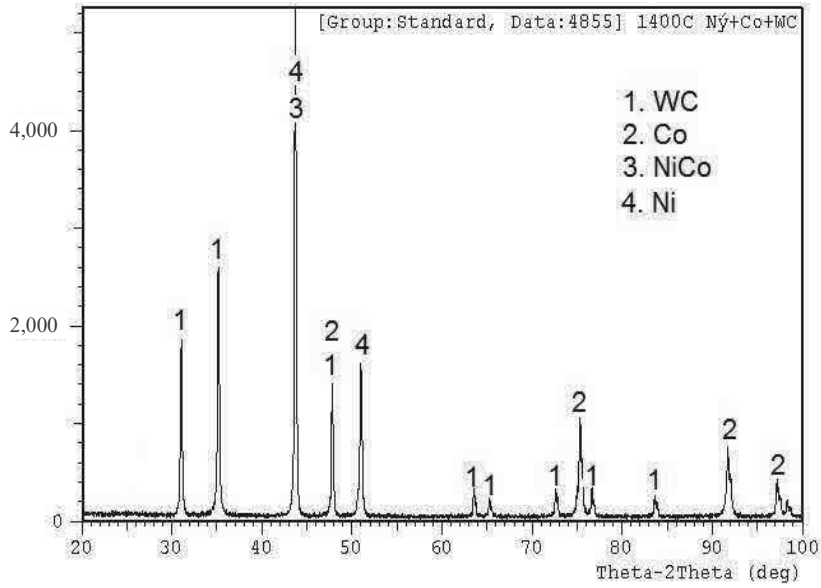

Figure 9. The XRD analysis (Ni-Co-WC) composite Sintered in tube furnace at 1,400 °C.

CONCULUSION

Ni-Co and WC mixture powders were produced samples were investigated. Metal powders are reinforced with ceramic powder. The samples produced at different temperatures were characterized. Ni-Co-WC metallographic analysis of samples produced at 1,300 °C in samples of manufactured sintered powders showed good way. The best sintering temperature of 1,300 °C was found to be investigated compositions.

The following results were concluded from the experimental findings

- The highest density in composite made from (%60Ni-%20Co-%20WC) powders sintered at different temperatures was obtained as 1,400 °C The highest density sample was found as 8, 563 gr cm^{-3} at 1,400 °C.
- The highest microhardness in (%60Ni-%20Co-%20WC) composite samples fabricated using powder metallurgy method was found as 174.16HV at 1,400 °C.
- The highest shear strength in (%60Ni-%20Co-%20WC) composite samples fabricated using powder metallurgy method was found as 85.51MPa at 1,400 °C.
- It was also found out for composition (%60Ni-%20Co-%20WC) at 1,400 °C suggest that the best properties.

ACKNOWLEDGEMENTS This research was supported by the University of Afyon Kocatepe project no: 15.TEKNOLOJI.04 We would like to extend our gratitude to the Scientific Research Coordination Unit.

REFERENCES

Ekemar, S., Lindholm, I. & Hartzcll, T. 1982. Nickel as a binder in WC-based ccmentcd carbides. *Int.I. Refi Metuls & Hard Mater*. **1**, 37–40.

Fiedler, M.-L. & Stadelmaier, H.H. 1975. The ternary system nickel-tungsten carbon. *Z. Metallkde* **66**, 402–404.

Gavriliu, S. & Calu, N. 1979. Etude de *l'oxydation dansl'air du systeme carbure de wolfram-cobalt*. *Bull. Inst. Politechn. Jasi*, **25**(2), 9–16.

Kang, S.G. & Fromm, E. 1981. *Reaction von MO& W2C, WC und WC-Co - Hartmetallen mit Sauerstoff beiHohen Temperaturen*, *Proc. 10th Plansee Seminar* **2**, pp. 679–93.

Kieffer, R. & Kolbl, F. 1950. Uber das Zunderverhalten und der Oxydationsmechanismus warm- und zunderfester Hartlegierungen, insbesondere solcher auf Titankarbid-Basis. *Z. Anorg. Chem*. **262** 229–247.

Koc, R., Kodambake, S.K., Euro, J. 2000. *Ceramic Materyals* **20**, 1859.

Kovalchenko, M.S., Sverdcl, V.V., Cyr Yurchuk, N.A. 1991. *The ultra-fine grained cemented tungsten carbides with a nickel binder. Abstracts Mat-Tech'91* – The Second European Em-West Symposium on Materials and Processes, Helsinki, Finland, p. 1.

Liu, W., Song, X., Zhang, J., Zhang, G., Liu, X. 2008. Thermodynamic Analysis For In Situ Synthesis Of WC–Co Composite Powder From Metal Oxides, *Materials Chemistry And Physics* **109**, 235–240.

Ma, X. M., Ji, G., 1996, Nanostructured WC-Co Alloy Pepared By Mechanical Alloying. *Journal of Alloys And Compounds* **245**, 30–32.

McCandlish, L., Kear, B.H., Kim, B.K., 1992, Processing And Properties Of Nanostructured WC-Co. *Nanostructured Materials* **1**, 119–124.

Nassaj, E.T., Mirhosseini, S.H. 2003. An in situ WC–Ni Composite Fabricated By The SHS Method. *Journal Of Materials Processing Technology* **142**, 422–426.

Shmatko, O.A., Larikov, L.N., Tishkova, T.T. & Tyshkevich, V.M. 1989. Investigation of oxidation kinetics of W-Co and WC-Co alloys. *Zasch. Metall.* **25** 659–60.

Upadhyaya, G.S., Bhaumik, S.K. 1988. Sintering Of Submicron WC–10% Co Hardmetals Containing Ni And Fe. *Materyal Sciences Engineering-A* **249**, 105–106.

Voitovich, R.F. & Pugach, E.A. 1973. Features of hightemperature oxidation of transition metal carbides of VI groups. Poroshk. *Metall*. **4** 59–64.

Voitovich, R.F. 1981. The Oxidation of Carbides and Nitrides. Naukova Dumka, Kiev.

Xiong, Y., Lau, K., Zhou, X., Schoenung, J.M. 2008. A Streamlined Life Cycle Assessment On The Fabrication Of WC-Co Cermets. *Journal of Cleaner Production* **16**, 1118–1126.

Webb, W.W., Norton, J.T. & Wagner, C. 1956. Oxidation studies in metal-carbon systems. *J. Electrochem. Sot.* **103** 112–7.

Zhang, Q., Wul, M. & Wen, Z. 2005. Electroless nickel plating on hollow glass microspheres *Surface & Coatings Technology* **192**, 213–219.

Agronomy Research **14**(Sp.1), 1138–1146, 2016

Low-cyclic fatigue test of adhesive bond reinforced with glass fibre fabric

J. Zavrtálek[1,*], M. Müller[1] and V. Šléger[2]

[1]Czech University of Life Sciences in Prague, Faculty of Engineering, Department of Material Science and Manufacturing Technology, Kamýcká 129, CZ 165 21 Prague, Czech republic
[2]Czech University of Life Sciences in Prague, Faculty of Engineering, Department of Mechanical Engineering, Kamýcká 129, CZ 165 21 Prague, Czech republic
[*]Correspondence: zavrtalek@tf.czu.cz

Abstract. Epoxy resins are widely used polymers, which are popular due to their workability, high tensile strength and a chemical resistance. The glass fibre fabric interlayer was used for improving the tensile and the quasi-.static lap shear strength of joints bonded with an epoxy adhesive.
The aim of the experiment is to clarify a fatigue behaviour (low-cyclic tests of the fatigue) of structural two-component epoxy adhesive applied to a constructional steel S235J0. The fabric was composed from type E glass fibres in a plain weave. For optimization of properties of the composite bond it was used various weights in grams of the fabric in the extent of 80, 110, 160 g m^{-2} for the fabric treated by a wax, where this treatment is determined for better spinning of fibres at the production of the fabric, and weights of grams of 80, 110, 163 g m^{-2} at the fabric with a chemical dressing determined for improving the adhesion between the fibres and the epoxy resin. The specimens for quasi-static and lap shear strength tests were made in accordance with EN 1465:2009. The difference of the saturation of the various types of fabrics with the epoxy adhesive was observed with SEM (Scanning Electron Microscopy). It is obvious from the experiment results that it came to the improvement of the quasi-static loading at all adhesive bonds reinforced with glass fibres. The adhesive bonds specimens A110, A160, B110 and B160 resisted to required 200 cycles at 80% loading. The test specimens without the fabric showed worse properties.

Key words: adhesive bond, low-cycle fatigue, lap-shear strength, two-component epoxy adhesive.

INTRODUCTION

Adhesive bonds are often used in constructions exposed to a cyclic stress. An application of an adhesive bonding technology is limited by a cyclic loading of an adhesive bond (Messler, 2004; Šleger & Müller, 2015).

The adhesive bonding technology is used as a connecting element, e.g. in the constructions of bodies of agricultural machines, automobiles, trains, etc. The machine is exposed to considerable vibrations in the case of a drive of the agricultural machines at the soil processing.

The low cycle fatigue of the adhesive bond can lead to a failure of the bonds (Kelly, 2006; Hafiz et al., 2010). The low-cyclic fatigue of the adhesive bonds has to be analysed for determining limits of the given adhesive bonding technology application (Kelly, 2006; Hafiz et al., 2010).

Service conditions can often involve an exposure to the cyclic fatigue, which is probably the most destructive form of a mechanical loading. The fatigue damage is an irreversible process which can occur at relatively low stress levels due to the presence of high peel and shear stresses at the overlap edges. These stresses reduce both the static strength and the fatigue life of bonded structures (Broughton et al., 1999).

Epoxy resins are widely used polymers, which are popular due to their workability, high tensile strength and a chemical resistance. The glass fibre fabric interlayer was used for improving the tensile and the quasi-static lap shear strength of joints bonded with the epoxy adhesive.

A specific problem with adhesive applications is bad integrity of used adhesive and bonded material caused by defects in the adhesive layer and construction faults (Hafiz et al., 2010). The bond with the irregular thickness of the adhesive layer can´t provide a regular deformation in the adhesive layer under the loading (Messler, 2004; Müller, 2014). This leads to a crack propagation in the adhesive layer under the cyclic loading (Messler, 2004; Hafiz et al., 2010; Müller, 2014), and causes the bond failure (especially the adhesion failure).

To ensure the regular adhesive layer thickness several methods are used, one of them is using particles (Messler, 2004; Müller, 2011; Naito et al., 2012) or fabrics as fillers. It can be expected that using the fibre fabric to make the regular adhesive layer thickness will lead to an improvement of the adhesive bond durability under the cyclic loading.

Glass fibres in a form of the fabric were used within the experiment to reach even layer of the adhesive. Mechanical properties of fibre composite materials depend on a composition of particular layers, their orientation, a specific weight and a chemical treatment (Karbhari & Abanilla, 2007; Maheri, 2010) influencing a wettability. The wettability of the surface is very important aspect of adhesive applications (Rudawska, 2014), that´s why the fabrics treated by a wax and a chemical dressing were used.

MATERIALS AND METHODS

The aim of the experiment is to clarify a fatigue behaviour (low-cyclic tests of the fatigue) of the structural two-component epoxy adhesive applied to a constructional steel S235J0. The aim of the research was to evaluate a service life of the adhesive bond in terms of its fatigue stressing at the quasi-static shear test. The two-component epoxy adhesive cured at the laboratory temperature 22 ± 2 °C was used for bonding test samples.

The fabric was composed from the type E glass fibres in a plain weave. For an optimization of properties of the composite bond it was used various plain weights in grams of the fabric in the extent of 80, 110, 160 g m^{-2} for the fabric treated by a wax (marked as A), where this treatment is determined for better spinning of fibres at the production of the fabric, and weights of grams of 80, 110, 160 g m^{-2} (marked as B) at the fabric with a chemical glaze determined for improving the adhesion between the fibres

and the epoxy resin. The specimens for quasi-static and lap shear strength tests were made in accordance with ČSN EN 1465 (2009).

The surface of the adhesive bonded material was treated by a mechanical treatment – grit blasted F 80 (Al_2O_3) and a chemical treatment. The chemical treatment was performed in a bath of acetone (dimethylketon). Acetone is used for greasing of adhesive bonded surfaces. It is a colourless liquid which is used as a dissolving agent of organic substances.

The blasting was performed in a manual blasting chamber ITB 65 with a foot control of a compressed air. On a reciprocating compressor the pressure was set to 3.5 MPa.

Roughness parameters Ra and Rz were measured on the surface of adherents designed for the bonding. Roughness parameters were measured with a portable profilometer Mitutoyo Surftest 301. A limit wavelength cut-off was set at 0.8 mm.

After the described surface preparation method, the adhesive material was applied and the adhesive bond was loaded with a weight of 495 ± 5 g under laboratory conditions with the temperature 22 ± 2 °C. The lapping was according to the standard 12.5 ± 0.25 mm.

One batch of samples was bonded only with the adhesive. The fabric with glass fibres was applied into the adhesive bond in other series and so called 'composite layer' came into being. Parameters warp and weft at used fabrics were following: 80 g m^{-2} 12 x 12 cm, 110 g m^{-2} 16 x 15 cm and 160 g m^{-2} 12 x 12 cm.

Laboratory tests were performed using the universal tensile strength testing machine LABTest 5.50ST (a sensing unit AST type KAF 50 kN, an evaluating software Test & Motion). The failure type according to ISO 10365 was determined at the adhesive bonds.

Six test specimens were tested in each batch. The reference value of the adhesive bond strength was determined for each tested adhesive according to the standard ČSN EN 1465. The upper and lower limits for low-cyclic tests were calculated from the average value.

The test specimens were cyclically loaded in a such way the loading tension pulsated between the minimum value determined from the reference strength of the adhesive bond without the fabric (i.e. 5%) and chosen percentage value 60% and 80% from the reference strength of the adhesive bond without the fabric (average maximum strength values determined according to the ČSN EN 1465). The loading speed was always set at 6 mm min^{-1}. The endurance at the maximum and minimum force was 1 s. The number of cycles was 200. In a case that the failure did not occur during the cycling, the cycling was automatically stopped after 200 cycles. In the case that the adhesive bond was not destructive damaged after 200 cycles, the adhesive bond was subsequently broken, i.e. the testing machine developed a force by the speed 6 mm min^{-1} as long as the test specimens were broken.

Statistical hypotheses were also tested at measured sets of data by means of the program STATISTICA. A validity of the zero hypothesis (H_0) shows that there is no statistically significant difference ($p > 0.05$) among tested sets of data. On the contrary, the hypothesis H_1 denies the zero hypothesis and it says that there is a statistically significant difference among tested sets of data or a dependence among variables ($p < 0.05$).

The difference of the saturation of the various types of fabrics with the epoxy adhesive was observed with SEM (Scanning Electron Microscopy).

RESULTS AND DISCUSSION

The Fig. 1 presents the strength results after the cyclic loading. The results show that examined specimens reach variable values of the static bond strength (marked as 0 cycles) in the interval 11.6 to 14.4 MPa. The adhesive bonds reinforced with various types of the fabric reach significantly better values of the static strength than the bonds without the fabric. The increase of the static strength was about 20%. More significant increase of the static strength was observed in the bonds reinforced with the fabric marked as the type B, i.e. with the chemical dressing.

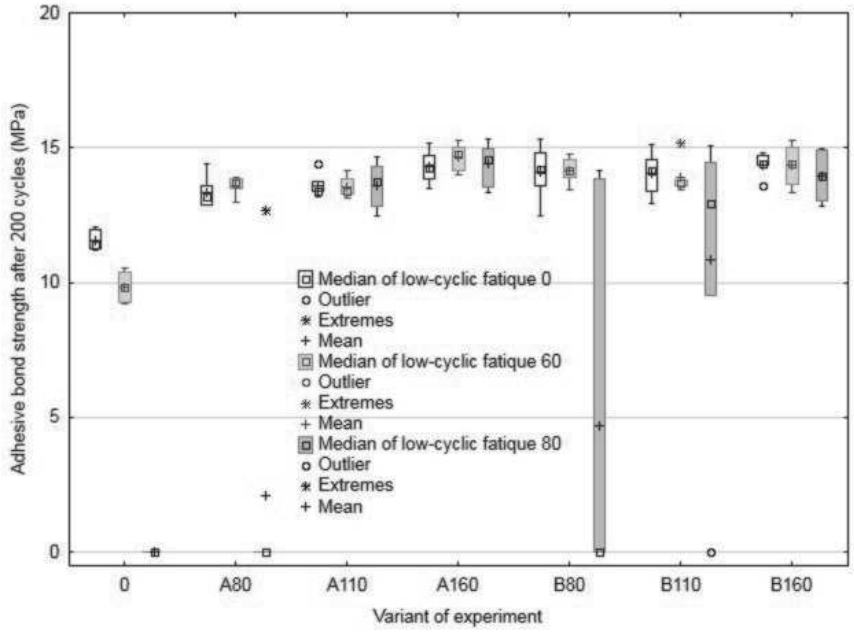

Figure 1. Influence of low-cycle fatigue on adhesive bond strength.

Other results showed in Fig. 1 represent the values of the bond strength after the quasi-static testing, i.e. the low cycle fatigue after reaching 200 cycles. It is evident from the results that there is no significant change in the bond strength after the quasi-static testing at 60% of the reference strength. An average decrease of the bond strength was 1.3%. A significant decrease was observed at adhesive bonds without the glass fibre fabric, it is 15.5%.

The significant changes of the maximum bond strength were observed in the quasi-static testing at 80% of the reference strength. Only adhesive bonds reinforced with glass fibre fabrics of types A110, A160 and B160 reached 200 cycles (Fig. 2). Other variants of adhesive bonds were destroyed before reaching 200 cycles and the final bond strength couldn´t be measured. The number of cycles absorbed by adhesive bonds is presented in Fig. 2.

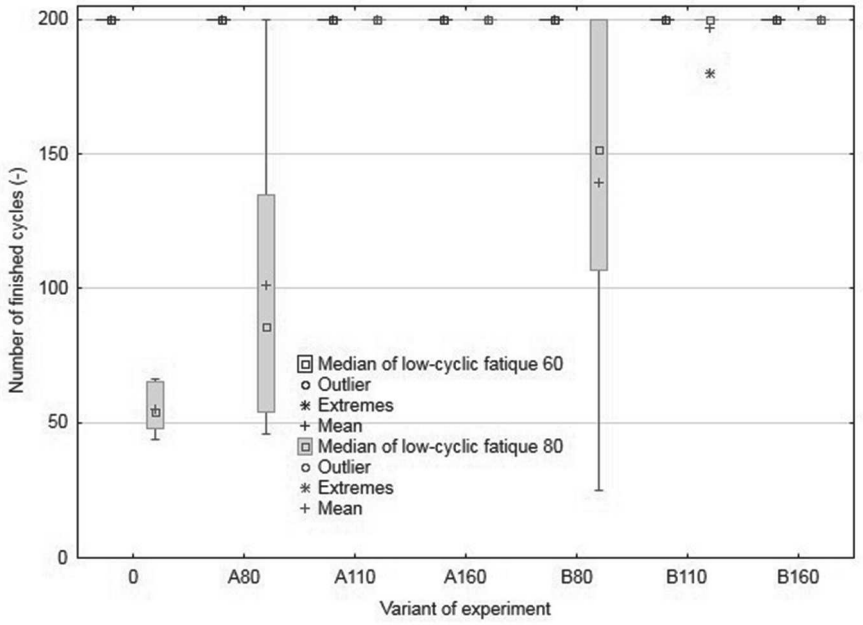

Figure 2. Influence of low-cycle fatigue of adhesive bonds on number of finished cycles

Adhesive bonds which weren´t reinforced with glass fibre fabrics were able to absorb 55 ± 9 cycles of 200. The results show that adhesive bonds without fabrics badly resist to the low-cycle fatigue under the repeated stress at 80% of the reference strength.

In terms of the influence of the quasi-static testing on the bond strength, the results of ANOVA F-test are following:

The hypothesis H_0 was not confirmed when comparing all variants of the low-cycle fatigue of the adhesive bond under 60% ($p = 0.0000$) and 80% ($p = 0.0000$) in the significant level 0.05, i.e. there is a difference among single tested variants of the adhesive bonds 0, A80, A110, A160, B80, B110, B160. It was demonstrated that the type and the plain weight of the glass fibre fabric used as the reinforcing layer has the effect on the adhesive bond strength under the quasi-static loading.

The hypothesis H_0 was confirmed when comparing the low-cycle fatigue of the adhesive bond under 0, 60% and 80% for experiments A110 ($p = 0.9722$), A160 ($p = 0.6141$), B110 ($p = 0.1988$) and B160 ($p = 0.5072$), i.e. there is no difference among single tested variants in the significance level 0.05. It is not statistically proved any effect of the type and the plain weight of the glass fibre fabric used as the reinforcing layer on the low-cycle fatigue strength of the adhesive bond.

The hypothesis H_0 was not confirmed for the low-cycle fatigue under 80% load, i.e. there is a difference among single tested variants 0, A80, A110, A160, B80, B110 and B160 depending on the reached number of cycles. It was demonstrated that the type and the plain weight of the glass fibre fabric used as the reinforcing layer has the effect on the adhesive bond strength under the quasi-static loading in the significance level 0.05.

The hypothesis H_0 was confirmed for the low-cycle fatigue at 60% load, i.e. there is no difference among single tested variants 0, A80, A110, A160, B80, B110 and B160 depending on the reached number of cycles. It is not statistically proved any effect of the

type or the plain weight of the glass fibre fabric on the low-cycle fatigue strength of the adhesive bond.

The testing process is presented on the diagrams below. Fig. 3 represents the quasi-static testing at 60% of the reference strength of the adhesive bond. If the test reaches 200 cycles, the bond is then destroyed by the static loading.

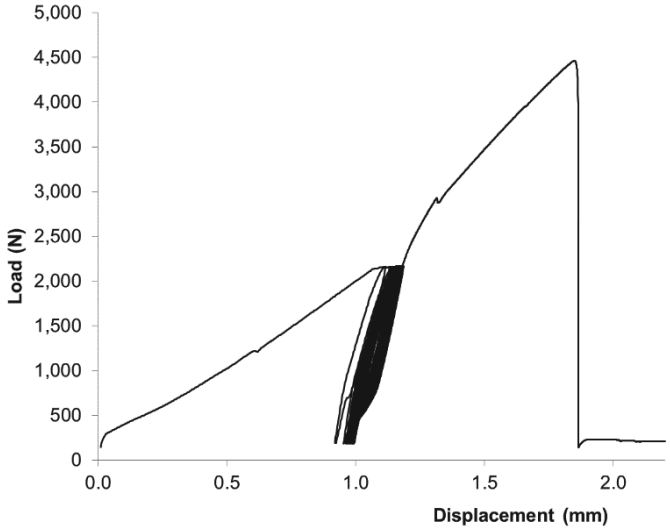

Figure 3. Quasi-static testing (60%, A110, 200 cycles).

Fig. 4 shows the typical quasi-static testing proces at 80% load of the reference strength before reaching 200 cycles, i.e. the bond was destroyed before reaching 200 cycles.

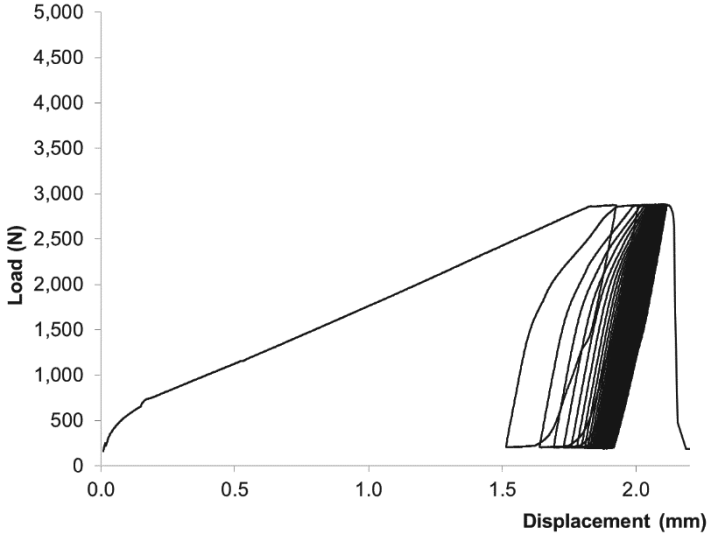

Figure 4. Quasi-static testing (80%, A80, 46 cycles).

Fig. 5 shows typical quasi-static testing proces at 80% load of the reference strength, i.e. the bond reached 200 cycles.

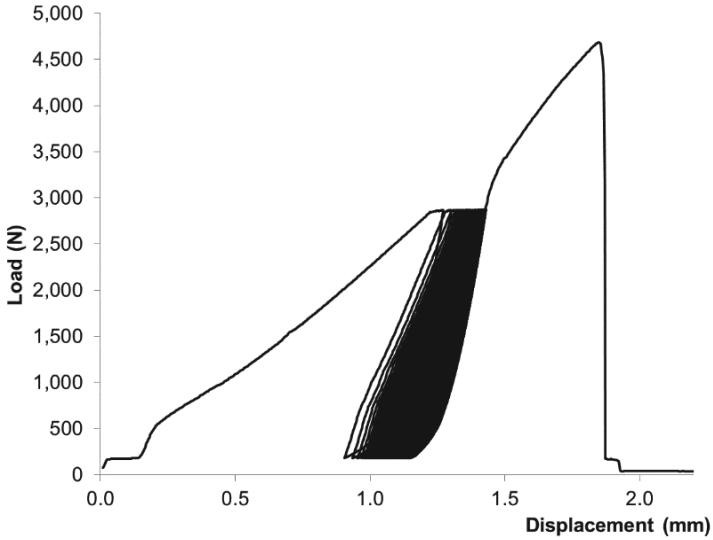

Figure 5. Quasi-static testing (80%, A110, 200 cycles).

The effect of the quasi-static loading on the fracture surface wasn´t proved. Only the adhesion type of the fracture surface was observed (Fig. 6). The glass fibre fabric wetted with the adhesive is visible in Fig. 6. This layer was divided from the adhesive bonded material.

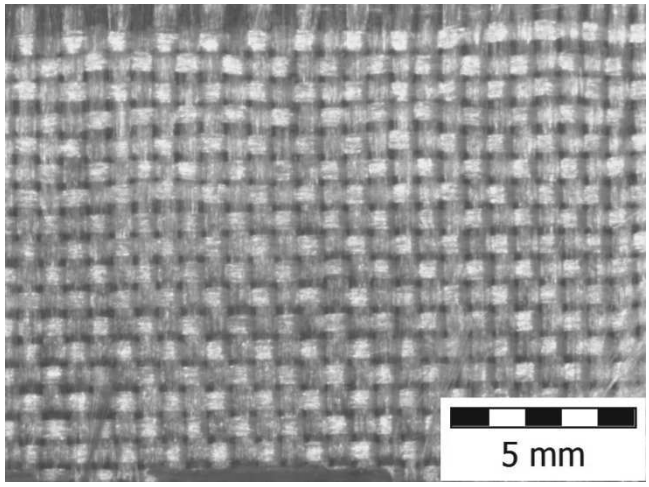

Figure 6. Typical fracture surface – cohesive type of failure of adhesive bond.

The results show that the quasi-static loading with high loads (Broughton et al., 1999; Šleger & Müller, 2015) (f.e. 80% of the reference strength) can lead to early failure of the adhesive bond at low number of cycles. The reason is a cumulative effect of the

cyclic shear stress. The experiment results proved that this cumulative effect can be reduced using the glass fibre fabric layer in the adhesive bond.

Fig. 7 (a, b) show a cut through the composite adhesive bond with the use of the electron microscope Tescan Mira 3. Fig. 7a presents a layout of the glass fibre layer in the adhesive bond cut. They are crossed fibres. Using the electron microscopy within the experimental research a good interaction of the glass fibres with the matrix in the form of the epoxy was proved.

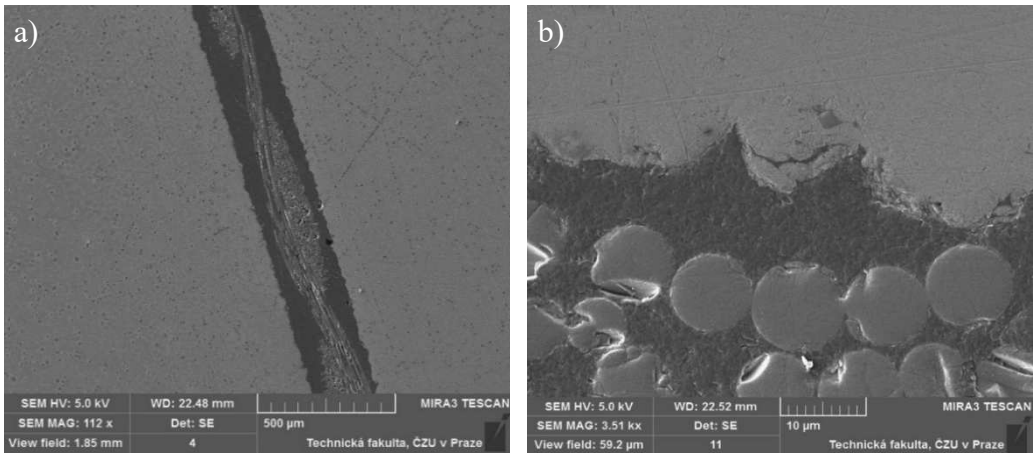

Figure 7. SEM images of cut of composite adhesive bond – type B160.

It was proved that the adhesive wetted the inserted layer of the glass fibre fabric. The failure of the cohesiveness between the adhesive and the reinforcement which is notified by Ashcroft et al. (Ashcroft et al., 2001) in their research was not confirmed within the research.

Fig. 7a shows the regular thickness of the adhesive layer in the bond, the violence of the measured thickness was only 6% from the average value 185 µm. The layer thickness at adhesive bonds without the glass fibre fabric interlayer wasn´t regular. The ireegular layer of the adhesive decreases the strength of the adhesive bond (Kotousov, 2007; Grant et al., 2009; Müller, 2014).

CONCLUSIONS

The experiment results proved the improvement of the bond strength under the quasi-static loading at all adhesive bonds reinforced with the glass fibre fabric. Adhesive bonds reinforced with the glass fibre fabric of types A110, A160, B110 (197 cycles) and B160 succesfully reached 200 cycles under 80% load. The test specimens without the fabric showed worse properties. Adhesive bonds reinforced with the glass fibre fabric of the type A80 resisted to 101 ± 53 cycles and B80 resisted to 139 ± 61 cycles of the quasi-static loading under 80% load. The test specimens without the fabric resisted to only 55 ± 9 cycles of the quasi-static loading under 80% load.

Good interaction between the glass fibres and the epoxy adhesive matrix was confirmed based on conclusions from the mechanical testing and microscopy results.

The effect of various plain weights of the glass fibre fabric on the quasi-static strength of adhesive bonds wasn´t confirmed.

A use of the interlayer from the glass fibre fabrics increases the endurance to the low-cycle fatigue comparing to the normal adhesive bond. The glass fibre fabric interlayer acts against the crack propagation in the adhesive bond. It can be assumed that the fabric geometry and the plain weight have the effect on blocking of the crack propagation too.

REFERENCES

Ashcroft, I.A., Hughes, D.J. & Shaw, S.J. 2001. Mode I fracture of epoxy bonded composite joints: 1. Quasi-static loading. *International Journal of Adhesion and Adhesives* **21**(2), 87–99.

Broughton, W.R., Mera, R.D., Hinopoulos, G., for Materials Measurement, N.P.L. (Great B.C., & Technology. 1999. *The Performance of Adhesive Joints: Project PAJ3 – Combined Cyclic Loading and Hostile Environments 1996-1999; Report No. 8 – Cyclic Fatigue Testing of Adhesive Joints Test Method Assessment*. National Physical Laboratory. Great Britain, Centre for Materials Measurement and Technology. Retrieved from https://books.google.cz/books?id=rJUYMwEACAAJ

Grant, L.D.R., Adams, R.D., & da Silva, L.F.M. 2009. Experimental and numerical analysis of single-lap joints for the automotive industry. *International Journal of Adhesion and Adhesives* **29**(4), 405–413.

Hafiz, T.A., Abdel Wahab, M.M., Crocombe, A.D., & Smith, P.A. 2010. Mixed-mode fracture of adhesively bonded metallic joints under quasi-static loading. *Engineering Fracture Mechanics* **77**(17), 3434–3445.

Karbhari, V.M., & Abanilla, M.A. 2007. Design factors, reliability, and durability prediction of wet layup carbon/epoxy used in external strengthening. *Composites Part B: Engineering* **38**(1), 10–23.

Kelly, G. 2006. Quasi-static strength and fatigue life of hybrid (bonded/bolted) composite single-lap joints. *Composite Structures* **72**(1), 119–129.

Kotousov, A. 2007. Effect of a thin plastic adhesive layer on the stress singularities in a bi-material wedge. *International Journal of Adhesion and Adhesives* **27**(8), 647–652.

Maheri, M.R. 2010. The effect of layup and boundary conditions on the modal damping of FRP composite panels. *Journal of Composite Materials* **45**(13), 1411–1422.

Messler, R.W. 2004. *Joining of Materials and Structures*. *Joining of Materials and Structures*. Elsevier. http://doi.org/10.1016/B978-075067757-8/50000-2

Müller, M. 2011. Influence of surface integrity on bonding process. *Research in Agricultural Engineering* **57**(4), 153–162.

Müller, M. 2014. Setting of causes of adhesive bonds destruction by means of optical analysis. *Manufacturing Technology* **14**(3), 371–375.

Naito, K., Onta, M., & Kogo, Y. 2012. The effect of adhesive thickness on tensile and shear strength of polyimide adhesive. *International Journal of Adhesion and Adhesives* **36**, 77–85.

Rudawska, A. 2014. Selected aspects of the effect of mechanical treatment on surface roughness and adhesive joint strength of steel sheets. *International Journal of Adhesion and Adhesives* **50**, 235–243.

Šleger, V. & Müller, M. 2015. Quasi static tests of adhesive bonds of alloy AlCu4Mg. *Manufacturing Technology* **15**(4), 694–698.

Agronomy Research **14**(Sp.1), 1147–1152, 2016

Hybrid aspen clone wood mechanical properties

M. Zeps[1,*], A. Gailis[1], J. Smilga[1], O. Miezite[2], L. Sisenis[2] and I. Zariņa[1]

[1]Latvian State Forest Research Institute 'Silava', Rigas 111, Salaspils, LV 2169, Latvia
[2]Latvia University of Agriculture, Forest Faculty, Akademijas 11, LV 3001 Jelgava, Latvia
[*]Correspondence: martins.zeps@silava.lv

Abstract. The hybrid aspen is believed to be a suitable alternative to the European aspen for raw material supply, but information on its wood properties and their variations among clones is lacking. Nevertheless, its fast growth is associated with a decrease of wood density and mechanical strength. The aim of the study was to assess wood mechanical properties of the hybrid aspen clones and their relationship with growth traits. The tree height and diameter at breast height (DBH), basic wood density, compressive strength, modulus of rupture (MOR), and modulus of elasticity (MOE) were measured for three sample trees from 22 hybrid aspen clones and one common aspen clone. Significant (all $P < 0.001$) differences of assessed wood properties and growth traits were found among the hybrid aspen clones. At the clone mean level, compressive strength ranged from 26.6 ± 1.3 to 36.7 ± 0.8 N mm^{-2} and MOR and MOE were from 57.9 to 74.5 N mm^{-2} and from 7338.5 to 9734.6 N mm^{-2}, respectively. The mean wood density was 383 ± 3.1 kg cm^{-2}. It correlated significantly ($P < 0.001$) with MOR ($r = 0.66$), MOE ($r = 0.63$), and compressive strength ($r = 0.71$) at the individual tree level. All mechanical properties of the wood showed non-significant (all $P > 0.05$) correlation with growth traits. Therefore, selection of fast-growing clones will not interfere with the mechanical quality of wood. However, the suitability for structural applications should be cautiously tested due to the clonal variations.

Key words: *P. tremula* × *P. tremuloides*, basic wood density, bending strength, compressive strength.

INTRODUCTION

European aspen (*Populus tremula*) wood is used for high quality niche products as well as bulk or pulp and paper production, while its logging residues are suitable for bioenergy (Junkkonen & Heräjärvi, 2007; Bjurhager et al., 2008). The proportion of the available assortments (providing most of the financial income) is reduced, mainly due to wood discoloration, heart rot, and browsing (Borrega et al., 2009; Myking et al., 2011; Zeps et al., 2016). The hybrid *P. tremula* × *P. tremuloides* has similar or superior growth in comparison to other tree species or hybrids (Jansons, 2013, 2014a) as well as to its parental species (Yu et al., 2001), allowing the reduction of the rotation period to ca. 20 years (Rytter & Stener, 2005) in order to continuously select clones able to produce the highest increment in particular climatic conditions (Jansons et al., 2014b; Šēnhofa et al., 2016) and to further increase the increment with fertilisation (Bardule et al., 2013). Due to the fast growth and relatively short rotation in comparison to native species, the hybrid

aspen has been increasingly planted in northern Europe (Tullus et al., 2012). It has similar wood properties to the European aspen (Junkkonen & Heräjärvi, 2007); therefore, it might be used as a suitable alternative to raw material supply. A number of mechanical properties are genetically determined (Zobel & Buijtenen, 2012), but rapid growth is associated with decreased wood density, which might limit wood processing possibilities. However, this relationship notably differs between species (Zhang, 1995) and might also differ between hybrid aspen clones. Therefore, the aim of the study was to assess (1) the mechanical properties of the wood of the hybrid aspen clones and (2) their relationship with growth traits.

MATERIALS AND METHODS

The study site is located in the central part of Latvia, near Iecava (56°60′ N, 24°15′ E), established with the initial density of 2500 trees ha^{-1}. At the age of 12 years, tree height and diameter at breast height (DBH) were measured for 22 hybrid aspen (*Populus tremula* L. × *P. tremuloides* Michx.) clones and one European aspen (*P. tremula* L.) clone, each represented by three to 49 trees. Afterwards, three sample trees (ramets) from each clone were cut. The sample trees were randomly selected from three diameter groups: close to the average, smallest diameter quartile, and largest diameter quartile of the particular clone. From each sample tree, the stem section was cut from the height of 1.3–3.3 m. These sections were dried to 10.6 ± 0.06% moisture content. Afterwards, from each section, samples of a precise size of the clear wood (without defects) were cut. For compressive strength, the size of the cut sample was 20 × 20 × 30 mm. For bending strength, represented by the modulus of rupture (MOR) and modulus of elasticity (MOE), the size of the sample was 20 × 20 mm transversely and 360 mm longitudinally. In total, 275 samples from 23 clones and 94 samples from eight clones were measured for compressive and bending strength, respectively. Each clone was represented by 10–15 wood samples for compressive strength and 10–15 wood samples for MOR and MOE. The parallel-to-grain compressive strength was measured according to standard DIN 52185, and the parallel-to-grain bending strength was measured according to standard DIN 52186. For each sample, basic wood density and moisture content were measured.

The Shapiro-Wilk test was used to assess the normality of the data. The one-way analysis of variance was used to assess differences of basic wood density, compressive strength, MOR, MOE, tree height, and DBH among the clones. Pearson's correlation was used to assess the relationship between the measured parameters among the clones. All tests were performed at $\alpha = 0.05$. All calculations were done in R 3.0.2. (R Core Team, 2013).

RESULTS AND DISCUSSION

The suitability of wood for certain types of production depends on its mechanical properties, namely wood density and bending and compressive strength (Bjurhager et al., 2008; Groover et al., 2010). In our study, the basic density of clones was from 337 ± 14 to 432 ± 16 kgm^{-3} (Table 1), which is considered relatively low in comparison to other species in the region (Rytter et al., 2013). Our results are in range of previously

reported values for European and hybrid aspens. The latter tend to have lower basic density, while noticeable variations between studies occur. For instance, Bjurhager et al. (2008) found wood density to be 211 and 284 kg m^{-3} for hybrid and European aspens, respectively; Heräjärvi & Junkkonen (2006) reported densities of 376 and 363 kg m^{-3}. Similarly, Hart et al. (2013) found higher wood densities for intraspecific crossings between *P. tremula* clones (436.2 kg m^{-3}) in comparison to hybrid aspens (413.3 kg m^{-3}). Density variation ($P < 0.001$) was found among the clones, also confirmed by other studies (Zhang et al., 2003; Pliura et al., 2007).

Table 1. Mean values and confidence intervals of measured mechanical properties and growth traits of clones

Clone	Basic density, kg m^{-3}	Compressive strength, N mm^{-2}	MOR, N mm^{-2}	MOE, N mm^{-2}	Height, m	DBH, cm
34	432 ± 16.4	35.8 ± 1.40			15.6 ± 0.41	12.8 ± 0.73
26	422 ± 10.8	34.1 ± 0.93			13.9 ± 1.82	12.6 ± 2.41
36	422 ± 16.0	35.3 ± 2.04			15.4 ± 0.54	10.8 ± 0.59
4	420 ± 7.1	36.6 ± 2.24	74.5 ± 3.27	9735 ± 469.4	17.4 ± 0.48	13.8 ± 0.80
9	412 ± 10.0	36.7 ± 0.79			17.2 ± 0.33	13.4 ± 0.62
20	398 ± 8.6	34.8 ± 1.52			16.1 ± 0.49	13.7 ± 0.82
22	394 ± 6.1	34.2 ± 0.61	70.5 ± 5.08	8532 ± 584.8	16.0 ± 0.57	13.5 ± 0.94
15	394 ± 12.2	32.5 ± 2.30			16.2 ± 0.62	12.7 ± 1.00
19	393 ± 8.5	34.2 ± 0.93	67.0 ± 4.03	8242 ± 351.0	16.7 ± 0.53	13.4 ± 0.74
24	391 ± 6.3	34.8 ± 0.66			14.4 ± 0.66	11.6 ± 1.11
27	387 ± 9.8	30.9 ± 1.18	66.7 ± 1.80	8586 ± 273.5		
6	386 ± 8.7	31.5 ± 1.38			16.1 ± 0.27	12.1 ± 0.66
16	385 ± 9.4	33.7 ± 0.96			16.5 ± 0.31	13.9 ± 1.01
21	373 ± 8.0	33.0 ± 1.17			14.0 ± 1.12	10.6 ± 2.90
10	373 ± 4.4	32.4 ± 1.07	66.7 ± 2.77	7660 ± 245.0	16.7 ± 0.51	14.2 ± 0.87
12	373 ± 12.9	32.0 ± 1.11			14.0 ± 0.68	12.5 ± 0.91
25	372 ± 4.7	32.4 ± 1.01	64.2 ± 2.65	8045 ± 362.9	15.4 ± 0.67	12.5 ± 1.37
EA	371 ± 6.9	30.3 ± 1.10			14.7 ± 0.62	11.2 ± 1.01
3	366 ± 7.8	29.0 ± 0.49			15.7 ± 0.55	12.1 ± 0.80
41	362 ± 5.0	32.2 ± 0.98	64.1 ± 2.63	8068 ± 175.5		
28	353 ± 17.6	28.5 ± 1.78			14.2 ± 0.78	11.2 ± 0.69
30	341 ± 5.1	29.7 ± 1.16	57.9 ± 1.95	7338 ± 534.4	16.0 ± 0.45	14.0 ± 0.71
2	337 ± 14.2	26.6 ± 1.31			15.1 ± 0.4	14.1 ± 1.11
EA	371 ± 6.9	30.3 ± 1.10			14.7 ± 0.62	11.2 ± 1.01
mean	383 ± 3.1	32.6 ± 0.39	66.2 ± 1.38	8262 ± 193.4	15.7 ± 0.20	12.7 ± 0.15

EA – European aspen.

The MOR and MOE represent the bending strength and stiffness of wood, respectively. The MOR and MOE varied from 57.9 to 74.5 N mm^{-2} and from 7338.5 to 9734.6 N mm^{-2} (Table 1). Our results are somewhat higher than the mean values reported by Peters et al. (2002) for 11 hybrid poplar clones: 52.3 and 5680 N mm^{-2}, respectively. Results similar for MOR (53 to 62 N mm^{-2}) but lower for MOE (5314 to 6732 N mm^{-2}) were observed by De Boever et al. (2007) for *P. trichocarpa* × *P. deltoides* clones. Yet, significant (both $P < 0.001$) differences for both parameters among the clones were found in our study, also noted between other *Populus* hybrids

and their clones (Carlson & Berger, 1998; Peters et al., 2002; De Boever et al., 2007). Like the other mechanical traits, the compressive strength showed significant differences between clones ($P < 0.001$) and was from 26.6 ± 1.3 to 36.7 ± 0.8 N mm^{-2}.

Wood density correlated significantly (all $P < 0.001$) with other mechanical properties at the individual tree level; the correlation coefficients were 0.66, 0.63, and 0.71 for MOR, MOE, and compressive strength, respectively. Similarly, a strong relation between density and MOR and MOE was found at the clone level (De Boever et al., 2007). A strong ($r = 0.84$, $P < 0.001$) correlation between MOE and MOR was found, as observed for other diffuse porous hardwoods (Heräjärvi, 2004).

The DBH and height showed significant (both $P < 0.001$) differences between clones and was from 10.6 ± 2.9 to 14.2 ± 0.9 cm and from 13.9 ± 1.8 to 17.4 ± 0.5 m, respectively. None of the clones showed noticeable superiority of DBH, while few clones (e.g., Clone 36) had significantly lower DBH than the mean of the rest of the clones. The height variation was more pronounced — several clones (e.g., Clones 12 and 24) were significantly lower, but Clone 4 and Clone 9 significantly exceeded most of the other clones. However, no significant relation between growth (DBH and height) and mechanical parameters was found at the clone mean level (Table 2). This is consistent with other findings that indicate a non-significant relationship between wood density and DBH or height for hybrid aspen (Ilstedt & Gullberg, 1993), *Populus xiaohei* (Jiang et al., 2007), and several other *Populus spp*. hybrids (Zhang et al., 2003). No clear relation between growth rate and wood density has been found for other diffuse porous hardwoods (Zhang, 1995) and, in specific cases, also for clones of softwoods (Jansons et al., 2016). In contrast, other studies reported negative significant relations between density and growth traits for *Populus* × *euramericana* clones (Hernández et al., 1998) as well as for several other *Populus spp*. clones (Pliura et al., 2007).

Table 2. Pearson's correlation coefficients and their *p*-value for the wood properties and growth traits at the clone mean level

Growth traits	Basic density		Compressive strength		MOR		MOE	
	r	*P*	*r*	*P*	*r*	*P*	*r*	*P*
DBH	-0.05	0.39	0.08	0.72	0.02	0.97	-0.09	0.87
H	0.26	0.26	0.37	0.10	0.62	0.19	0.60	0.21

CONCLUSIONS

Significant (all $P < 0.001$) differences of assessed wood properties (basic density, compressive strength, MOR, and MOE) and growth traits (tree height and DBH) were found among the hybrid aspen clones. All mechanical properties of wood significantly intercorrelated (all $P < 0.001$) and showed non-significant (all $P > 0.05$) correlation with growth traits. Therefore, the results suggest that selection of fast-growing clones will not interfere with the mechanical quality of the wood. However, the suitability for structural applications should be cautiously tested due to clonal variations.

ACKNOWLEDGEMENTS. This study was funded by the Latvian Council of Science project 'Adaptive capacity of forest trees and possibilities to improve it' (No 454/2012).

REFERENCES

Bardule, A., Rancane, S., Gutmane, I., Berzins, P., Stesele, V., Lazdina, D. & Bardulis, A. 2013. The effect of fertiliser type on hybrid aspen increment and seed yield of perennial grass cultivated in the agroforestry system. *Agronomy Research* **11**(1), 13–24.

Bjurhager, I. 2008. *Mechanical behaviour of hardwoods: effects from cellular and cell wall structures*. Department of Fibre and Polymer Technology, Royal Institute of Technology (KTH), Stockholm, Sweden, 37 pp.

Boever De, L., Vansteenkiste, D., Van Acker, J. & Stevens, M. 2007. End-use related physical and mechanical properties of selected fast-growing poplar hybrids (Populus trichocarpa× P. deltoides). *Ann. For. Sci.* **64**(6), 621–630.

Borrega, M., Nevalainen, S. & Heräjärvi, H. 2009. Resistance of European and hybrid aspen wood against two brown-rot fungi. *Eur. J. Wood Wood Prod.* **67**(2), 177–182.

Carlson, M. & Berger, V. 1998. *Solid Wood Products Opportunities from Short Rotation Hybrid Poplar Trees. April 1, 1997 – September 1998, Final Report*. Ministry of Forests Kalamalka Forestry Centre Vernon, B.C., 14 pp.

Groover, A.T., Nieminen, K., Helariutta, Y. & Mansfield, S.D. 2010. Wood formation in Populus. In Jansson S., Bhalerao R.P. & Groover A.T. (eds.): *Genetics and Genomics of Populus*. Springer Science+Business Media, 201–114.

Hart, J.F., de Araujo, F., Thomas, B.R. & Mansfield, S.D. 2013. Wood quality and growth characterization across intra-and inter-specific hybrid aspen clones. *Forests* **4**(4), 786–807.

Hernández, R.E., Koubaa, A., Beaudoin, M. & Fortin, Y. 1998. Selected mechanical properties of fast-growing poplar hybrid clones. *Wood Fiber Sci*. **30**(2), 138–147.

Heräjärvi, H. & Junkkonen, R. 2006. Wood density and growth rate of European and hybrid aspen in southern Finland. *Balt. For*. **12**(1), 2–8.

Heräjärvi, H. 2004. Static bending properties of Finnish birch wood. *Wood Sci. Technol*. **37**(6), 523–530.

Ilstedt, B. & Gullberg, U. 1993. Genetic variation in a 26-year old hybrid aspen trial in southern Sweden. *Scand. J. For. Res*. **8**(1–4), 185–192.

Jansons, Ā., Matisons, R., Krišāns, O., Džeriņa, B. & Zeps, M. 2016. Effect of initial fertilization on 34-year increment and wood properties of Norway spruce in Latvia. *Silva Fennica* **50**, id 1346, 8 p.

Jansons, A., Sisenis, L., Neimane, U. & Rieksts-Riekstiņš, J. 2013. Biomass production of young lodgepole pine (*Pinus contorta* var. *latifolia*) stands in Latvia. *iForest – Biogeosciences and Forestry* **6**, 10–14.

Jansons, Ā., Zeps, M., Rieksts-Riekstiņš, J., Matisons, R. & Krišāns, O. 2014b. Height increment of hybrid aspen *Populus tremuloides* × *P. tremula* as a function of weather conditions in south-western part of Latvia. *Silva Fennica* **48**, id 1124, 13 p.

Jansons, A., Zurkova, S., Lazdina, D. & Zeps, M. 2014a. Productivity of poplar hybrid (*Populus balsamifera* x *P. laurifolia*) in Latvia. *Agronomy Research* **12**(2), 469–478.

Jiang, Z.H., Wang, X.Q., Fei, B.H., Ren, H.Q. & Liu, X.E. 2007. Effect of stand and tree attributes on growth and wood quality characteristics from a spacing trial with Populus xiaohei. *Ann. For. Sci*. **64**(8), 807–814.

Junkkonen, R. & Heräjärvi, H. 2007. Physical properties of European and hybrid aspen wood after three different drying treatments. In Kurjatko S., Kúdela J., Lagaňa R. (eds.): *Wood structure and properties'06*. Arbora Publishers, Zvolen, Slovakia, 257–264.

Myking, T., Bøhler, F., Austrheim, G. & Solberg, E.J. 2011. Life history strategies of aspen (*Populus tremula* L.) and browsing effects: a literature review. *Forestry* **84**(1), 61–71.

Peters, J.J., Bender, D.A., Wolcott, M.P. & Johnson, J.D. 2002. Selected properties of hybrid poplar clear wood and composite panels. *Forest Prod. J*. **52**(5), 45–54.

Pliura, A., Zhang, S.Y., MacKay, J. & Bousquet, J. 2007. Genotypic variation in wood density and growth traits of poplar hybrids at four clonal trials. *For. Ecol. Manage.* **238**(1), 92–106.

R Core Team. 2013. *R: A language and environment for statistical computing*. R Foundation for Statistical Computing, Vienna, Austria. URL http://www.R-project.org/.

Rytter, L., Johansson, K., Karlsson, B. & Stener, L.G. 2013. Tree species, genetics and regeneration for bioenergy feedstock in northern Europe. In Kellomäki S., Kilpeläinen A. & Alam A. (eds.): Fo*rest BioEnergy Production. Management, Carbon Sequestration and Adaptation*. Springer Science+Business Media NewYork, 268 pp.

Rytter, L. & Stener, L.G. 2005. Productivity and thinning effects in hybrid aspen (Populus tremula L. × P. tremuloides Michx.) stands in southern Sweden. *Forestry* **78**(3), 285–295.

Šēnhofa, S., Zeps, M., Matisons, R., Smilga, J., Lazdiņa, D. & Jansons, Ā. 2016. Effect of climatic factors on treering width of *Populus* hybrids in Latvia. *Silva Fennica* **50**, id 1442, 12 p.

Zeps, M., Senhofa, S., Zadina, M., Neimane, U. & Jansons, A. 2016. Stem damages caused by heart rot and large poplar borer on hybrid and European aspen in Kalsnava, Latvia. *Baltic Forestry* (accepted).

Zhang, S.Y. 1995. Effect of growth rate on wood specific gravity and selected mechanical properties in individual species from distinct wood categories. *Wood Sci. Technol*. **29**(6), 451–465.

Zhang, S.Y., Yu, Q., Chauret, G. & Koubaa, A. 2003. Selection for both growth and wood properties in hybrid poplar clones. *For. Sci*. **49**(6), 901–908.

Zobel, B.J. & Buijtenen Van, JP. 2012. Genetic controls in wood formation. In Zobel, B.J. & Buijtenen Van, JP. (eds.): *Genetics of Wood Production*. Springer Science & Business Media, 337 pp.

Tullus, A., Rytter, L., Tullus, T., Weih, M. & Tullus, H. 2012. Short-rotation forestry with hybrid aspen (Populus tremula L.× P. tremuloides Michx.) in Northern Europe. *Scand. J. For. Res.* **27**(1), 10–29.

Yu, Q., Tigerstedt, P.M.A. & Haapanen, M. 2001. Growth and phenology of hybrid aspen clones (Populus tremula L. × Populus tremuloides Michx.). *Silva Fenn*. **35**(1), 15–25.

II POWER ENGINEERING
&
RENEWABLE ENERGY

Agronomy Research **14**(Sp.1), 1155–1160, 2016

Practical usage of additional heat from biogas plant

M. Bloch-Michalik* and M. Gaworski

Warsaw University of Life Sciences, Department of Production Management and Engineering, Nowoursynowska str. 164, PL 02-787 Warsaw, Poland
*Correspondence: marta_michalik@sggw.pl

Abstract. Biogas plants are one of the most stable and cost-effective energy sources. The better volume of produced biogas is used for parallel electricity and heat production in CHP gas engines. The heat from the engine is conveniently used for heating the digester but the additional amount causes lot of problems and is wasted despite its large potential. The inefficiency in energy use is a bottleneck in current biogas production, causing macroeconomic and microeconomic losses and challenges in the context of increasing land use competition. As a major output of the biogas management process research provide by authors, this article was elaborated in order to introduce the results of theoretical heating system analysis.

Key words: biogas, heat balance, CHP.

INTRODUCTION

In order to management the heat produced additionally in the process of electricity generation it is necessary to consider its usage instead of release into the environment. Biogas heat and power plant driven by a combustion engine produces heat at different temperatures (Borowski et al., 2014; Żak et al., 2014). The largest amount of heat can be recovered by a cooling engine. Due to its temperature, this heat can be used to provide heating energy, or the energy for the biogas production process (i.e. fermentation).

The highest and usually only demand for heat occurs in winter time whereas lost in other months of year.

Average demand for heat use to provide constant fermentation process covers about 25–40% of produced heat (Jäkel, 2002).

The so called waste heat from biogas plants, like any kind of heat is characterized by the temperature level and by the quantity. For the development of waste heat concepts, the temperature and the amount of heat are important, since the heat user always needs a certain minimum level of both figures. The temperature of the waste heat source needs to be always higher than the temperature of the heat sink. The magnitude of the temperature difference between the heat source and sink is an important determinant of the quality of waste heat.

With higher waste heat temperatures, more opportunities for its use exist. Examples typical for the use of waste heat from biogas plants can be divided by minimum temperatures needed in different uses areas like (Ramanauskaire et al., 2012):

- Hot water supply: 50–80 °C;
- Residential heating: 50–80 °C;

- Rankine cycles (ORC, CRC): 60–565 °C;
- Dryer for agricultural products: 60–150 °C.

As the exhaust gas temperature of CHP units in biogas plants is typically about 450–520 °C, the use of waste heat from biogas plants is limited.

Calculations contained in this paper base on case study object and due to that authors have assumed that the best solution for heat management in existing biogas units is to enable distribution of heating to own edifices or to third parties. This seems well-grounded for the biogas plants cooperating with sewage treatment plants, because of their characteristic:

- permanent supply of feedstock (sewage sludge),
- suitable for media distribution infrastructure,
- (frequently) the optimum location – urban periphery, where is demand for cost competitive network heating.

Therefore, paper will present the methodology of the tests performed on typical sewage biogas plant containing heat and economic balances, as well as comparison of the development concept for manage surplus heat for own non-processing needs (i.e. heating social accommodation) and external sales.

MATERIALS AND METHODS

Not utilising heat from incineration amounts to wasting the energy. Wasting heat is not just illogical as it wastes energy, but also results in macroeconomic and microeconomic losses. European countries, likewise Poland are heavily dependent on energy imports, climate change is forcing the EU to decrease its CO_2 emissions, and climate change policies highlight the need for renewable resources. Biogas represents a renewable and domestic resource that plays a role in all these fields. Its potential for efficient use, i.e. utilising the surplus heat, brings major benefits as it results in a decreased primary energy demand.

Overlook of heat from biogas production in Poland

On Polish biogas market we can identify three main types of biogas plants differentiate between main substrates (Bloch-Michalik & Gaworski, 2015):

- Landfill biogas plant, which are ‘running on’ organic wastes.
  Organic wastes mean separate collected fruit and vegetable wastes, flower soil, flowers, eggshells, coffee and tea filters and other organic leftovers also leftovers from cutting gardens or parks which do not contain woody matter – due to the Polish practice all organic wastes find its way into landfill.
- Sewage biogas plants use communal sludge.
  Communal sewage sludge with percentage of dry matter varies between 20 and 30%.
- Agricultural biogas plants that’s producing biogas from different wastes from a wide-mean agriculture and farming.
  Farming wastes implied as liquid or solid manure from animal farming, energy crops and industrial food waste from vegetable, fruit or meat production sites or process.

As a number of biogas plants in Poland increases as well heat production become more significant (Fig. 1).

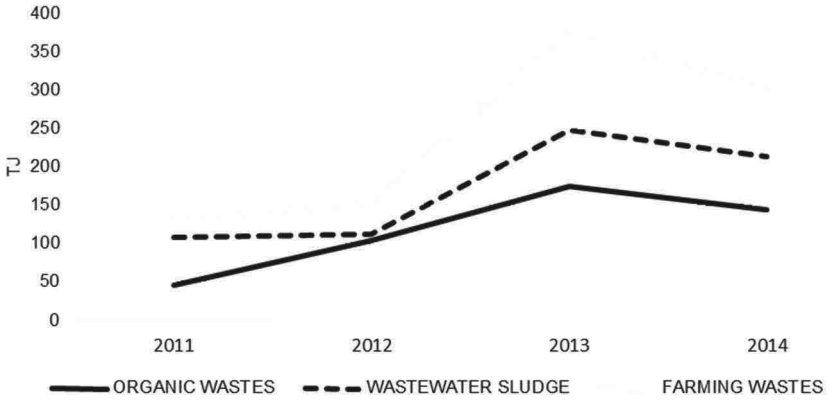

Figure 1. Heat produced from different types of biogas in Poland; 2011–2014 (GUS, 2015).

In Polish circumstances produced biogas is converted into energy in three ways:

- spark ignition engines or turbines;
- adapted gas boilers
- CHP units.

The most common technical equipment comprises boilers use first and foremost on wastewater treatment biogas plants and landfill biogas plants. However, from over 170 landfill biogas plants in Poland less than a half use produced biogas for energetic reason.

Even so all farming biogas plants (nearly 80) are equipped with CHP units (ARR, 2016) and farming wastes generate the greatest amount of heat from all the types of biogas plants (Table 1).

Table 1. Production of heat from different biogas types in Poland in 2014 (GUS, 2015)

Substrates categories	Annual heat production TJ
Organic wastes	69
Communal sewage sludge	86
Farming wastes	144

Polish biogas heat has a great and untapped potential. There are various technical options when it comes to utilising heat. A one-size-fits-all recommendation does not exist. The way to optimally use heat depends very much on the specifications and capacity of the biogas plant, the location of the plant and offset markets, and the legal framework.

Study case

The subject of research in the following thesis is sewage treatment plant covers an area of about 8 hectares. The property is designed for an average amount of treated

wastewater in quantities of 38,000. Sewage treatment plant is equipped with a mechanical-biological technology purification. Obtained in the process of wastewater treatment sludge is subjected to mesophilic methane fermentation process in a separate digester. The biogas, which is produced by sludge fermentation composed mainly of methane (approx. 66%) and carbon dioxide. Annual production of biogas is determined on average level of 990,000 m^3. Its calorific value is 26 MJ m^{-3}. For the studying wastewater treatment plant was proposed (Michalik, 2013) an individual CHP unit which manage to generate on average 2,2 TWh of net thermal energy per year.

To balance heat demand with its production it was necessary to inspect the energy audit for buildings are part of treatment plant infrastructure. Energy audit is an expert appraisement make and implement in terms of reducing heating costs. Results of audit calculations also helps to find solutions for reducing the environmental impacts associated with the utilization of conventional energy resources, energy conservation and energy efficiency offer attractive solutions (Krarti, 2011). All characteristics in audit were calculated for the common conditions (Hasanbeigi & Price, 2010; Krzemień, 2012) according to the methodology describes in Polish law (MoT, 2008; Michalik, 2013).

Theory and modelling

Theoretical support for suggested solutions underline calculations base on heat balance for case study. At the beginning it was important to estimate whole heat production possible to gain.

Gross heat production:

$$Q_{th} = P_{th} \cdot t \tag{1}$$

where: P_{th} – CHP heat power; t – working time for CHP

Second step was to define an amount of additional heat and its purpose as it was said before for own needs:

Annual heat demand for social buildings:

$$Q_{H,nd} = S_{th} \cdot (H_{tr} + H_{ve}) - \eta_{H,s} \cdot (Q_{\text{int}} + Q_{sol}) \tag{2}$$

where: S_{th} – heating degree days; H_{tr} – infiltration heat loss; H_{ve} – ventilation heat loss; $\eta_{H,s}$ – coefficient of heat gain; Q_{int} – annual internal energy gain; Q_{sol} – annual solar heat gain; or external sale.

Method used for annual heat demand calculation is applicable for existing buildings that are not retrofitted, with an average heat transfer coefficient of the building envelope greater than $0.8\ W \cdot (m^2\ K)^{-1}$ with natural ventilation.

RESULTS AND DISCUSSION

Total heat consumption was defined for amount of 3 078 147 kWh (11 081 GJ). From case study calculation comes out biogas plant heat demand – 967,200 kWh (3,481 GJ) (Table 2) and social building heat demand – 104,880 kWh (377 GJ) (Table 3). To calculate treatment plant heat demand, it is necessary to carry out few simple computes.

Table 2. Heat balance for studying object in scenario without social buildings demand (own elaboration)

Month	Working time	CHP heat production	Heat demand		Difference	
			Biogas plant	Wastewater treatment plant		
	hours			MWh		GJ
January	677	272.85	81.85	170.34	20.66	74.38
February	612	246.44	73.93	153.89	18.62	67.03
March	677	272.85	81.85	170.34	20.66	74.38
April	655	264.04	79.21	164.88	19.95	71.82
May	677	272.85	81.85	170.34	20.66	74.38
June	655	264.04	79.21	164.88	19.95	71.82
July	677	272.85	81.85	170.34	20.66	74.38
August	677	272.85	81.85	170.34	20.66	74.38
September	655	264.04	79.21	164.88	19.95	71.82
October	677	272.85	81.85	170.34	20.66	74.38
Noveber	655	264.04	79.21	164.88	19.95	71.82
December	677	272.85	81.85	170.34	20.66	74.38

In order to use the heat from the biogas plant, the plant operator is always allowed to sing long-term contract with the potential consumers or offer warm water supplied by the biogas plant.

Table 3. Heat balance for studying object in scenario with social buildings demand (own elaboration)

Month	Working time	CHP heat production	Heat demand			D ifference	
			Biogas plant	Wastewater treatment plant	Social buildings		
	hours			MWh		G J	
January	677	272.85	81.85	170.34	20.19	0.47	1.69
February	612	246.44	73.93	153.89	15.88	2.74	9.86
March	677	272.85	81.85	170.34	4,.36	16.30	58.68
April	655	264.04	79.21	164.88	3.68	16.27	58.57
May	677	272.85	81.85	170.34	0.12	20.54	73.94
June	655	264.04	79.21	164.88	0	19.95	71.82
July	677	272.85	81.85	170.34	0	20.66	74.38
August	677	272.85	81.85	170.34	0	20.66	74.38
September	655	264.04	79.21	164.,88	9.35	10.60	38.16
October	677	272.85	81.85	170.34	14.74	5.92	21.31
Noveber	655	264.04	79.21	164.88	22.23	-2.28	-8.21
December	677	272.85	81.85	170.34	23.69	-3.03	-10.91

The benefits for the owners of wastewater treatment plant could be significant as they did not have to take care about the heating installation system.

The monetary value of the heat depends first of all on the end-use of the heat, regional infrastructure and national policies.

Spatially, heat from biogas plants can be used for industry or in houses or buildings in the area of the production plant. The heat energy is transferred through (underground)

pipe connections. For heat as a final product, experience indicates that reasonable distances can be 1 to 5 kilometres away from the plant (Ramanauskaire et al., 2012), depending on the local circumstances.

CONCLUSIONS

Great potential for heat use are purifying and draining processes which require large amount of this medium. Other alternative for heat used is coupling of heating, power and cooling. Nowadays is considered a great potential in further use of the heat which should provide economic reliability. However, so far projects and solutions possible to implementation are questionable from an economic point of view but it seems to sales of thermal energy can create additional sources of income that can significantly contribute to the profitability of the entire biogas plant.

REFERENCES

Bloch-Michalik, M. & Gaworski, M. 2015. A proposition of management of the waste from biogas plant cooperating with wastewater treatment. *Agronomy Research* **13**(2), 455–463.

Borowski, P., Gawron, J., Golisz, E., Kupczyk, A., Piechocki, J., Powałka, M., Redlarski, G., Samson-Bręk, I., Sikora, M., Szwarc., M. & Tucki, K. 2014. Influence of CO_2 emissions reduction on functioning the biofuels sectors for transport in Poland. *ADAM Editor*, Warsaw, 239 pp. (in Polish).

Central Statistical Office of Poland (GUS). 2015. *Energy from RES in 2014*. GUS, Warsaw (in Polish).

Hasanbeigi, A. & Price, L. 2010. Industrial energy audit guidebook: Guidelines for conductiong an energy audit in industrial facilities. *Berkeley*: Ernest Orlando Lawrence Berkeley National Laboratory.

Jäkel, K. 2002. Managementunterlage Landwirtschaftliche Biogaserzeugung und – verwertung. *Sächsische Landesanstalt für Landwirtschaft* (in German).

Krarti, M. 2011. Energy audit of building systems. An engineering approach. *CRC Press*, Boca Raton.

Krzemień, J. 2012. Produkcja i wykorzystanie biogazu w oczyszczalniach ścieków na Śląsku. *Ochrona Środowiska i Zasobów Naturalnych*, **54**, 210–220 (in Polish).

Michalik, M. 2013. Energetic and economic analysis of alternative digestate management. Master thesis, manuscript, *Warsaw University of Life Sciences*, Warsaw.

Ministry of Transport, Construction and Maritime Economy Regulation (Dz. U. z 2008 r. Nr 201, poz. 1240) of 6th November 2008 a methodology for calculating the energy performance of the building and an apartment building or part of a whole which is the independent technical-utilitarian and the preparation and presentation of certificates of energy performance (in Polish).

Ramanauskaire, R., Rutz, D., Amman, S., Amann, Ch., Abramović, J., Vorisek, T., Allegue, L., Hinge, J., Dzene, I., De Filippi, F., Surowiec, M., Adamescu, C. & Ofiteru, A. 2012. Biogas markets and the use of heat of biogas plants in Austria, Croatia, Czech Republic, Denmark, Germany, Italy, Latvia, Poland and Romania. *BIOGASHEAT*, Munich, Germany.

Żak, A., Golisz, E., Tucki, K. & Borowski, P. 2014. Perspectives of biofuel sector development in Poland in comparison to CO_2 emission standards. *Journal of Agribusiness and Rural Development* **3**(33), 299–311.

Agronomy Research **14**(Sp.1), 1161–1168, 2016

Operation reliability of induction motors at egg processing plant 'Balticovo'

A. Gedzurs

Latvia University of Agriculture, Faculty of Engineering, Institute of Energetics, J. Cakstes blvd. 5, LV-3001 Jelgava, Latvia; e-mail: aleksejs.gedzurs@llu.lv

Abstract. In hen houses air quality plays an important role in egg production volume. However, failure of fan induction motors often occurs and it is important to improve reliability of these. A motor reliability study was conducted in the egg processing plant 'Balticovo' in Iecava. Results show that 86% of failed number from 2010–2015 occur in hen houses and more than 50% of them were failures of motors which drive the fan. Annual failure rate of fan induction motors each year was increasing and in 2015 it was 6%. Investigations of the faulty motors showed the following defects – stator turn to turn failure of stator winding insulation leadwire and stator winding insulation thermal stress and mechanical damage of stator core resulting in the damaged stator winding leading to a short circuit. Results show that conditions that could contribute to such defects are excessive heating and vibrations.

Key words: induction motor, reliability, failure, fan, egg processing plant, hen houses.

INTRODUCTION

Induction motor (IM) drives are widely used in industry, agriculture, commercial and residential sectors. A failure of an induction motor can result in stoppage of the production process, therefore causing economical losses. A survey of the reliability of induction motors in the petroleum and chemical industry is presented in (IEEE, 1985; 1987; Thorsen & Dalva, 1995; Penrose, 2012) and root cause analysis for IM (Bonnett, 2010) show that failures were caused by following failed components and causes: bearings – in 51% of the failure cases; stator windings – 16%; external (environment, load and voltage) – 16%; others – 17%. In agriculture facilities, 70% of failures occur due to failed stator windings; 20% – due to environment or voltage effects; 10% – bearing damages (Sniders, 1995; Homutov, 2010). The average annual failure rate of motors is 3.4% and in places of extreme operation conditions is 9.3% and can reach up to 12% (Venkataraman et al., 2005)

In the hen houses 20–30% of egg production volume depends on microclimate quality (Kobzistij, 2000; Shipalov, 2009), so it is important to ensure the required parameters of temperature, humidity, air flow and etc. Therefore, a failure of induction motors driving the fans in the hen houses can lead to a decrease of egg production or even the death of poultry. In this paper a survey of induction motors drive systems and failures in the egg processing plant 'Balticovo' in Iecava, Latvia is presented.

MATERIALS AND METHODS

The study was conducted at the egg processing plant 'Balticovo' in Iecava. First, information about the main technologies of the plant was collected and observed. Then induction motor data from all of the plants facilities was obtained from electrical diagrams, available data and manual recording of induction motors data.

The technological facilities and induction motor distribution are shown in Fig. 1. Plant 'Balticovo' consists of the following facilities – grain dryer; grain processing; oil production; hen houses; egg sorting and processing; egg boiling; egg powder production. Most of the facilities were modernized or built during 2000–2014. The total number of induction motors in the plant is 2107, 1453 of which are located in hen houses. 43% of total IM count are 1.1 kW motors and mainly are used in hen houses to drive fans, 33% – are lower than 1 kW and are used in transportation systems, e.g., egg and hen feeding transportation (Fig. 2.). IM over 10 kW are used in grain processing facilities. The most powerful motors at the plant are the 132 kW motor used in oil press application and the 110 kW motor that drives a grain mill.

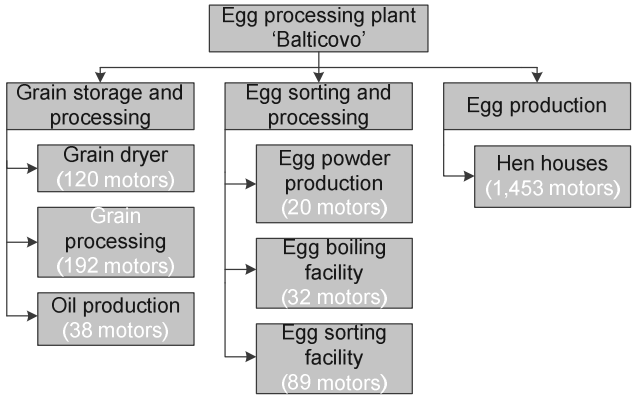

Figure 1. Statistics of induction motors in each of technological facility of the egg processing plant in Iecava.

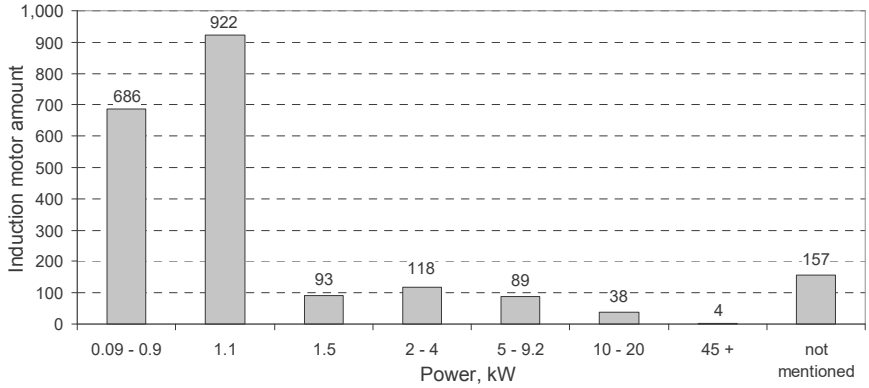

Figure 2. Power and number of induction motors in the egg processing plant in Iecava.

The ‘Balticovo’ plant has 14 hen houses, two of them are older than ten years and others were built during 2004 to 2014, approximately one hen house a year. In each hen house fan drives are divided into two groups. The first group, called ‘ecoclimate’, consist of three motor group with different motor count in each group – 5, 7 and 8 motors. The ‘ecoclimate’ group is operated all year long. The second group, called ‘emergency’, has two motor groups – 10 and 15 motors. ‘Emergency’ motor group is operated when bigger air flow is required, mostly during warm periods of the year. In each hen house an automation system is measuring temperature in four locations and controls the operation of the fans. A v-belt drive system is used to connect induction motor with the fan.

During 2010–2015 information of IM with stator winding failures was registered at ‘Balticovo’. All of the faulty IM are delivered straight to electric motor repair companies and no data regarding the motor defects, possible reasons of failures is recorded. During the study at the egg plant five faulty 1.1 kW fan induction motors, defects and possible reason of the faults were analysed.

RESULTS AND DISCUSSION

The number of failures of IMs annually is increasing and in 2015 reached 59 failures, two times more than in 2011 (Fig. 3). Annual failure rate of IM is about 2–3% for the past 4 years. More than 90% of total faulty motors are 1.1 kW and lower.

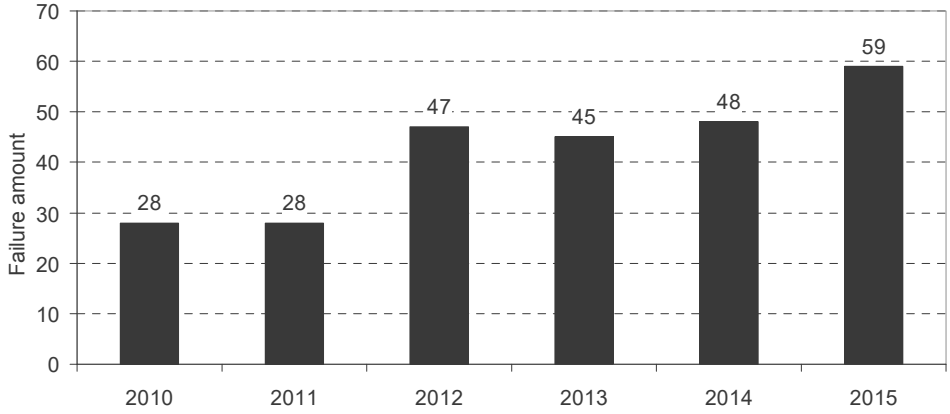

Figure 3. Annual failure rate of induction motors in the egg processing plant ‘Balticovo’.

Around 86% (213 failures) of total induction motor failures in the plant occurred in the hen houses for the past six years (Fig. 4.). From 213 failures, 123 of these were ABB 1.1 kW, M2AA90S-4, 1,410 rpm, 230/400 V, 4.6/2.66 A induction motors that are driving fans in the hen houses. Apart from fans, other failures occurred in egg and hen feeding transporting drives. Results show that almost 50% of total IM failures are related to fans in the hen houses and it is important to analyse the failures and to increase the reliability of induction motors.

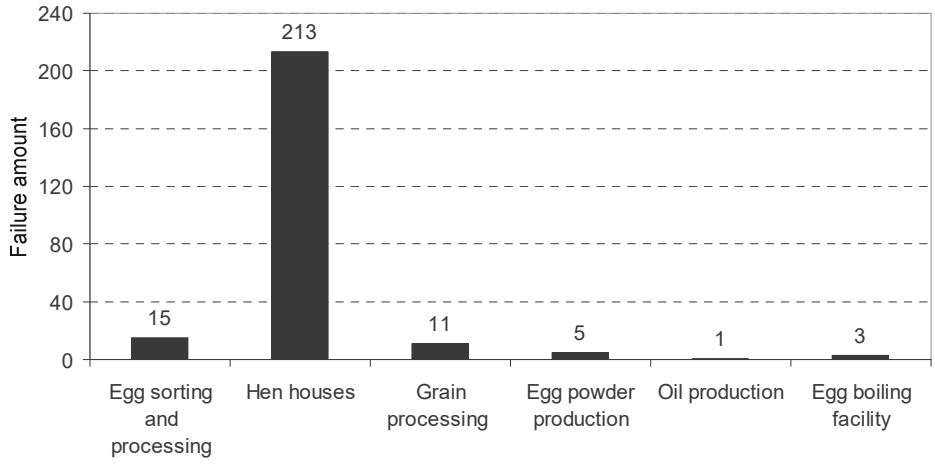

Figure 4. Failure amount of induction motors in different facilities from 2010–2015.

During the last six years the annual failure rate of fan induction motors was increasing each year (Fig. 5). The highest failure amount was in year 2015 – 41 faulty motors or 6% of total fan induction motors in the hen houses.

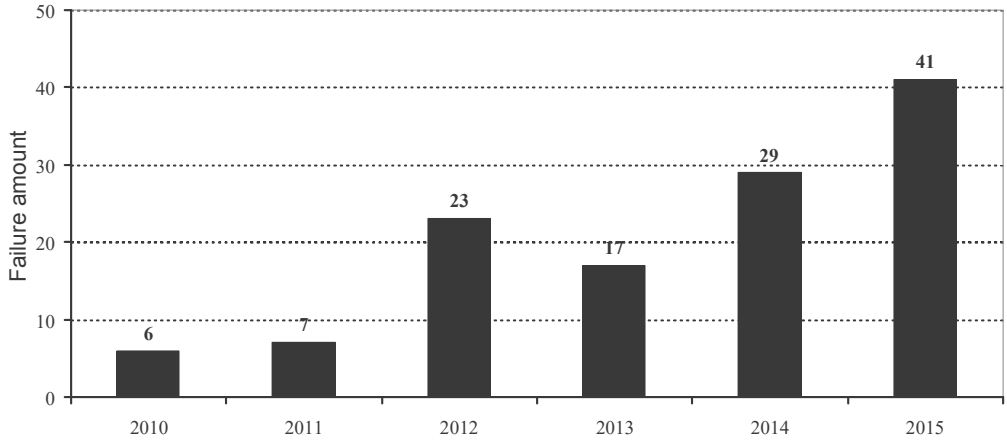

Figure 5. Annual failure rate of fan driving induction motors in hen houses.

Average operation time before failure of the axial fan driving induction motors in hen houses (Shipalov, 2009) is 3.1 years with an average operation time of 2800 hours a year. Operation time before failure for 56 faulty fan induction motors at 'Balticovo' is show in Fig. 6 and the average operation time is 5 years. However, since fans are divided in two groups ('Ecoclimate' and 'Emergency'), the 'Ecoclimate' group has significantly higher operation time due low air flow needs in the winter time and the 'Emergency' group fans are not operating nearly as much. Therefore, without a proper failure register

of which group fans fail, it is hard to evaluate precise reliability parameters of induction motors.

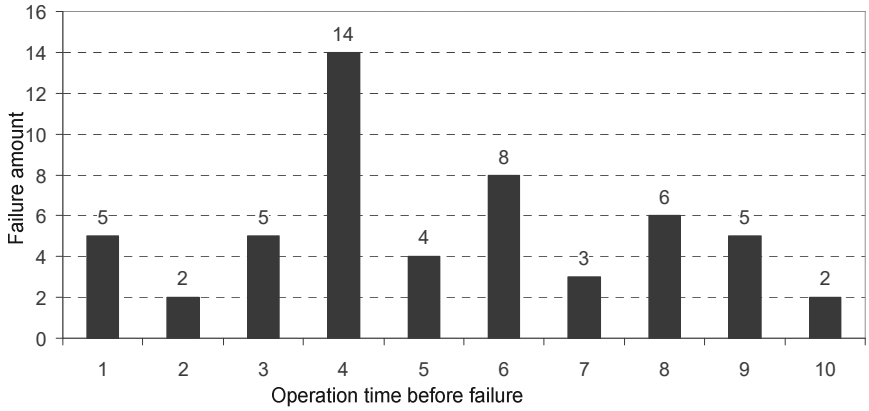

Figure 6. Operation time of fan driving induction motors before first failure in the chicken raising and hen houses.

During the past six years, there have been 8 cases where a 1.1 kW fan induction motor has been rewound after failure and after certain operation time failed a second time. Ine one of the cases the motor failed a total of three times. This is presented in Fig. 7 where the operation time between first and second failure is shown. The motor that was fixed for a third time had a significantly lower operation time than after its first failure, having operated roughly a third of the time it did after first repair. The shortest operation time after first repair was 3 month, while the longest was 30 months before failing again. The average operation time of a rewound motor is roughly 1.5 years, which is more than three times lower than what the average operation time is before first failure.

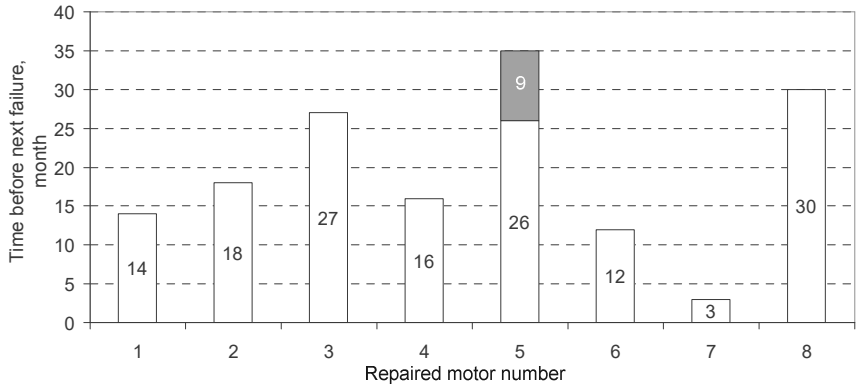

Figure 7. Failure amount of induction motors in different facilities from 2010–2015.

When a repaired motor was looked at it was noted that the bearings had not been changed. After further study into the repair costs of motors in 2015, 4 out of 41 had a higher repair cost and this difference was the equivalent of bearings being changed. So it is presumed that most repaired motors go back into operation with the original bearings. Because of this it could be assumed that the lower operation time after a repair could be related to the old bearings failing, and so is suggested that during the repair process the bearings are always changed to help increase overall lifespan of the motors parts.

Research of five faulty 1.1 kW fan induction motors at 'Balticovo' shows the following major defects turn to turn insulation failure of the stator winding; stator winding cut in stator core slot by stator tooth; cracks in leadwire insulation. A turn to turn insulation failure of stator winding is shown in Fig. 8, a. Cracks in the stator winding insulation were found and that can be a clue to how the short circuit occurred. A common reason for insulation cracks occuring is thermal stress. A phase to earth short circuit situation can be seen in Fig. 8, b where stator core teeth are smashed into the winding inside the stator slot. The cause of this defect is friction between the stator and rotor. In Fig. 8, c, d is shown that leadwire insulation is cracked and coming apart. This defect might not cause failure of motor straight away but wires can potentially cause short circuit against each other or against the motor frame. In this case also thermal stress can cause wire insulation cracking. Defect analyses shows that excessive heating and vibration are the main reason that cause these defects to occur.

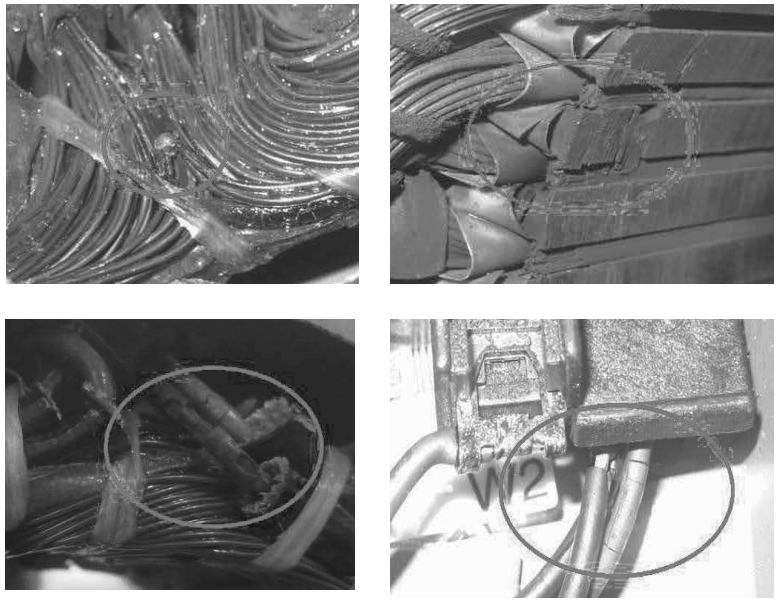

Figure 8. Defects of faulty fan induction motors.

Analysis of the failure of fan induction motors in hen houses show that up to 57% of failures are related to thermal ageing of stator winding insulation (Kobzistij, 2000). Main factors causing the overheating of stator windings and decreasing life span of the insulation are a voltage unbalance and a loss of one of the phase supplies resulting in

single phasing (up to 47%). Another factor is the rotor stalling caused by frozen fan blades during winter time. Another analysis shows that 50% are caused by single phasing (Shipalov, 2009). Both analyses show that bad voltage quality is one of the main root causes of induction motor failures. However, the egg processing plant 'Balticovo' is located close (around 1 km) to an electrical power distribution substation and does not have problems with voltage quality.

Analysing operation conditions and defects of the fan induction motors, the following conditions needs to be taken into account to find the root causes of the failure – dust and aggressive gases; long operation time of fans (especially in summer); V-belt drive system. Fan induction motors are covered by dust from grains resulting in decreased heat dissipation of the induction motor which causes overheating. Aggressive gasses can decrease the life span of electrical equipment, especially the stator winding insulation. An over-tight V-belt will cause excessive wear on bearings (Harman & Hongwei, 2009). From the 5 inspected faulty motors during the study 4 motors had signs of friction between the stator and rotor in the fan side of the motor. Taking into account all the facts analysed above, the following conclusion can be made that the root cause of failures is likely to be excessive wear on bearings that causes an increase in vibrations of the induction motor. However, more data and detailed investigations are required to understand the process and root causes of the failure of the fan induction motors in the hen houses at 'Balticovo'.

The survey of failures of induction motors in the egg processing plant 'Balticovo' show that failures of fan induction motors often occur in the hen houses and statistics show that each year the annual failure rate of fans is increasing by 1% of the total fan number. Failure of fans might cause lower air delivery and decrease ventilation quality thus can reduce egg production. Analysing the root causes of the failures is essential to increase the reliability of the induction motors to decrease production costs and reduce any losses. Also protecting and preventing motors from failure is important, therefore, a method to detect bearing damage is needed. A vibration and acoustic emission analyses are often used to diagnose bearing condition, but the sensors are expensive. Motor current sisnature analysis (MCSA) and different signal-and-data-processing algorithms are used to detect bearing defects (Riley, 1997; Jung et al., 2006; Blödt, 2008). Further investigations are needed to determine if the MSCA methods can be applied to detect bearing damage and used in IM maintenance I the Balticovo.

CONCLUSIONS

1. In hen houses 20–30% of egg production depends on quality of air, this justifies that reliability of fan induction motors is an important factor and a failure of these fan induction motors can decrease egg productivity.

2. Induction motor failure rate analysis at the egg processing plant 'Balticovo' show that annual failure rate is 2–3% of total induction motor number, but failure rate of induction motors driving fans in the hen houses is 6% of the total. It shows that measures are required to increase the reliability of induction motors in hen houses.

3. Analysis shows that average life span of new fan induction motors is 5 years and life span of repaired ones is more than 3 times lower – 1.5 years. Investigation of repaired motors show that only stator windings are rewound but in many cases bearings are not

changed. Taking into account long operation time, typical for the fans, that is why bearings should be changed for each repaired motor.

4. Investigation of faulty fan induction motors show following defects – stator winding turn to turn short circuit, cracks in insulation of stator winding and leadwires, mechanical damages of stator core resulting into damaged stator winding and short circuit to earth. It shows that main factors to cause these defects are overheating and vibrations that could be caused by bearing damage. Therefore, further investigations are needed to find a cost effective method to detect bearing damage during operation time of the induction motors and prevent damage to the motor, reducing repair costs and time.

REFERENCES

Bonnett, A.H. 2010. Root cause failure analysis for AC induction motors in the petroleum and chemical industry. In: *The 57th annual Petroleum and Chemical Industry Conference*. IEEE, San Antonio, USA, pp. 1–13.

Blödt, M. 2008. Models of bearing damage detection in induction motors using stator current monitoring. *IEEE Transactions on Industrial Electronics* **IA-55**(4), 1813–1822.

Harmon, J.D. & Hongwei, X. 2009. Livestock Industry Facilities and Environment: Choosing fans for livestock and poultry ventilation. *Agriculture and Environment Extension Publications* **40**, 1–4.

Homutov, S.O. 2010 *Reliability improvement system of electric motors based on complex diagnostics and effective technology of insulation repair in agriculture*, 526 pp. (in Russian)

IEEE 1985. Report of large motor reliability survey of industrial and commercial installations, Part I. *IEEE Transactions on Industry Applications* **IA-21**(4), 853–864.

IEEE 1985. Report of large motor reliability survey of industrial and commercial installations, Part II. *IEEE Transactions on Industry Applications* **IA-21**(4), 865–872.

IEEE 1987. Report of large motor reliability survey of industrial and commercial installations, Part III. *IEEE Transactions on Industry Applications* **IA-23**, 153–158.

Jung, J.H., Lee, J.J., Kwon, B.H., 2006. Online Diagnosis of induction motors using MCSA. *IEEE Transactions on Industrial Electronics* **IA-53**(6), 1842–1852.

Kobzistij, O.V. 2000. *Modernization of electric motor protection against unbalance voltage. Zernograd*, 144 pp. (in Russian)

Penrose, H.W. 2012. Large electric motor reliability: What did the studies really say?. *Maintenance technology* **25**(4), 18–23.

Riley, C.M., Lin, B.K., Habelter, T.G. & Kliman, G.B. 1997. Stator current-based sensorless vibration monitoring of induction motors. In: *12th Annual Apllied Power Electronics Conference and Exposition*. IEEE, Atlanta, USA, pp. 142–147.

Shipalov, V.I. 2009. *Operation efficiency of fan electric drive with induction voltage regulator in hen houses*. Krasnodar, 142 pp. (in Russian)

Sniders, A., 1995. Reliability and protection of induction motors during overload regimes. *Baltic Electrical Engineering Review* **2**, 25–28.

Venkataraman, B., Godsey, B., Premerlani, W., Shulman, E., Thakur, M. & Midence, R. 2005. Fundamentals of a motor thermal model and its applications in motor protection. In: *The 58th annual conference 'Protective Relay Engineers'*. Black & Veatch Corporation, Kansas City, USA, pp. 127–144.

Agronomy Research **14**(Sp.1), 1169–1179, 2016

Methodology for determining the mixing ratio of selected solid recovered fuels

V. Malijonytė[1,2], E. Dace[1,*], F. Romagnoli[1] and M. Gedrovics[1]

[1]Riga Technical University, Institute of Energy Systems and Environment, Azenes 12/1, LV-1048 Riga, Latvia
[2]Kaunas University of Technology, Institute of Environmental Engineering, Donelaičio g.20, LT-44239 Kaunas, Lithuania
[*]Correspondence: elina.dace@rtu.lv

Abstract. Energy recovery is a preferable waste management method for waste that cannot be reused or recycled. For energy recovery, various types of waste with differing properties are being used, e.g. mixed municipal solid waste or end-of-life tires. To achieve a more stable and homogeneous characteristics of the waste derived fuels (RDF, SRF), they can be mixed in a number of ratios. The paper presents a methodology for determining the optimal mixing ratio of three selected waste derived fuels (mixed municipal solid waste, sewage sludge, end-of-life tires) considering environmental and economic aspects. The developed method is based on combining life cycle assessment method, mass balance calculations and multi-criteria analysis (the technique for order of preference by similarity to ideal solution – TOPSIS). The results show that mixing the various waste derived fuels allows obtaining a more sustainable solution than in the case of each separate waste derived fuel.

Key words: Life cycle assessment, end-of-life tires, method integration, multi-criteria analysis, municipal solid waste, sewage sludge.

INTRODUCTION

Energy recovery from waste has become a popular management method for municipal solid waste (MSW). In the Baltic States, new municipal waste sorting plants are being opened, where solid recovered fuel (SRF) is produced. Lithuania is in the process of opening nine mechanical-biological treatment (MBT) facilities that will serve the whole country. In the country, one waste incineration plant is in operation, where refuse derived fuel (RDF) and SRF can be incinerated. Meanwhile Estonia has planned opening of four MBT plants (EEA, 2013), while a combined heat and power plant with waste mass incineration has been opened in 2013 near Tallinn (Eesti Energia, 2014). In Latvia, ten MBT plants have been set into operation (Dace et.al., 2015). The primary aim of the MBT plants is to pre-treat wastes prior to landfilling. Though, as a secondary target generation of RDF is considered (Dace & Blumberga, 2012). Currently in Latvia no waste incineration plants are installed or planned, except for a cement kiln that uses RDF and end-of-life tires for fuel (MEPRD, 2012).

In the study by Malijonyte et al. (2016), life cycle assessment (LCA) scenarios were developed for assessing the environmental impact and potential benefits generated

during the gate-to-gate life cycle of preparation of the end-of-life (EoL) tires, SRF produced from MSW, and SRF produced from separate fraction of pre-composted sewage sludge and biomass residues. It was concluded that energy recovery from EoL tires generates the lowest environmental impact among the selected scenarios. Yet, a relatively small amount of EoL tires is generated as compared to MSW or sludge. While SRF from MSW or from sludge are low quality fuels to be incinerated alone. Therefore, a solution would be to mix SRF with other type of fuel or waste that has a higher calorific value, e.g. EoL tires.

Benefits obtained by increasing the calorific value of SRF should be balanced with energy inputs for producing the fuel, and with environmental impacts and economic costs and benefits. LCA allows for evaluating the environmental aspects, while evaluation of economic aspects is limited. The aim of this study is to develop a methodology that assists in selecting an optimal strategy for waste fuel mixing by considering the environmental, economic and energy aspects.

MATERIALS AND METHODS

The logical framework of the method proposed within this study is shown in Fig. 1. The starting point is the statement of a problem, which, in this specific study, has been addressed towards enhancing energy recovery from waste fuels by combining them together according to an estimated mixing ratio.

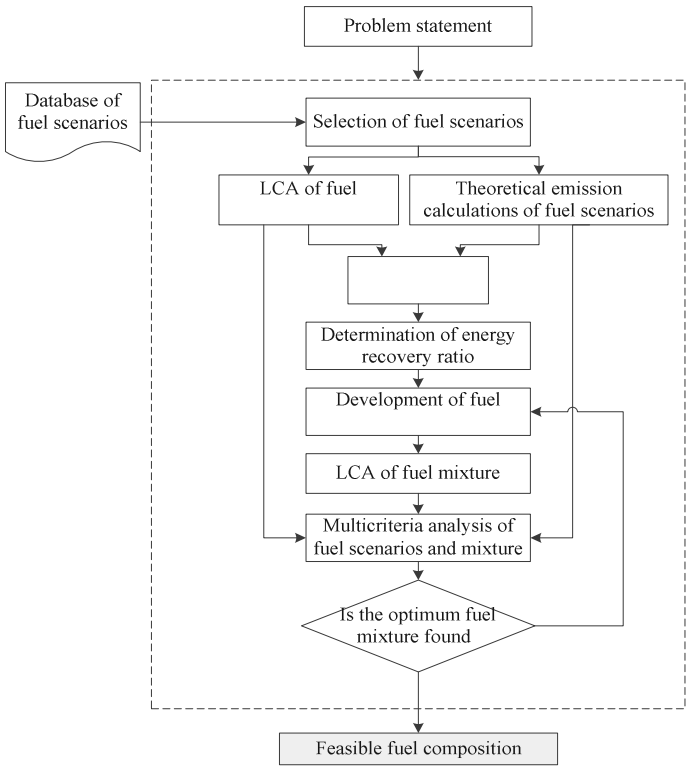

Figure 1. Logical framework of the method.

First stage of the methodology consists of selecting several potential waste fuel scenarios and conducting LCA of their production processes (described in detail by Malijonyte et al., 2016). Then, impact of processes outside LCA boundaries (in this study – waste incineration and outputs generated during the incineration process) are estimated by applying a theoretical calculations method. Further, the results obtained in LCA and theoretical calculations method are used for conducting multi-criteria analysis, where a technique for order preference by similarity to ideal solution (TOPSIS) is applied to compare the selected scenarios. TOPSIS is based on the concept that the best alternative should be as close as possible to the ideal solution, as the obtained results allow selecting the best of a finite number of alternatives (Dace et al., 2014). Current method is selected as it is suitable for combining different results for receiving a numerical output of preference ranking.

Application of the numerical preference ranking facilitates estimating the optimum mixing ratio of the selected waste fuel scenarios. LCA and theoretical calculations method is applied to estimate the impact of the fuel mixture and assessed again by conducting the multi-criteria analysis, this time by comparing with the initially developed waste fuel scenarios. If the developed fuel mixture demonstrates high environmental and economic performance then the initial fuel scenarios, it is selected for the feasible fuel composition.

The methodology of theoretical calculations, multi-criteria analysis and fuel mixing ratio is described in more detail in the following subsections.

Theoretical calculations of incineration outputs

The theoretical calculations include incineration process, during which ash and emissions to air are generated as process outputs. Each output is estimated separately, applying equations 1–7 (Nagla et al., 1981). The amount of produced ash is estimated according to the amount of fuel incinerated and ash content in the material (see Eq. 1).

$$M_{ash} = (M_{fuel} \cdot A^r) / 100\% \quad (1)$$

where: M_{ash} – mass of generated ash, kg; M_{fuel} – mass of fuel, kg; A^r – ash content in fuel as received, %.

In the study the main emissions estimated are SO_2, N_2, CO, CO_2 and NO_x. Volume of SO_2 (in $m^3\ kg^{-1}$) produced during the incineration of fuel is calculated using Eq. 2.

$$V_{SO_2} = 0.0069 \cdot S^r \quad (2)$$

where: S^r – sulphur content in fuel as received, %.

Volume of N_2 (in $m^3\ kg^{-1}$) produced during incineration of fuel is calculated according to the Eq. 3.

$$V_{N_2} = V^o_{N_2} + 0.79\,(\alpha - 1) \cdot V^o \quad (3)$$

where: $V^o_{N_2}$ – theoretical volume of nitrogen, when $\alpha = 1$, defined within the Eq. 4, $m^3\ kg^{-1}$; α – air excess coefficient (real case $\alpha > 1$, selected value for solid fuels $\alpha = 1.4$); V^o – necessary theoretical amount of air, calculated by Eq. (5), $m^3\ kg^{-1}$.

$$V_{N_2}^{o} = 0.79 \cdot V^{o} + 0.008 \cdot N^{r} \quad (4)$$

$$V^{o} = 0.0889(C^{r} + 0.375 \cdot S^{r}) + 0.265 \cdot H^{r} - 0.0333 \cdot O^{r} \quad (5)$$

where: H^r – hydrogen content in fuel as received, %; N^r – nitrogen content in fuel as received, %; O^r – oxygen content in fuel as received, %.

The heat losses q_3 in the furnace due to chemically incomplete combustion have been considered. The value of q_3 normally ranges from 0 to 1.0%. In the calculations, several scenarios are assessed, where q_3 increases by 0.2%.

Volume of CO_2 (in $m^3\ kg^{-1}$) produced during incineration of fuel is calculated as follows:

$$V_{CO_2} = 0.01866 \cdot C^{r} \quad (6)$$

where: C^r – carbon content in fuel as received, %.

The main parameters used for calculations are ρ_{CO} = 1.249 $m^3\ kg^{-1}$ (density at normal conditions); LHV_{CO} = 12,648 kJ m^{-3}; LHV_{fuel} = 33,353.5 kJ kg^{-1}. The total mass of NO_x is calculated using Eq. 7 (Charkov, 1997).

$$M_{NO_x} = 0.001 \cdot B \cdot LHV_{fuel} \cdot K_{NO_x} (1 - \beta), t \quad (7)$$

where: B – incinerated amount of fuel, kg; K_{NOx} – parameter characterizing amount of released nitrogen oxides, during production of 1 GJ of heat energy, K_{NOx} = 0.1 kJ kg^{-1}; β – coefficient depending on nitrogen oxides emissions decreasing due to technological modifications, β = 0; LHV_{fuel} – lower heating value of the selected fuel, MJ kg^{-1}.

Multi-criteria analysis

To carry out the method, a decision matrix is constructed where *m* (row dimension) represents the set of fuel scenario alternatives (scenarios A-C) and *n* (column dimension) represents the selected criteria in terms of: LCA results for each scenario, amount of produced ash estimated by theoretical calculations, calculated air emissions, which are converted using corresponding equivalents and economic costs. Economic costs are selected within an average value of produced SRF cost in the market and costs of treatment, usually applied within waste treatment facilities. Thus, the selected criteria are LCA result (mPt), amount of ash (kg), CO_2 emission equivalent (kg), acidifying potential equivalent (kg), Tropospheric ozone forming potentials (TOFP) equivalent (kg), particulate formation equivalent (kg), produced fuel cost (Euro), and avoided waste treatment cost (Euro). The calculated air emissions are converted using suitable equivalents. Conversion data are presented in Table 1. Using converted units it is possible to sum up values of the emission equivalents of same environmental issue and to compare the scenarios to each other in a simplified way. An exception is applied to CO_2 equivalent results for scenario C where SRF consists of renewable sources, thus being a 'carbon neutral' fuel (Kliopova & Makarskienė, 2015).

Table 1. Conversion to equivalents data (De Leeuw, 2002)

Pollutant	Issue	Conversion	Units
CO_2	Global warming potential	1.0	kg CO_2 equivalent
NO_x	Acidifying potential	0.022	kg Acidifying potential equivalent
SO_2	Acidifying potential	0.031	kg Acidifying potential equivalent
CO	TOFP	0.110	kg TOFP equivalent
NO_x	TOFP	1.220	kg TOFP equivalent
SO_2	Particulate formation PM_{10}	0.540	kg Particulate formation equivalent
NO_x	Particulate formation PM_{10}	0.880	kg Particulate formation equivalent

The next step of the applied TOPSIS technique, is to construct the normalized decision matrix, where various criteria dimensions are transformed into non-dimensional criteria, what allows comparison across the criteria. To determine normalized decision matrix Eq. 8 is applied.

$$r_{ij} = \frac{x_{ij}}{\sqrt{\sum_{i=1}^{m} x_{ij}^2}} \tag{8}$$

Then the weighted normalized decision matrix is constructed – each column of the normalized decision matrix is multiplied by its weight w_j, to get v_{ij}. Weight for each criterion is assigned by the importance or dangers to the environment (see Table 2).

Table 2. Weight for each criterion

Criteria	LCA result, mPt	Ash, kg	CO_2 equivalent, kg	Acidifying potential equivalent, kg	TOFP equivalent, kg	Particulate formation equivalent, kg	Produced fuel cost, Euro	Avoided waste treatment cost, Euro
Weight	0.3	0.05	0.15	0.1	0.1	0.1	0.1	0.1

After weighted normalized decision matrix is completed, ideal and negative-ideal solutions are determined. First, ideal solution A^+ for each criteria is determined. In selected case, it is ideal when criteria values related with environmental issues are minimal, as well minimal produced fuel cost. And avoided waste treatment cost is maximal, what would give the biggest benefit. Second, negative-ideal solution A^- is found. In this case, it is the opposite to ideal solution: criteria related with environmental issues and produced fuel cost are maximal, waste treatment cost is minimal.

Further, separation measures from the solutions are calculated. In order to do so, separation from ideal solution S_i^+ has to be calculated for each row j, using Eq. 9. Separation from negative-ideal solution S_i^- is calculated analogically by applying Eq. 9.

$$S_i^* = \sqrt{\sum_{j=1}^{n} (v_{ij}^* - v_{ij})^2} \tag{9}$$

After determination of separation values, the relative closeness to the ideal solution is calculated using the following equation:

$$c_i^* = \frac{S_i^-}{(S_i^+ + S_i^-)} \quad (10)$$

where: $0 < c_i^+ < 1$; $c_i^* = 1$ if $A_i = A^+$; $c_i^* = 0$ if $A_i = A^-$.

Preference order is ranked by results of relative closeness to the ideal solution. Selected energy recovery scenarios are ranked by preference according to the descending order of c_i^*.

Determination of fuel mixture ratio

The ranking results are used for determining the energy recovery ratio ER_i (Eq. 11) for each initial fuel scenario.

$$ER_i = c_i^* \cdot 100\% \Big/ \sum c_i^* \quad (11)$$

According to the amount of recovered energy by each fuel, mass of the fuel in the mixture is calculated and final SRF mixture ratio is estimated.

Characterisation of the fuel mixture

An LCA study is carried out on the preparation of the obtained fuel mixture. Data from the initial LCA scenarios presented by Malijonyte et al. (2016) are used. For the mixture, to generate 1 GJ of fuel input all initial fuel scenarios (A, B, and C) are used, according to the fuel mix composition. According to amount of recovered energy by each fuel scenario, mass of the fuel is calculated. Characteristics of the fuel mixture are calculated with respect to the share of each initial fuel scenario. Generated environmental impact by 1 GJ fuel input production using fuel mixture is allocated according to the share of each initial fuel scenario. Finally, the performance of the fuel mixture (scenario D) is compared with the performance of each individual fuel scenario (scenarios A, B and C) by applying the same criteria that were used in the multi-criteria analysis stage.

RESULTS AND DISCUSSION

Results of theoretical emission calculations

The results of the theoretical emission calculations are presented in Table 3. The scenarios assessed are as follows: A – shredded EoL tires, B – SRF from MSW, and C – SRF from separate fraction of pre-composted sewage sludge and biomass residues. The functional unit (FU) used for calculations is 1 GJ of fuel energy.

Table 3. Theoretical calculations results per functional unit (kg FU^{-1})

Scenario	Ash	SO_2	CO	CO_2	N_2	NO_x
A	1.193	0.742	23.565	44.013	359.416	100.00
B	14.070	0.137	25.472	47.574	350.305	100.00
C	20.490	1.937	23.150	42.238	363.590	100.00

It can be seen that the amount of produced ash in scenario A is significantly lower, compared to scenarios B and C. This is due to the low ash content in EoL tires (about

4%) and the comparatively low amount of fuel necessary for ensuring 1GJ of fuel energy. The largest difference among scenarios is for SO_2 emissions. In scenario B, SO_2 emissions are the lowest, while for scenario C they reach 1.94 kg per FU. The amount of SO_2 depends only on sulphur content in the fuel. Results for CO, CO_2 and N_2 emissions are very close for all scenarios. NO_x emissions for all scenarios are the same, as they are estimated by the amount of heat produced. It has to be noted, that, in scenario C, CO_2 emissions assumed to be 'carbon neutral', as the fuel consists of renewable bio-sources (Kliopova & Makarskienė, 2015).

Results of multi-criteria analysis of scenarios preference

Corresponding to the selected criteria and results for each criterion given by scenarios A, B, and C, a decision matrix was created (see Table 4), followed by generating the normalized decision matrix r_{ij} (see Table 5), and the weighted normalized decision matrix v_{ij} (see Table 6).

Table 4. Decision matrix

	LCA result, mPt	Ash, kg	CO_2 equivalent, kg	Acidifying potential equivalent, kg	TOFP equivalent, kg	Particulate formation equivalent, kg	Produced fuel cost, Euro	Avoided waste treatment cost, Euro
A	1.460	1.193	44.013	2.197	124.592	88.401	5.426	8.720
B	46.741	14.070	47.574	2.178	124.802	88.074	2.740	6.291
C	31.000	20.490	0.00	2.234	124.547	89.046	2.283	11.822

Table 5. Normalized decision matrix

Scenario	LCA result, mPt	Ash, kg	CO_2 equivalent, kg	Acidifying potential equivalent, kg	TOFP equivalent, kg	Particulate formation equivalent, kg	Produced fuel cost, Euro	Avoided waste treatment cost, Euro
A	0.026	0.048	0.679	0.576	0.577	0.577	0.836	0.546
B	0.833	0.565	0.734	0.571	0.578	0.575	0.422	0.394
C	0.553	0.823	0.000	0.585	0.577	0.581	0.352	0.740

Table 6. Weighted normalized decision matrix

Scenario	LCA result, mPt	Ash, kg	CO_2 equivalent, kg	Acidifying potential equivalent, kg	TOFP equivalent, kg	Particulate formation equivalent, kg	Produced fuel cost, Euro	Avoided waste treatment cost, Euro
A	0.008	0.002	0.102	0.058	0.058	0.058	0.084	0.055
B	0.250	0.028	0.110	0.057	0.058	0.057	0.042	0.039
C	0.166	0.041	0.000	0.059	0.058	0.058	0.035	0.074

In the following TOPSIS step, results for the ideal solution A^+ and negative-ideal solution A^- were determined for each criterion:

A^+={0.008, 0.002, 0.000, 0.057, 0.058, 0.057, 0.035, 0.074}

A^- ={0.250, 0.041, 0.110, 0.059, 0.058, 0.058, 0.084, 0.039}

The obtained results for separations from the ideal solutions, S_i^+ and S_i^-, and the relative closeness to the ideal solution, c_i^*, for each scenario are presented in Table 7. The selected energy recovery scenarios are ranked by preference according to the descending order of c_i^*.

Table 7. Separations from ideal solution and ranking results

Scenario	S_i^+	S_i^-	c_i^*	Preference
A	0.114	0.246	0.682	Best
B	0.270	0.043	0.139	Worst
C	0.163	0.151	0.481	

The preference ranking results allow us to conclude that energy recovery from EoL tires is the most preferable having the highest ranking result. Recovering energy from fuel scenario C is the second most preferable, although having small disparity from scenario A. Finally, energy recovery from SRF produced from MSW (scenario B) is the least preferable with significantly lower result.

Fuel mixture ratio and characteristics

Based on the TOPSIS ranking results, the energy recovery ratio, ER_i, was determined. Based on that, the optimum fuel mixture ratio was created (see Table 8).

Table 8. Composition of the estimated feasible fuel mix

Scenario	ER_i, %	Energy recovered, MJ	LHV, MJ kg^{-1}	Fuel mass, kg	SRF mixture ratio, %
A	52.406	524.062	33.353	15.713	30.967
B	10.640	106.404	15.327	6.942	13.682
C	36.953	369.534	13.158	28.084	55.350

Characterisation results of the fuel mix are presented in Table 9, while the incineration emissions and generated amount of ash estimated by applying the theoretical calculations method are presented in Table 10.

Table 9. Characteristics of the fuel mixture

Fuel	Composition, wt. %							HHV, MJ kg^{-1}	LHV, MJ kg^{-1}
	Carbon	Hydrogen	Oxygen	Nitrogen	Sulphur	Ash	Moisture		
MIX	47.913	5.398	16.405	1.395	1.134	18.899	8.856	21.358	19.922

Table 10. Theoretical calculations results for the fuel mixture per functional unit (kg FU^{-1})

	Ash	SO_2	CO	CO_2	N_2	NO_x
MIX	9.486	1.121	23.868	44.578	360.067	100.00

LCA and TOPSIS results of all four scenarios

Using inventory data (see Appendix 1), gate-to-gate life cycle for energy recovery from mixed SRF was created. The network includes processes used for modelling of the individual scenarios (see the study by Malijonyte et al. (2016)). The LCA results show,

that the impact created by producing the fuel mixture with 1 GJ of fuel energy input is 16.6 mPt. If compared with the impact result of the initial scenarios A, B and C, the obtained result of the fuel MIX is lower than in scenarios B (46.74 mPt) and C (31.0 mPt), but higher that in scenario A (1.46 mPt) (see Fig. 2).

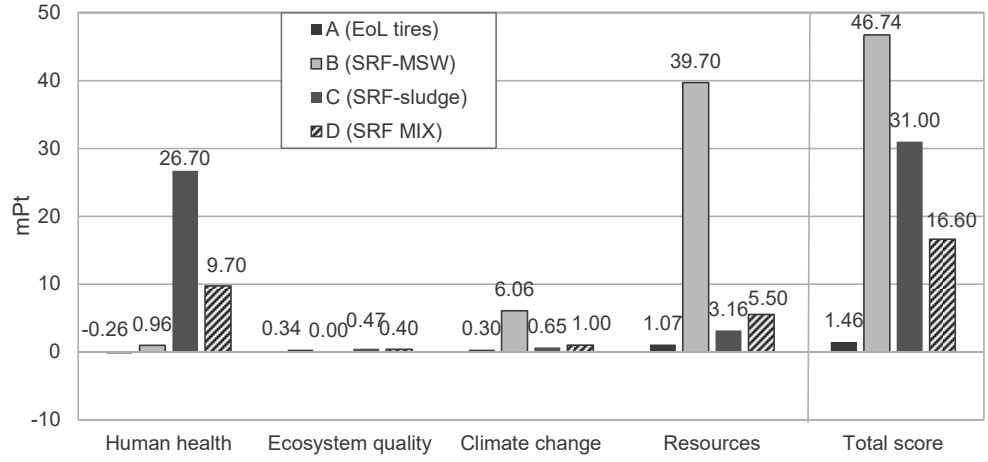

Figure 2. LCA results of fuels A, B, C and MIX.

In scenario MIX, the largest impact is generated the fraction of SRF-sludge, as it composes more than half of the fuel mixture's mass and requires electric energy for dewatering and pelleting processes. Another large part of the impact is generated by the fraction of SRF-MSW that requires a set of treatment processes. Biomass transportation has slightly lower impact than MSW treatment. The remaining processes, such as shredding of EoL tires, pre-composting of sludge and biomass, and material transportation generate relatively small environmental impact. Some of the processes are not visible in the network, as processes creating minor impact are cut-off. Yet, impact by cut-off processes is included in the final result.

Results show, that impact on human health created by SRF-sludge is reduced approximately 5 times in the case of fuel MIX by adding other fuel types in the mixture (EoL tires, SRF-MSW). Whereas, the presence of SRF-MSW increases the overall impact of fuel MIX on resource depletion. Impact of the fuel MIX on ecosystem quality and climate change does not differ much from the impact of other scenarios, and is comparatively low.

The results of the multi-criteria analysis of all four scenarios are presented in Table 11. The preference ranking results show that the fuel MIX has the second highest preference after the EoL tires.

Table 11. Ranking results of all four scenarios

Scenario	c_i^*	Preference
A	0.712	Best
B	0.129	Worst
C	0.460	
MIX	0.558	2nd best

CONCLUSIONS

In this paper, a methodology is proposed, where LCA and multi-criteria analysis methods are integrated for determination of the optimum mixing ratio of selected solid recovered fuels for energy recovery. Four scenarios using different waste fuels have been compared. Considering the varying quality and environmental and economic aspects of the fuels assessed, multi-criteria analysis was applied to estimate the most feasible type of fuel. Results of the multi-criteria analysis formed the basis for finding the optimum fuel mixing ratio to be evaluated by LCA. The LCA results indicated that the impact of the developed fuel mixture is lower than the impact of individually used SRF from MSW or SRF from sludge. Finally, additional multi-criteria analysis of all four fuel scenarios indicated that the developed fuel mixture is more preferable than SRF from MSW or SRF from sludge. Thus, mixing higher quality less-available fuel (EoL tires) with lower quality more-available fuel (MSW and sludge) should be applied whenever possible. Mixing three types of fuel would provide a higher utilization rate of MSW and sludge for producing fuel and recovering energy, rather than when used alone due to quality and economic reasons.

ACKNOLEDGEMENT. The work has been supported by the National Research Program 'Energy efficient and low-carbon solutions for a secure, sustainable and climate variability reducing energy supply (LATENERGI)'.

REFERENCES

Charkov. 1997. *Teršalų, išmetamų į atmosferą iš pagrindinių technologinių mašinų gamybos įrenginių, normatyviniai rodikliai. (Tomas I).* 1 paragrafas 'Kuro deginimas'. 1.2 punktas 'Metodinės gairės, vertinant teršalų išmetimus į aplinkos orą, deginant nedideliuose kurą deginančiuose katiluose'.

Dace, E., Rusanova, J., Gusca, J. & Blumberga, D. 2014. Selecting a catalyst for methanation process: Technical and economic performance based TOPSIS analysis. *Proceedings of the 27th International Conference on Efficiency, Cost, Optimization, Simulation and Environmental Impact of Energy Systems*, ECOS 2014.

Dace, E., Blumberga, D., Kuplais, Ģ., Bozko, L., Khabdullina, Z. & Khabdullin, A. 2015. Optimization of Landfill Gas Use in Municipal Solid Waste Landfills in Latvia. *Energy Procedia* **72**, 293–299.

Dace, E. & Blumberga, D. 2012. An Assessment of the Potential of Refuse Derived Fuel in Latvia. *Management of Environmental Quality: An International Journal* **23**(5), 503–516.

De Leeuw, F.A.A.M. 2002. A set of emission indicators for long-range transboundary air pollution. *Environmental Science & Policy* **5**(2), 135–145.

Eesti Energia, 2015. *Corporate Social Responsibility Report 2014*.

EEA. 2013. European Environmental Agency. *Municipal waste management in Estonia.*

Kliopova, I. & Makarskienė, K. 2015. Improving material and energy recovery from the sewage sludge and biomass residues. *Waste Management* **36**, 269–276.

Malijonyte, V., Dace, E., Romagnoli, F., Kliopova, I., Gedrovics, M. 2016. A comparative life cycle assessment of energy recovery from end-of-life tires and selected solid waste. *Energy Procedia.* In press.

MEPRD, 2012. *State Waste Management Plan of Latvia 2013–2020*. Available at: http://polsis.mk.gov.lv/documents/4276. (in Latvian).

Nagla, J., Saveļjevs, P., Ciemiņš, R., 1981. Siltumtehnikas pamati [in Latvian]. Riga, Zvaigzne.

APPENDICES

Appendix 1. Inventory analysis for preparation of fuel mixture

Material	Amount	Unit
Input		
End-of-life tires	20.099	kg FU^{-1}
Municipal solid waste	17.535	kg FU^{-1}
Sewage sludge	70.302	kg FU^{-1}
Biomass waste	70.302	kg FU^{-1}
Transportation	Amount	unit
Transport tires (collection points to shredding facility)	5.045	tkm[1]
Transport tires (shredding facility to incineration plant)	7.437	tkm
Transportation of MSW (collection points to MBT)	0.544	tkm
Transportation of SRF from MSW (MBT to incineration plant)	1.879	tkm
Transportation of biomass (diesel consumption)	3.374	kg FU^{-1}
Transportation of SRF from sludge and biomass (production facility to incineration plant)	0.889	tkm
Processing	Amount	Unit
Used tire shredding (for incineration)	20.099	kg FU^{-1}
Input		
Lubricating oil	0.0045	kg FU^{-1}
Electricity mix	4.165	kWh FU^{-1}
Output (waste to treatment)		
Inert waste	0.563	kg FU^{-1}
Scrap metal (for recycling)	3.649	kg FU^{-1}
MSW treatment in MBT	17.535	kg FU^{-1}
Input		
Electricity mix	45.933	kWh FU^{-1}
Output (waste to treatment)		
Paper and cardboard (recycling)	0.594	kg FU^{-1}
Plastic (recycling)	1.365	kg FU^{-1}
Glass (recycling)	0.765	kg FU^{-1}
Metals (recycling)	0.393	kg FU^{-1}
Other waste not suitable for treatment (landfilling)	0.526	kg FU^{-1}
SRF pre-composting	140.604	kg FU^{-1}
Input		
Diesel for Residues milling, composting,	0.068	kg FU^{-1}
Water	0.014	m^3 FU^{-1}
Industrial oil	0.0013	kg/FU
Output		
Compost for further composting	32.029	kg FU^{-1}
Waste water	0.052	m^3 FU^{-1}
Dewatering and pelleting of SRF	27.793	kg FU^{-1}
Input		
Electricity mix	0.156	kWh FU^{-1}
Water	0.014	m^3 FU^{-1}
Output		
Waste water	0.014	m^3 FU^{-1}
PM emissions from pelleting process	0.551	kg FU^{-1}

[1] tkm – ton-kilometre, a unit quantifying freight transportation, which represents the transport of one ton of waste over a distance of one kilometre

Agronomy Research **14**(Sp.1), 1180–1190, 2016

Analysis and Evaluation of the Waste Management in the Municipality

M. Mimra*, M. Kavka and R. Renfus

Czech University of Life Sciences Prague, Faculty of Engineering, Department of Machinery Utilisation, Kamýcká 129, CZ 165 21 Prague 6–Suchdol, Czech Republic
*Correspondence: mimra@tf.czu.cz

Abstract. Objective of this paper was to analyse the waste management on an example of the municipality Nový Bor in the Czech Republic. The analysis is performed on comparison of Municipal Solid Waste (MSW) production in Nový Bor which systematically separates between mixed and sorted waste as commodities with a second life span. It was noted that the average amount of mixed MSW came to approximately 200 kg×person^{-1}×year^{-1} in Nový Bor in 2014 which was 24% below the Czech average value of 263 kg×person^{-1}×year^{-1} from the identical year. Comparison of the sorted waste production in 2014 showed that Nový Bor achieved better results than the Czech average of 39.7 kg×person^{-1}×year^{-1}; a common resident of Nový Bor separated 24.4% more waste via recycling containers (= 49.5 kg×person^{-1}×year^{-1}) and 11.6% more via Bag Collecting System (BCS) which means 54 kg×person^{-1}×year^{-1} in total. Unfortunately, approximately 80% of MSW from Nový Bor is landfilled so its energy producing utilisation is totally neglected. Generally, the decision how to dispose of waste depends more or less on price: disposal of MSW by landfill costs about 700 CZK×t^{-1}, whereas in an incinerator about 2,000 CZK×t^{-1}. The personalised, registered BCS clearly ensures a better, diligent waste separation (impurity only max. 10%) compared to the mixture found in 'anonymous' recycling containers placed all over the city where the impurity of sorted waste varies between 20–40%.

Key words: bag collecting system (BCS), municipal solid waste (MSW), mixed waste, sorted waste, waste collection system.

INTRODUCTION

Wilson et al. (2015) stated that the solid Waste Management (WM) belongs to the most important functions of a city government. Hoornweg & Bhada-Tata (2012) stated that poorly managed waste has essential impact on the health of the city residents, local and global environment. Equally, Sivakumar & Sugirtharan (2010) reported that solid waste generating depends on the economy of the population as well as the level of income of the respective family or individual.

According to the Czech Waste Act No. 185/2001 Coll. 'The Hierarchy of Waste Management', within the waste management framework, the following hierarchy has to be respected firstly: Waste prevention, preparation for re-use of waste, recycling of waste, another utilisation of waste (e.g. energy generating utilisation), and waste disposal – landfilling. Aleksic (2013) stated that around 70% of MSW generated in the Czech Republic is still being landfilled. As noted by Fisher (2013), the Czech Republic must fulfil recycling EU targets and enhance the WM by re-using of 50% of MSW by the

beginning of the year 2020. As a consequence, the Czech Ministry of Environment (2014) stated on 22 December 2014 that the Government of the Czech Republic approved a new Waste Management Plan for the period 2015–2024 with a special focus on the mentioned targets.

The Bag Collection System (BCS) proved to be one of the ways how to increase the yield and purity of the separated components of the municipal waste. Consequently, the aim of this research was to verify the potentially increased purity of sorted waste collected via BCS and to compare it with the results of the stable recycling containers. Increase in the proportion of separated components will reduce the overall amount of MSW.

The aim of this article is also to present the results of the utilisation of the BCS in the municipality and to outline its positive influence on increasing amount of collected, diligently separated waste, as well as to indicate the BCS as one of the effective tools supporting improvements in waste management. Change for the better was reached by the personalised registration of the collectors/contributors – anonymity can obviously mislead some citizens to some carelessness – and also by the financial reward offered to them. The impact of the BCS was documented on the data gained from the cities which implemented and kept using this system.

MATERIALS AND METHODS

Even two adjoining cities in one district may decide to engage different companies for their WM services – a good example is Nový Bor and Česká Lípa (only 10 km distance) in the Czech Republic. Nový Bor utilises BCS, whereas Česká Lípa does not and also, they are engaging different waste disposal companies.

13,144 habitants lived in Nový Bor in 2014. 58.6% thereof lived in family houses. In year 2008, municipality Nový Bor adopted the BCS for recyclable waste. The personalised stickers serve for identification of each registered person and of the selected commodity. BCS has been used for three types of waste commodities so far: plastic, paper and since 2012 also for small electrical appliances (e.g. broken radio, electric razor, mobile phone). All the volunteers who are participating in BCS get rewarded at the end of the year, nevertheless they do not receive any banknotes handed out physically to them but the corresponding counter-value is deducted from their obligatory fee for MSW services in the next year.

In this article, we will compare the amount of generated waste for the period 2008–2014 in both of the above mentioned cities. For each kind of waste in the respective year, the average amount of waste per person in kilos and percentage changes; it was calculated by using the following equations:

Calculation of the specific amount of the waste

$$SPA = \frac{TAW \cdot 1000}{NH} \tag{1}$$

where: SPA – specific amount of waste [kg×person^{-1}×year^{-1}]; TAW – amount of waste [t], NP – number of habitants.

Calculation comparing the amount of the waste between the single years

$$YYCH = \frac{SPA - \left(SPA^{n-1}\right)}{SPA^{n-1}} \times 100[\%], \quad (2)$$

where: YYCH – year-on-year change in production of the waste [%];, SPA – specific amount of the waste [kg×person^{-1}×year^{-1}]; SPA^{n-1} – specific amount of the waste in previous year [kg×person^{-1}×year^{-1}].

Calculation of the comparison with the referential year

$$CHRY = \frac{SPA - (SPA^{r})}{SPA^{r}} \times 100[\%]. \quad (3)$$

where: CHRY – change of the waste production from the referential year; SPA – specific amount of the waste [kg×person^{-1}×year^{-1}]; SPA^{r} – specific amount of the waste in the referential year [kg×person^{-1}×year^{-1}].

RESULTS AND DISCUSSION

All MSW generated from Nový Bor is only disposed in a landfill which does not seem to be really eco-sensitive, let alone that the incinerator in Liberec is only 10 km farther than the landfill. The price for the disposal in a landfill is around 700 CZK×t^{-1} and about 2,000 CZK×t^{-1} in an incinerator. Since the WM is a business as any other, its managers search for the cheapest option of how to handle the garbage disposal. That is the reason why some firms and plants rather opt for the landfilling than for the incineration of the waste.

From 2000 to 2003, the production of mixed municipal waste increased by 40% in the Czech Republic. Unavailable support of an energy generating utilisation as well as the higher price of waste incinerating causes that the waste ends buried in the landfilling. According to the data obtained in 2003, alarming 87% of the municipal waste were landfilled and only 13% were recycled or re-used. In 2014, the share of the separated waste soared on 20% and the production of MSW dropped to 80%. Habid et al. (2013) stated that incineration of MSW may be used for the heating in the city as well as for generating of electricity. MSW has a great heating potential which varies from Low Heating Value (LHV) between 8–12 GJ×tone^{-1} to Upper Heating Value (UHV) of 18–20 GJ×tone^{-1} where the LHV corresponds with approximately 42% of the fuel value of bituminous coal (23.9 GJ×tonne^{-1}). This demonstrates that even if a material recovery is not economically feasible, its energy recovery can still bring us some environmental and economical benefits.

Comparison of the collected mixed MSW in cities Nový Bor, Česká Lípa and the Czech Republic overall

In the graph below (Fig. 1), data of mixed MSW production are presented. These data were obtained from the Department of Management of Technical Services from the City Administrative Office of Česká Lípa, and the City Administrative Office of Nový Bor; also, the average amount of waste in the Czech Republic published by ISWM in

2015 is used. The volumes are expressed as a specific amount of waste by using equation 1. The total average amount of waste in the Czech Republic is recalculated per person and is marked as 'theoretical'. The data show the course of the last 5 years and give an overview about the production of waste in Nový Bor and Česká Lípa on a district scale as well as on a nationwide scale.

This shows that the waste production in Nový Bor is almost at the midpoint between the highest and the lowest value of the MSW production. The generation of the waste has constantly decreased in the entire analysed period. Also, it can be expected that this decreasing trend will continue in the following period. Nový Bor has had a higher MSW production than Česká Lípa – apparently due to the character of the city and the prevailing number of family houses, which gives the city the character between 'Mixed development of cities' and 'Rural development' according to the criteria mentioned in ISWM (2015). The specific amount of the MSW comes from a certain housing developments but it does not include the commercial waste which is similar to the household waste by its nature; the amount of that household waste is estimated by 50–60% of the entire production of MSW (households and other waste similar to that) in 'Urban development' and by 20–30% in 'Rural development'.

The changes in the generated amount of the mixed MSW from 2010 to 2014 can be seen from the values in Fig. 1. In Česká Lípa, a reduction of the collected mixed MSW by 1.54 kg×person^{-1}×year^{-1} occurred in these years, whilst the index of determination was quite weak. In the analysed period of time, a certain interannual decrease occurred only during two years (drop-off by 4.07 and 3.47%); the other years have shown a slight increase (by 1.54% and 0.42%). In the Czech Republic, this interannual decrease in the production of the mixed MSW leveled off at 9.2 kg×person^{-1}×year^{-1} whilst in Nový Bor, it was 11.42 kg×person^{-1}×year^{-1}. In both cases the index of determination is quite strong. In Nový Bor, the slight decrease moved between 0.32% in 2013 and 7.27% in 2011.

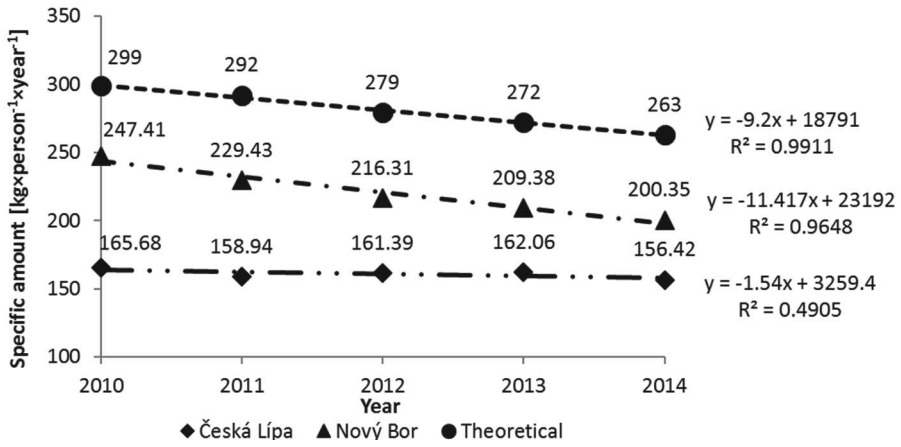

Figure 1. Comparison of specific amount of mixed MSW.

Collection of the sorted waste in Nový Bor

In the following part of this article, data collected from Nový Bor (which were used for the extended calculations presented in the methodology) are shown. Approximately 50% of the residents do actively collect recyclable waste.

Paper waste collected via stable recycling containers

In Fig. 2 and Table 1 placed below, data concerning paper waste collection within seven years are displayed; also data about the number of habitants, etc. are displayed. At first view, it can be registered that 2010 was the strongest year; a significant increase of paper production was observed nationwide. In 2010, prices of the collected commodities soared up because companies needed to stimulate and motivate people's willingness to bring more paper to the waste collection. In this year, the repurchasing price of paper was about 2 CZK per kg which has been the highest in the past dozen of years. Consequently, it can be noticed that the production of paper rose by 25.53% as opposed to the beginning of 2008. Further development slightly went down. For calculation in the below tables , equations 1, 2 and 3 were used.

Table 1. Collection of paper via stable recycling containers in Nový Bor

Year	Number of habitants	Amount [t]	Specific amount [kg×person^{-1}×year^{-1}]	Year-on-year [%]	From 2008 [%]
2008	11,380	338.60	29.75	0.00	0.00
2009	11,383	330.70	29.05	-2.36	-2.36
2010	11,434	417.00	36.47	25.53	22.57
2011	12,329	405.50	32.89	-9.82	10.54
2012	12,831	444.98	34.68	5.44	16.56
2013	12,892	407.90	31.64	-8.77	6.34
2014	13,144	351.15	26.72	-15.56	-10.21

Plastic waste collected via stable recycling containers

In Fig. 2, we present data concerning plastic waste collected via stable recycling containers; the course is fluctuating within the whole range: there was the strongest year 2011 with almost twelve kilos per person. Opposite to the peak from 2011 is the year 2009 which was the weakest one within observed period with the collected amount of 9 kg per person. Nevertheless, it can be stated that the production of Nový Bor is more or less stable and varies around 10 kilos per person per year.

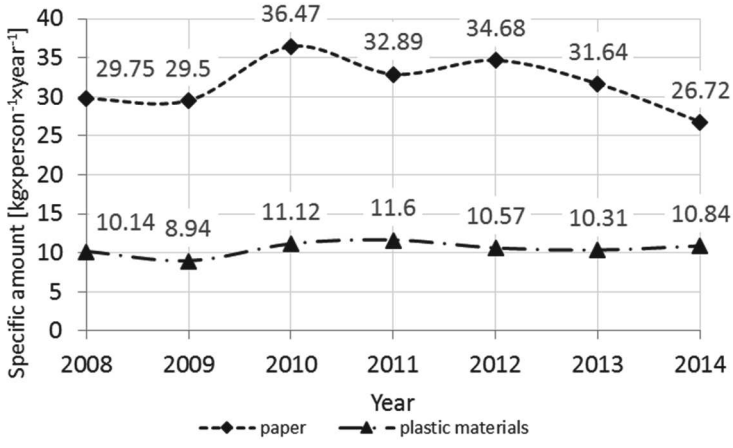

Figure 2. Collection of paper and plastic materials via stable recycling containers in Nový Bor.

The Bag Collection System (BCS) for separated waste in Nový Bor

The following part deals with the data regarding a relatively new collection system called BCS, which is used in the households. With this system, the waste is separated into bags marked with personalised barcodes (see Fig. 3). Although this system is not widespread yet and is currently used in only a few municipalities, it can be considered a unique tool. This tool supports diligent separation and collection of municipal waste generated by households. The BCS system was implemented in Nový Bor in 2008, and the following Fig. 4 displays the entire course of the system from the beginning until 2014.

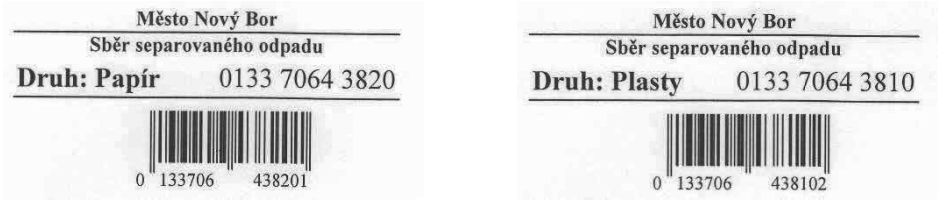

Figure 3. Example of the stickers with printed barcode for paper and plastic separation.

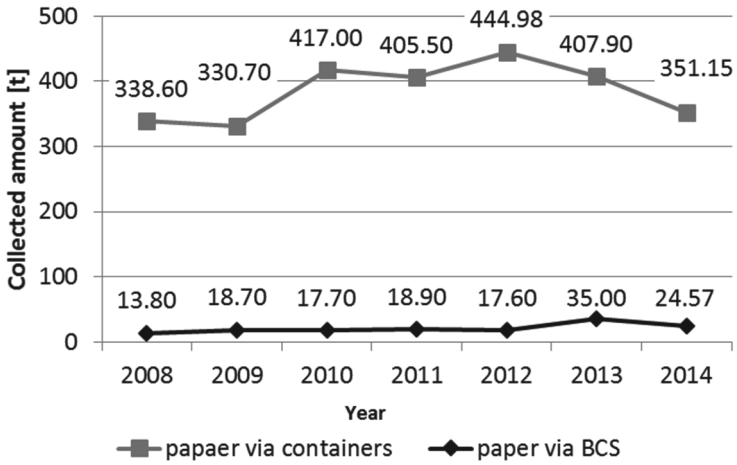

Figure 4. Comparison of the total collected amount of paper via recycling container and via BCS.

'Subjects' here apply to either individuals or a representative of a family. The number of subjects is multiplied by 3.8 for practical calculation to discover how many people actually are involved in the system. It is not really likely that one person would be able to produce and collect for instance about 50 kilos of plastic waste in one year's time. A further issue which has to be taken into account is that the number of subjects is registered as a total number of all subjects. The City Administrative Office has not registered single numbers of subjects for each commodity as it did not consider it economically feasible. Furthermore, the current situation does not make it desirable.

Paper waste collected via BCS

Fig. 5 shows the total amount of the commodity collected in each year, but more important is the specific amount of this commodity per year. In terms of percentage, the highest production per person was in 2013. Although the percentage rate tends to decrease, the number of the participants collecting paper increases dramatically: compared with the referential year 2008, in 2013 the number was more than double.

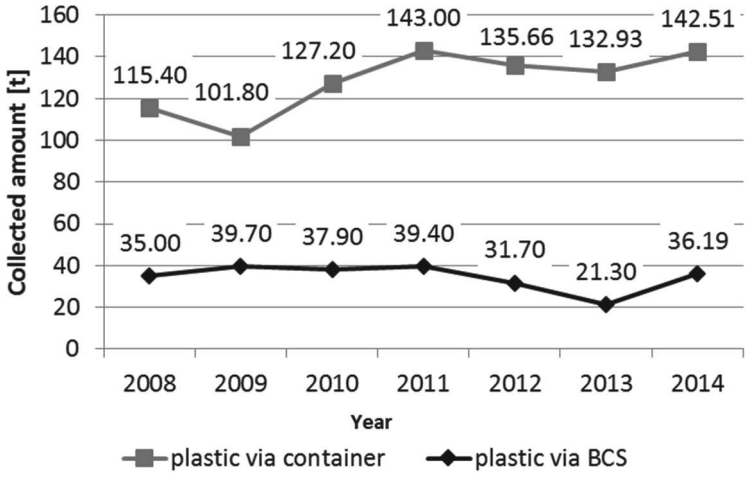

Figure 5. Comparison of the total collected amount of plastic via recycling containers and via BCS.

As we can see from Fig. 4, the amount of paper collected via stable containers increased gradually till 2012. From this point, it started decreasing. However, the growth did not really correspond to the increased number of inhabitants as it is obvious from the decreased amount of collected paper per person with the maximum of 36.47 kg×person^{-1}×year^{-1} in 2010. After 2010, it fell. The paper collected via BCS reached its peak in 2013 at the maximum of 35 kg×person^{-1}×year^{-1}. In the entire analysed time, by means of the stable containers the amount of 31.6 kg×person-1×year-1 was collected. By means of the BCS, it was 36.8 kg×person^{-1}×year^{-1}. According to Fig. 4, BCS contributed to the improvement concerning the collected amount of paper from 3.9% in 2012 to 7.9% in 2013. The share of participants in the BCS increased from 2.86% (from the total number of inhabitants of Nový Bor) in 2008 to 6.7% in 2014. Therefore, it is obvious that the amount collected per participant via BCS was higher than the amount collected via stable containers.

Plastic waste collected via BCS

In Fig. 5, data regarding amounts of collected plastic waste via BCS are displayed. At first view, the increasing number of subjects (in 2008, 325 subjects; in 2015, 900 subjects) can be noticed. We can conclude from these numbers that the installation of such a system is successful. The incentive which motivates people to collect a substantial amount of plastic waste is apparently the 1.50 CZK per kilo payment they receive.

As we can see from Fig. 5, the development of plastic material collection via stable recycling containers does not show a distinct trend. In 2009, there was a slight decrease

of the collected amount to 101.8 t. In 2010 and 2011, the amount slightly increased and reached its peak for all the analysed period with 143 t. The pace of growth of collected plastic material neither reflected the increase of inhabitants nor the better economic situation. The average yield of plastic waste collected via stable containers during the analysed period of time was only 10.5 kg×person^{-1}×year^{-1}. In contrast to that, the average yield of the same material collected via BCD was 66.5 kg×person^{-1}×year^{-1}. From this comparison, we can clearly state that the BCS for plastic materials is much more efficient than the stable containers. However, we also noticed that BCS was even more efficient at the beginning of its implementation in 2008 with the yield of 107.69 kg×person^{-1}×year^{-1}. Then it started decreasing to 41.13 kg×person^{-1}×year^{-1} in 2014. From Fig. 5, it is clear that the share of waste collected via the BCS changed with regard to the overall collected amount from 14% in 2013 to 28% in 2009.

Scrap metal from small electrical appliances collected via BCS

This recyclable segment was implemented four years ago so there is not much representative information about it yet. In Table 2, data regarding the number of small electrical appliances collected via BCS are displayed. In 2012, people were apparently informed about the new sorting of these goods. In the following year 2013, the number of the active participants increased and the collected amount peaked at 0.81 kg per person per year. The latest monitored year 2014 was even lower than the year 2008 because people had already disposed of all the unnecessary or broken electrical devices gathered at home. The development of the collection of scrap metal depends on people's behaviour – concerning whether they decide to keep or replace old electric appliances. It is necessary to understand that people do not really like throwing away expensive devices; hence, the process of disposal of old electronic appliances can take some time.

Table 2. Scrap metal from small electrical appliances collected via BCS in Nový Bor

Year	Number of subjects	Amount [t]	Specific amount [kg×person^{-1}×year^{-1}]	Year-on-year [%]	From 2008 [%]
2012	635	0.33	0.52	0.00	0.00
2013	750	0.61	0.81	54.64	54.64
2014	880	0.35	0.40	-50.84	-23.98

Collection of such appliances for recycling purposes does not have a long history in our country. The available results are too fluctuating so as to be able to determine a representative outcome. However, it is certainly a very good approach to collect all the broken or obsolete appliances. Volume of this waste is not so high; thus, there are not so many recycling containers designed especially for these devices. In addition, people often dispose of their outdated electronic devices in the mixed waste. By contrast, the BCS motivates people to separate their electronic appliances at home and put them in the appropriate bags for recycling.

The amount of the respective materials collected via BCS can be seen in Fig. 6. As the graph shows, there is not a definite trend in the development of the amount of collected waste. The yield of the waste production is affected by several factors. One of them is the economic development of the country. The interesting fact is that with economic progress, the purchase increases: people can afford to buy more and consequently produce more waste. Unfortunately, more wealth does not insure a better

separation of waste. Therefore, it is highly recommendable to motivate people (already starting at a very young age with this 'education' whenever possible) to adopt some positive recycling habits and to care about the environment.

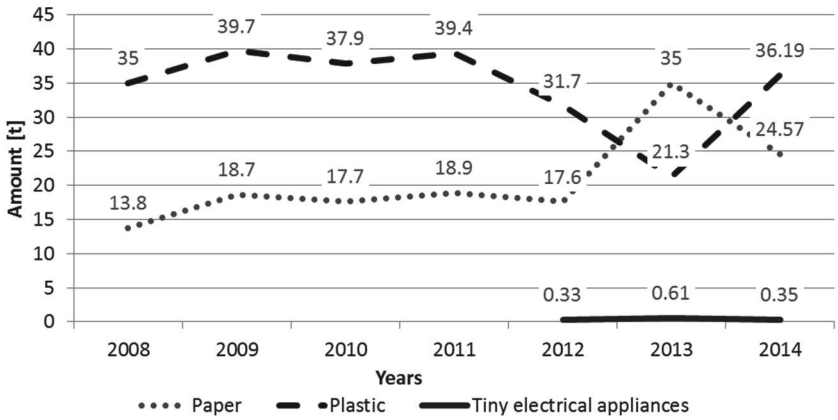

Figure 6. Graph displays the development of collected amount of separated waste by BCS.

CONCLUSIONS

Mixed MSW generation in Nový Bor has tended to decrease; this decline is constant and it is apparently still going to continue. However, the MWS production in Česká Lípa is even lower – seemingly due to a different character of the city. And the overall results of Nový Bor are still remarkably good.

Bing at al. (2014) found out that the success of the separated waste collection system results from the optimised reverse logistics network. This makes the overall recycling system more efficient and sustainable while taking into account the interests of various stakeholders (municipalities, households, etc.). According to a research paper published by EKO-KOM (2014), if you ask people to bring their waste to a container which is located more than 400 m away from their house, only 5% of the population will be willing to walk there. The collection network can also be supplied via BCS, collection yards, etc. Rousta et al. (2015) stated that the statistical analyses of the research results indicated a significant decrease (-28%) of packaging and newsprint found in the residual waste after establishing a collection system close to the people's residences. Hence, a shorter distance to the drop-off points definitely contributes to a better waste recycling.

According to the results of the analysis of Nový Bor and the related experiences from other Czech municipalities, the BCS can be recommended as a fully functional system worth adopting. As stated by EKO-KOM (2013), every Czech citizen sorted on average 39.7 kg of recyclable waste, that is paper, plastic, glass and carton. According to the conducted analyses, every inhabitant of Nový Bor sorted on average 49.4 kg of the waste via stable recycling containers (not including the BCS) and 54 kg altogether via both systems (containers + BCS) in 2014. In fact, the BCS in Nový Bor is still a relatively new idea so people are getting used to it, but the participation in this system has progressively increased from about 300 subjects at the beginning to the current almost 900 active subjects. As stated by Rousta & Ekstrom (2013), the results of their

research showed that in a medium sized Swedish city, approximately 68 wt% of the combustible fraction and 29 wt% of the food waste were not sorted correctly. Therefore, it would be a very good idea to change some factors such as the inhabitants' anonymity (by using personalised barcode stickers for a quick and easy identification) and to offer a financial motivation (financial reward or at least a discount for MSW services or other) in order to enhance the inhabitants' involvement in the waste management system.

In view of the recorded findings and shared experience about the execution of the BCS, it is obvious that this system is strongly recommendable in order to obtain a higher yield and to maintain a cleaner separation of the respective recyclable materials. The quality and accuracy of waste separation definitely improve as soon as the respective collectors are no longer anonymous. This can be achieved by using the personalised stickers with barcodes on the bags. In general, this system is advisable for the parts of the cities with family houses. It is not so recommendable for multistory buildings, where the participation has been considerably lower so far. Moreover, this system works well in small and medium-sized cities, where people tend to know one another.

This paper was carried out as a part of the project no. MSM6046070905 supported by the Czech Ministry of Education, Youth and Sports.

REFERENCES

Aleksic, D. 2013. *Municipal waste management in the Czech Republic*. Regional Environmental Center. ETC/SCP. 16 p. Webpages of the corporation: *http://www.rec.org.* Accessed on January 13, 2016.

Bing, X.Y., Bloemhof-Ruwaard, J.M. & van der Vorst, J.G.A.J. Sustainable reverse logistics network design for household plastic waste. *Flexible services and manufacturing journal*. **26**(1–2), 119–142.

Czech Republic 2001. Waste Act no. 185/2001. Collection of Laws of Czech Republic. 2001. Collection of Laws of Czech Republic (Sbírka zákonů České Republiky). 71. p. 4074–4128. Also available from: http://aplikace.mvcr.cz/sbirka-zakonu. Accessed on January 13, 2016.

Data regarding waste management in Nový Bor obtained from the City Administrative Office of Nový Bor. Data provided from city's information system based on an interview with Mr Petr Škop.

Data regarding waste management in Česká Lípa obtained from the City Administrative Office of Česká Lípa. Data provided from city's information system based on an interview with Ms Ivana Bínová.

EKO-KOM 2013. EKO-KOM company. Available at: http://www.ekokom.cz/en/other/our-company. Accessed on January 13, 2016.

Fisher, C. 2013. Municipal waste management in Germany. *Copenhagen Resource Institute*, ETC/SCP. 18 p.

Habid, K., Schmidt, J.H. & Chritensen, P. 2013. A historical perspective of Global Warming Potential from Municipal Solid Waste Management. *Institute of Chemical Engineering, Biotechnology and Environmental Technology, University of Southern Denmark*, Niel's Bohr Alle 1, Odense M, Denmark. 18 p.

Hoornweg, D. & Bhada-Tata, P. 2012. What a Waste: A Global Review of Solid Waste Management. *Urban Development & Local Government Unit*, World Bank. NO 15. 116 p. DOI: 68135.

ISWM, 2015. Information System of the Waste Management (Informační systém odpadového hospodářství) *Statistical Yearbook of the Environment of the Czech Republic*. (Statistické

ročenky životního prostředí ČR) Available at: *http://issar.cenia.cz/issar/page.php?id=1730*. Accessed on January 10, 2016.

Ministry of Environment of the Czech Republic. 2014. Government approved new Waste Management Plan for the Czech Republic (Vláda schválila nový Plán odpadového hospodářství ČR) Available at: *http://www.parlamentnilisty.cz/politika/politici-volicum/Vlada-schvalilanovy-Plan-odpadoveho-hospodarstvi-CR-351288.* Accessed on January 13, 2016.

Rousta, K., Bolton, K., Lundin, M. & Dahlen, L. 2015. Quantitative assessment of distance to collection point and improved sorting information on source separation of household waste. *Waste Management* **40**. 22–30.

Rousta, K. & Ekstrom, K. M.2013 Assessing Incorrect Household Waste Sorting in a Medium-Sized Swedish City. *Sustainability* **5**(10), 4349–4361.

Sivakumar, K. & Sugirtharan, M. 2010. Impact of family income and size on per capita solid waste generation: a case study in Manmunai North Divisional Secretariat Division of Batticaloa. *J Sci. University Kelaniya* **5**, 13–23.

Wilson, D.C., Rodic, L., Cowing, M.J., Velis, C.A., Whiteman, A.D., Scheinberg, A., Vilches, R., Masterson, D., Stretz, J. & Oelz, B. 2015. 'Wasteware' benchmarket indicator for integrated sustainable waste management in cities. *Waste Management* **35**, p. 329–342.

Agronomy Research **14**(Sp.1), 1191–1199, 2016

Correlation between temperatures of air, heat carrier liquid and seabed sediment in renewable low energy network

A. Mäkiranta*, J.B. Martinkauppi and E. Hiltunen

University of Vaasa, Faculty of Technology, Electrical Engineering and Energy Technology, P.O. Box 700, FI-65101 Vaasa, Finland
*Correspondence: anne.makiranta@uva.fi

Abstract. The low energy network based on renewable seabed sediment heat has been monitored for several years in Vaasa, Finland. In this study the temperatures of air, heat carrier fluid and seabed sediment are compared to each other and correlations between them are investigated. In this study data from one year 2014, was used. Correlations between these subjects clearly exist. The sizing of installed network seems to be correct; no overuse was detected.

Key words: Renewable energy, heat energy, sediment energy, carbon-free, distributed temperature sensing (DTS) method.

INTRODUCTION

The local renewable energy sources are available everywhere. The harvesting of those sources is going on worldwide in order to mitigate the global warming. The seabed sediment heat is one geothermal heat energy source which has been utilized in Vaasa, Finland since 2008. Actually this heat source is mostly generated by the sun which is common with heat sources near the soil surface. In Finland the impact of seasonal variation in air temperatures is observed to affect even in the depth of 10–15 meters from the soil surface. In Vaasa the seabed sediment heat is delivered to total of 42 households via heat collection pipes and heat pumps. This low energy network has also been used for cooling those houses in the summertime. There have been implemented temperature measurements of air, heat carrier liquid and sediment during 8 years. Mäkiranta et al. (2015) have noticed in their measurements that in the seabed sediment the temperature difference between October and the coldest month stays stable at 8 degrees.

Hiltunen et al. (2015) have investigated the dependency between air temperature and fluid temperature on the area. They observed that the heat carrier liquid achieved its maximum temperature typically after one month of the peak value of the air temperature. In this study the sediment temperature will be compared to the values of fluid and air temperature and the correlation of these three variables is analysed. The aim is to discover if the collection pipeline is sized correctly: if a high correlation between these subjects exists, then a proper interaction is likely.

MATERIALS AND METHODS

The observations of air temperature were acquired from Finnish Meteorological Institute. The heat carrier fluid temperatures were measured by one resident of the sediment heat network. The sediment heat temperatures were measured by the renewable energy research group of University of Vaasa. Temperatures of seabed sediment have been acquired by optical measurement device. The distributed temperature sensing (DTS) method observes the data with the spatial resolution of even 1 m. The optical cable (sensor) is installed along one 300 m long heat collection tube. Temperature data is collected on the shore from the distribution well. The data indicates the sediment temperatures in the 3–4 m depth, starting at the shore and extending to the distance of 300 m in the sea.

DTS method

The temperatures of the seabed sediment are measured by distributed temperature sensing (DTS) method where optical fibre functions as linear sensor. Temperatures can be measured as a continuous profile along the whole fibre not only at some points. In other words temperature measurement is distributed. Fibres can be even several kilometres long and they are typically made from doped quartz glass.

DTS-measurement device emits short optical pulses (laser light), which illuminate the glass core of an optical fibre. Different types of scattering are subjected to optical pulse while it moves along the core of fibre. One type of scattering is Raman scattering which consists of Anti-Stokes and Stokes band. Anti-Stokes band is temperature dependent, while Stokes band is not. The ratio of the Anti-Stokes and Stokes light intensities indicates the local temperature of optical fibre. The speed of optical pulse is used to evaluate the spatial position of the temperature (Ukil et al., 2012).

Measurements on the site

Seabed sediment temperature measurements were made by Oryx DTS device. The patch cord was used to calibrate the device and to secure cleanliness of the channels in the device. The rugged laptop (Fig. 1) acquired the data instantly at the measurement site. One measurement took 10 minutes which means 20 measurements totally by one measurement channel. Temperature changes are relatively slow at the seabed sediment. That is why one measurement session per month was justified and 10 minutes for data acquiring per session was observed to be long enough.

Figure 1. DTS-device was in commission at the low energy network site in Suvilahti.

The original measurement data of seabed sediment temperatures for one year period is shown in Fig. 2.

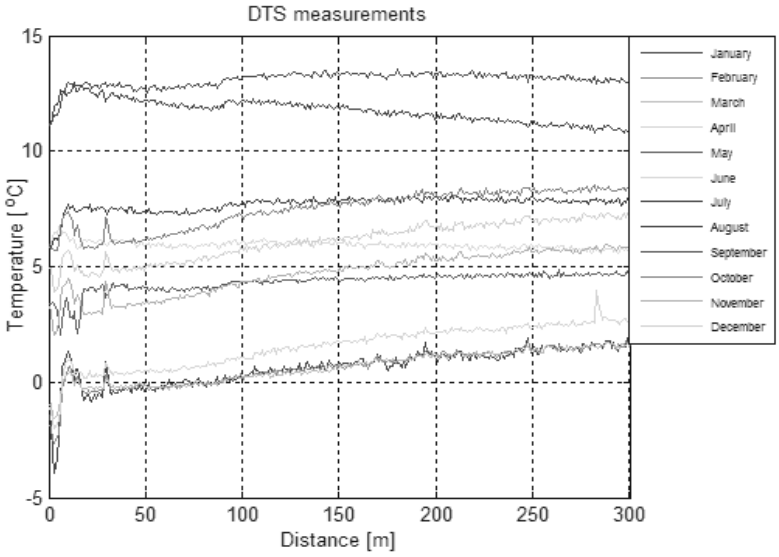

Figure 2. The original data for DTS measurements in year 2014.

Analysing method for data

First, the original data was analysed on the basis of its temperature profile. This provides a very rough estimate about the sediment temperature behaviour.

The next phase is to compare the sediment temperature to the air and heat carrier fluid temperatures. As the air and liquid temperatures are scalar, we have selected temperature data at two different points. A problem is that the temperature data is very noisy due to nature of the measurement itself, environment and other factors. This was solved using moving average-method to smooth the data. The selected window size is nine; i.e. a point value is replaced with an average of values from the point and from four other points before and after the point.

Theory and modelling

Correlations were evaluated between the following data: I air temperature and liquid temperature, II air temperature and sediment temperature and III sediment temperature and liquid temperature. The correlation was calculated using Pearson product-moment correlation coefficient and Spearman's rank correlation coefficient. A short description is provided in this article, as a more comprehensive overview is available in many statistical textbooks (e.g. Sprinthall 2012).

Pearson product-moment correlation coefficient (Pearson r) measures linear correlation or dependence between one subject's temperature data (symbol x) and another subject's temperature data (symbol y). The r –values can be between +1 and -1 where 1 is total positive correlation, -1 total negative correlation and 0 is no correlation.

The Pearson *r* is defined as

$$r_{x,y} = \frac{cov(x,y)}{\sigma_x \sigma_y} = \frac{E[(x-\mu_x)(y-\mu_y)]}{\sigma_x \sigma_y} \quad (1)$$

where *cov* indicates covariance, σ is the standard deviation, μ is mean, *E* is expectation, subindex *x* indicates the first subject's data, and subindex *y* indicates the second subject's data. The entire range of each subject's data is assumed to be normally distributed. The temperature values (Celcius degrees here) naturally belong to interval data.

The significance of Pearson *r* is tested against the null hypothesis: the correlation is due to chance. The significance is assessed using Pearson *r* table with the degree of freedom (the number of pairs of scores minus 2) (Sprinthall 2012).

Another metric used is Spearman's rank correlation coefficient (Spearman's r_s) which is a nonparametric measure. All temperature data values for each subject are converted into ordinal ranks. For each month, the absolute difference *d* between temperature ranks is calculated and squared. The Spearman's r_s is calculated using the following formula:

$$r_s = 1 - \frac{6\sum d^2}{N(N^2-1)} \quad (2)$$

where *N* is the number of pairs. It is used here to evaluate the statistical dependence between temperatures. This metric compares their relationship to a monotonic function. The values are again between +1 and -1.

RESULTS AND DISCUSSION

Correlations between the fluid temperature and sediment temperature as well as the air temperature and sediment temperature are evaluated. The sediment temperature is measured at different distances along the pipe but two different points (distances 150 m and 250 from the shore) are used for correlation calculations. A high correlation is assumed to mean that sizing of the pipeline is done correctly. The appropriate and adequate sizing is vital for improvement of renewable low energy network.

The DTS temperature profile was noticed to change depending on the month. Fig. 3 shows profiles from January to April as well as from October to December. The measured temperatures are lower near the shore than further away in the bay. These months are also the typical months when a heating is needed for the houses in Finland. Also the month November has lower temperature values than month December. This might be due to appearance of ice cover or stratification effect in bay water in December.

Fig. 4 displays the temperature profiles for the warm months from May to September. The temperature profiles exceed their highest temperature at September. The form of temperature profile is different than in Fig. 3 which contains the cold months.

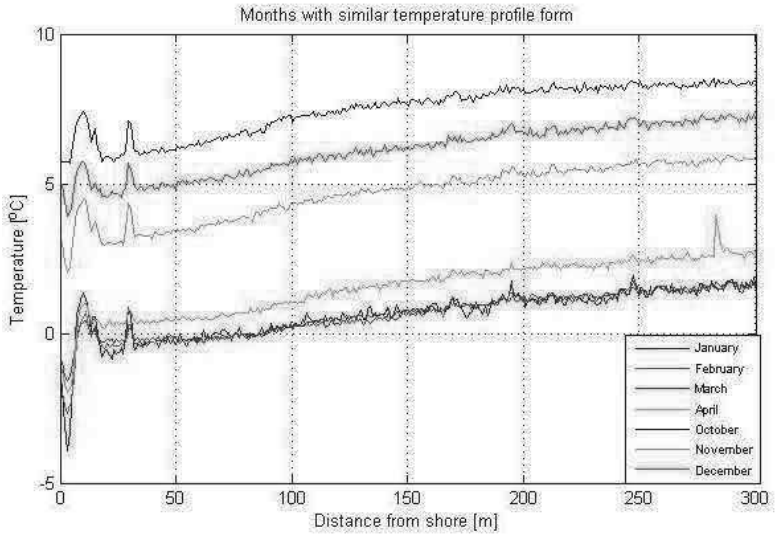

Figure 3. The temperature profiles for seven cold months in year 2014.

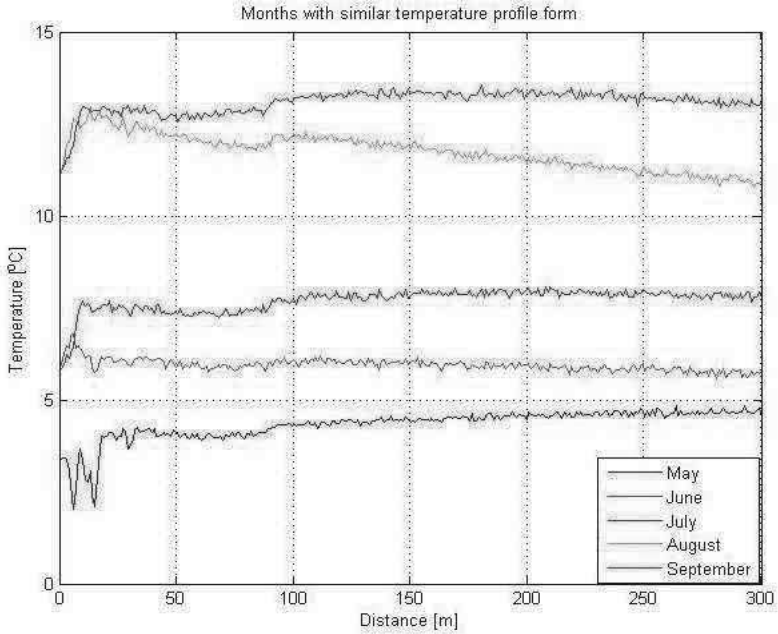

Figure 4. Temperature profiles for 5 warm months in year 2014.

The temperature profiles for year 2014 indicate that the sediment reach the maximum temperature at the late summer as well as there is a minimum temperature limit under which the current usage cannot drive.

The original data was subjected smoothing with a moving average method with window size of nine. The results for smoothing as well as selected points for correlation calculations are shown in Fig. 5. The selected analysing points were taken of the distances of 150 m and 250 m from the shore.

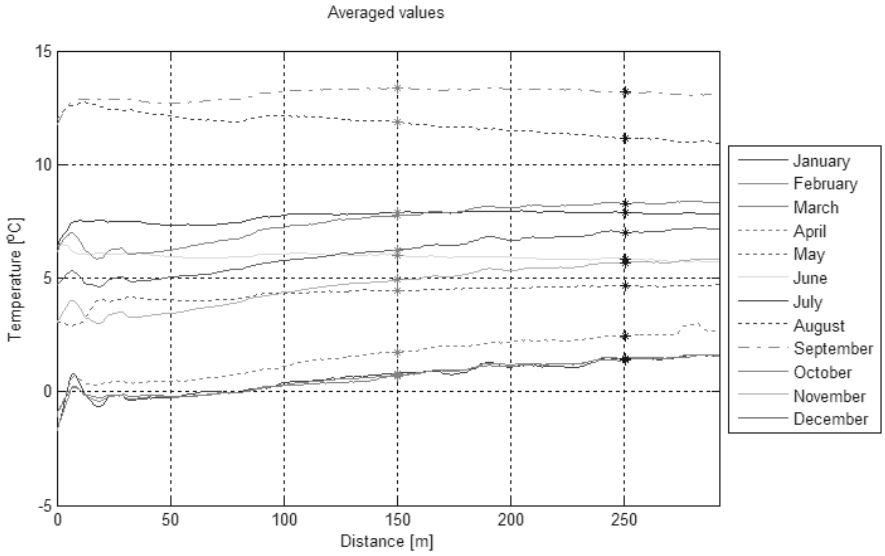

Figure 5. The averaged values are shown for each month. The selected analysing points (150 m and 250 m) are indicated with * marker.

Air, liquid and sediment temperatures were plotted as a function of time in Fig. 6. Naturally, the biggest range appears in the air temperature.

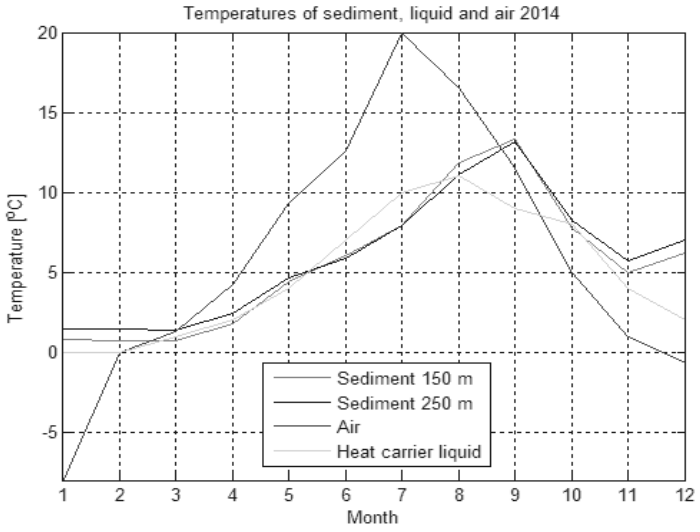

Figure 6. Temperature data from January to December 2014.

During the warmest months (June and July) the heat carrier liquid temperature exceeds the sediment temperatures. This can be understood due to the need for cooling in the houses.

Table 1 shows the correlation coefficient values calculated for different subject pairs. In the first three rows, the correlation between air data and liquid or sediment data is calculated as well as between air data and delayed or advanced liquid or sediment data. As in our earlier paper (Hiltunen et al. 2015), the highest correlation between air and liquid data occurs between liquid data is taken one month later than corresponding air data. There seems to exist also a high correlation between air temperature and temperature of sediment after one or two months.

The last two rows show the correlation between sediment data and liquid data (as well as delayed or advanced data). The correlation is high when the subjects data measured at the same time as well as when the sediment data is compared against previous months liquid data. One could interpret this so that when the liquid heats or cools sediment this affects also sediment temperature at the next months.

Table 1. Correlations

Data	Pearson coefficient	Spearman coefficient
Air temperature and liquid temperature	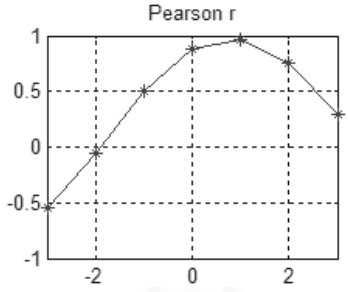	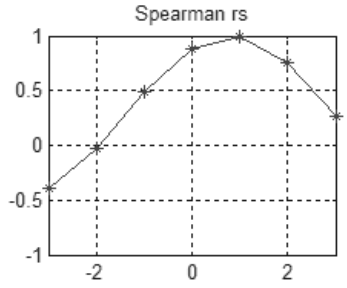
Air temperature and sediment temperature 150 m	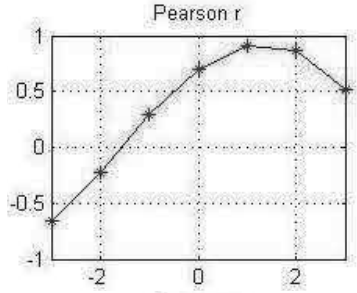	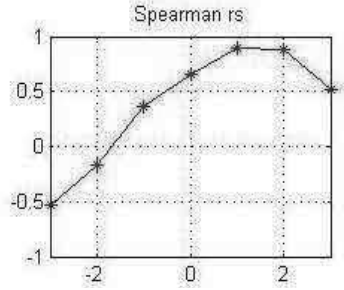
Air temperature and sediment temperature 250 m	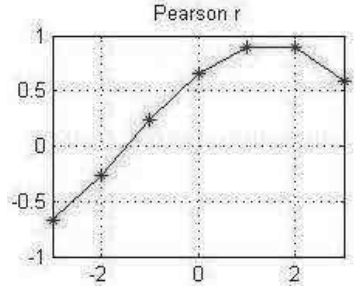	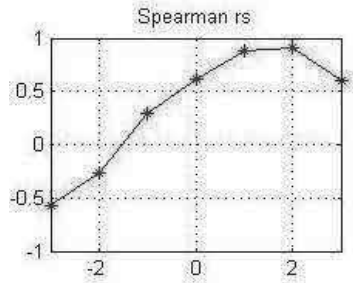

Table 1 (continued)

Sediment temperature 150 m and liquid temperature	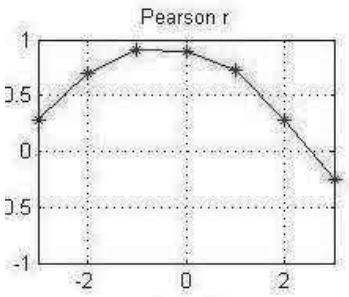	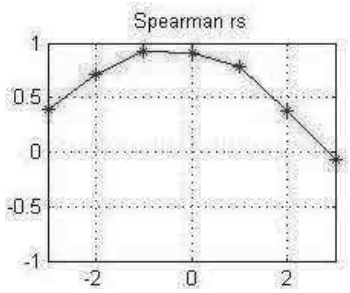
Sediment temperature 250 m and liquid temperature	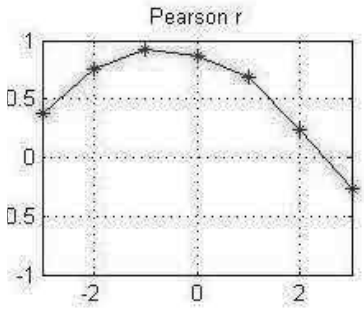	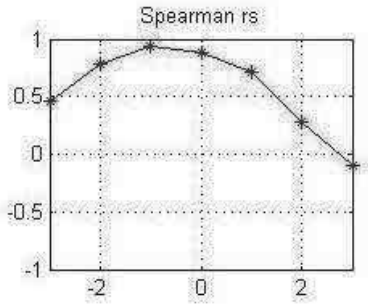

CONCLUSIONS

There was noticed high correlation between the heat carrier liquid temperature and sediment temperature. Especially, liquid temperature and sediment temperature of next month, as well as, liquid and sediment temperature of the same month are correlating strongly. This may indicate that the low energy system is really working. In winter time the sediment is getting cooler due to the usage for heating. In summer time sediment is warming due the cooling of the houses. Of course there are also other factors that are affecting to the sediment temperatures.

The sediment temperature curve (Fig. 2) seems to rise slightly to the end even in winter time. This might indicate the fact that the sizing of this site`s pipeline is played safe. In other words this network is sized bigger than would have been necessary. This is natural in pilot systems.

The high and significant correlation between air temperature and temperature of sediment after one or two months was also observed. The sediment temperature is indicating the previous weather conditions.

ACKNOWLEDGEMENTS. We thank Mr. Juhani Luopajärvi for implementing the liquid temperature measurements.

REFERENCES

Hiltunen, E., Martinkauppi, J.B., Mäkiranta, A., Rinta-Luoma, J. & Syrjälä, T. 2015. Seasonal temperature variation in heat collection liquid used in renewable, carbon-free heat production from urban and rural water areas. *Agronomy Research* **13**, 485–493.

Mäkiranta, A., Martinkauppi, J.B., Hiltunen, E. & Lieskoski, M. 2015. Seabed Sediment Heat Measurements at the House Fair Area in Vaasa. (submitted)

Sprinthall, R.C. 2012, *Basic statistical analysis*. 9th edition. Pearson. 660 pp. (in the USA).

Ukil, A., Braendle, H. & Krippner, P. 2012. Distributed Temperature Sensing: Review of Technology and Applications. *IEEE Sensors Journal* **12**, (5), 885–892.

Agronomy Research **14**(Sp.1), 1200–1211, 2016

Optimization of a solar power station with $LiFePO_4$ accumulators

V. Papez[1] and S. Papezova[2,*]

[1]Czech Technical University in Prague, Faculty of Electrical Engineering, Department of Electrotechnology, Technicka 2, CZ 166 27 Pague 6, Czech Republic
[2]Czech University of Life Sciences in Prague, Faculty of Engineering, Department of Electrical Engineering and Automation, Kamycka 129, CZ 165 21, Prague 6 - Suchdol, Czech Republic; [*]Correspondence: papezovas@tf.czu.cz

Abstract. The paper describes the design and construction of an isolated solar power station supplying energy at weekends to a remote location. The system comprises two parts: a photovoltaic system generating electric energy in sunlight, and an accumulator accumulating energy to be permanently available and to be able to supply a peak power of several kW. The design of the system optimized with respect to maximum reliability, ease of operation and minimum purchase costs. The control circuits were therefore constructed by means of simple analog circuits. To use microcomputers, which are nowadays used in battery management systems most often available on the market, is not appropriate. Such a system, compared with a simpler analog system, is less reliable. Power circuits are again designed in order to ensure minimum complexity of the system. The resulting design is absolutely different from conventional designs offered by suppliers of photovoltaic systems. The photovoltaic part of the system is designed for optimum adaptation of the load characteristic of the photovoltaic generator to the charging characteristic of the accumulator. By selecting photovoltaic panels with appropriate parameters and their appropriate interconnection, possibly by an automatic change of their interconnection during the charging cycle, it is possible to achieve more effective utilization of the charging power of the photovoltaic generator than by using charging DC/DC converters. The accumulator used in the system is formed by an assembly of $LiFePO_4$ accumulators which thanks to their outstanding durability in spite of their high price currently show the lowest cost per accumulated kWh.

Key words: $LiFePO_4$ accumulator, solar power, photovoltaic panel characteristic.

INTRODUCTION

The system charging the accumulators with the power from a photovoltaic (solar) generator is usually designed according to the block circuit diagram shown in Fig. 1.

The solar generator is connected to the charged accumulator via a controlled switch-mode DC/DC converter controlled by a microcomputer.

The operating voltages of the solar generator and accumulator, if they are in an area where the DC/DC converter can work, do not play a significant role in the operation of the system. The controlling computer adjusts the operation of the DC/DC converter to optimize it according to the selected criteria.

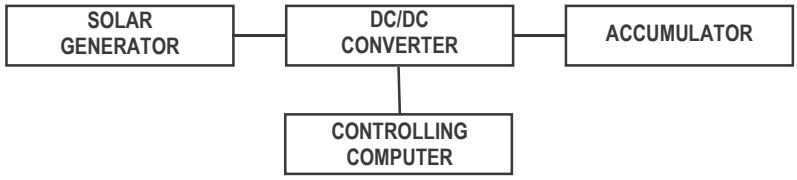

Figure 1. Accumulator charger with a DC/DC converter.

Systems with photovoltaic generators are usually operated in maximum power point tracking (MPPT). The converter transforms the MPP voltage and current from a solar generator to values corresponding to the charging characteristic of the accumulator. Power transmission efficiency reaches up to 98%, as declared by the manufacturers and mainly by the distributors of DC/DC converters for solar systems. In practice, under good conditions, a 90% efficiency (Riawan & Nayar, 2007; Darla, 2007) is reported.

In addition to losses, the main setbacks of these charging systems are the not very high reliability of comprehensive computer-controlled systems and high acquisition costs. Approximately the same efficiency can be achieved without using a DC /DC converter and without the mentioned setbacks if the load characteristic of the solar generator and the charging characteristic of the accumulator are chosen to be as close as possible.

MATERIALS AND METHODS

A typical current-voltage characteristic (I–V curve) of a solar panel for a defined lighting and temperature (1,000 Wm^{-2}, 25 °C = STC–standard test conditions), is in Fig. 2. The dependence was determined as an average of measurements on 10 SH-100S5 (Huashun Solar, 2015) panels. The measurements were performed on a PASAN – Sun Simulator IIIc equipment at the Czech Technical University in Prague (CTU in Prague, 2016). A panel comprising photovoltaic in-series connected cells can be represented by an electric model which is similar to the model standardly used for an individual photovoltaic cell shown in Fig. 3.

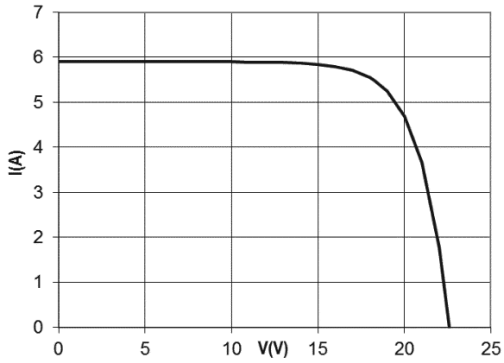

Figure 2. Example of a solar panel load characteristic.

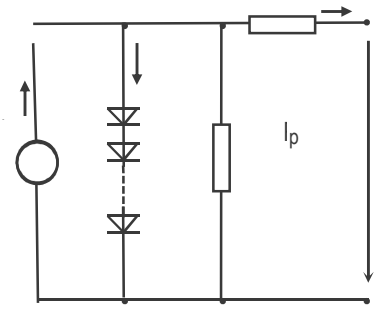

Figure 3. Electric model of a solar panel.

The current from photoelectric cells represents the source of current, a diode string N represents forward biased cell PN junctions, resistance R_s represents the resistance of the interconnecting panel array and resistance R_p represents parallel leak resistances in the panel. The current I supplied by the panel at a terminal voltage V can be expressed by (1). The magnitude of the photovoltaic current I_{ph} is almost proportional to the lighting of the panel. The characteristic of N diodes is expressed in the form of a Shockley approximation of the I–V PN junction characteristic corrected by the ideality factor n of the diode junction, $1 \le n \le 2$. Its temperature dependence is represented by the temperature dependence of the terminal voltage of the panel. In practical use the influence of parallel resistance is neglected and thus the last term in equation (1) is eliminated. Also the terminal voltage can be expressed from the simplified equation as a function of the current (2).

$$I = I_{ph} - I_o\left[\exp\left(\frac{e(V + IR_s)}{NnkT}\right) - 1\right] - \frac{V + IR_s}{R_p} \tag{1}$$

where: I – output current of the solar array (A); I_{ph} – current of the solar array proportional to light intensity (A); I_o – diode saturation current; R_s and R_p – equivalent series and parallel resistance (Ω); N – number of series cells in the solar array; n – diode ideality factor; k – Boltzman constant ($k = 1.381 \times 10^{-23}$ J K^{-1}); e – electronic charge ($e = 1.602 \times 10^{-19}$ C); T – cell temperature (K); V – output voltage of the solar array (V).

$$V = \frac{NnkT}{e}\ln\left(\frac{I_{ph} + I_o - I}{I_o}\right) - IR_s \quad \text{if } R_p \to \infty \tag{2}$$

The electrical output P supplied by the panel can be expressed in the form of (3). A typical diagram of the dependence of the proportional output power supplied by the panel on the load current is shown in Fig. 4. The maximum power point tracking current I_{MPP} is almost directly proportional to the lighting of the panel and only to a very low extent depends on the working temperature of the panel.

$$P = VI = \left[\frac{NnkT}{e}\ln\left(\frac{I_{ph} + I_o - I}{I_o}\right) - IR_s\right]I \tag{3}$$

The state when the panel gives maximum output (P_{MPP}) can be determined by finding the extreme of function (3) according to equation (4).

$$\frac{\partial P}{\partial I} = \left[\frac{NnkT}{e}\ln\left(\frac{I_{ph} + I_o - I}{I_o}\right) - IR_s\right] - I\left[R_s + \frac{NnkT}{e(I_{ph} + I_o - I)}\right] = 0 \tag{4}$$

The dependence of the proportional output power of the panel on the load voltage is similar and is illustrated in Fig. 4.

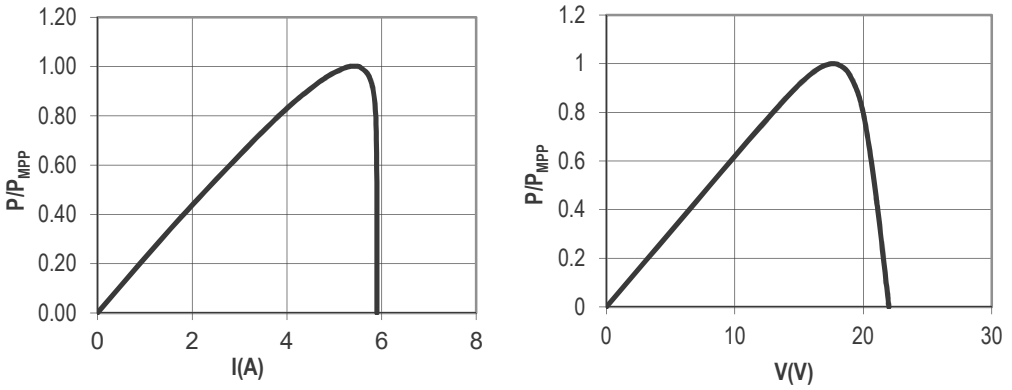

Figure 4. Dependence of the proportional output power on the current and load voltage for panel SH-100S5 (Huashun Solar, 2015) with an *I-V* curve according to Fig. 2.

The voltage V_{MPP} depends on the panel lighting only to a very low extent; at a constant temperature, it is also almost constant. The temperature dependence of V_{MPP} corresponds to the temperature dependence of the voltage on the forward biased p-n junction. In the temperature range where the panel can operate; i.e. from 0 °C to 75 °C, the value of V_{MPP} decreases by about 30% of P_{MPP}, similarly as the maximum output V_{MPP}.

At a constant temperature a PV panel gives an output greater than 90% of P_{MPP} in voltage ranges around V_{MPP}, the width of which is approximately 25% of V_{MPP}. Considering the above mentioned facts, in order to achieve maximum power transfer from the panel to the energy consumer, it is more advantageous to load the panel with a load where the constant terminal voltage is independent of the passing current.

CHARGING ACCUMULATORS FROM THE SOLAR GENERATOR

A typical dependence of the voltage on the supplied charge during the charging of a $LiFePO_4$ accumulator is in Fig. 5.

Voltage depends almost entirely on the supplied charge. The cells show very low internal resistance. In the area of low charging currents, i.e. in case the charging current changes which numerically corresponds to a tenth of the ampere-hour cell capacity, the terminal voltage changes by less than 1%. In the case of constant current charging the voltage of a cell during 96% of the charging time is in a band 25% wide around the mean value. During 90% of the charging time the voltage is in a band 10% wide around the mean value.

If the solar generator and the accumulator are assembled in a way that V_{MPP} is approximately the same as the charging voltage of the accumulator in the middle of the charging cycle, the solar generator will supply up to 96% of P_{MPP} during the charging time. In this case, the efficiency of power transfer from the solar generator to the accumulator can be higher than with the DC/DC converter.

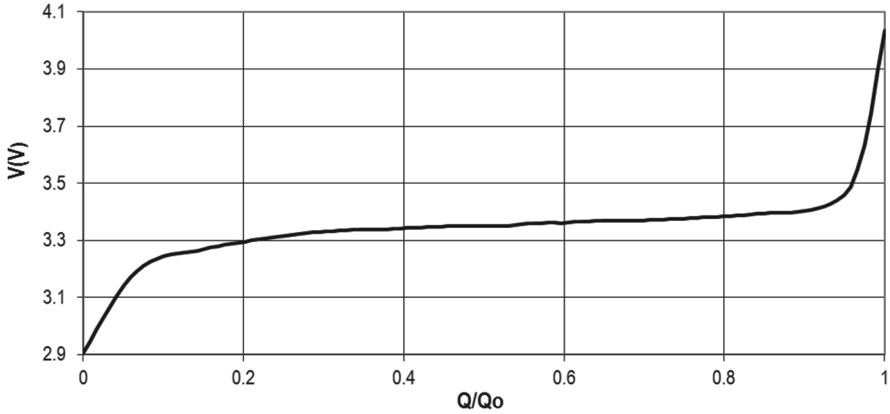

Figure 5. Typical dependence of voltage on the supplied charge during charging (Thunder Sky, 2015; Global World Logistic, 2015).

Nevertheless, the situation is complicated by the temperature dependence of the solar generator. Both V_{MPP} and output depend on the instantaneous temperature of the photovoltaic cells, whereas the temperature further depends on the ambient temperature, sunshine intensity and technique of the solar generator assembly and speed of the wind. The typical dependence of P_{MPP} on the terminal voltage for different temperatures of solar panel cells is in Fig. 6.

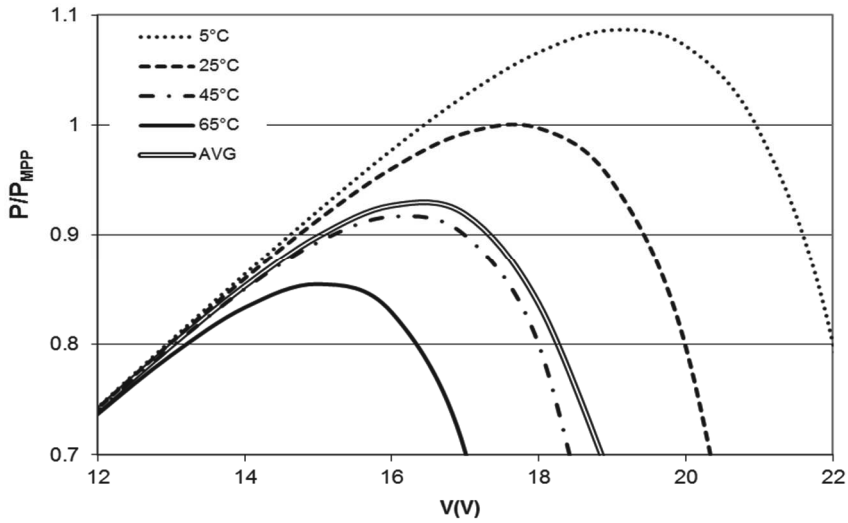

Figure 6. Typical dependence of P_{MPP} on the terminal voltage for different temperatures of the solar panel cells SH-100S5 (Huashun Solar, 2015).

The stated temperatures represent typical temperatures of solar cells in various seasons with regard to the temperature and sunlight. A 5 °C temperature represents winter, 25 °C and 45 °C temperatures represent transitional periods both in autumn and spring, and a 65 °C temperature represents summer. The annual average was weighted

with respect to the operating time of panels at temperatures considered during the year. It is obvious that due to the temperature dependence of V_{MPP}, a high level of efficiency of the solar panels can be achieved only in a narrower range of temperatures. At higher temperatures, exceeding approximately 50 °C, the lower output voltage of the solar generator would not be sufficient to charge the accumulator fully.

The solution might be to design a solar generator in a way that its load characteristic (*I–V* curve) in a wide temperature range would be similar to the charging characteristic of the accumulator. Charging the accumulator fully can be reached by adjusting the voltage levels. The efficiency of the charging process can be optimized by adjusting the current temperature dependences.

The issue of the optimal adaptation of the solar generator characteristic and that of the accumulator was solved by assembling the generator from conventional 36–cell panels and their series–parallel interconnection into two different branches interconnected via a diode gate. Such an optimization can also be achieved by the choice of the number of $LiFePO_4$ cells.

Optimization of the solar generator design was performed by simulations according to the measured characteristics both of the solar panels and accumulators for different operating temperatures of the panels and for different nominal currents on the branches of the solar generator.

If the average voltage during the charging and the maximum charging voltage are considered, the ratio of the operating voltages of both branches close to the value of 1.2 can be determined by evaluating the voltages during the charging of the $LiFePO_4$ accumulator. When conventional panels were used we selected a variant with the first branch with 4 in-series connected panels (i.e. panel groups), and the second branch with 5 in-series connected panels. The number of accumulator cells and the ratio of the nominal currents of the branches were chosen as simulation parameters. With respect to standard climatic conditions in the time of operation of the system, the operating cell temperature was set in the range 5 °C – 65 °C. In order to analyze the simulation, the ratio was chosen between the power transferred to the accumulator during charging and the maximum energy which could be supplied by the solar generator. The energy was taken as a product of the charging period and P_{MPP}. This product is hereafter denoted as the system efficiency.

The results of the simulation for a 20–cell accumulator, at temperatures within the selected range and the nominal current of the branch with higher voltage in the range from 0 to a value equal to the nominal current of the second branch, are summarized in the diagram in Fig. 7. It is obvious that at operating cell temperatures in the range 25 °C – 45 °C, an efficiency exceeding 95% can be achieved provided the relation of the nominal voltages of the generator and accumulator are chosen appropriately.

At a low temperature the operating conditions of the system do not change significantly. The system efficiency decreases by about 5% as V_{MPP} increases with a decrease of the temperature and the voltage on the accumulator terminals is temperature-independent.

A different situation occurs at high operating cell temperatures. The decrease in V_{MPP} and open-circuit voltage leads to a situation when the charging current of the first branch of the solar generator rapidly decreases or even approaches zero at the end of charging. The charging is then completed only by the current from the second branch. Higher efficiency in this area is achieved by selecting a higher nominal current of the

second branch. Hence the charging process is shortened and likewise the time, when the first branch operates no-load (YEAR).

The graph in Fig. 7 shows the average values of efficiency corresponding to the weighted averages of all considered temperature dependences. The behaviour marked by YEAR represents the average values at a higher share of the transitional periods, i.e. temperatures 25 °C and 45 °C and SUMMER represents the average values at a higher share of summer, i.e. temperature in the range 45 °C – 65 °C.

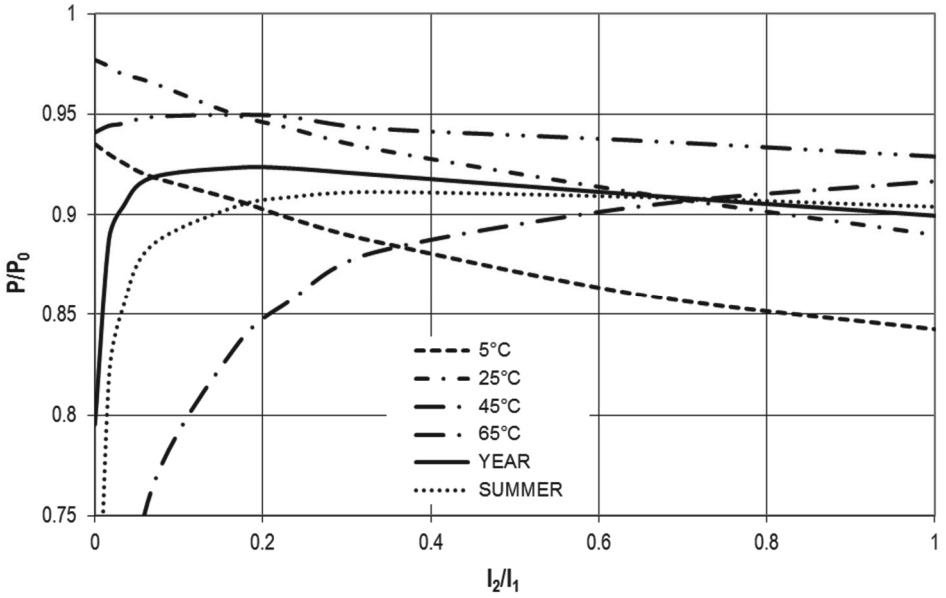

Figure 7. Dependence of the efficiency of the solar system on the ratio of the currents of the branches for different cell temperatures.

The final evaluation of the two curves is approximately the same: nominal current of the second branch should be selected as 1/3 or 1/2 of the nominal current of the first branch. An achievable average value of the efficiency of the system for the whole year ranges from 90% to 92%. As stated earlier, the solar power system can reach approximately the same efficiency without using a DC/DC converter to match the solar generator and accumulator. The advantage of the system with the matched generator and accumulator is its lower purchase cost and significantly higher reliability compared with the system using the DC/DC converter. Moreover, any interference caused by the DC/DC converter switches and all problems associated with the suppression of interferences are eliminated.

System controlling circuits

An analog control system based on the design described in (Papež & Papežová, 2015) is used to control the operation of the accumulator. Microcomputer systems which are now currently available on the market (Petchjatuporn et al., 2005) cannot be recommended for an unattended control system since they are much less reliable than simpler analogue systems. The reliability of their operation is also reduced by the

influence of external atmospheric and random disturbances. If other electronic devices processing low level signals work in their vicinity, the radiation of the timing signal from the microcontroller and its harmonic signals can cause such interference.

The evaluation of the required actual limiting values is performed by simple analog comparators the output signal of which is processed by conventional combinatory circuits. All protective circuits starting from the comparators up to the power switches are duplicated and sometimes triplicated in order to ensure maximum reliability of the control of the operation of the accumulator. A block diagram of the control system is in Fig. 8.

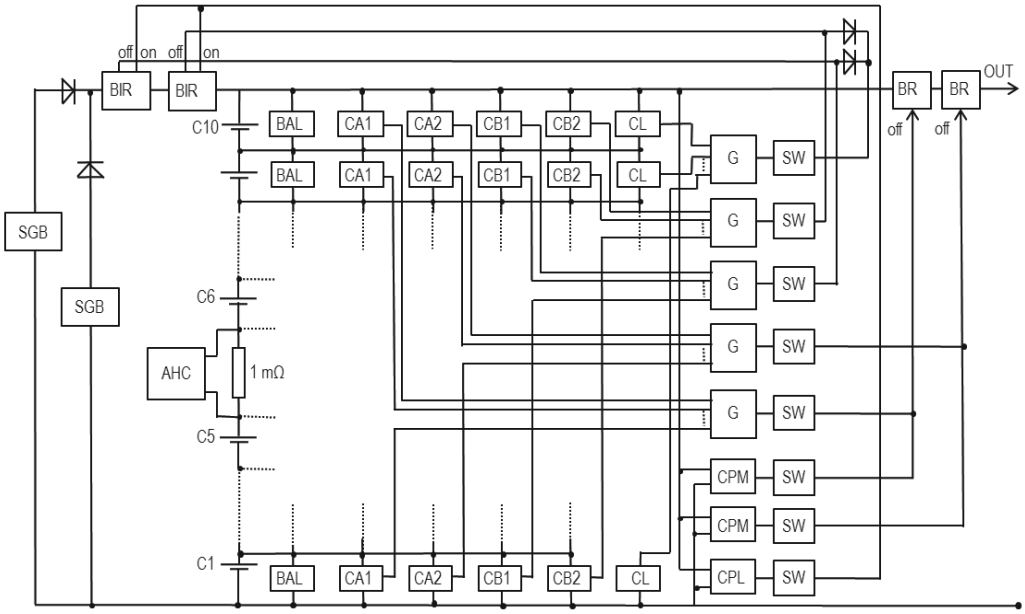

Figure 8. Block diagram of the control system: AHC – ampere-hour counter; BAL – balancer; BIR – bistable relays; BR – breaker; C1 – C10 accumulator cells; CA1, CA2 – minimum cell voltage sensors; CB1, CB2 – maximum cell voltage sensors; CL – charging–off cell voltage sensors; CPL – charging –on accumulator voltage sensor; CPM – accumulator voltage minimum sensor; G – analog gate; SGB – solar generator branch; SW – relay coil current switch.

The control system comprises five comparator networks independently evaluating voltages of individual cells the signals of which are combined and evaluated together and three independent comparators evaluating the total voltage of the accumulator.

Tested values

The minimum voltage of individual cells of the accumulator is evaluated by two independent comparator networks which at a risky drop of the voltage on one of the cells turns off two series-connected circuit breakers.

The minimum voltage of the accumulator is simultaneously evaluated by two independent comparators which independently turn off the same series-connected circuit breakers just as the previous network has done it.

The maximum voltage of individual cells of the accumulator is evaluated by two independent comparator networks which, when one of the cells is overcharged, turns off two series-connected bistable relays and thus disconnects the charging.

The final charging voltage of individual cells is evaluated by a comparator network. When all accumulator cells are fully charged the identical series-connected bistable relays are independently turned off in the same way as in the previous network.

The starting voltage for charging the accumulator is evaluated by a comparator which turns on the bistable relays connecting the solar generator during charging.

The issue of preventing cells which are not entirely identical from overcharging is solved by their balancing. Balancing is provided by passive balancers (Papež & Papežová, 2015; Albertronic, 2015). When the voltage of the cells reaches a value signifying that they are charged, the balancers draw the charging current supplied by the PV panels from the cells of the accumulator. Charging continues until the voltage of all cells reaches the value corresponding to the charge and all cells are fully charged.

Measurements show that the average time the balancer operates on all cells in the accumulator is approximately 1% of the charging time of the accumulator. The total energy consumed by the balancers from all accumulator cells is about 1.2% of the energy necessary for charging the accumulator. This is because the balancers operate at the end of the charging cycle when the cells are loaded with the highest voltage.

The state of the accumulator during the operation is evaluated by an Up/Down ampere-hour counter which indicates the charge available in the accumulator.

RESULTS AND DISCUSSION

A solar power station was built as a source of electricity at weekends for an amateur radio station and other facilities in a remote location. For economical reasons the system was designed as a half of the optimal configuration described above.

The accumulator comprises 10 WB- LYP300AHA Winston Battery cells (300 Ah capacity, average discharge voltage about 3.15 V, (Global World Logistic, 2015; Thunder Sky, 2015)), see Fig. 9.

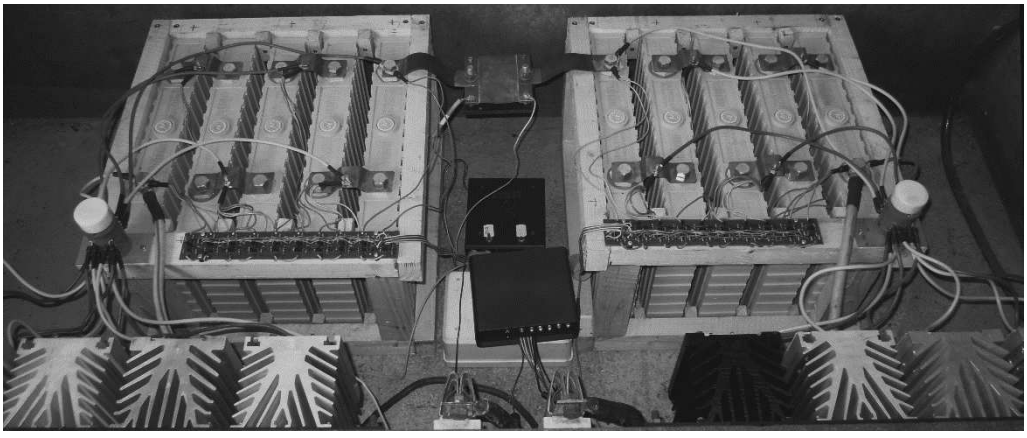

Figure 9. Accumulator of the solar power station.

The solar generator consists of 9 type SH-100S5 Ningbo Huashun Solar Energy Technology Co., Ltd. solar panels (see Fig. 10). The panel is equipped with 36 cells (125 x 125 mm). Under standard conditions, it supplies 100 W at a 18.25 V voltage (Huashun Solar, 2015). The panels are interconnected in two branches: 1) a low voltage branch with 3 in-parallel connected groups each comprising 2 in-series connected panels and 2) a high-voltage branch comprising 3 panels connected in series. The high voltage branch has an operating voltage corresponding to a 1.5 multiple of the voltage on the low voltage branch, i.e., higher than the optimum voltage, which results in a reduction of the efficiency of the system by about 5% compared with the theoretical value.

Figure 10. Solar generator of the solar power station.

The state of the charge of the accumulator in a solar power station for standard operation of the amateur radio station at weekends from May to December 2015 is in Fig. 11.

Sharp charge drops indicate the accumulator discharge during a radio amateur contest when the transmitter consumes a peak power of up to 3 kW. After that the accumulator is fully charged by the solar system. In summer the longest charging time is 5 days with an 85% discharge. In autumn (November) charging lasts about 12 days with a 50% discharge.

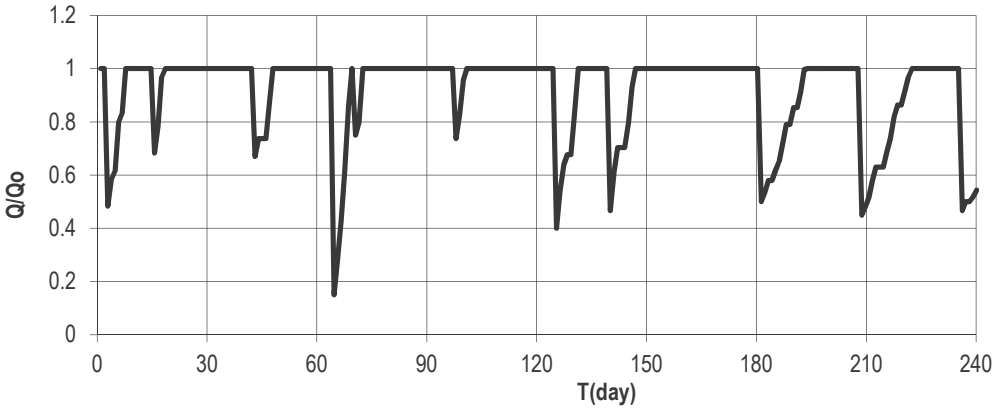

Figure 11. Accumulator charge level in May-December, 2015.

CONCLUSIONS

The design of the PV power station described in the present paper consistently avoids the use of controlling switch-mode DC/DC controllers and controlling microcomputers. The described analog system utilizes exclusively linear control. When the parameters of the PV generator and accumulator are appropriately selected this system has approximately the same efficiency as the system with pulse control for which maximum efficiency is usually assumed.

An advantage of the design of the analog system, compared with the pulse system, is the negligible risk of production of disturbing signals and higher reliability of the simpler analog system.

A complete review of the properties of the designed system will be possible only after the evaluation of the life of the accumulator which is the most expensive component of the system.

ACKNOWLEDGEMENTS. Thanks for cooperation are due to the Laboratory of Photovoltaic Systems Diagnostics, Faculty of Electrical Engineering, Czech Technical University in Prague and Faculty of Engineering, Czech University of Life Sciences in Prague, IGA 31200/1312/3118.

REFERENCES

Albertronic, B.V. http://www.123electric.nl. Accessed 22.12.2015.

CTU in Prague, Faculty of Electrical Engineering, Laboratory of Photovoltaic Systems Diagnostics http://pasan.feld.cvut.cz/en/index.html. Accessed 22.03.2016.

Darla, R.B. 2007. *Development of Maximum Power Point Tracker for PV Panels Using SEPIC Converter.* In: 29th International Telecommunications Energy Conference. INTELEC 2007. IEEE. Roma. pp. 650–655.

Global World Logistic Ltd. http://www.ev-power.eu/docs/GWL-LFP-Product-Spec-260AH-7000AH.pdf. Accessed 22.12.2015.

Ningbo Huashun Solar Energy Technology Co., Ltd. http://www.enfsolar.com/pv/panel-datasheet/Monocrystalline/10875. Accessed 22.12.2015.

Papez, V. & Papezova, S. 2015. Isolated Solar Power Station. In: *14th International Scientific Conference Engineering for Rural Development Proceedings*. Latvia University of Agriculture. Jelgava. pp. 458–465.

Petchjatuporn, P., Sirisuk, P., Ngamkham, W., Kiranon, W., Khaehintung, N. & Kunakorn, A. 2005. *A Solar-powered Battery Charger with Neural Network Maximum Power Point Tracking Implemented on a Low-Cost PIC-microcontroller* In: International Conference on Power Electronics and Drives Systems. PEDS2005. IEEE. Kuala Lumpur, pp.507–510.

Riawan, D.C. & Nayar, C.V. 2007. *Analysis and Design of a Solar Charge Controller Using Cuk Converter*. Power Engineering Conference. AUPEC 2007. Australasian Universities. IEEE. Perth, pp. 1–6.

Thunder Sky Winston Battery. http://en.thunder-sky.com/index.php/products/download-center/category/battery-lyp. Accessed 22.12.2015.

Agronomy Research **14**(Sp.1), 1212–1221, 2016

Automated Measuring Station for Accumulator Testing

S. Papezova[1,*] and V. Papez[2]

[1]Czech University of Life Sciences in Prague, Faculty of Engineering, Department of Electrical Engineering and Automation, Kamycka 129, CZ 165 21, Prague 6 - Suchdol, Czech Republic
[2]Czech Technical University in Prague, Faculty of Electrical Engineering, Department of Electrotechnology, Technicka 2, CZ 166 27 Pague 6, Czech Republic
[*]Correspondence: papezovas@tf.czu.cz

Abstract. The paper describes the design and implementation of the system allowing the testing of the lithium-iron-phosphate ($LiFePO_4$) cell parameters during long-term loading. Manufacturers and retailers, in particular, accentuate their beneficial properties – the possibility of charging and discharging by high currents, minimum influence of the discharge time on capacity, long durability. At the same time, their operational conditions are a lot more strictly defined than those for other types of accumulators. The proposed testing system enables loading the accumulators, consisting of several cells, by periodic discharging and charging processes with various operating currents and various levels of cell discharging. The charging and discharging process control is fully automated; the measuring of the cell operational state is performed automatically during charging and discharging. The data is recorded, and continuously evaluated for the purposes of process management. The measurements enable the comparison of the catalogue data with the parameters of the real products. The testing system design is based on the application of a digital control block, which is completed with an analog control block. The core of the digital control unit is a control computer equipped with a multifunctional input-output card and an array of logically controlled circuit-breakers. An accumulator management algorithm, implemented as a control program of the computer, ensures the operation of the accumulator in subsequent charging and discharging periods. The actual accumulator control is based on the evaluations of voltage levels at the cell terminals.

Key words: $LiFePO_4$ accumulator, testing, Ah capacity, limit parameters.

INTRODUCTION

A lithium-iron-phosphate ($LiFePO_4$) accumulator is nowadays considered to be one of the best types of accumulators with higher capacity (Scrosati et al., 2013; Liberty, 2014). The accumulator belongs to the polymer Li-on accumulators; it was developed at the University of Texas in 1996. It is used whenever high capacity at low weight, volume and longevity are required.

The main advantages of $LiFePO_4$ accumulators are high voltage, low internal resistance and, consequently, very flat volt /coulomb characteristic during discharging and charging. In operational terms, the accumulators are characterized by high lifetime, temperature stability; they do not represent any fire or explosion hazard, even in case of improper handling and they do not contain any toxic metals, acids or alkaloids. They can

be charged and discharged by high current; at minimum, by the current corresponding to a one-hour discharge period. Some manufacturers indicate their lifetime up to 2,000 discharge cycles at 100% deep discharge, whereas their capacity is more than 80% of their initial capacity (Scrosati et al., 2013; Liberty, 2014).

$LiFePO_4$ accumulator manufacturers declare their operating conditions and stick to their strict observation. If the accumulators are used improperly, they can be damaged very easily. It can occur; e.g., when the maximum voltage exceeds its limit during charging, or when discharging continues even after reaching a defined minimum voltage, and at the states that may arise due to non-compliant internal parameters of the cells connected in series caused by their ageing (Thunder Sky, 2015a; Thunder Sky, 2015b; Thunder Sky, 2015c; Thunder Sky, 2015d; Sinopoly, 2015; Global, 2015).

Manufacturers and especially distributors indicate that $LiFePO_4$ accumulator operational costs are lower, when compared to other kinds of accumulators, although their acquisition costs are much higher, which is thanks to the fact that they have much longer lifetime.

The aim of the project is to implement an automated measuring workplace for testing cells, which allows setting the operational parameters of the real cells and comparing them with the parameters declared by the manufacturer. The measurements of the parameters are performed by a cyclic discharging of the cells up to the minimal voltage and by their recharging to maximum value. The gradual parameter deterioration after multiple repetitions of the cycles is observed, as well (Cenek, 2003; Lust, 2010).

MATERIALS AND METHODS

The evaluation of operational parameters of specific $LiFePO_4$ cells during the long-term measurement is performed by a special testing system. Charging and discharging processes are controlled by a computer and are fully automated. Operating parameters of the tested accumulator are continuously scanned, recorded and evaluated by the server (Srovnal, 2002; Kreidl & Svarc, 2006).

Individual cells are equipped with balancing and protection circuits that prevent the cell from exceeding the maximum voltage during charging and also from voltage drops below the minimum level during discharging.

The testing system consists of a power supply, electronic load, switch control unit, cell balancers, input-output card and a server, see Fig. 1.

A laboratory power supply MANSON HCS 3402 with a maximum output voltage of 32 V and 20 A current is used as a charger. Selecting both charge current and charge voltage is possible manually, i.e. by setting the source. The source can also be controlled by the computer.

An accumulator discharge is performed by STATRON 3227 Electronic Load. It can operate at a maximum voltage of 80 V, 25 A current and total power dissipation of 200 W. Discharge current is set manually and it is stabilized by electronic load at a preset value. The discharge current stability is better than 1% of the set value, within the range of the discharge voltage at a four-cell $LiFePO_4$ accumulator. Power circuits in the testing system are controlled by relay switches. The relays have a robust construction, and therefore they are extremely reliable. Moreover, polarized bistable relays used in the system do not need permanent operating current. The relays are controlled by logic

signals from the input-output card. The signals pass through photocouplers to the transistor switches that control relay coils.

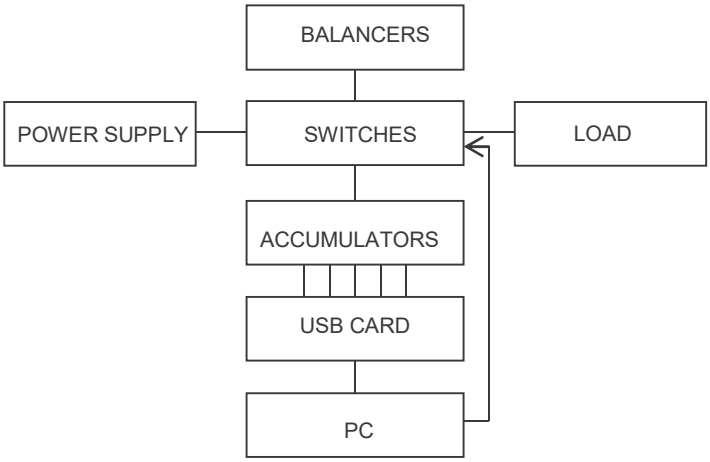

Figure 1. Block diagram of the testing system.

Complying with the desired operating parameters during the charging process is furthermore ensured by a network of analog balancers connected in parallel to each cell. The balancer prevents the cells, which are charged the fastest of all in the charging process, from overcharging. If the applied voltage of the cell reaches the selected value, the balancer consumes charging current supplied from the cell and stabilizes the applied voltage at a selected value. Charging continues until the voltage at all cells reaches the selected value and all cells are not fully charged without exposing any cells to overcharging.

Fig. 2 shows the real voltage courses of two cells at the end of the charging cycle, during the last 5% of the charging time, when the balancing is applied.

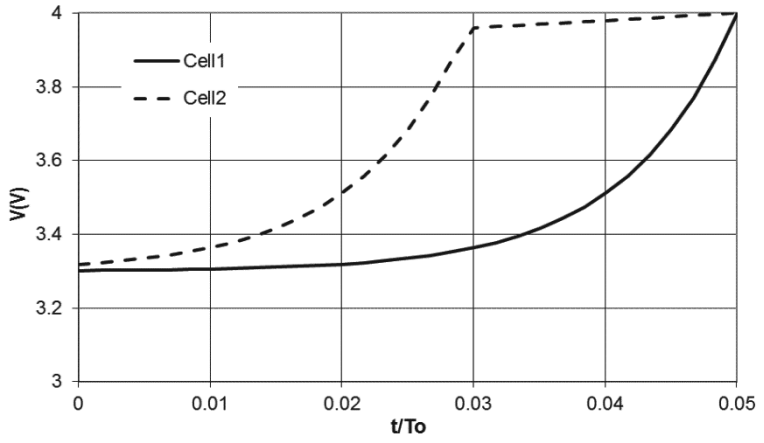

Figure 2. Real voltage waveforms of two cells when applying the balancer.

Herein used balancers are simple analogue circuits autonomous for each cell. A balancer circuit comprises three transistors, a reference diode and five resistors. The balancer also includes two photocoupling ports that can serve for indicating the cell voltage. The balancer I–V characteristic is shown in Fig. 3. When charging at 4.04 V voltage, the current can reach even 12 A, which is higher than the current supplied by the source of the charging current. In an idle-circuit condition, the balancer consumes the current that is less than 5 mA. Such a low current causes only negligible undesirable cell discharge.

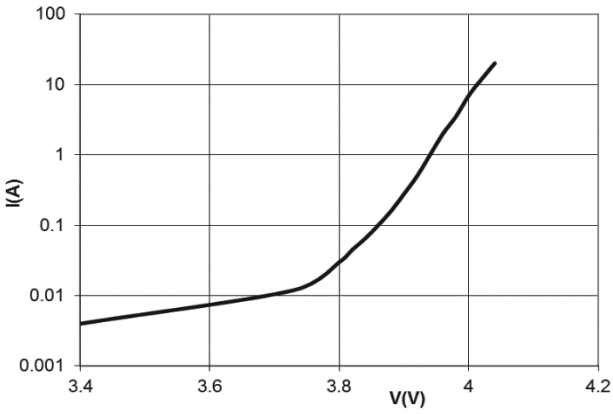

Figure 3. Balancer I–V characteristic.

The testing workplace control is provided by the program in a system-design platform LabVIEW implemented in the PC.

The program structure is based on the workplace block diagram, as shown in Fig. 4.

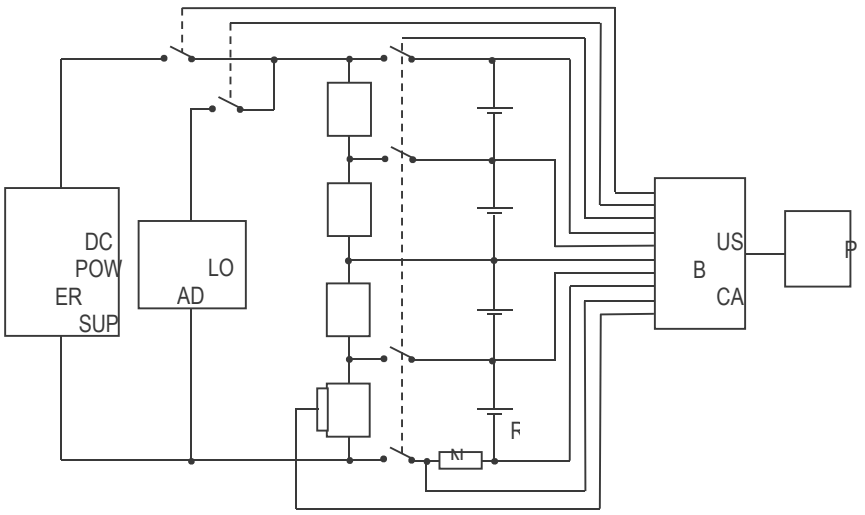

Figure. 4. Block diagram of a testing workplace. B – balancer; SC – charging relay; SD – discharging relay; J – breaker; T – thermometer; RN – ammeter shunt.

The balancers are connected via protective circuits, whose circuit breakers J control the continuous charge and discharge states by means of the program. In this way, the balancers eliminate the state when the accumulators could be severely damaged or completely destroyed. The charging and discharging networks of accumulators are operated by SC and SD switches. At the same time they are controlled by command signals from the LabVIEW program.

During the accumulator charging, the charging source is connected by an SC switch. The diode in the power supply secures the device in case of power failure or malfunction of the charging source. The accumulator discharge occurs by discontacting the SC switch and subsequent contacting the SD switch, which connects STATRON 3227.1 electronic load to the accumulators. The load is manually adjusted to the desired mode, i.e. the discharge by a nominal 10 A current.

Scanning the analogue signals from the accumulators and generating control signals for controlling the function of switches, which set the desired mode and ensure continuous emergency protection of the operating modes, is provided by a measuring card USB 6211. An input card with 16-bit converters enables achieving an absolute error in determining cell voltage of 0.3 mV at a chosen input range of the ± 10 V analogue inputs. Switches SC and SD are controlled by the logic signals of the card.

Control program functions

A control program for the diagnostic workplace is created in a graphically oriented environment LabVIEW on a PC or laptop. Using a laptop is preferable due to its safe circuitry stripping from the mains (Tumova, 2009). The block diagram of the program created in LabVIEW graphical environment is presented in Fig. 5.

In some cases, depending on the accumulator type and manufacturer, the program enables presetting technical parameters of the cells specified by the manufacturer to prevent their overrange limit (Cenek, 2003; Richter, 2014; Global, 2015; Sinopoly, 2015; Thunder Sky, 2015a; Thunder Sky, 2015b; Thunder Sky, 2015c; Thunder Sky, 2015d). Required parameter compliance is provided by a control program which generates a signal, whenever the threshold limit is reached, and consequently, the circuit breakers are switched off. The accumulators are disconnected both from the voltage supply and the load, and thus, they are protected from any further damage.

For the accumulator cells are generally set these parameters:

V_{max_L} – maximum cell voltage at which the voltage protection is disabled;

V_{max_C} – final charge voltage at which the system function is switched to discharging;

V_{min_D} – final discharge voltage at which the function is switched to charging;

V_{min_L} – minimum cell voltage at which the voltage protection is disabled.

The set parameters at Winston Battery cells are presented in Table 1.

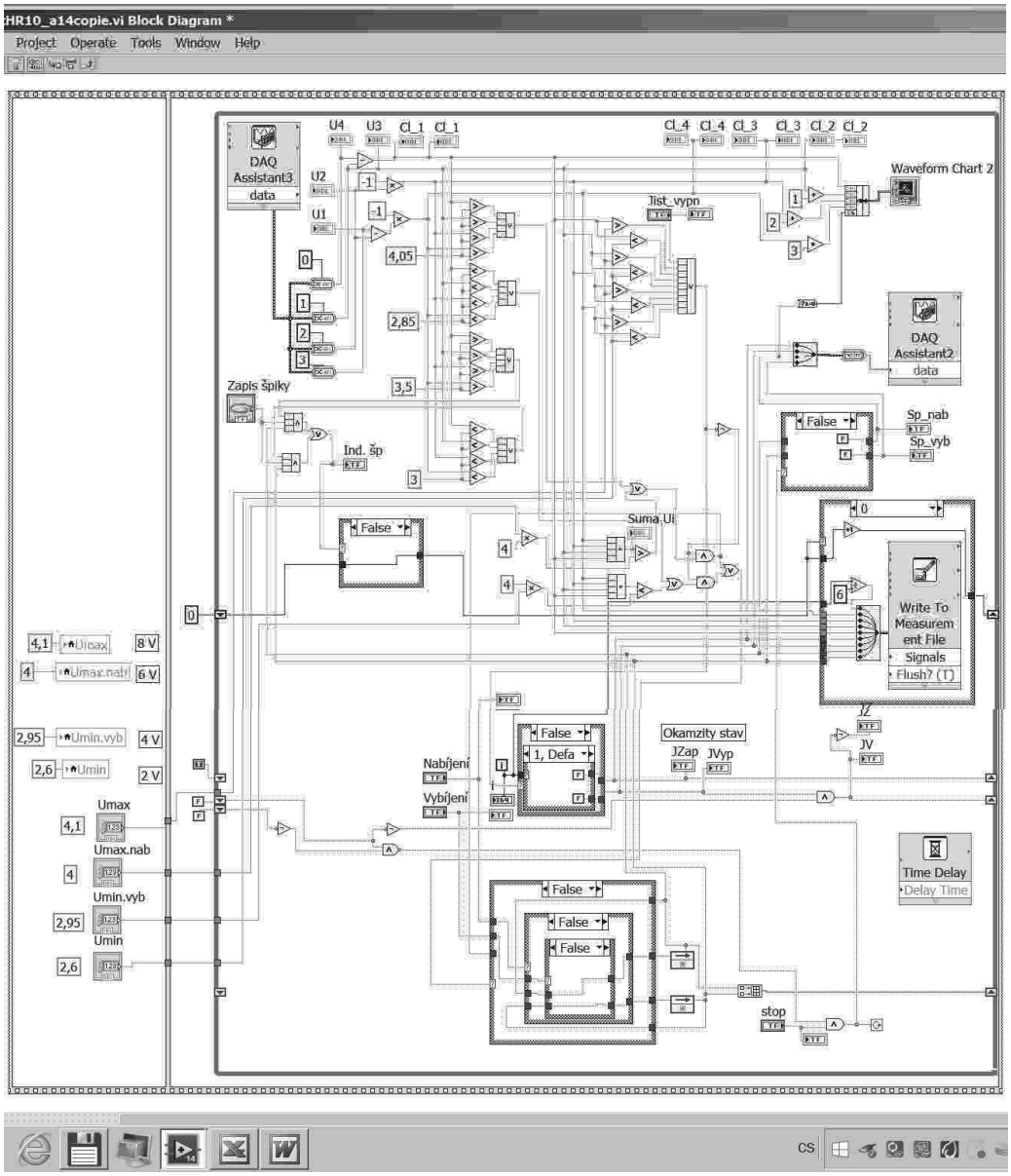

Figure. 5. Block diagram of the LabVIEW control program.

Table 1. The set parameters at Winston Battery cells

V_{max_L} (V)	V_{min_L} (V)	V_{max_C} (V)	V_{min_D} (V)
4.1	2.6	4	2.95

During charging, the maximum charge voltage is primarily controlled by the balancers, whose voltage value is set closely under 4 V. In case this value is reached, the balancer decreases the charge current by consuming its operating current and thus stabilizes the charge voltage.

The cell voltage is further monitored by the control program, and in case the balancer fails to prevent the voltage growth, and subsequent overvoltage V_{max_L}, the control system provides the disconnection of the circuit breakers.

The regular switching the charging and discharging processes is controlled by the control program according to the total battery voltage V_{bat}. If the condition $V_{bat} \geq 4.V_{max\_C}$ is fulfilled, the control program switches automatically from the charge mode to the discharge mode. If the condition $V_{bat} \leq 4.V_{min\_D}$ occurs, the program automatically switches the discharge mode to the charge mode.

One charge/discharge cycle takes about 4 hours at the tested accumulators with nominal capacity of 40 Ah and selected charge/ discharge current of 10 A. Since the voltage at the cells varies during the most of charging and discharging periods very slowly (PowerStream, 2015), for the data record was selected a two-minute interval. Only during a short period of time, taking only a few minutes before the end of the charge/discharge process, in which a rapid change in voltage occurs, it is possible to choose a frequent record, with a 10 s period.

The frequent record is switched off always at the end of the charge/discharge process. The example of the record is presented in Fig. 6.

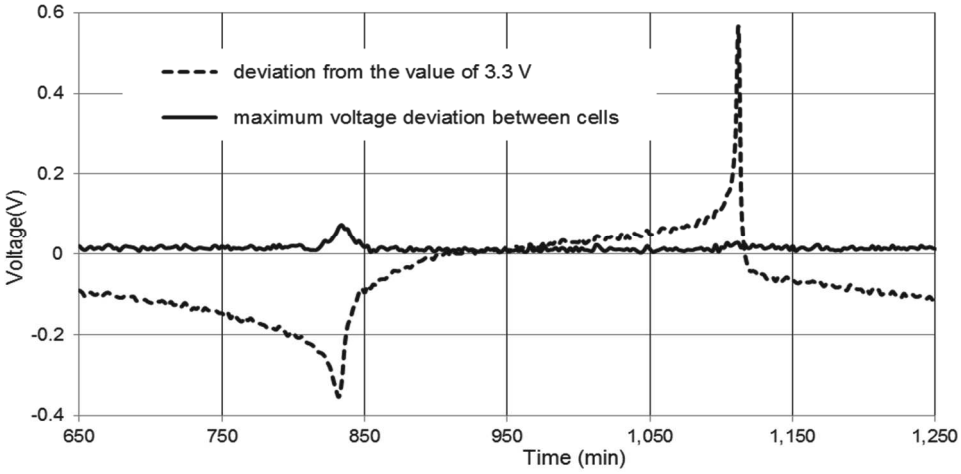

Figure 6. Course of voltage variation at individual 4 cells during the charge cycle.

RESULTS AND DISCUSSION

The measuring system was assembled from commercially available components: laboratory power supply MANSON HCS 3402, electronic load STATRON 3227, measuring card USB 6211, notebook HP Pavilion and other special components, which were developed for this purpose. These are balancers, relay switches and their control circuits.

The operation of the measuring system is controlled by a program implemented in a notebook. The program enables not only continuous recording of the measured values to the file, but also their reading and further displaying in a graphical form. Continuous monitoring of the measured data is also provided by the graphic recording to the Waveform graph placed on a virtual front panel in a LabVIEW program. There are

recorded all four cell voltage waveforms (for better clarity always mutually shifted by 1 V), together with a current status of the charge signal (log 1) or discharge signal (log 0). Apart from a continuous display of the measured data and control signals for charging or discharging on the front panel, the data is also recorded directly into the archive file.

The data serves for displaying the charge and discharge waveforms, and if necessary, the data can be subjected to further analysis. The example of the measured data record for a period of 1,424 minutes, which corresponds to three charge and discharge cycles, is shown in Fig. 7.

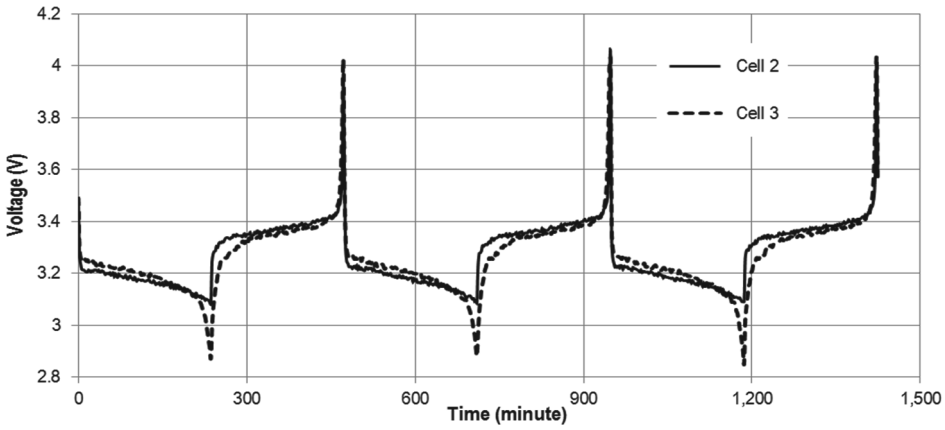

Figure 7. Example of the measured voltage waveforms on the cells within 1,424 minutes.

The measuring workplace in operation is shown in Fig. 8. Fig. 9 presents the view of a computer front panel in operation.

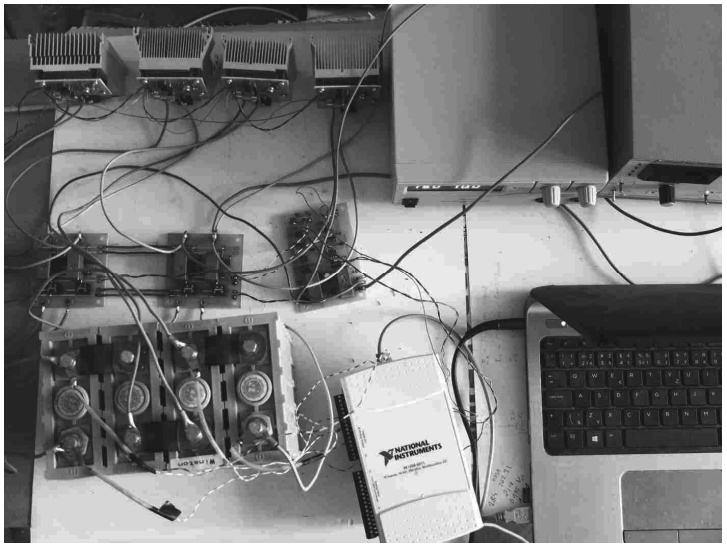

Figure 8. Photo of a measuring workplace.

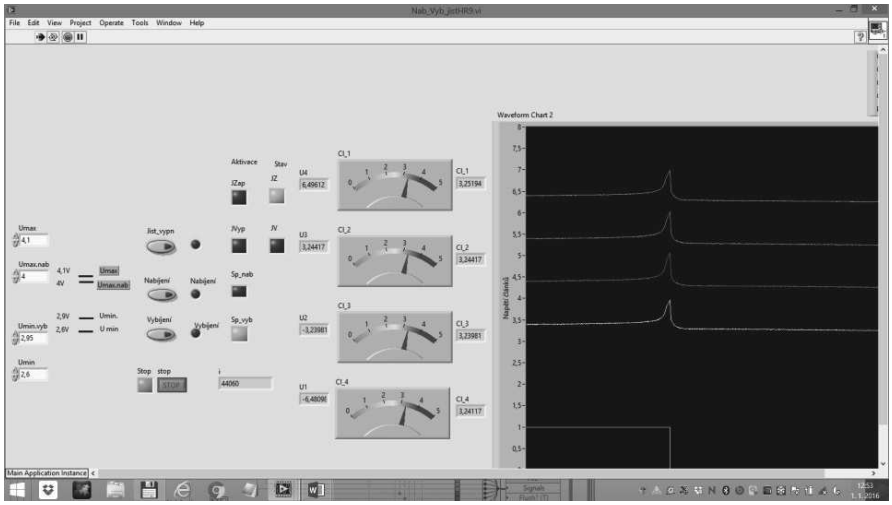

Figure 9. Front panel of the control program in LabVIEW; transition from the charge mode to the discharge mode.

Two equivalent workplaces were realized, one set of batteries was tested on each workplace. The first set was bought in 2013, and before the test started in herein described system, the cells were in operation for about 150 charge and discharge cycles. The second set was bought in 2015 and the cells were applied in the test immediately after initial charging. The results are presented in Table 2. The initial capacity of the cells in the first series was 99% of the nominal capacity; after one hundred cycles with 100% discharge, their capacity decreased to 97% of the nominal capacity. The charge required to charging varied around 102% of the charge consumed during the discharge.

The initial capacity of the cells in the second series was 116% of the nominal capacity; after one hundred cycles with 100% discharge, their capacity decreased to 110% of the nominal capacity. The charge required to charging again varied around 102% of the charge consumed during the discharge.

Table 2. Test results of 4 cells WB-LYP40AHA Winston Battery

	End of discharging voltage (V)	End of charging voltage (V)	Full discharge (Ah)	Full charge (Ah)	Charging efficiency (%)
Set 1 start	12	15.9	39.3	39.6	99.2
Set 1/100 c.	11.92	16	38.6	39	99
Set 2 start	11.84	15.8	46.3	46.6	99.3
Set 2/100 c.	11.84	15.9	44.4	45	98.7

Battery voltage at the end of the charging or discharging is approaching value that corresponds to equivalent at all cells (charging 16 V, discharging 11.8 V) during an operation. This means that the difference between the initially different characteristics of each cell is reduced.

This measurement system is designed for operation with 4 battery cells, it can be reprogrammed to work with fewer battery cells. It is possible to choose the battery charging current within the range of 0.5 A up to 16 A. The battery discharging current

can be set within the range of 0.5 A up to 12.5 A. Additionally it is possible to increase maximum discharging current of 16 A by addition of fixed resistor of approximately 0.5 Ω (power dissipation 150 W) into the discharging circuit. The electrical current values are stabilized with an accuracy of ± 1%, the values of cut-off voltages are held with a maximum deviation of 10 mV.

CONCLUSIONS

Measuring workplace described in this paper allows the evaluation of the real accumulator parameters. It enables their potential users to invest their money reasonably, i.e., on the basis of the real verified data and not only on unverified information from producers and traders. At best, they provide positive results of selected tests, whose testing conditions usually do not correspond to the real operation.

A workplace function was verified by more than one hundred cyclic tests on two sets of Winston Batteries. There were verified voltage waveforms of both sets during charge and discharge by a constant current in the range of voltage levels recommended by the manufacturer. Their ampere-hour capacity and charging efficiency was also determined.

ACKNOWLEDGEMENT. Supported by the Internal Grant Agency of the Faculty of Engineering, Czech University of Life Sciences in Prague No: 2015:31200/1312/3118.

REFERENCES

Cenek, M. 2003. *Accumulator from principle to practice*. FCC Public. Praha. 248 pp. (in Czech).

Global World Logistic Ltd. *http://www.ev-power.eu/CALB-40Ah-400Ah*. Accessed 22.12.2015.

Liberty Electric Bikes. *http://www.iloveebikes.com/batteries.html.* Accessed 10.12.2014.

Kreidl, M. & Svarc, R. 2006. *Technic Diagnostic*. BEN – technicka liteartura. Praha, 408 pp. (in Czech).

Lust, R. 2010. *Accumulator Capacity Measurement*. Bachelor's thesis. VUT Brno. Supervisor Kolka .Z, 36 pp. (in Czech).

PowerStream Technology. *http://www.powerstream.com/LLLF.htm*. Accessed 21.11.2015.

Richter, Pavel. 2014. *http://pavelrichter.net/2012/04/sestaveni-lifepo4-akumulatoru-a-iniciacni-nabijeni/*. Accessed 21.11.2014.

Scrosati, B., Abraham, M., Schalkwijk, W. & Hassoun, J. 2013. *Lithium Batteries Advanced Technologies and Applications.* Wiley. New Jersey, 392 pp.

Sinopoly Battery Limited. *http://www.sinopolybattery.com/userfiles/files/SP-LFP40AHA.pdf*. Accessed 15.11.2015.

Srovnal, V. 2002. *Electrotechnical Measurements*. BEN – technicka literatura. Praha, 255 pp. (in Czech).

Thunder Sky Winston Battery. *http://en.winston-battery.com/index.php/products/power-battery/item/wb-lyp40aha?category_id=176*. Accessed 15.11.2015a.

Thunder Sky Winston Battery. *http://en.thunder- sky.com/index.php/products/download center/category/battery-lyp.* Accessed 15.11.2015a.

Thunder-Sky Battery. *http://en.thunder-sky.com.* Accessed 17.11.2015c.

Thunder Sky Winston Battery. *http://en.winston-battery.com/index.php/products/power-battery/item/wb-lyp300aha?category_id=176*. Accessed 15.11.2015d.

Tumova, O. 2009. *Metrology and process evaluation.* BEN – technicka literatura. Praha, 232 pp. (in Czech).

Agronomy Research **14**(Sp.1), 1222–1231, 2016

Thermal properties and reduction of energy consumption of buildings

Týbl, J.* and P. Kic

Czech University of Life Sciences Prague, Faculty of Engineering, Kamycka 129, 16521, Prague 6, Czech Republic; *Correspondence: tybljiri@seznam.cz

Abstract. The aim of this paper is to summarize and present all relations, which are essential in determination of winter heat balance of the buildings, and that enable a reduction of energy consumption or heating costs. These questions should be realized and taken into account already in the proposal of building design. This paper shows the methods of calculation of winter heat balance and results of measurements which verify theoretical conclusions in real conditions. These factors are applied on two existing buildings. There are due to their different shapes and constructions proposed different solutions of improvement. Two different buildings were selected for this research work: a large ground floor building and a high hall. In the case of the first building (the large ground floor building) it appears to be a major problem not sufficient thermal properties of the envelope constructions. The enormous heat losses caused high heating costs. The existing heating method of the second building (the high hall), is not suitable. The temperature distribution in the interior is undesirable, which results in very high energy consumption. The use of radiant ceiling panels could enable to achieve favourable conditions in the working area and considerable energy savings.

Key words: heat balance, high building, radiant heating, thermal insulation.

INTRODUCTION

Energy consumption is in the interest and attention of all owners of family houses as well apartment buildings. Rather big attention is also paid to the heating problems of various buildings for community facilities (Visockis et al., 2011). There are many standards and recommendations for the reduction of energy consumption in these houses. The question of energy savings in large warehouses and industrial buildings is not so often solved in the literature. Heating of large buildings represents together with ventilation or air conditioning very important issue, which significantly affects the operation of these facilities.

Nevertheless there is not paid sufficient attention to solve the energetic and heating problems in this type of industrial and agricultural buildings in Czech Republic. It can be assumed that a similar situation and problems exist also in other European countries. The situation in many non-European countries is even worse.

This article is aimed at those buildings used in industry, agriculture or in other branches. These buildings are used year-round and must be maintained for the required air temperature, corresponding to the requirements of workers or technological processes. These buildings are characterized by a large surface area, different shape, in

some cases high height, and the overall large volume. This creates a need for substantial inputs for heating, which together with the high cost of energy can manifest itself quite significantly in the efficiency of production, or in satisfaction and functional reliability of these buildings.

There are different information from the literature about the heating and ventilation of these buildings. Recommendations of several authors are focused on the radiant heating by different type of heating systems and panels (Cihelka, 1961; Kotrbaty & Kovarova, 2002; Basta, 2010; Vio, 2011; Kic, 2013; Zajicek & Kic, 2014; Kic, 2015), nevertheless this type of heating, especially with ceiling radiant panels, is still not so common in the practice.

Although currently the considerable attention is paid to energy savings for heating, many buildings are still not designed conceptually from the viewpoint of energy savings, usually only layer of thermal insulation is increased. In some cases it is possible to achieve energy savings in heating by choosing appropriate shape of the building and by the solution of adequate heating method which respects the shape of the building.

The following article briefly summarizes some of these ideas, calculation procedures and results of measurements in several options for achieving reductions in energy consumption, or a reduction of heating costs, including factors that have a direct effect on the heat balance. These facts are in this work applied on two existing buildings; and with regard to their different conception there were also chosen different solutions. The results of this applied research can be therefore considered as a good new approach also for the future scientific work which can bring not only theoretical background in scientific literature but also a useful progress in practise.

MATERIALS AND METHODS

Two different industrial buildings were chosen for this research work: a large ground floor building and a high hall. Both buildings do not meet modern ideas about the thermal properties of buildings. There are identified their main weaknesses, which for each of them have different character. Both buildings were examined initially by quasistationary calculation method for determination of annual heat balance with an interval of one heating season. On this basis, there were proposed methods for improvement.

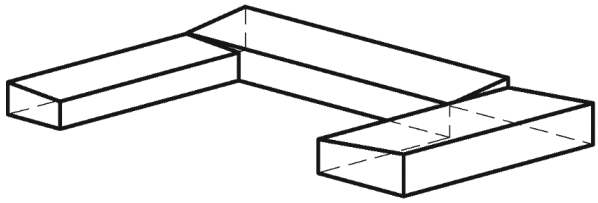

Figure 1. Building A, a large ground floor building.

In the case of the first building A, i.e. the large building, it appears to be a major problem not sufficient thermal properties of the envelope constructions. The first building A is a large ground floor building, which consists of three parts. Scheme of hall A is shown in Fig. 1. All parts are interconnected and together have a floor area of

404 m^2. Heating is provided by a central boiler on natural gas and heat is distributed by pipeline heating system with heating radiators throughout the building. The building is currently used as a warehouse for office supplies, dry goods and some durable food.

The second building B is a large-capacity compact ground floor brick building, which is not particularly spatially divided. The total floor area is about 418 m^2, the building has a gabled roof, the ridge of which has a height of almost 8 m. Heating is provided by a central boiler on natural gas heat is distributed by pipeline heating system with radiators throughout the building. Now the building serves as a carpentry workshop.

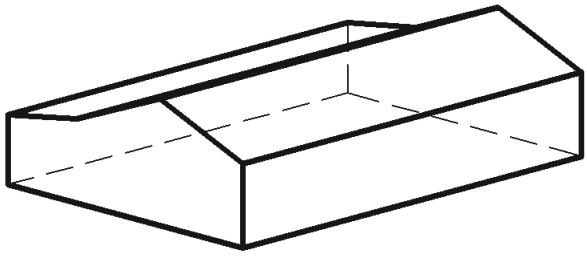

Figure 2. Building B, a large compact building with a height 8 m.

Air temperatures were measured by thermocouples NiCr-Ni type K with the thermometer THERM 2253-2 with temperature operative range -100 to 1,370 °C with accuracy ± 0.1 K. This thermometer was used also for the measurement of the temperature profile in the high building B. The surface temperatures of the walls, ceiling and floor were measured by Pyrometer Amir 7811 with temperature operative range -32 to 600 °C with accuracy ± 0.1 K.

The obtained results of dust measurements were processed by Excel software and verified by statistical software Statistica 12 *(ANOVA* and *TUKEY HSD Test*). Different superscript letters (a, b, c, d, e, f) in common are significantly different from each other in the rows of the tables *(ANOVA; Tukey HSD Test; $P \leq 0.05$)*, e.g. if there are the same superscript letters in all the rows it means the differences between the values are not statistically significant at the significance level of *0.05*.

RESULTS AND DISCUSSION

Results of temperature measurement in the buildings

As a part this research is to perform basic measurements of indoor temperatures and compare obtained results as a background for the improvement proposal. There were measured the surface temperature of floor, air temperature in level 1 m above the floor, and surface temperature of the wall and ceilings. The results are summarised in the Table 1.

Measurements were carried out at the building A and B at outdoor temperature from 1.7 °C to 3.5 °C when the heating of rooms was reduced. In the working area the desired temperature not reached of 12 °C, but only 7 °C. The difference between the outside temperature and the temperature in the working area was therefore very small. Nevertheless, the measurement confirmed not suitable temperature distribution in the

interiors. It can be assumed that with a larger temperature difference could also increase the negative impacts of these phenomena.

Table 1. Average surface temperature of floor, air temperature in level 1 m above the floor, and surface temperature of the wall and ceilings. Different superscript letters (a, b, c, d, e, f) are the sign of high significant difference (*ANOVA; Tukey HSD Test*; $P \leq 0.05$)

Building	A	B
Measured part	Temperature, °C ± SD	Temperature, °C ± SD
Floor	7.8 ± 0.86^{a}	7.8 ± 0.94^{a}
Air in 1 m	7.2 ± 0.88^{b}	7.2 ± 0.92^{b}
Walls	7.4 ± 0.92^{c}	8.9 ± 0.76^{d}
Ceiling	7.1 ± 1.27^{e}	6.0 ± 1.25^{f}

SD – Standard deviation

The air temperatures in the height of 1 m above the floor do not indicate high dispersion nor is there apparent dependency on other circumstances. A small scattering is also in the case of internal surface temperatures of external walls, but there is noticeable and a slight increase of temperatures with increasing height.

More interesting is the situation in the building B at the surface temperature of the inside of the ceiling. The temperature difference in the ridge and in the lower foothills of the roof structure is up to 4.2 °C. There was observed dependence of temperature increase towards the ridge, where it holds the hottest air.

Measurements confirmed that the current thermal conditions in both buildings are unfavourable. The appropriate solution of this problem seems to be an improvement of thermal properties of envelope constructions of building A and a change of heating system in the building B.

Specific overall heat transfer through the buildings envelope

Due to the considerable amount of data there are given only general formulas (1) to (4) for calculation of the heat transfer and specific heat loss; the results of numerical calculation of the buildings A and B are presented in the Tables 2 and 3.

$$R_n = \frac{d_n}{\lambda_n} \tag{1}$$

where: R_n – thermal resistance of the n-th layer, m^2 K W^{-1}; d_n – thickness of the n-th layer in the structure, m; λ_n – thermal conductivity of the n-th layer, W m^{-1} K^{-1}.

$$R_{Tj} = R_{si} + R_j + R_{se} \tag{2}$$

where: R_{Tj} – resistance to heat transmission j-th component of the envelope, m^2 K W^{-1}; R_{si} – internal resistance to heat transfer, m^2 K W^{-1}; R_j – thermal resistance of j-th component layer of the envelope, m^2 K W^{-1}; R_{se} – external resistance to heat transfer, m^2 K W^{-1}.

$$U_j = \frac{1}{R_{Tj}} \tag{3}$$

where: U_j – heat transfer coefficient for the j-th component of the envelope, W m^{-2} K^{-1}.

$$H_{Tp} = \sum_{j=1}^{n} A_j \cdot U_j \tag{4}$$

where: H_{Tp} – specific heat loss by the heat transfer through the structure envelope, W K^{-1}; A – external surface area of j-part of surrounding structure envelope, m^2; n – data-set extent.

For a comparison of buildings in terms of energy efficiency serves its inclusion in the appropriate class, so called House Energy Rating, according to the European Union energy label. As a basic indicator of the energy performance of a building are used a weighted average of heat transfer coefficients of sub-components of the surrounding structure. It is used for comparison with a weighted average of standard heat transfer coefficients of so-called reference building. The reference building is actually the same as a compared building; just each surrounding component of the envelope has a standard overall heat transfer coefficient.

Table 2. Properties of structure for calculation of the heat transfer and specific heat loss of the large ground floor building A in its original state

Structure component	A_j, m^2	R_{tj}, m^2 K W^{-1}	U_j, W m^{-2} K^{-1}	H_{Tp}, W K^{-1}
Bricks 30	33.87	0.564	1.774	60.09
Bricks 45	232.91	0.744	1.343	312.90
Bricks 60	44.00	0.925	1.081	47.56
Concrete 20	117.15	0.342	2.923	342.49
Ytong	10.10	1.356	0.737	7.45
Windows and doors	54.97	0.5373	1.861	102.31
Roof	477.33	0.2694	3.711	1,771.50
Total				2,644.30

Table 3. Properties of structure for calculation of the heat transfer and specific heat loss of the compact high building B in its original state

Structure component	A_j, m^2	R_{tj}, m^2 K W^{-1}	U_j, W m^{-2} K^{-1}	H_{Tp}, W K^{-1}
Bricks 30	64.97	0.564	1.774	115.26
Bricks 45	133.70	0.744	1.343	179.61
Windows and doors	119.04	0.22	4.54	540.0
Roof	454.26	0.27	3.69	1,675.50
Total				2,510.36

According to (Bernardinová & Mareš, 2013) the average overall heat transfer coefficient U is determined by the equations (5) and (6). The values in the Table 4 are calculated according to these equations:

$$U = \frac{\sum_{j=1}^{n} U_j \cdot A_j}{\sum_{j=1}^{n} A_j} \tag{5}$$

where: U – average overall heat transfer coefficient, W m^{-2} K^{-1}; U_j – overall heat transfer coefficient of j-surrounding wall, W m^{-2} K^{-1}; A_j – surface area of j-surrounding wall, m^2; n – data-set extent.

The reference overall heat transfer coefficient U_R is determined by the following equation:

$$U_R = \frac{\sum_{j=1}^{n} U_j \cdot A_j}{\sum_{j=1}^{n} A_j} \tag{6}$$

where: U_R – reference overall heat transfer coefficient, W m^{-2} K^{-1}; U_N – standard overall heat transfer coefficient of j-surrounding wall, W m^{-2} K^{-1}; A_j – surface area of j-surrounding wall, m^{-2}; n – data-set extent.

As the required internal temperature sufficient for both buildings is only 12 °C, required fundamental value of the reference overall heat transfer coefficient U_R is changed to value U_{R12}. Nevertheless, the average overall heat transfer coefficient U is three and half times higher than overall heat transfer coefficient U_{R12} of the reference building.

Table 4. Classification of evaluated objects according to the European Union energy label

Building	U	U_R	U_{R12}	U : U_R	Classification
A – large ground floor building	2.725	0.386	0.772	3.5	G – extremely non-economical
B – compact high building	3.252	0.493	0.986	3.3	G – extremely non-economical

Improvement of the large ground floor building A

On the example of a large ground floor building A it is suitable to demonstrate the impact of geometric characteristics on the total heat losses. It is not expected that it would be a suitable method of improvement of the winter heat balance for existing buildings, as demands to change layout of the existing building is practically equal to construct a new house, but theoretical considerations on this subject is interesting and practical example is very illustrative.

The large building A will be compared with the theoretical compact building of the same floor area and height of construction. The current use of the buildings A does not allow locating a usable area into several floors, so the theoretical building will be also ground floor. To compare thermal properties of both buildings the average heat transfer coefficient of the building cladding is used for the calculation.

Due to the fact that the real and theoretical structures being compared have the same floor space, as well as both are ground floor with the same slope of the roof, the area of roofs is identical. Also the heat losses by ventilation are considered identical. To the average heat transfer coefficient are included windows, doors etc., thus the quality of both vertical claddings is comparable.

The theoretical compact building is a structure of the same floor area, which is 403.9 m^2 but with a square plan, therefore a usable area is 20.1 · 20.1 m, built-up area of 21 · 21 m. The overall height of the building is 3.7 m. Both constructions are shown

schematically in the Fig. 3. The calculation of the heat losses by heat transmission through surrounding vertical envelope are based on the equation (4). The resulting values for both compared buildings with the same average heat transfer coefficient are shown in the Table 5.

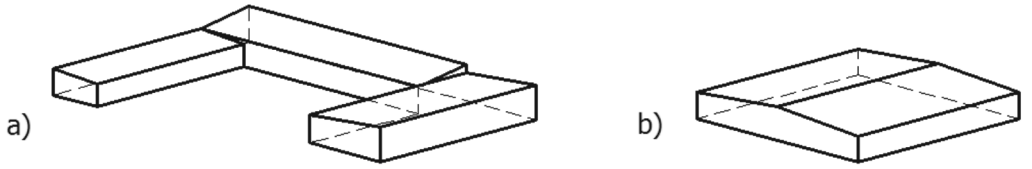

Figure 3. Scheme of: a) the real large ground floor building, b) theoretical compact building.

Table 5. Differences of specific heat losses for both variants of the geometric arrangement of buildings

Specific heat losses	A – large ground floor building	Theoretical compact building	Difference	Savings, %
Surrounding vertical envelope H_{Tp}, W K^{-1}	872.80	550.00	322.80	37.0
Soil, W K^{-1}	253.53	1,77.23	76.30	30.1
Roof and ventilation, W K^{-1}	2,058.60	2,058.6	0.00	0.00
Total, W K^{-1}	3,184.93	2,785.83	399.1	12.5

Practical improvement measures of heat balance in this massive structure will be an additional thermal insulation of claddings, roof and replacing windows and doors. For insulation of surrounding envelope is considered Styrotrade EPS polystyrene foam with a thermal conductivity $\lambda = 0.04$ W m^{-1} K^{-1}. It is assumed that the other parts of the structure after the exchange will exactly achieve the required standard values of the heat transfer coefficient. Relevant parameters of the thickness and the thermal insulation parameters are shown in the Table 6.

Parameters in the Table 6 are: d_x – required thickness of thermal insulation of the j-th component of the envelope, m, U_x – heat transfer coefficient for the j-th component of the envelope after improvement of thermal insulation, W m^{-2} K^{-1}, H_{Tpx} – specific heat loss by the heat transfer through the structure envelope after improvement of thermal insulation, W K^{-1}.

Table 6. Properties of structure specific heat loss of the large ground floor building A after improvement of thermal insulation

Structure component	A_j, m^2	d_x, m	U_x, W m^{-2} K^{-1}	H_{Tpx}, W K^{-1}
Bricks 30	33.87	0.120	0.28	9.46
Bricks 45	232.91	0.100	0.30	69.87
Bricks 60	44.00	0.100	0.29	12.78
Concrete 20	117.15	0.120	0.30	34.88
Ytong	10.10	0.080	0.30	2.99
Doors and windows	54.97	-	1.14	62.79
Roof	477.33	0.16	0.23	111.35
Total, W K^{-1}				304.12

Improvement of the high compact ground floor building B

In the case of a high building B the reduction of energy consumption by improvement of thermal properties of this building would be very expensive, especially because of a large area of glass structures. But inappropriate in this building is mainly the heating system by radiator heating elements installed on the walls. The results of measurements of vertical air temperature profile in twelve height levels from the floor toward the ceiling in the building B are presented in Table 7.

The results of the measurements show the great influence of the height in the hall on air temperature. With increasing height increases the air temperature which shows quite significantly even during this situation with minimum heating and under conditions in the hall with low air temperatures. The difference between the air temperature at floor level (7.1 °C) and temperature at the highest point near the ceiling (10.9 °C) is 3.8 K, which is at these low temperatures very significant difference.

The results of measurement of vertical temperature profile in different parts of the building B show that there is a big difference between the temperature near the floor (working area) and the top of the room (near the ceiling). It causes huge heat losses of the buildings. In conditions of higher air temperatures inside the hall this difference could be increased even more, and cause greater heat loss through the roof to outside air (Zajicek & Kic, 2014). This is the problem of many similar buildings.

It would be better to use for heating radiant ceiling panels. The proposal of necessary components for installation and estimated cost are shown in the Table 8. According to the information available from the literature (Kotrbaty, & Kovarova, 2002; Zajicek & Kic, 2014) achieved energy savings in large buildings are about 40 to 60% of costs.

Table 7. Vertical profile of average air temperatures from the floor toward the ceiling in the building B. Different superscript letters (a, b, c, d, e, f) are the sign of high significant difference (*ANOVA; Tukey HSD Test*; $P \leq 0.05$)

Height from the floor, m	Temperature, °C ± SD
7.7	10.9 ± 0.78^{f}
7.0	10.9 ± 0.48^{f}
6.3	10.6 ± 0.20^{f}
5.6	$10.5 \pm 0.27^{e,f}$
4.9	9.9 ± 0.14^{e}
4.2	9.3 ± 0.17^{d}
3.5	$9.0 \pm 0.18^{c,d}$
2.8	$8.9 \pm 0.12^{c,d}$
2.1	$8.5 \pm 0.17^{b,c}$
1.4	8.2 ± 0.20^{b}
0.7	7.7 ± 0.37^{a}
0	7.1 ± 0.29^{a}

SD – Standard deviation

Table 8. Elements used in the implementation of heating with mounted radiant ceiling panels

Part	Unit, m; pcs	Unit costs including work, €	Total costs including work, €
Radiant strip KSP-750	57 m	73.85	4,209.45
Distribution pipelines	76 m	17.31	1,315.56
Fittings	9 pcs	23.65	212.85
Modification of boiler	1 pcs	173.08	173.08
Control unit	1 pcs	311.54	311.54
Total cost including VAT	-	-	7,466.54

Comparison of average vertical temperature profile in current (measured) status with estimated profile using radiant ceiling panels is presented in the Fig. 4. The value of the vertical temperature profile with ceiling radiant panels are derived from the previous research work (Kotrbaty & Kovarova, 2002; Zajicek & Kic, 2014).

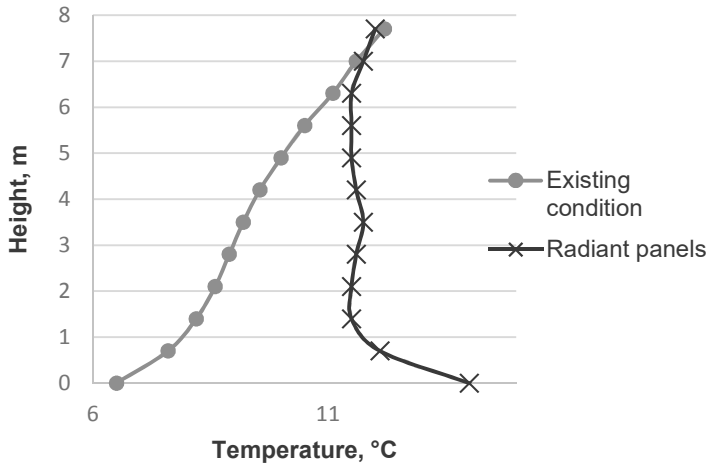

Figure 4. Comparison of vertical temperature profiles current (measured) situation and estimation using radiant ceiling panels.

CONCLUSIONS

This paper shows an overall view on the issue of thermal properties of buildings and some of methods of reduction of energy consumption in large industrial or agricultural buildings. The basic ideas and principles are presented and verified using the example of two different buildings which indicates that:

- in the large ground floor building is the biggest shortage not suitable geometric characteristics of the building and the large area of envelope constructions. The useful method and approach for improvement is comparison of new project with the theoretical compact building and consequently choosing appropriate shape of the building and arrangement of adequate heating method with respect to the shape of the building.
- The solution which can be used for existing large ground floor buildings is improvement of the thermal insulation and replacement of old windows and doors,
- in the large and high building with large glass parts of the structure the suitable solution is to change the heating system; radiant ceiling panels are in this case the most suitable solution,
- described changes should be considered for modernization of older buildings,
- basic ideas outlined in this article should be taken into the account during the design of new buildings; architectural and structural design should take into the consideration the need to minimize energy for heating since the beginning of project preparation.

REFERENCES

Bernardinová, A. & Mareš, M. 2013. *Processing of building energy performance certificate: a practical guide for all owners of houses and apartment buildings, housing and real estate agents*. Linde, Praha, 148 pp. (in Czech).

Basta, J. 2010. *Large Radian Heating*. Grada Publishing, Praha, 128 pp. (in Czech).

Cihelka, J. 1961. *Radian Heating*. SNTL, Praha, 373 pp. (in Czech).

Kic, P. 2013. Hot-air heating of family houses with accumulation of energy in the floor. *Agronomy Research* **11**(2), 329–334.

Kic, P. 2015. Hot-air distribution in the floor heating. *Agronomy Research*, **13**(2), 494–499.

Kotrbaty, M. & Kovarova, Z. 2002. Heating by suspended radiant panels. *Vytapeni, vetrani, instalace* **4**, 134–138. (in Czech).

Vio, M. 2011. *Climatization with Radiant Systems.* Editoriale Delfino, Milano, 264 pp. (in Italian).

Visockis, E., Vucenlazdans, P., Ansone, V. & Morozova, I. 2011. Research on possibilities for decreasing heat losses in buildings. In: *10th International Scientific Conference Engineering for Rural Development*. Latvia University of Agriculture, Jelgava, 342–347.

Zajicek, M. & Kic, P. 2014. Heating of large agricultural and industrial buildings. *Agronomy Research* **12**, 237–244.

Agronomy Research **14**(Sp.1), 1232–1240, 2016

Numerical Modelling of Transient Phenomena in a Synchronous Machine

Z. Vondrášek

[1]Czech University of Life Sciences Prague, Faculty of Engineering, Department of Electrical Engineering and Automation, Kamýcká 129, CZ 16521 Praha 6 – Suchdol, Czech Republic; e-mail: vondrasek@tf. czu.cz

Abstract. The present contribution deals with the idea of identification of electromagnetic transient phenomena pages in a synchronous machine – namely of distant short circuits – by numerical modelling. Phenomena in AC windings of a synchronous machine (stator) have a backswing effect on the phenomena in DC windings – namely the excitation one. Concerned is namely the current stress of the excitation circuit during the transient phenomenon. The computer model is created in the Famulus- vers. 3 – environment. The time behaviour of AC circuit currents in components d, q and the excitation circuit is monitored on the example of a 3-pole distant short circuit in a synchronous machine (via the impedances of connecting elements). The results are compared of models with a simpler structure (one damper circuit in the rotor) with those with a more complicated structure (two damper circuits in the rotor).

Key words: electromagnetic system, synchronous machine, transient phenomena, modelling.

INTRODUCTION

Specific problems appear in the process of creating mathematical models of physical systems. The most essential issue appears to be the description of mutual relations between individual elements of the system and their mathematical interpretation. An important aspect of the created model is the possibility of modifications in a form allowing elimination of potential inaccuracies or minimization of their effect. Simulation experiments allow creation of alternative forms of models and their structures which enable the results of models to be in closest agreement with the behaviour of real electrodynamic systems (e. g. a synchronous machine supplying an independent network). The tool used for this purpose is the Famulus programme environment created at Charles University. Compared with the globally used simulation programme Matlab, its advantage is that it requires less sophisticated hardware but on the other hand it requires at least a minor knowledge of programming. Modelling of synchronous machines is important for estimating their behaviour in various modes of operation. This is based on the fact that synchronous machines are used in a broad range of applications. For example, for research on the effect of the excitation system of a synchronous machine on the power engineering network Jonaitis (2013) used the Heffron-Phillips model. Transients on exciting and damper windings on synchronous

machine during de-excitation are explored by Hořan (2015). Machines with permanent magnet exciting are frequently used for driving applications. The verification of modell-parametters for this construction of synchronous machine is described by Novák et al. (2012). Comparison of simulation results of Park-Gorevs model structures with a various number of damper circuits in the rotor is performed on a 3-pole distant short circuit in a synchronous machine.

MATERIALS AND METHODS

Theoretical Solutions

The model of a synchronous machine is created by means of the Park-Gorev transformation of coordinates into d, q, 0 components. Under conditons of linearity a similar model was created by T. Laible, described by Hora & Navrátil (1976) and Laible (1957) and modified according to Canay (1980). In the most basic case a description is necessary by means of systems of voltages (u), currents (i) and linked magnetic fluxes (ψ), possibly also by conversion relations of phase and component quantities. Another type of description can be performed either by means of physical quantities or proportional ones related to specific quantities of the investigated machine. Proportional (per-Unit) quantities (p. U.) were selected for further description.

The description of a synchronous machine in the d-q-0 system by means of proprotional (p. U.) quantities is performed in accordance with Fig. 1 by the system of equations (1) for voltages, currents and linked magnetic fluxes. It includes additional connecting elements with circuit parameters – resistance r_V and reactance x_V – between the machine and the short circuit location.

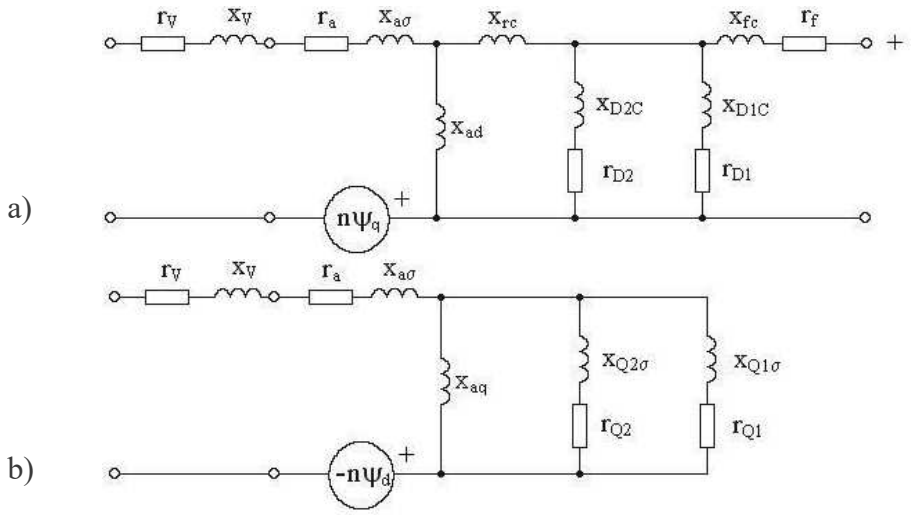

Figure 1. Schematic arrangement of equivalent circuits of a synchronous machine with two damper circuits: a) direct axis; b) transversal axis.

$$
\begin{aligned}
u_d &= -\left(r_V + r_a\right)\times i_d - \frac{d\psi_d}{dt} + n\times\psi_q \\
u_q &= -\left(r_V + r_a\right)\times i_q - \frac{d\psi_q}{dt} - n\times\psi_d \\
u_0 &= -\left(r_V + r_a\right)\times i_0 - \frac{d\psi_0}{dt} \\
u_f &= r_f \times i_f - \frac{d\psi_f}{dt} \\
0 &= u_{D1} = r_{D1}\times i_{D1} - \frac{d\psi_{D1}}{dt} \\
0 &= u_{D2} = r_{D2}\times i_{D2} - \frac{d\psi_{D2}}{dt} \\
0 &= u_{Q1} = r_{Q1}\times i_{Q1} - \frac{d\psi_{Q1}}{dt} \\
0 &= u_{Q2} = r_{Q2}\times i_{Q2} - \frac{d\psi_{Q2}}{dt}
\end{aligned}
\tag{1}
$$

where r_V is the proportional resistance of the circuit connecting the machine and the short circuit location, r_a is the proportional resistance of the stator winding of the machine, r_{D1} & r_{D2} are the proportional resistances of rotor damper windings in the direct axis of the machine, r_{Q1} &d r_{Q2} = proportional resistance of rotor damper windings in the direct axis of the machine and n is the propotional magnitude of rpm of the machine. The indexes of circuit quantities (*u, i, ψ*) have the following meaning: *d* = relation to the direct machine axis, *D1* & *D2* = relation to damper windings in the direct axis of the rotor in corresponding sequence, *f* = relation to the excitation winding (in the rotor), *q* = relation to the transversal axis of the stator, *Q1* & *Q2* = relation to damper windings in the transversal axis of the rotor in corresponding sequence, *0* = relation to 'non-rotating' quantities of the stator, *a* = relation to stator windings, *V* = relation to connecting elements between the machine and the short circuit location.

In contrast with the system of forming linked magnetic fluxes, which has a certain variability, the decribed system of equations for the voltage of the system will not substantially change The system according to Canay (1980), which can use in a linear approximation with advantage a matrix notation, can be applied for comparison.

$$
\begin{bmatrix} \psi_d \\ \psi_{D1} \\ \psi_{D2} \\ \psi_f \end{bmatrix} = \begin{bmatrix} \left(x_V + x_{a\sigma} + x_{ad}\right) & x_{ad} & x_{ad} & -x_{ad} \\ x_{ad} & \left(x_{ad} + x_{rC} + x_{D1C}\right) & \left(x_{ad} + x_{rC}\right) & -\left(x_{ad} + x_{rC}\right) \\ x_{ad} & \left(x_{ad} + x_{rC}\right) & \left(x_{ad} + x_{rC} + x_{D2C}\right) & -\left(x_{ad} + x_{rC}\right) \\ -x_{ad} & -\left(x_{ad} + x_{rC}\right) & -\left(x_{ad} + x_{rC}\right) & \left(x_{ad} + x_{rC} + x_{fC}\right) \end{bmatrix} \times \begin{bmatrix} i_d \\ i_{D1} \\ i_{D2} \\ i_f \end{bmatrix}
$$

$$
\begin{bmatrix} \psi_q \\ \psi_{Q1} \\ \psi_{Q2} \end{bmatrix} = \begin{bmatrix} \left(x_V + x_{a\sigma} + x_{aq}\right) & x_{aq} & x_{aq} \\ x_{aq} & \left(x_{aq} + x_{Q1\sigma}\right) & x_{aq} \\ x_{aq} & x_{aq} & \left(x_{aq} + x_{Q2\sigma}\right) \end{bmatrix} \times \begin{bmatrix} iq \\ i_{Q1} \\ i_{Q2} \end{bmatrix} \tag{2}
$$

$$
\psi_0 = x_0 \times i_0
$$

where x_{ad} = proportional main reactance in the direct stator axis, $x_{a\sigma}$ = proportional leakage reactance of stator windings, x_{rc} = proportional coupling reactance of rotor windings in the direct axis with respect to the main flux according to Canay (1980), x_{D1c} and x_{D2c} = proportional leakage reactances of rotor damper windings according to Canay (1980), x_{fc} = proportional leakage reactance of the excitation winding, x_{aq} = proportional main reactance in the transversal axis of the stator, $x_{Q1\sigma}$ and $x_{Q2\sigma}$ = proportional leakage reactances of rotor damper windings in the transversal axis in corresponding sequence, x_0 = proportional reactance of the non-rotating stator component, x_v = proportional reactance of the connecting lead between the machine and the short circuit location.

$$
\begin{aligned}
\frac{d\psi_d}{dt} &= -u_d - (r_V + r_a)\times i_d + n\times\psi_q \\
\frac{d\psi_q}{dt} &= -u_q - (r_V + r_a)\times i_q - n\times\psi_d \\
\frac{d\psi_0}{dt} &= -u_0 - (r_V + r_a)\times i_0 \\
\frac{d\psi_f}{dt} &= u_f - r_f\times i_f \\
\frac{d\psi_{D1}}{dt} &= -r_{D1}\times i_{D1} \\
\frac{d\psi_{D2}}{dt} &= -r_{D2}\times i_{D2} \\
\frac{d\psi_{Q1}}{dt} &= -r_{Q1}\times i_{Q1} \\
\frac{d\psi_{Q2}}{dt} &= -r_{Q2}\times i_{Q2}
\end{aligned}
\qquad (3)
$$

The method of solution is as follows: voltage equations (1) are modified into the form (3), where on one side of the equation are time derivatives of linked magnetic fluxes and on the other side the remaining parts. The fact is taken into consideration that linked magnetic fluxes do not variate suddenly compared with other circuit quantities. During the short circuit in a particular winding this winding tries to maintain a constatnt magnitude of the linked magnetic flux, which, however, changes its magnitude compared with that at the moment of the short circuit due to the rotation of the rotor. The time variations of the magnitudes of linked magnetic fluxes can be quantified by means of the system of equations (3).

Experimental Implementation

The implementation is carried out for a ŠKODA synchronous alternator with a typical 250 MVA output which is used for short circuit tests at the test plant of the former Heavy Current Electrical Engineering Research Institute (VÚSE) Prague-Běchovice. The parameters of the alternator are in Table 1.

Table 1. Parameters of synchronous machine Škoda (type HB 644862/2)

S = 250 MVA	U_{1n} = 13 kV	I_{1n} = 11.1 kA	X_d' = 0.0825 Ω	T_d" = 0.026 s
n_n = 3,000 min^{-1}	f_n = 50 Hz	GD^2 = 19 t. m^2	X_d" = 0.0635 Ω	T_d' = 0.647 s
U_f = 139 V	I_f = 700 A	R_f = 0.197 Ω	X_0 = 0.05766 Ω	T_a = 0.091 s
R_a =1.985 mΩ	Z_n = 0.67595 Ω	X_d = 1.0806 Ω	X_2 = 0.659 Ω	T_{d0}' = 8.473 s

The parameters are transformed in the simulation programme into per-unit-quantities and all time quantities are transformed into angular ones in radians for the specific frequency and rpm of the alternator. The Runge-Kutta method according to Ralston (1978) usually gives more accurate results (standard procedure of the Famulus programme) is used for the calculation of the simulation. Another alternative is the Euler incrementation method, which is according to Ralston (1978) not as accurate as the Runge-Kutta method, but is easier in completing the model with further elements and effects.

The synchronous generator was connected with the short circuit location with connecting elements. The parameters of the connecting elements are in Table 2.

Table 2. Parameters of connecting elements for short circuit tests

Test – denotation	Connecting element – denotation	X_V [Ω]	x_V [P. U.]	R_V [mΩ]	r_V [P. U.]
62195	X45	0.65033	0.962032	10.10	0.014941
62198	X13	0.086168	0.1274749	1.44	0.0021303

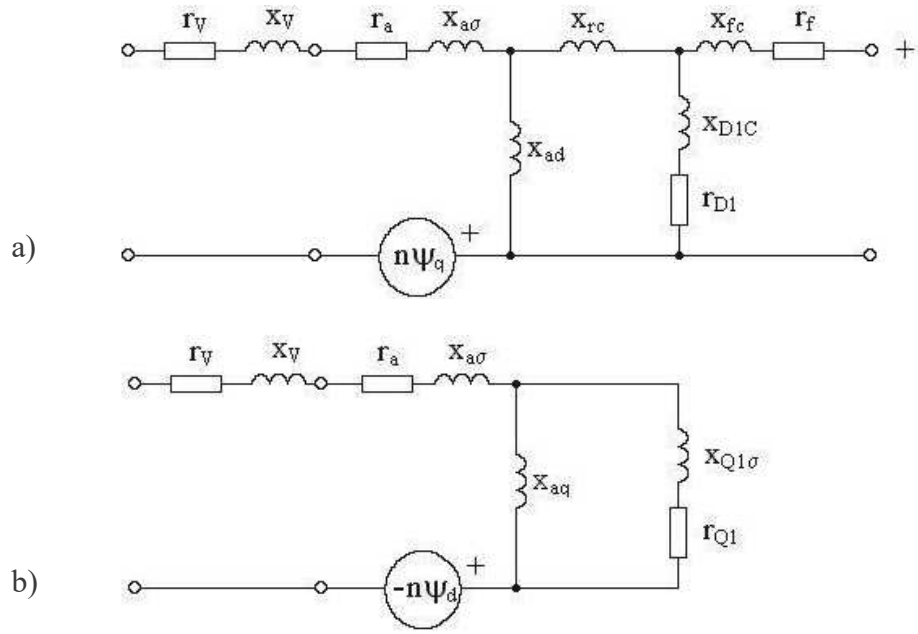

Figure 2. Schematic arrangement of equivalent circuits of a synchronous machine with one damper circuit in the rotor: a) direct axis; b) transversal axis.

RESULTS AND DISCUSSION

The calculations of currents during a transient phenomenon are performed assuming constant rpm of the machine ($n = n_S = const.$) and a constant magnitude of the excitation winding voltage applying connecting impedance X13 according to Test 62198 (more severe operating short circuit). For the analysis only a 3-pole symmetrical short circuit was considered, during which a non-rotating component i_0 of the stator windings current is not developed, and the whole calculation of the conditions for the current during a short circuit is as easy as possible.

Fig. 3 shows the time behaviour of equivalent stator currents in the direct and transversal axis and the excitation current after reduction into unit initial excitation values applying a more complicated model structure with two damper circuits according to Fig. 1. The result of the numerical calculation of a short circuit after approx. 0.1 sec. (i. e. at $\omega t \approx 30$ rad) diverges. The divergence primarily affects the transversal component of the stator currents, and in a further 0.2 sec (i. e. at *0.3 s*, or $\omega t \approx 120$ rad) affects also all other monitored currents. Experiments both with changes of circuit parameters and shortening of the calculation step did not lead to an elimination of this divergence. In fact the results are actually devalued and are absolutely different from those in the oscillogram of a real short circuit – comparing Figs 3 & Fig. 5.

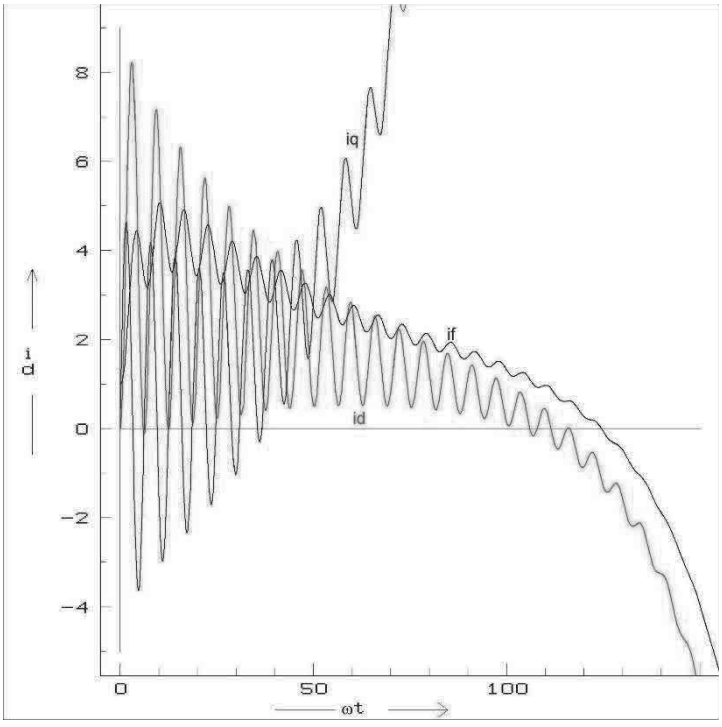

Figure 3. Result of numerical calculations of the time behaviours of currents in equivalent stator windings in the direct axis (i_d, i_q) and the excitation current (i_f) during a more severe operating short circuit applying a more complicated structure model.

Fig. 4 shows the time behaviour of excitation and equivalent stator currents in individual axes applying a simpler structure model according to Fig. 2. By comparison with the real behaviour of currents during the short circuit test on the oscillogram in Fig. 5 it can be observed that the calculated behaviour of the excitation cuurent is very similar to that on the real oscillogram. The magnitude of the maximum amplitude of oscillation of the excitation current shows a dissimilarity – in the calculation it is by 10.5% higher than the recorded reality. For the dimensioning of serial elements of the excitation circuit such a partial 'overestimation' of the expected magnitude of the excitation current compared with reality can be an advantage since it reduces the risk of damage of additional elements of the excitation circuit Also the identification of parameters of equivalent model diagrams, due to the above minimum difference of the simulation results from the real state appears to be correct.

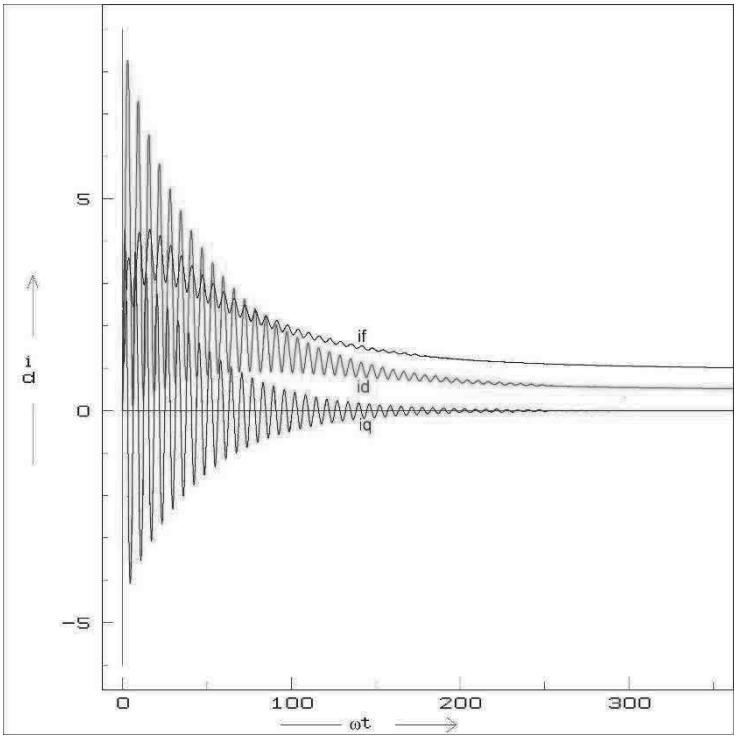

Figure 4. Result of numerical calculation of the time behaviours of circuits in equivalent stator windings in the direct and transversal axis (i_d, i_q) and the excitation current (i_f) during a more severe operating short circuit applying a simpler model structure.

By the application of a simpler structure of equivalent diagrams with one damper circuit in the rotor, paradoxically more correct results are obtained of the calculation of transient phenomena in a synchronous machine. The more complicated structure with a larger number of damper windings has a questionable calculation stability of long-term phenomena. Numerical divergence of a more complicated structure can be eliminated only with difficulty and hitherto has not been sucessfully accomplished.

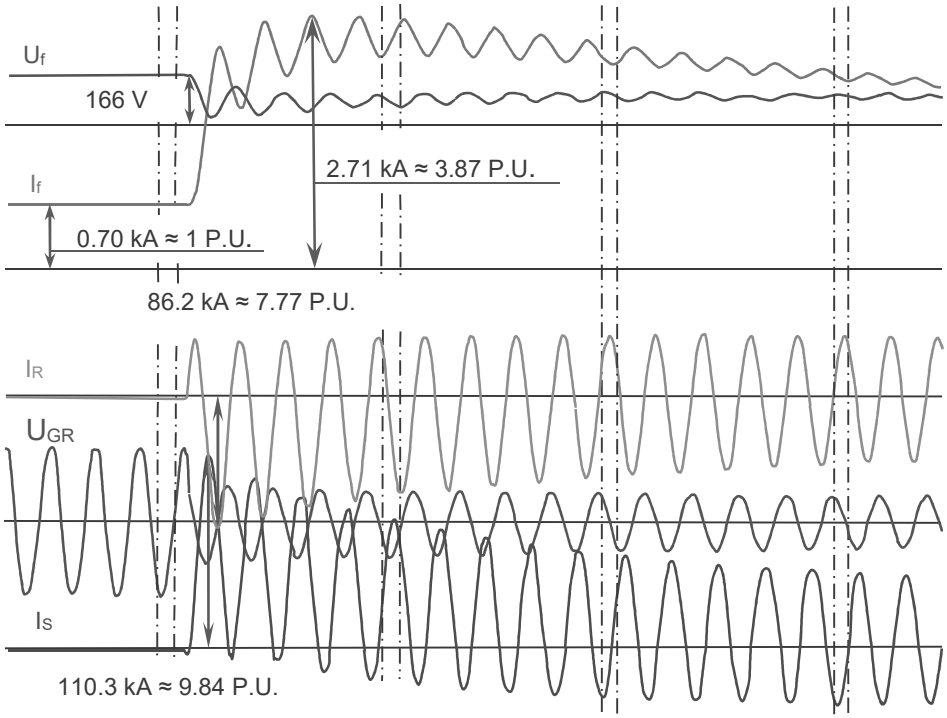

Figure 5. Real oscillogram of an exciting current (I_f) and stator windings curents (I_R, I_S) on more severe operating short circuit by speed 3,000 rpm (machine output frequency 50 Hz).

CONCLUSIONS

By the application of a simpler structure of equivalent diagrams with one damper circuit in the rotor, paradoxically more correct results are obtained of the calculation of transient phenomena in a synchronous machine meanly comparising between Fig. 4 and Fig. 5. The more complicated structure with a larger number of damper windings has a questionable calculation stability of long-term phenomena, see Fig. 3 and Fig. 5. Numerical divergence of a more complicated structure can be eliminated only with difficulty and has not been sucessfully accomplished.

ACKNOWLEDGEMENTS. Especially acknowledgements for company Zkušebnictví a.s., primarily Ing. Mastný Vladimír and Ing. Křemen Pavel CSc. for granting of archival oscilograms of try-out for verifying on modelling.

REFERENCES

Canay, M. 1980. *Equivalent Diagrams of a Synchronous Machine and Calculation of Characteristic Values with Examples*. Lausane, École polytechnique de l'Université de Lausane, 151 pp. (in German).

Dvořák, L., Ledvinka, T. & Sobotka, M. 1992. *Famulus Etc. – User Manuals of the Famulus 3.5 System.* Prague, Famulus Etc, 307 pp. (in Czech).

Hora, O. & Navrátil, S. 1976. *Controlling of Electrical Machines*. Prague, SNTL-Theoretical Engineers Library, 483 pp. (in Czech).

Hořan, M. 2015. De-Excitation Action of Synchronous Machine. In: *Elektrotechnika a informatika 2015 – Elektrotechnika, elektronika, elektroenergetika*. Pilsen, University of West Bohemia in Pilsen, pp. 59–62. ISBN: 978-80-261-0514-5. (in Czech).

Jonaitis, A. 2013. Impact of Increased Frequency Excitation System on Stability of Synchronous Generator. In: *Elektronika ir Elektrotechnika* **19**(4), 29–32.

Laible, T. 1957. *Theory of Synchronous Machine during Transients.* Moscow, Gosudarstvennoe energeticheskoe izdatelstvo, 169 pp. (in Russian).

Novák, M, Novák, J. & Chyský, J. 2012. Experimental verification of high-speed permanent magnet synchronous motor model. In: *20th International Conference on Electrical Machines*, *ICEM 2012*, 2435–2440. ISBN 978-1-4673-0143-5

Ralston, A. 1978. *Fundamentals of Numerical Mathematics*. Prague, Academia, 635 pp. (in Czech).

Vondrášek, Z. 2009. *Identification of Parameters of a Synchronous Machine*. Prague, Czech University of Life Sciences, doctoral dissertation, 91 pp. (in Czech).

INSTRUCTIONS TO AUTHORS

Papers must be in English (British spelling). English will be revised by a proofreader, but authors are strongly urged to have their manuscripts reviewed linguistically prior to submission. Contributions should be sent electronically. Papers are considered by referees before acceptance. The manuscript should follow the instructions below.

Structure: Title, Authors (initials & surname; an asterisk indicates the corresponding author), Authors' affiliation with postal address (each on a separate line) and e-mail of the corresponding author, Abstract (up to 250 words), Key words (not repeating words in the title), Introduction, Materials and methods, Results and discussion, Conclusions, Acknowledgements (optional), References.

Layout, page size and font

- Use preferably the latest version of **Microsoft Word**, doc., docx. format.
- Set page size to **B5 Envelope or ISO B5 (17.6 x 25 cm)**, all margins at 2 cm.
- Use single line spacing and justify the text. Do not use page numbering. Use indent 0.8 cm (do not use tab or spaces instead).
- Use font Times New Roman, point size for the title of article **14 (Bold)**, author's names 12, core text 11; Abstract, Key words, Acknowledgements, References, tables and figure captions 10.
- Use *italics* for Latin biological names, mathematical variables and statistical terms.
- Use single ('…') instead of double quotation marks ("…").

Tables

- All tables must be referred to in the text (Table 1; Tables 1, 3; Tables 2–3).
- Use font Times New Roman, regular, 10 pt. Insert tables by Word's 'Insert' menu.
- Do not use vertical lines as dividers; only horizontal lines (1/2 pt) are allowed. Primary column and row headings should start with an initial capital.

Figures

- All figures must be referred to in the text (Fig. 1; Fig. 1 A; Figs 1, 3; Figs 1–3). Use only black and white or greyscale for figures. Avoid 3D charts, background shading, gridlines and excessive symbols. Use font **Arial** within the figures. Make sure that thickness of the lines is greater than 0.3 pt.
- Do not put caption in the frame of the figure.
- The preferred graphic format is EPS; for half-tones please use TIFF. MS Office files are also acceptable. Please include these files in your submission.
- Check and double-check spelling in figures and graphs. Proof-readers may not be able to change mistakes in a different program.

References

- **Within the text**

In case of two authors, use '&', if more than two authors, provide first author 'et al.':

Smith & Jones (1996); (Smith & Jones, 1996);
Brown et al. (1997); (Brown et al., 1997)

When referring to more than one publication, arrange them by following keys: 1. year of publication (ascending), 2. alphabetical order for the same year of publication:

(Smith & Jones, 1996; Brown et al., 1997; Adams, 1998; Smith, 1998)

- **For whole books**

Name(s) and initials of the author(s). Year of publication. *Title of the book* (*in italics*). Publisher, place of publication, number of pages.

Shiyatov, S.G. 1986. *Dendrochronology of the upper timberline in the Urals*. Nauka, Moscow, 350 pp. (in Russian).

- **For articles in a journal**

Name(s) and initials of the author(s). Year of publication. Title of the article. *Abbreviated journal title* (*in italic*) volume (in bold), page numbers.

Titles of papers published in languages other than English, German, French, Italian, Spanish, and Portuguese should be replaced by an English translation, with an explanatory note at the end, e.g., (in Russian, English abstr.).

Karube, I. & Tamiyra, M.Y. 1987. Biosensors for environmental control. *Pure Appl. Chem.* **59**, 545–554.

Frey, R. 1958. Zur Kenntnis der Diptera brachycera p.p. der Kapverdischen Inseln. *Commentat.Biol.* **18**(4), 1–61.

Danielyan, S.G. & Nabaldiyan, K.M. 1971. The causal agents of meloids in bees. *Veterinariya* **8**, 64–65 (in Russian).

- **For articles in collections:**

Name(s) and initials of the author(s). Year of publication. Title of the article. Name(s) and initials of the editor(s) (preceded by In:) *Title of the collection (in italics)*, publisher, place of publication, page numbers.

Yurtsev, B.A., Tolmachev, A.I. & Rebristaya, O.V. 1978. The floristic delimitation and subdivisions of the Arctic. In: Yurtsev, B. A. (ed.) *The Arctic Floristic Region*. Nauka, Leningrad, pp. 9–104 (in Russian).

- **For conference proceedings:**

Name(s) and initials of the author(s). Year of publication. Name(s) and initials of the editor(s) (preceded by In:) *Proceedings name (in italics)*, publisher, place of publishing, page numbers.

Ritchie, M.E. & Olff, H. 1999. Herbivore diversity and plant dynamics: compensatory and additive effects. In: Olff, H., Brown, V.K. & Drent R.H. (eds) *Herbivores between plants and predators. Proc. Int. Conf. The 38th Symposium of the British Ecological Society*, Blackwell Science, Oxford, UK, pp. 175–204.

.....……

Please note

- Use '.' (not ',') for decimal point: 0.6 ± 0.2; Use ',' for thousands – 1,230.4;
- Use '–' (not '-') and without space: pp. 27–36, 1998–2000, 4–6 min, 3–5 kg
- With spaces: 5 h, 5 kg, 5 m, 5°C, C : D = 0.6 ± 0.2; $p < 0.001$
- Without space: 55°, 5% (not 55 °, 5 %)
- Use 'kg ha^{-1}' (not 'kg/ha');
- Use degree sign ' ° ' : 5 °C (not 5 ^{O} C).